



**HAL**  
open science

# Biomarkers Identification and Disease Modeling using Multimodal Neuroimaging Approaches in Polyglutamine Diseases

Isaac Mawusi Adanyeguh

► **To cite this version:**

Isaac Mawusi Adanyeguh. Biomarkers Identification and Disease Modeling using Multimodal Neuroimaging Approaches in Polyglutamine Diseases. *Neurons and Cognition [q-bio.NC]*. Université Pierre et Marie Curie - Paris VI, 2017. English. NNT: 2017PA066279 . tel-02289619v1

**HAL Id: tel-02289619**

**<https://theses.hal.science/tel-02289619v1>**

Submitted on 17 Sep 2019 (v1), last revised 18 Sep 2019 (v2)

**HAL** is a multi-disciplinary open access archive for the deposit and dissemination of scientific research documents, whether they are published or not. The documents may come from teaching and research institutions in France or abroad, or from public or private research centers.

L'archive ouverte pluridisciplinaire **HAL**, est destinée au dépôt et à la diffusion de documents scientifiques de niveau recherche, publiés ou non, émanant des établissements d'enseignement et de recherche français ou étrangers, des laboratoires publics ou privés.

Université Pierre et Marie Curie

Ecole Doctorale Cerveau Cognition Comportement

*Institut du Cerveau et de la Moelle Épinière*

**Biomarkers Identification and Disease Modeling using  
Multimodal Neuroimaging Approaches in Polyglutamine  
Diseases**

Par **Isaac ADANYEGUH**

Thèse de doctorat de **Neurosciences**

Dirigée par Fanny MOCHEL

Présentée et soutenue publiquement le 15 Septembre, 2017

Devant un jury composé de :

Dr RONEN Itamar	Directeur de Recherche	Rapporteur
Pr TRANCHANT Christine	Professeur des Universités	Rapporteur
Dr BETUING Sandrine	Maître de conférences	Représentant de UPMC
Dr BROUILLET Emmanuel	Directeur de Recherche	Examineur
Pr DURR Alexandra	Professeur des Universités	Examineur
Dr HENRY Pierre-Gilles	Directeur de Recherche	Examineur
Pr FLAMAND ROZE Emmanuel	Professeur des Universités	Examineur
Dr MOCHEL Fanny	Maître de conférences	Directeur de thèse



*Dedicated to all patients suffering from neurodegenerative disorders especially Huntington disease and spinocerebellar ataxia*



# Table of Contents

<b>Remerciements</b> .....	<b>ix</b>
<b>List of publications</b> .....	<b>xi</b>
<b>List of tables</b> .....	<b>xiii</b>
<b>List of figures</b> .....	<b>xiv</b>
<b>List of abbreviations</b> .....	<b>xvi</b>
<b>Abstract</b> .....	<b>xviii</b>
<b>Résumé</b> .....	<b>xx</b>
<b>Introduction</b> .....	<b>1</b>
<b>Chapter 1</b> .....	<b>4</b>
<b>Polyglutamine disorders</b> .....	<b>5</b>
1.1 Huntington disease .....	6
1.1.1 Genetics and mitochondrial dysfunction in HD .....	7
1.1.2 Pathogenesis and symptoms of HD .....	9
1.2 Spinocerebellar ataxia .....	11
1.2.1 Spinocerebellar ataxia type 1 (SCA1) .....	12
1.2.2 Spinocerebellar ataxia type 2 (SCA2) .....	14
1.2.3 Spinocerebellar ataxia type 3 (SCA3) .....	16
1.2.4 Spinocerebellar ataxia type 7 (SCA7) .....	18
1.3 Diagnosis and treatment of polyglutamine diseases.....	21
<b>Magnetic resonance (MR) approaches to biomarker identification</b> .....	<b>23</b>
1.4.1 Principles of MR.....	23
1.4.2 Evaluating atrophy and axonal damage .....	26
1.4.3 Determination of brain metabolic alterations with MRS.....	29
<b>Objectives</b> .....	<b>33</b>
<b>Chapter 2</b> .....	<b>34</b>
<b>Study 1: Validation of a functional biomarker and its use to evaluate an anaplerotic therapy in HD.</b> .....	<b>35</b>
2.1 Introduction and objectives .....	35

2.2	Materials and methods.....	35
2.3	Principal results .....	36
2.4	Published article .....	37
2.6	Perspective.....	44
2.6.1	TRIHEP3 .....	44
2.6.2	REVHD .....	46
2.6.3	Key role of MRI-MRS evaluations in both studies.....	48
<b>Chapter 3</b>	.....	<b>49</b>
	<b>Study 2a: Understanding the biochemical basis of altered bioenergetics in HD using <sup>31</sup>P MT .....</b>	<b>50</b>
3.1.1	Introduction and objectives.....	50
3.1.2	Materials and methods.....	50
3.1.3	Results.....	51
	<b>Study 2b: Proton spectroscopy in the visual cortex and striatum of HD.....</b>	<b>53</b>
3.2.1	Introduction and objectives.....	53
3.2.2	Materials and methods.....	53
3.2.3	Principal results .....	54
3.2.4	Submitted paper for publication .....	54
3.3	Perspective: Identifying biomarkers of dynamic energy metabolism (HDeNERGY).....	79
3.3.1	<sup>31</sup> P magnetization transfer .....	79
3.3.2	Diffusion weighted spectroscopy .....	80
3.3.3	Resting state functional MRI (rsfMRI) .....	82
3.3.4	Structural analysis .....	85
3.3.5	Protocol setup.....	86
<b>Chapter 4</b>	.....	<b>87</b>
	<b>Study 3: Standardization and optimization of <sup>1</sup>H MRS protocol at 3T using short-echo, single-voxel semi-LASER protocol .....</b>	<b>88</b>
4.1	Introduction and objectives .....	88
4.2	Materials and methods.....	88
4.3	Results .....	89

4.5	Published article .....	89
<b>Chapter 5</b>	.....	<b>98</b>
	<b>Study 4: Application of the validated <sup>1</sup>H MRS protocol in SCAs.....</b>	<b>99</b>
5.1	Introduction and objectives .....	99
5.2	Materials and methods.....	99
5.4	Principal results .....	99
5.5	Published article .....	100
<b>Chapter 6</b>	.....	<b>115</b>
	<b>Study 5: Autosomal dominant ataxia: identification of imaging biomarkers with high effect size .....</b>	<b>116</b>
6.1	Introduction and objectives .....	116
6.2	Materials and methods.....	117
6.2.1	Participants .....	117
6.2.2	Imaging protocol .....	118
6.2.3	Volumetric analysis.....	118
6.2.4	Rate of atrophy .....	119
6.2.5	Diffusion tensor imaging.....	119
6.2.6	Tractography - Fixel based analysis.....	120
6.2.7	Statistical analysis .....	121
6.3	Results .....	122
6.3.1	Clinical score.....	122
6.3.2	Volumetric analysis.....	122
6.3.3	Diffusion tensor imaging.....	123
6.3.4	Fixel Based Analysis .....	123
6.3.5	Effect size .....	123
6.4	Discussion.....	135
<b>Chapter 7</b>	.....	<b>138</b>
	<b>Study 6: A strategy for multimodal data integration: application to biomarkers identification in spinocerebellar ataxia .....</b>	<b>139</b>
7.1	Introduction and objectives .....	139



7.2	Materials and methods.....	139
7.3	Principal results .....	140
7.4	Perspective.....	140
7.5	Published article .....	140
<b>Chapter 8</b>	.....	<b>155</b>
<b>Conclusion</b>	.....	<b>156</b>
<b>References</b>	.....	<b>158</b>
<b>Annex</b>	.....	<b>177</b>
	Triheptanoin dramatically reduces paroxysmal motor disorder in patients with GLUT1 deficiency. ....	177

# Remerciements

Je tiens à remercier tous les participants des diverses études qui ont rendu ce projet possible.

Mes remerciements vont au CENIR, CIC, CMRR et la plateforme de Bioinformatique et Biostatistique de l'ICM pour leur soutien technique et leurs ressources humaines. Je remercie Romain Valabregue de m'avoir donné des instructions sur la programmation et le traitement du signal en Matlab, Mélanie Didier pour l'acquisition de données quand je n'étais pas disponible, Francesca Branzoli pour son assistance en spectroscopie, Vincent Perlbag pour la programmation en Python et les analyses statistiques, et Stéphane Lehericy et Eric Bardinet pour avoir permis de réaliser des études pilotes. Je remercie Pierre-Gilles Henry, Dinesh Deelchand et Gulin Oz pour les tutoriels sur la physique et pour leur grande disponibilité lorsqu'il s'agit de conseil en traitement et quantification des données spectroscopiques.

Toutes ces études ne se seraient pas déroulées sans la coordination des assistants de recherche clinique. Je suis donc reconnaissant à Daisy Rinaldi, Marie Pierre Luton, Mariana Atencio Segura, Magali Barbier, Tiffany Monnier, Céline Jauffret, Elodie Petit, Sandra Benaich et Sarah Boster.

Je saisis cette occasion pour remercier également Tra My Nguyen, pour m'avoir aidé à affiner mes compétences en acquisition de données.

Je remercie Alexis Brice qui m'a accueilli dans son laboratoire et m'a donné un soutien académique et administratif lors de ma thèse. Je tiens à remercier Alexandra Durr pour ses enseignements sur les maladies neurodégénératives, en particulier les ataxies spinocérébelleuses.

Mes sincères remerciements à mon superviseur de thèse, Fanny Mochel, pour m'avoir donné une chance et l'occasion de développer et d'améliorer mes compétences en neuroimagerie. Son dévouement à la recherche et sa motivation pour développer des talents chez les autres, en particulier les jeunes scientifiques, sont uniques.

J'aimerais remercier mes collègues – Fernando Pérez García, Fatma Gargouri, Sophie Sebille et Eric Moulton – que j'ai pu déranger à tout moment afin de discuter de problèmes de programmation.

Mes sincères remerciements à mon père et mes frères et sœurs pour tous leurs encouragements.

Enfin, je suis pour toujours redevable à ma femme, Joana Adanyeguh et à ma petite fille Arielle Adanyeguh, pour leur force et leur soutien pendant tout le temps où nous avons été séparés durant ma thèse.

# List of publications

## Published articles

Garali I, **Adanyeguh IM**, Ichou F, Perlberg V, Seyer A, Colsch B, Mozer I, Guillemot V, Durr A, Mochel F, Tenenhaus A. A strategy for multimodal data integration: application to biomarkers identification in spinocerebellar ataxia. *Brief Bioinform* 2017: Epub July 03. <https://doi.org/10.1093/bib/bbx060>

**Adanyeguh IM**, Rinaldi D, Henry PG, Caillet S, Valabregue R, Durr A, Mochel F. Triheptanoin improves brain energy metabolism in patients with Huntington disease. *Neurology* 2015;84(5):490-495. <https://doi.org/10.1212/WNL.0000000000001214>

**Adanyeguh IM**, Henry PG, Nguyen TM, Rinaldi D, Jauffret C, Valabregue R, Emir UE, Deelchand DK, Brice A, Eberly LE, Öz G, Durr A, Mochel F. In vivo neurometabolic profiling in patients with spinocerebellar ataxia types 1, 2, 3, and 7. *Mov Disord* 2015;30(5):662-670. <https://doi.org/10.1002/mds.26181>

Deelchand DK, **Adanyeguh IM**, Emir UE, Nguyen TM, Valabregue R, Henry PG, Mochel F, Öz G. Two-site reproducibility of cerebellar and brainstem neurochemical profiles with short-echo, single-voxel MRS at 3T. *Magn Reson Med* 2015;73(5):1718-1725. <https://doi.org/10.1002/mrm.25295>

## Submitted articles

**Adanyeguh IM**, Monin ML, Rinaldi D, Freeman L, Durr A, Lehericy S, Henry PG, Mochel F. Expanded neurochemical profile in the early stage of Huntington disease using proton magnetic resonance spectroscopy.

**Adanyeguh IM**, Perlberg V, Henry PG, Rinaldi D, Petit E, Valabregue R, Brice A, Durr A, Mochel F. Autosomal dominant ataxia: identification of imaging biomarkers with high effect sizes.

## **Additional contributions**

Masingue M, **Adanyeguh I**, Nadjar Y, Sedel F, Galanaud D, Mochel F. Evolution of structural neuroimaging biomarkers in a series of adult patients with Niemann-Pick type C under treatment. *Orphanet J Rare Dis* 2017;12(1):22. <https://doi.org/10.1186/s13023-017-0579-3>

Mochel F, Hainque E, Gras D, **Adanyeguh IM**, Caillet S, Héron B, Roubertie A, Kaphan E, Valabregue R, Rinaldi D, Vuillaumier S, Schiffmann R, Ottolenghi C, Hogrel JY, Servais L, Roze E. Triheptanoin dramatically reduces paroxysmal motor disorder in patients with GLUT1 deficiency. *J Neurol Neurosurg Psychiatry* 2016;87(5):550-553. <https://doi.org/10.1136/jnnp-2015-311475>

## List of tables

Table 1: Properties of nuclei that can be used in MRS .....	30
Table 2: Demographic parameters of participants (BIOSCA) .....	125
Table 3: Effect size of clinical scores and brain imaging parameters (BIOSCA).....	126

## List of figures

Figure 1: Pathogenesis of polyglutamine disorders .....	6
Figure 2: CAG-repeat length correlates with the age of symptoms onset in HD.....	7
Figure 3: Mechanisms that contribute to metabolic/mitochondrial dysfunction in HD.....	9
Figure 4: CAG repeat length correlates with the age of symptoms onset in SCAs .....	12
Figure 5: Neuropathological observations in SCA1 .....	14
Figure 6: Neuropathological observations in SCA2 .....	16
Figure 7: Neuropathological observations in SCA3 .....	18
Figure 8: Neuropathological observations in SCA7 .....	20
Figure 9: Genetic testing may offer an opportunity to take advantage of the therapeutic window before symptoms onset.....	21
Figure 10: Dipole moment and free induction decay.....	25
Figure 11: Relaxation times introduce endogenous contrast between tissue types.....	26
Figure 12: Brain boundary shift integral application in HD .....	27
Figure 13: Equation of equilibrium reaction of the exchange of high-energy phosphate group between ATP and PCr.....	32
Figure 14: Representative spectra and the coil and region of interest for the <sup>31</sup> P experiment.....	37
Figure 15: Design of the multi-centric studies to test the efficacy of two therapeutic agents in improving metabolic dysfunction and slowing caudate atrophy in HD. ....	44
Figure 16: <sup>31</sup> P MT spectra from the visual cortex.....	51
Figure 17: Rate of CK measured with <sup>31</sup> P MT in the visual cortex of patients and controls.....	52
Figure 18: Preliminary results of the rate of CK measured with <sup>31</sup> P MT in the visual cortex of patients and controls .....	80
Figure 19: Preliminary results of DWS analysis.....	82
Figure 20: Preliminary network analysis (rsfMRI) on volunteers data.....	85
Figure 21: Change in clinical scores after 24 months (BIOSCA).....	127
Figure 22: Change in regional volume after 24 months (BIOSCA) .....	128
Figure 23: Rate of atrophy in the cerebellum and pons (BIOSCA).....	129
Figure 24: Tract based statistical analysis of FA and RD in SCAs and controls.....	130
Figure 25: The preprocessing steps of the diffusion data for FBA .....	131
Figure 26: Distribution of fibers in the CST in SCAs and controls .....	132

Figure 27: Connectivity-based fixel enhancement on FD, FC and FDC ..... 133  
Figure 28: FDC correlation with clinical scores and cerebellar atrophy (BIOSCA) ..... 134



## List of abbreviations

$^1\text{H}$ :	Proton
$^{31}\text{P}$ :	31-phosphorus
ADC:	Apparent diffusion coefficient
Ataxin:	Ataxin protein
ATP:	Adenosine triphosphate
ATXN:	Ataxin gene
<i>b</i> :	Strength and timing of diffusion gradients
$B_1$ :	Radiofrequency pulse
BISTRO:	B1-insensitive train to obliterate signal
BSI:	Boundary shift integral
CAG:	Cytosine-adenine-guanine
CCFS:	Composite Cerebellar Functional Severity Score
CK:	Creatine-kinase
DTI:	Diffusion tensor imaging
DWS:	Diffusion weighted spectroscopy
FA:	Fractional anisotropy
FASTMAP:	Fast automatic shimming technique with echo-planar signal trains using mapping along projections
FBA:	Fixel based analysis
FC:	Fiber cross-section
FD:	Fiber density
FDC:	Fiber density and cross-section
FID:	Free induction decay
FOV:	Field of view

HD:	Huntington disease
HTT:	Huntingtin gene
Htt:	Huntingtin protein
mHtt:	Mutant huntingtin protein
MRI:	Magnetic resonance imaging
MRS:	Magnetic resonance imaging
MT:	Magnetization transfer
PCr:	Phosphocreatine
Pi:	Inorganic phosphate
RD:	Radial diffusivity
RF:	Radiofrequency
rsfMRI:	Resting state functional magnetic resonance imaging
SARA:	Scale for the Assessment and Rating of Ataxia
SCA:	Spinocerebellar ataxia
SNR:	Signal to noise ratio
T <sub>E</sub> :	Echo time
T <sub>R</sub> :	Repetition time
UHDRS:	Unified Huntington Disease Rating Scale

## Abstract

Mutations in different gene loci that lead to the encoding of the unstable and expanded glutamine-encoding cytosine-adenine-guanine (CAG) repeats results in the group of diseases known as the polyglutamine diseases. The most common forms are Huntington disease (HD) and spinocerebellar ataxia (SCA) types 1, 2, 3 and 7. These are autosomal dominant neurodegenerative diseases responsible for severe movement disorders with primary atrophy of the striatum in HD and the cerebellum/pons in SCAs before spreading to several brain regions. HD and SCAs are purely genetic disorders. HD and SCAs are thought to share common pathophysiological pathways with a major emphasis on metabolic dysfunction. Metabolic dysfunction in these diseases coupled with their monogenic attribute make them important models to study and understand the pathophysiological processes of neurodegeneration especially for therapeutic interventions seeking to amend metabolic dysfunction. Furthermore, the availability of genetic testing and their predominantly adult onset opens a window for therapeutic intervention before their onset. However, current clinical scales – Unified Huntington Disease Rating Scale (UHDRS) for HD and the Scale for the Rating and Assessment of Ataxia (SARA) or the Composite Cerebellar Functional Severity Score (CCFS) for SCAs – have relatively low effect sizes, which implies the recruitment of large numbers of patients in therapeutic trials, and cannot be used to evaluate individuals at the presymptomatic stage. This prompts the need for biomarkers that are sensitive to macroscopic and microscopic changes that may occur prior to disease onset. Magnetic resonance imaging (MRI) and spectroscopy (MRS) techniques present non-invasive approaches to extract pertinent information that otherwise would not be possible with clinical scales. In this work, we present a combination of different MRI and MRS techniques to identify robust biomarkers in HD and SCA since it is unlikely for a single biomarker to have the power to be used alone in clinical trials. We also present therapeutic approaches that hold promise in HD.

In HD, we identified abnormal brain metabolic profile using  $^{31}\text{P}$  MRS coupled with visual stimulation. During visual stimulation, controls showed an increase in the inorganic phosphate/phosphocreatine ratio whilst there was no change in HD patients. This profile remained abnormal in the patients after one-month of follow-up. However, one-month anaplerotic therapy using triheptanoin improved brain metabolic profile in 10 HD patients. Two separate blinded randomized placebo controlled studies are ongoing to further test the

anaplerotic properties of triheptanoin, as well as a regulator of mitochondrial energy homeostasis, resveratrol, in 100 HD patients each for a year. To understand the underlying cause of the abnormal brain energy profile in HD, we used  $^{31}\text{P}$  magnetization transfer in another study to measure the rate of the creatine-kinase (CK) in HD patients and controls. We identified a reduced CK rate in HD, which could explain the abnormal brain energy profile. Furthermore, applying  $^1\text{H}$  MRS in HD allowed to identify other metabolites that showed alterations in HD. In order to better explain the abnormal profile in HD and identify robust biomarkers reflecting dynamic energy metabolism, a study is ongoing in a larger cohort of HD patients and presymptomatic carriers. This study combines multimodal MRI and MRS techniques including magnetization transfer, diffusion weighted spectroscopy and resting state functional MRI.

Additionally, using  $^1\text{H}$  MRS in a bicentric study, we showed that the lack of reproducibility of MRS results could be resolved when the same sequence and analytical procedures are used. We applied this validated protocol in SCAs and we identified alterations in several metabolites including decreased neuronal markers – total *N*-acetylaspartate and glutamate –, increased glial marker – *myo*-inositol –, and increased energetic marker – total creatine. Analysis of follow-up SCA data showed similar metabolic alterations. Clinical scores worsened and atrophy of the cerebellum and the pons significantly increased over two years. However, atrophy showed very large effect sizes compared to clinical scores. A novel tractography method accounting for different fiber populations in each voxel, called fixel-based analysis, showed changes in white matter fibers in all SCA groups compared to controls with reduced fiber density and fiber cross-section. In addition, we applied a multimodal biomarkers approach, aiming at the integration and visualization of multivariate datasets (i.e. volumetry, MRS, metabolomics and lipidomic) to best explain the pathology in SCAs.

**Keywords:** Biomarkers, Huntington disease, spinocerebellar ataxia, magnetic resonance spectroscopy, magnetic resonance imaging, disease modeling,  $^{31}\text{P}$  MRS,  $^1\text{H}$  MRS, magnetization transfer, diffusion weighted spectroscopy, resting state fMRI, diffusion tensor imaging, fixel based analysis.

## Résumé

Les maladies par expansion de polyglutamines sont des maladies neurodégénératives d'origine génétique dues à l'expansion du trinucléotide cytosine-adénine-guanine CAG codant pour une expansion d'homopolymère de glutamine dans les protéines mutées. Les formes les plus courantes sont la maladie de Huntington (MH) et les ataxies spinocérébelleuses (SCA) types 1, 2, 3 et 7. Ce sont des maladies neurodégénératives autosomiques dominantes, responsables de troubles moteurs graves avec une atrophie initiale du striatum dans la MH et du cervelet/pont dans les SCAs avant de s'étendre à plusieurs régions du cerveau. La MH et les SCAs sont des maladies purement génétiques et partagent des voies physiopathologiques communes, notamment en terme de dysfonction métabolique. Le dysfonctionnement métabolique et le caractère monogénique de ces maladies en font des modèles importants à étudier dans le but de comprendre les processus physiopathologiques de la neurodégénérescence, notamment pour les interventions thérapeutiques visant les dysfonctions métaboliques. En outre, la disponibilité des tests génétiques et le fait que la maladie débute le plus souvent à l'âge adulte offrent la possibilité d'une intervention thérapeutique avant l'apparition de symptômes. Toutefois, les échelles cliniques – Unified Huntington Disease Rating Scale (UHDRS) dans la MH et les échelles d'évaluation de l'Ataxie (SARA et CCFS) dans les SCA – ont une taille d'effet relativement faible, ce qui implique le recrutement d'un grand nombre de patients dans les essais thérapeutiques, ne sont pas assez sensibles et ne peuvent être utilisées pour évaluer les personnes au stade présymptomatique de la maladie. D'où la nécessité de trouver des biomarqueurs sensibles aux changements macroscopiques et microscopiques qui peuvent survenir avant l'apparition de la maladie. L'imagerie par résonance magnétique (IRM) et les techniques de spectroscopie (SRM) sont des approches non invasives permettant de recueillir des informations pertinentes, impossibles à obtenir avec les échelles cliniques. Dans ce travail, nous présentons une combinaison de différentes techniques IRM et SRM afin d'identifier des biomarqueurs robustes dans la MH et les SCA puisqu'il est peu probable qu'un biomarqueur unique puisse être utilisé seul dans les essais cliniques. Nous présentons également des approches thérapeutiques prometteuses dans la MH.

Dans la MH, l'utilisation du  $^{31}\text{P}$  SRM couplé à la stimulation visuelle nous a permis d'identifier un profil métabolique anormal au niveau du cerveau. Pendant la stimulation

visuelle, les témoins ont montré une augmentation du ratio entre phosphate inorganique et phosphocréatine alors que le ratio était inchangé chez les patients MH. Ce profil est resté anormal dans les patients qui ont été suivis pendant un intervalle d'un mois. A l'inverse, une thérapie anaplérotique à base de triheptanoïne administrée pendant un mois a corrigé le profil métabolique cérébral chez 10 patients MH. Deux études distinctes, randomisées, contrôlées, en double aveugle sont en cours afin de tester les propriétés anaplérotiques de la triheptanoïne, ainsi qu'un régulateur de l'homéostasie énergétique mitochondriales, le du resvératrol, chez 100 patients MH chacune. Pour comprendre la cause sous-jacente du profil énergétique cérébral anormal dans la MH, nous avons utilisé une technique de transfert de magnétisation afin de mesurer le taux de créatine kinase chez les patients MH et les témoins. Nous avons identifié une plus faible activité de la CK chez les patients MH qui pourrait expliquer leur profil énergétique cérébral. D'autre part, l'utilisation de la technique SRM du proton nous a permis d'identifier d'autres altérations métabolites chez les patients MH. Afin d'identifier des biomarqueurs dynamiques du métabolisme énergétique cérébrale, une étude est en cours chez un plus grand nombre de patients MH et d'individus présymptomatiques. Cette étude combine les techniques multimodales IRM et SRM, y compris le transfert de magnétisation, la spectroscopie pondérée en diffusion et l'IRM fonctionnelle à l'état de repos.

En utilisant la technique de SRM du proton dans une étude menée dans deux sites distincts, nous avons montré que le manque de reproductibilité des résultats de SRM pouvait être résolu lorsqu'on utilisait la même séquence et les mêmes procédures analytiques. Nous avons appliqué ce protocole validé dans les SCAs et nous avons identifié des altérations dans plusieurs métabolites, y compris la diminution de marqueurs neuronaux – *N*-acétylaspartate total et du glutamate –, l'augmentation d'un marqueur glial – *myo*-inositol – ainsi que l'augmentation d'un marqueur énergétique - créatine totale. Ces altérations métaboliques étaient stables sur deux ans chez les patients SCA. Les scores cliniques se sont aggravés et l'atrophie du cervelet et du pont s'est majorée sur deux ans. Toutefois, l'atrophie a montré des tailles d'effet bien plus importante que les scores cliniques. Une nouvelle méthode de tractographie qui tient compte des différentes populations de fibres au sein de chaque voxel, appelée «*fixel-based analysis*», a montré une altération des fibres de la substance blanche dans tous les groupes SCA par rapport aux témoins, avec une réduction de la densité des fibres et de leur section transversale. Par ailleurs, nous avons appliqué une approche biomarqueurs multimodale, qui vise à l'intégration et à la visualisation d'ensemble de données

multivariées (volumétrie, SRM, métabolomiques et lipidomiques), afin de mieux expliquer la physiopathologie des SCA.

**Mots-clés:** Biomarqueurs, maladie de Huntington, ataxie spinocérébelleuses, spectroscopie de résonance magnétique, imagerie par résonance magnétique, modélisation de la maladie,  $^{31}\text{P}$  SRM,  $^1\text{H}$  SRM, transfert de magnétisation, spectroscopie à diffusion ponctuelle, imagerie par tenseur de diffusion, fixel based analysis.

# Introduction

Polyglutamine diseases are a group of neurodegenerative disorders that result from mutations in different gene loci that contain the glutamine encoding cytosine-adenine-guanine (CAG) triplet repeats that leads to expansion and instability of the gene and affected proteins. There are different forms of polyglutamine disorders and they include Huntington disease (HD), several spinocerebellar ataxia (SCA), dentatorubral pallidoluysian atrophy (DRLPLA) and spinal bulbar muscular atrophy (SBMA).

This work focuses on HD and SCA types 1, 2, 3 and 7 as they remain the most common forms of polyglutamine diseases. They are autosomal dominant diseases that present with severe movement disorders in the form of chorea in HD and ataxia in SCAs. They are monogenic diseases with the possibility of genetic testing and hence serve as important models to study neurodegeneration unlike other neurodegenerative disorders such as Parkinson and Alzheimer. They are late onset, which opens a window for therapeutic intervention before symptoms develop. They also share common pathophysiological pathways with a major emphasis on metabolic dysfunction. The two main potential therapeutic interventions include targeting the polyglutamine protein to reduce their production or modify them, and metabolic interventions to reverse metabolic dysfunction. The problem of testing these therapies lies in the limitations of the clinical scales used to evaluate the disease progression. The major clinical scales are the Unified Huntington Rating Scale (UHDRS) to evaluate HD and the Scale for the Rating and Assessment of Ataxia (SARA) and the Composite Cerebellar Functional Severity Score (CCFS) to evaluate SCAs. However, in therapeutic trials of very rare disorders like SCAs, the low effect sizes of these clinical scales would likely require a large number of patients making these trials hardly feasible. Clinical scores are not able either to detect macro- and microstructural changes such as atrophy and metabolic alterations that may occur before, during and after symptoms onset. Another important caveat of clinical scales is that, by definition, they cannot be used to evaluate premanifest individuals. Hence, there is a need for biomarkers with effect sizes greater than clinical scores that can be used on small sample sizes of patients with HD or SCA.

The objectives of this work are to identify robust biomarkers of HD and SCA using non-invasive magnetic resonance imaging (MRI) and spectroscopy (MRS) techniques and to



assess the anaplerotic properties of potential therapeutic agents in improving metabolic dysfunction in HD. These biomarkers can then be used in models to explain disease progression. Currently, there has been a rise in the number of modalities used to characterize a given disease. These modalities include, but are not limited to, clinical, imaging, molecular biology, physiological, and biochemical methods. Since each modality differs in the type and number of variables they generate, conventional statistical tools are incapable of integrating these multimodal data into models while preserving the unique properties of each modality. Therefore, we applied new statistical tools based on multiblock analyses that allowed the integration and visualization of these multivariate datasets. The selection of a few meaningful variables can also enable their combination into composite scores, which are likely to provide both a better reflection of the disease process pathology and larger effect sizes than any biomarker alone.

The manuscript has therefore been organized into 7 parts as follows:

**Chapter 1** is a brief overview of the pathophysiology of HD and SCA types 1, 2, 3 and 7. This chapter also introduces different MRI and MRS techniques that can be used to study these disorders. Finally, this chapter presents the objectives of the thesis.

**Chapter 2** presents the application of a  $^{31}\text{P}$  MRS technique in biomarker identification study in HD and its use in a proof-of-concept anaplerotic study in HD. Likewise, I will present the follow-up of this anaplerotic study with the inclusion of diffusion tensor imaging (DTI) and boundary shift integral (BSI) approaches.

**Chapter 3** presents a study that resulted from the study in chapter 2. In this chapter, I present a method that aims at elucidating the biochemical basis of altered  $^{31}\text{P}$  profiles in HD. I also applied techniques allowing the analysis of an expanded neurochemical profile in HD patients. The next step involves the combination of metabolic, structural, and functional techniques in order to study the dynamics of brain energy metabolism in HD patients and presymptomatic individuals.

**Chapter 4** is a methodological study to test the reproducibility of a modified  $^1\text{H}$  MRS sequence in order to standardize acquisition and quantification protocols between study sites in view of multi-centric studies.

**Chapter 5** reports the application of the methods in chapter 4 to elucidate the metabolic dysfunction in the brain of SCA patients.

**Chapter 6** presents the use of diffusion imaging and volumetric analysis in biomarker identification in SCA.

**Chapter 7** presents a statistical approach that improves multimodal data integration for disease modeling.

# Chapter 1

## Organisation:

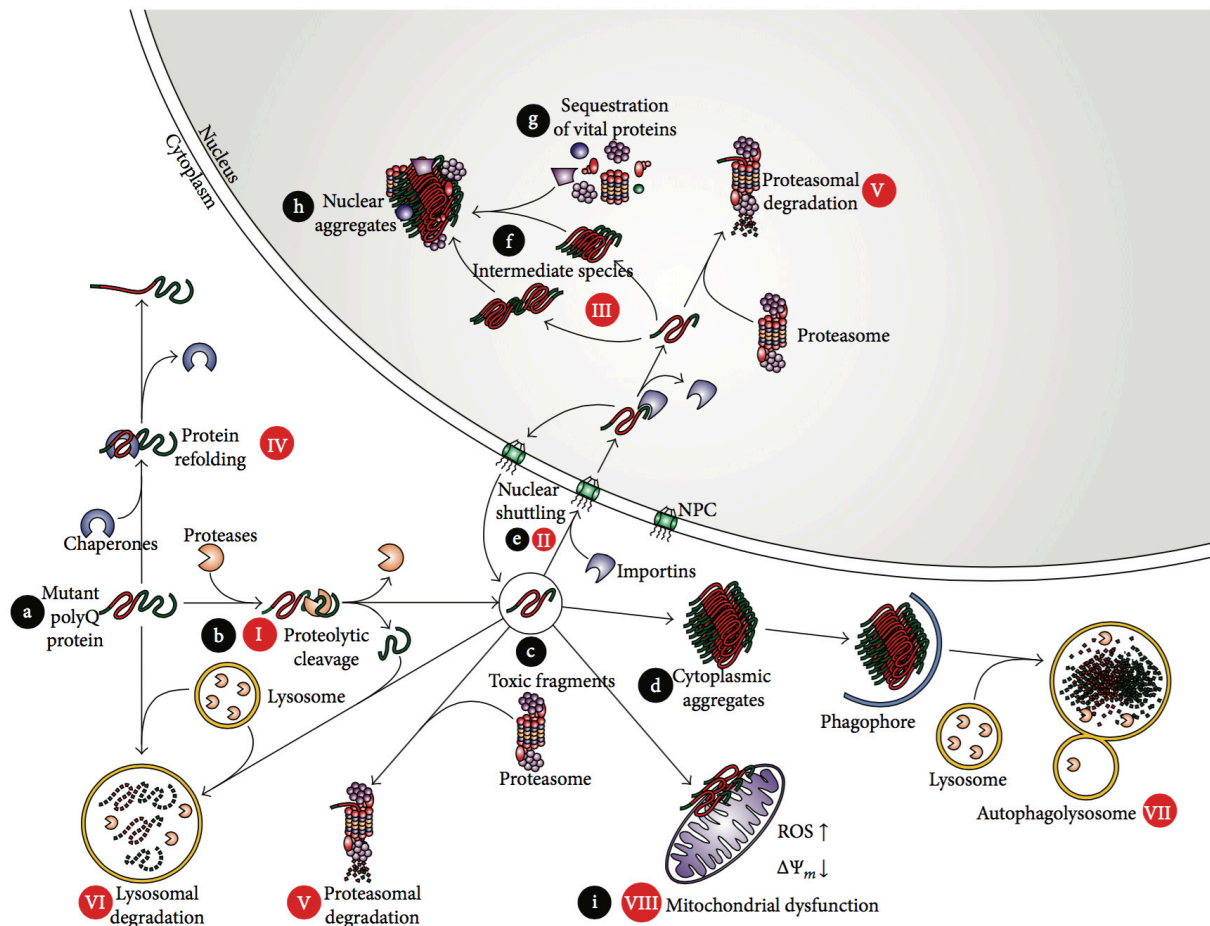
<b>Polyglutamine disorders .....</b>	<b>5</b>
1.1 Huntington disease .....	6
1.1.1 Genetics and mitochondrial dysfunction in HD .....	7
1.1.2 Pathogenesis and symptoms of HD .....	9
1.2 Spinocerebellar ataxia .....	11
1.2.1 Spinocerebellar ataxia type 1 (SCA1) .....	12
1.2.2 Spinocerebellar ataxia type 2 (SCA2) .....	14
1.2.3 Spinocerebellar ataxia type 3 (SCA3) .....	16
1.2.4 Spinocerebellar ataxia type 7 (SCA7) .....	18
1.3 Diagnosis and treatment of polyglutamine diseases.....	21
<b>Magnetic resonance (MR) approaches to biomarker identification.....</b>	<b>23</b>
1.4.1 Principles of MR.....	23
1.4.2 Evaluating atrophy and axonal damage.....	26
1.4.3 Determination of brain metabolic alterations with MRS.....	29
<b>Objectives.....</b>	<b>33</b>

## **Polyglutamine disorders**

The pathological expansion of CAG repeats in different gene loci gives rise to the different neurodegenerative disease known as polyglutamine disorders. They are all autosomal dominant disorders with the exception of the X-linked SBMA (Orr & Zoghbi, 2007). The genes involved are nonetheless unrelated as each disease has a different target protein that is defective. Still, they share common neurodegenerative pathway (Shao & Diamond, 2007; Fan et al., 2014). Even though the defective proteins are widespread in the body, it is not yet known why there is selective cellular damage such as in the striatum of HD and the vermis and pons in SCAs.

On average, the occurrence of more than 35 CAG repeats lead to the disease though the actual numbers vary depending on the disease (Paulson et al., 2000; Shao & Diamond, 2007). This expansion has an inverse correlation with the age of clinical manifestations, a phenomenon known as anticipation (Friedman, 2011). Therefore successive generations tend to have increased expansion of the CAG repeat, which in turn leads to earlier onset of the disease which is more severe than the previous generation. The progressive worsening of the disease is a common feature that continues for about 10 - 20 years.

The exact causes of polyglutamine disorders are not clearly understood but several mechanisms have been implicated as strong influencers on their pathophysiology. These mechanisms are summarized in Figure 1. These mechanisms will be further elaborated for HD and SCA types 1, 2, 3 and 7 which are the focus of this project.

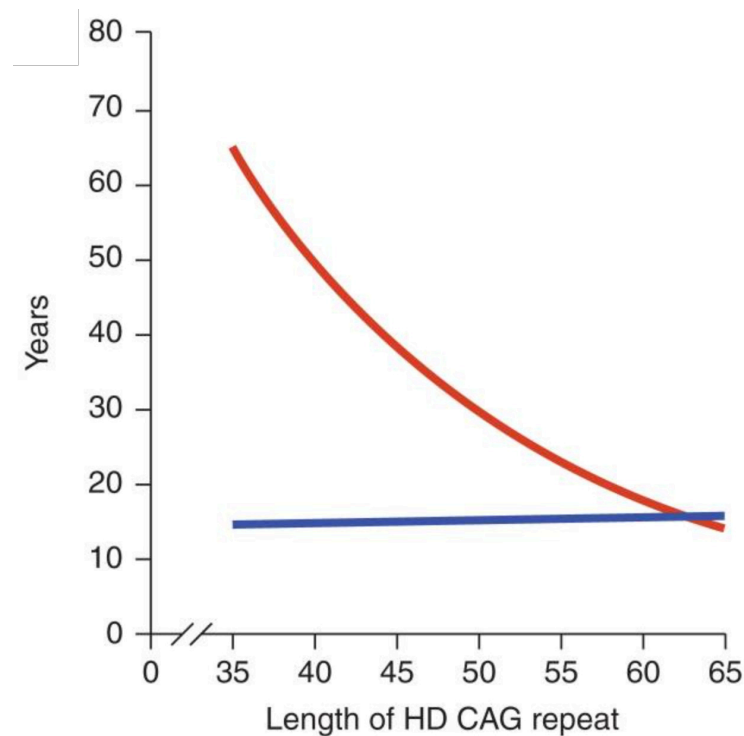


**Figure 1: Pathogenesis of polyglutamine disorders.** (a) The mutant protein (b) can be proteolytically processed (c) to form toxic fragments (d) that can form aggregates in the cytoplasm. (e) Breakdown down of these aggregates into toxic products can be shuttled into the nucleus (f) to form intermediate species (h) and nuclear aggregates (g) that can indirectly result in the sequestration of vital proteins. (i) The mutant protein aggregates can damage important cellular components such as the mitochondria (Weber et al., 2014).

## 1.1 Huntington disease

Huntington disease (HD) is an autosomal dominant neurodegenerative disorder that bears its name from the describing physician, George Huntington (Lanska, 2000). HD is a pure genetic disorder with complete penetrance. Even though there are juvenile forms, it is mostly a late-onset disease with symptoms appearing in affected individuals between the ages of 30 and 50 years. Anticipation is very important in HD (Figure 2) and more than 36 CAG repeats lead to the disease with incomplete penetrance between 36 and 39 CAG repeats (Kremer et al., 1994).

Evaluations of the prevalence of HD shows marked heterogeneity across different regions. The prevalence rate per 100,000 of the population is estimated at 0.40 (0.36-0.44) in Asia, 2.17 (1.95-2.41) in Central and Eastern Europe, 7.33 (6.94-7.74) in North America, 5.63 (5.61-6.25) in Oceania, 6.68 (6.40-6.97) in the United Kingdom, and 3.60 (3.50-3.69) in Western Europe (Rawlins et al., 2016).



**Figure 2: CAG-repeat length correlates with the age of symptoms onset in HD.** The lines represent age at neurological onset (red) and duration of disease from onset to death (blue). Source (Finkbeiner, 2011).

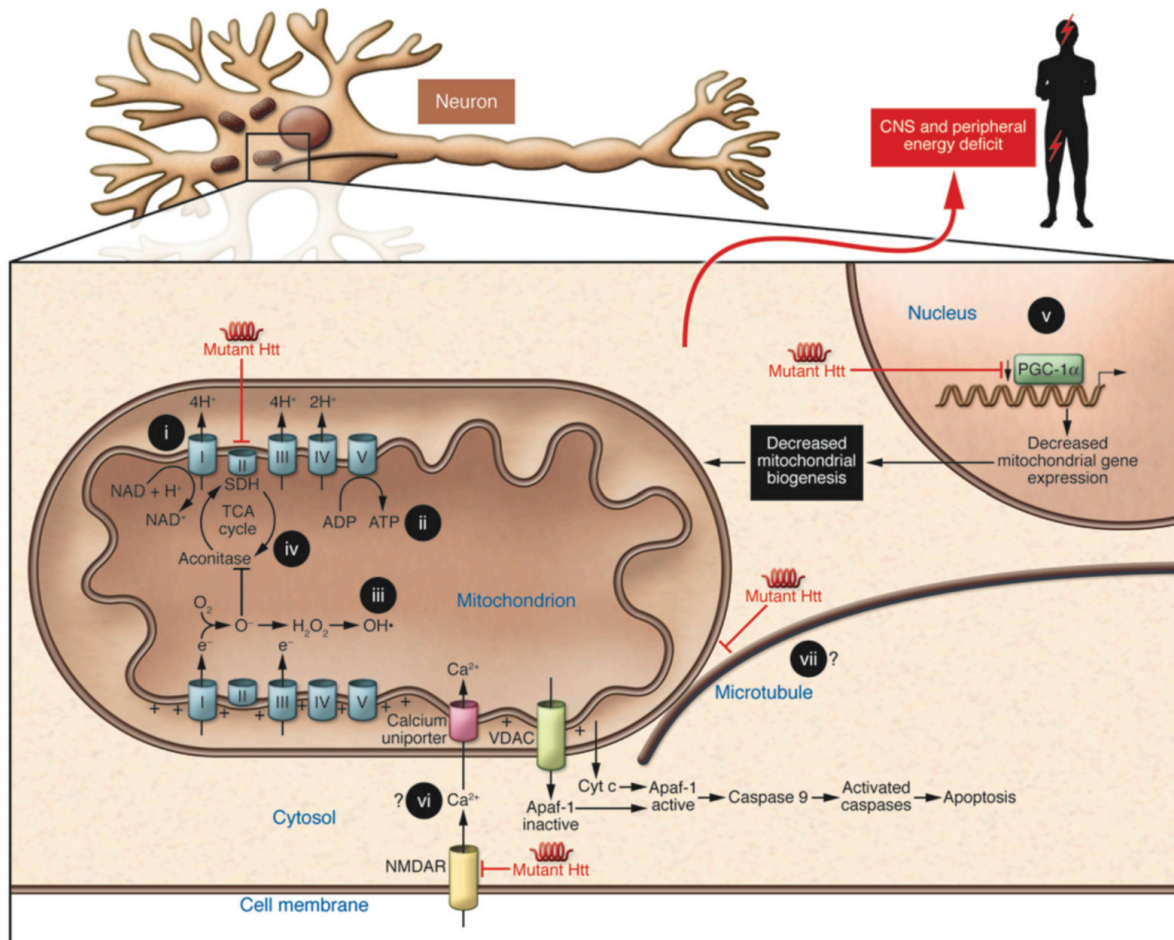
### 1.1.1 Genetics and mitochondrial dysfunction in HD

Several decades after its initial description in 1872, advancement in molecular biology allowed the mapping of the disease to chromosome 4p16.3 (Gusella et al., 1983). The disease was then linked to the unstable CAG expansion in the *IT15* gene (The Huntington's Disease Collaborative Research Group, 1993), also known as the huntingtin gene (*HTT*) which codes for the huntingtin protein (Htt). The discovery of *HTT* paved the way for extensive genetic studies to be performed on this disease. Htt is found throughout the body with the highest concentrations in the brain. Though its exact function is not completely understood, it has

been associated with normal function of the brain and development (Schulte & Littleton, 2011; Elias et al., 2014; Saudou & Humbert, 2016). Wild type Htt is involved in gene expression as it interacts with several transcription factors including CBP, SP1, TBP, p53, p300, Sin3a, and REST/NRSF. It interacts directly with  $\beta$ -tubulin in microtubules to facilitate vesicle transport and cytoskeletal anchoring. Furthermore, by binding directly to mitochondria and also indirectly regulating transcriptional co-activators such as PGC-1 $\alpha$ , it is implicated in the regulation of metabolism (Shao & Diamond, 2007; Mochel & Haller, 2011; Fan et al., 2014).

Mutations in the *HTT* result in the production of mutant Htt (mHtt) and this leads to the disruption in the normal function of Htt as well as its nuclear and cytoplasmic distributions. Most of the impact is on metabolism in HD (Figure 3). Interactions with mHtt affects gene transcription through the depletion of important factors such as CBP (Jiang et al., 2006) or the down-regulation of important co-factors such as PGC-1 $\alpha$  (Cui et al., 2006) necessary for mitochondrial biogenesis. Moreover, HD pathogenesis may also be influenced by impairment to intracellular and vesicular shuttling of organelles and other cellular content. Conditional knockout mice expressing less than 50% endogenous Htt showed decreased mitochondrial movement along neurites and this was even observed in asymptomatic HD mouse neurons (Trushina et al., 2004). The importance of mitochondria cannot be over-emphasized. Apart from serving as the principal energy source, they are also involved in maintaining homeostasis by regulating intracellular calcium (Ca<sup>2+</sup>); an important step to normal process of oxidative phosphorylation. An important enzyme complex that creates a critical link between the Krebs cycle and the respiratory chain is succinate dehydrogenase or mitochondrial complex II. Its activity is greatly disrupted by mHtt and leads to energy defects in HD and may play a critical role in the degeneration of striatal neurons in HD (Damiano et al., 2013). Likewise, reduced glucose metabolism has been found in the brain of HD patients even before symptoms onset (Grafton et al., 1992; Antonini et al., 1996). In addition, HD patients and presymptomatic carriers show signs of weight loss even when they are on high caloric diet (Djousse et al., 2002; Mochel et al., 2007). Metabolic dysfunction might not be limited to the brain only. Reduced branched chain amino acids (BCAA) – valine, leucine and isoleucine – were found in the plasma of patients at the early stage of HD despite high caloric intake (Mochel et al., 2007). Reduction in the BCAA might signify lack of substrates to fuel the Krebs cycle. Therefore impairment to the movement of mitochondria, disruption in Ca<sup>2+</sup> regulation, reduction in Krebs cycle substrates and decreased mitochondrial biogenesis

through downregulation of transcription factors likely contribute to mitochondrial dysfunction in HD. This further implies inability to replenish damaged mitochondria in certain regions, perturbation in meeting energy demands, calcium overload, increase in reactive oxygen species, release of cytochrome c and apoptosis (Lee & Wei, 2000; Nicholls, 2009).



**Figure 3: Mechanisms that contribute to metabolic/mitochondrial dysfunction in HD.** mHtt may lead to lack of substrates to fuel the Krebs cycle, impair  $\text{Ca}^{2+}$  buffering, disrupt vesicular transport and mitochondrial movement, and downregulate important transcription factors needed for mitochondrial biogenesis. Source (Mochel et al., 2007).

### 1.1.2 Pathogenesis and symptoms of HD

Severe atrophy of the caudate and putamen are significant neuropathological signs of HD (Vonsattel et al., 1985). The mHtt causes medium-sized spiny neurons in the striatum that contain  $\gamma$ -amino butyric acid (GABA) to undergo selective degeneration (Vonsattel &



DiFiglia, 1998). Cortical atrophy has also been reported (Hedreen et al., 1991). Progressive degeneration of neurons in the striatum and other regions of the brain present several symptoms that can be classified as motor, cognitive or psychiatric symptoms.

**Cognitive symptoms:** There are discrepancies in reporting cognitive symptoms in most studies and may be attributed to the subtle cognitive changes at the early stage of HD which might be overlooked for the more prominent motor symptoms (Chaganti et al., 2017). Cognitive decline normally precedes long-term memory loss and it might impact executive functions involved in day-to-day activities such as organizing, planning, checking, or adapting alternatives, and delays the acquisition of new motor skills (Walker, 2007). Visuospatial ability and judgment are impaired as the disease progresses further and global dementia is observed (Lauterbach et al., 1998).

**Motor symptoms:** Degeneration of the medium spiny neurons in the striatum are vital to the involuntary movements characteristic to HD – chorea; involuntary dance-like movement – and may be attributed to loss of the projection neurons (Mitchell et al., 1999), which make up the bulk of striatal neurons. Motor symptoms start with small involuntary movements that for example might resemble twitching of the eyelids and other muscles. As the disease progresses the subtle movements give way to more pronounced involuntary jerky movements. In addition, there is the inability to maintain voluntary muscle contraction at a constant level and incapacity to apply steady pressure during handshake. Gross motor coordination skills, including gait and postural maintenance, and fine motor skills, such as finger-tapping rhythm and rate, also deteriorate as the disease progresses. While comprehension is affected, the rate of speech deterioration is faster (Walker, 2007). Dystonia and myoclonus are other forms of movement disorders that may occur.

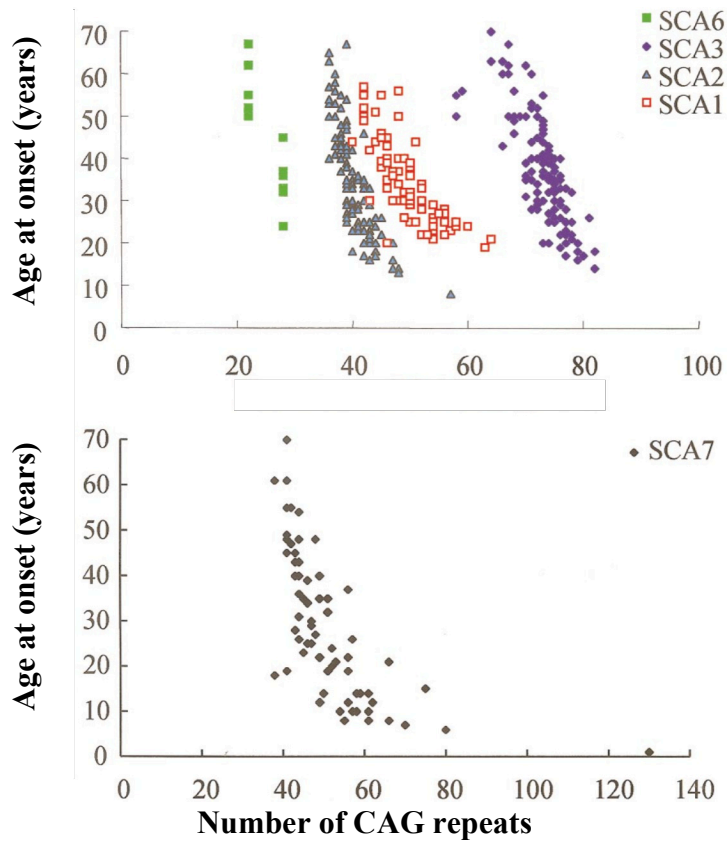
**Psychiatric symptoms:** Principal psychiatric symptoms are related to mood disorders. Chronic depression, irritability, impulsiveness and aggression, are variable and sometimes precede motor onset by years (Gusella & MacDonald, 2006). Patients tend to show personality changes, schizophrenia, anxiety, impulse control and sexual disorders (Lauterbach et al., 1998). Affected individuals contemplating suicide are higher in HD than other diseases such as stroke and Parkinson. Moreover, suicidal tendencies are observed as early as the presymptomatic stage and it increases following genetic testing (Almqvist et al., 1999).

**Other symptoms:** Aside the neuropsychological symptoms of HD, there are other non-neurological symptoms as well. One of such is the loss of weight even when affected individuals are on high caloric diet (Djousse et al., 2002; Mochel et al., 2007).

## **1.2 Spinocerebellar ataxia**

SCAs are a group of disorders with progressive and irreversible neurodegeneration that results in cerebellar ataxia leading to unsteady gait and movement coordination. They are clinically heterogeneous with many different subtypes whose numbering corresponds to the order of the identified gene (Manto, 2005). Some SCAs are more severe than others but generally 10-15 years after symptoms onset, most patients are wheelchair bound (Fan et al., 2014). Extensive cerebellar atrophy, particularly of the Purkinje cells, is common to SCAs. Involvement of the brainstem, spinal cord and peripheral nerves is another common feature. Severe ataxia is a predominant symptom in all SCAs, variably associated with pyramidal signs, parkinsonism, cognitive impairment and/or peripheral neuropathy. Though they share common features, others are very unique to each SCA type, such as retinal degeneration in SCA7 (Paulson, 2009).

The polyglutamine forms of SCA (SCAs 1, 2, 3, 6, 7 and 17) are autosomal dominant and just like HD, they have varying CAG repeat thresholds depending on the affected gene (Manto, 2005; Rüb et al., 2013). In addition, they are mostly late onset even though juvenile forms exist when the transmission is by an affected father. Furthermore, similar to HD, the age of onset is correlated to the number of CAG repeats (Figure 4). This work focuses on SCAs 1, 2, 3 and 7. The prevalence of the autosomal dominant polyglutamine SCAs is about 1 - 4 per 100,000 of the population with variable frequency of occurrence depending on the region or ethnic group (Durr, 2010; Fan et al., 2014).



**Figure 4: CAG repeat length correlates with the age of symptoms onset in SCAs** (Stevanin et al., 2000).

### 1.2.1 Spinocerebellar ataxia type 1 (SCA1)

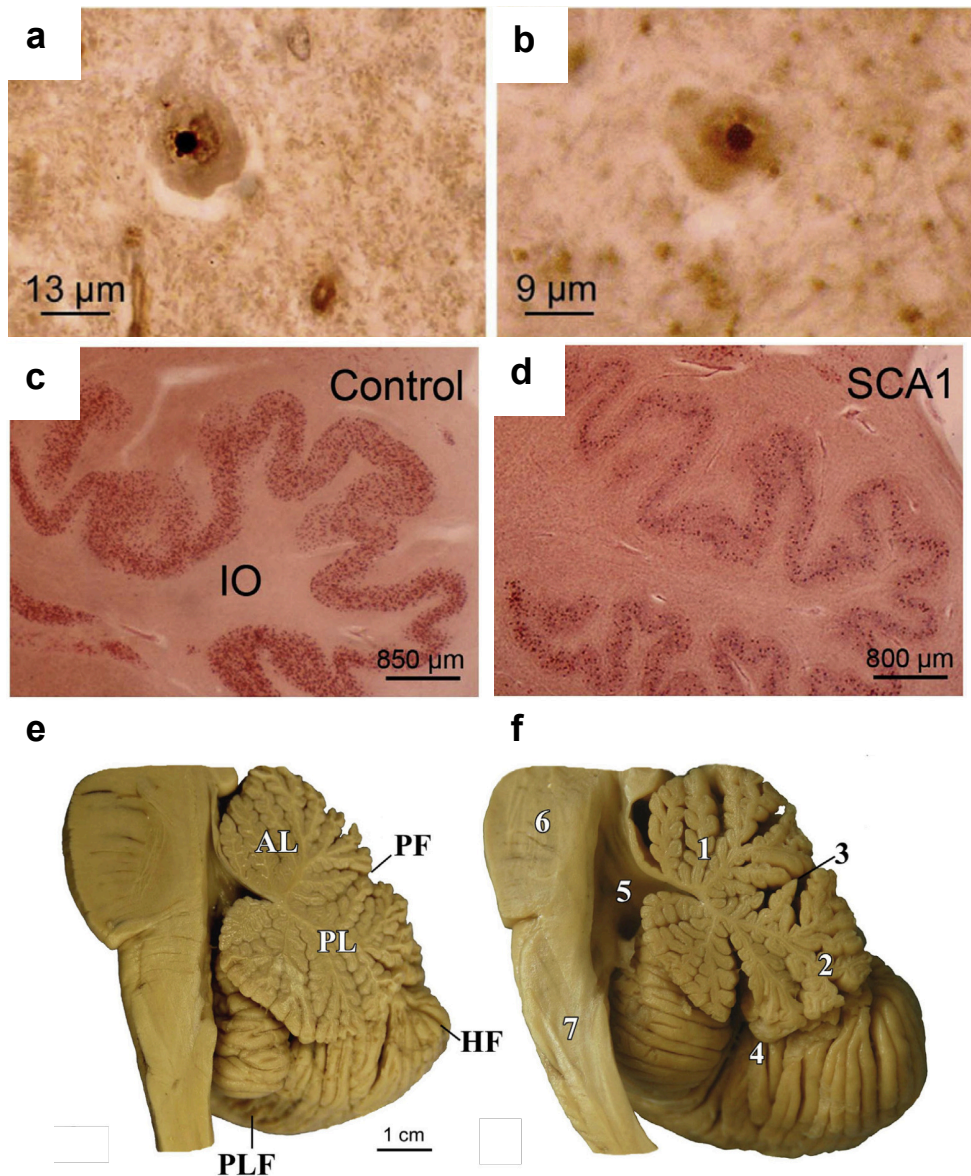
The dominantly inherited neurodegenerative SCA1 is caused by CAG expansion in the ataxin-1 gene (ATXN1) that is located on chromosome 6p23 (Orr et al., 1993) and which codes for the ataxin-1 protein. CAG repeats of more than 39 in ATXN1 is reported for SCA1 (Rüb et al., 2013).

Wild type ataxin-1 has been linked to RNA processing and shuttling of RNA between the nucleus and the cytoplasm (Irwin et al., 2005). It also mediates transcriptional repression by interacting with transcriptional co-repressor SMRT (silencing mediator of retinoid and thyroid hormone receptors) (Tsai et al., 2004). Likewise, it influences transcription by interacting with other transcription co-repressors such as PQBP-1 and Capicua (Okazawa et al., 2002; Lam et al., 2006) and the transcription factor critical for cerebellar development – ROR $\alpha$

(Serra et al., 2006). Disturbing this interaction through mutation in ataxin-1 is thought to contribute to the pathogenesis of SCA1. A study in transgenic mouse models of SCA1 showed that genes responsible for early Purkinje cells development were reduced in response to mutant ataxin-1 (Serra et al., 2006). Another study showed that mutant ataxin-1 interacts with PQBP-1 to further enhance the reduction of phosphorylated RNA polymerase II large subunit and repress transcription (Okazawa et al., 2002). A cerebellar transcriptomic study on two transgenic mouse models of SCA1 – one developed ataxia with Purkinje cell death (ATXN1[82Q]) whilst the other developed ataxia with no death of Purkinje cells (ATXN1[30Q]D776) – showed that two groups of co-expressed genes were highly correlated with the disease. Co-expressed genes with Cic-binding sites were downregulated whilst those devoid of Cic-binding sites within their upstream regions were upregulated in relation to the disease (Ingram et al., 2016). Further analysis of the ATXN1[30Q]D776 mice revealed highly expressed levels of the neuropeptide gene cholecystokinin. Deletion of this gene led to ATXN1[30Q]D776 mice developing symptoms similar to ATXN1[30Q]D776 mice with Purkinje cell death. This may imply that the cholecystokinin confers some form of neuroprotection and may be a potential therapeutic target (Ingram et al., 2016). Furthermore, other mechanisms independent of the polyglutamine tract are involved in the disease process. Haploinsufficiency in Pumilio1, an RNA-binding protein that binds ataxin-1 mRNA and regulates its stability, resulted in an increase in ataxin-1 levels and exacerbated the symptoms in SCA1 knock-in mice (Gennarino et al., 2015).

Studies into the neuropathology of SCA1 have revealed neuronal intranuclear inclusion bodies in SCA1 (Figure 5ab). This may directly or indirectly relate to the marked atrophy of the brainstem and cerebellum (Figure 5c). There is also the depletion of Purkinje cells in the cerebellum and loss of neurons in the pontine nuclei and inferior olivary nucleus (Yamada et al., 2008; Rüb et al., 2013).

Different SCA1 patients have variable phenotypes and anticipation depending on the size of the CAG repeats (Paulson, 2009). Pyramidal impairment and oculomotor palsy are observed at the early stages. At the later stages amyotrophic lateral sclerosis-like disorders and sensory disturbance are observed (Yamada et al., 2008; Durr, 2010). Likewise, there is variable expression of dysphagia, extrapyramidal motor symptoms and executive dysfunctions in addition to cerebellar ataxia, dysarthria and cerebellar oculomotor signs (Rüb et al., 2013).



**Figure 5: Neuropathological observations in SCA1.** Neuronal intranuclear inclusion bodies are found in the affected (a) inferior olive and (b) pontine nuclei. (d) The inferior olives are degenerated in SCA1 compared to (c) healthy controls. (f) Degeneration of the brainstem and cerebellum are observed in SCA1 with flattened brainstem and widened fissures in the cerebellum compared to (e) healthy controls (Rüb et al., 2013).

### 1.2.2 Spinocerebellar ataxia type 2 (SCA2)

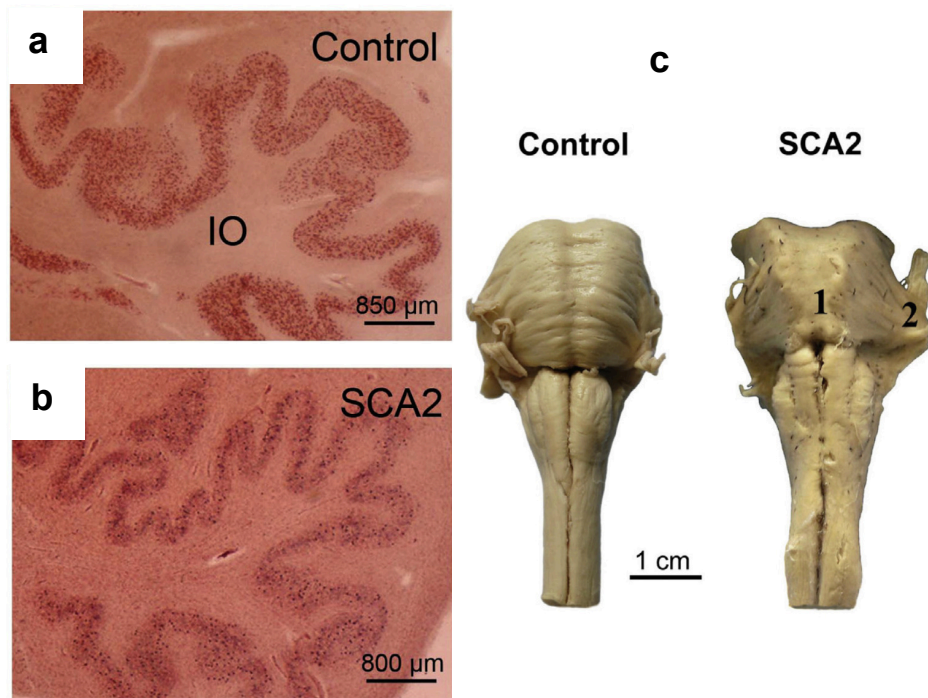
Mutations in the chromosome 12q24.1 has been linked to SCA2 (Pulst et al., 1996). This locus is for the ataxin-2 gene (ATXN2) which codes the ataxin-2 protein. Normal CAG

repeats can range from 13 - 32 repeats whilst expanded pathogenic repeats in ATXN2 are often between 33 - 77 CAG repeats (Stevanin et al., 2000; Rüb et al., 2013; Fan et al., 2014). However, repeats of 32 - 34 normally presents reduced penetrance (Paulson, 2009).

Ataxin-2 is ubiquitously expressed just like Htt. Its subcellular localization to the rough endoplasmic reticulum suggests its role in modulating endocytosis. It is also located in the plasma membrane and may aid in the internalization and signaling of receptor tyrosine kinases. Ataxin-2 in the nucleus is also implicated in fine-tuning mRNA translation and decay by binding to transcription factors and related proteins (Rüb et al., 2013). In addition, ataxin-2 is linked to cell specification, apoptosis and receptor-mediated signaling, formation of actin filaments, and secretion (Orr & Zoghbi, 2007). Mutant ataxin-2 reduces neuronal excitability by binding to intracellular calcium release channel and altering calcium signaling. It also renders Purkinje cells sensitive to glutamate-induced apoptosis (Liu et al., 2009).

Neuropathological findings are similar to SCA1 with the depletion of Purkinje cells and atrophy of the cerebellum and brainstem (Figure 6). The basal ganglia, thalamus and cerebral cortex may show mild degeneration in some patients (Yamada et al., 2008; Rüb et al., 2013). In contrast to the other SCAs, intranuclear inclusions are not of importance in SCA2.

Clinically, individuals with small CAG repeats tend to present postural tremor. Medium repeat is often associated with progressive cerebellar ataxia, decreased reflexes and slow eye movement. In addition to cerebellar ataxia, large repeats often present chorea and dementia. Furthermore, patients with very large repeats may have myoclonus, dystonia, cardiac failure, and retinal degeneration (Durr, 2010).



**Figure 6: Neuropathological observations in SCA2.** The inferior olives are degenerated in (b) SCA2 compared to (a) healthy controls and (c) the brainstem is particularly atrophied in SCA2 compared to healthy controls (Rüb et al., 2013).

### 1.2.3 Spinocerebellar ataxia type 3 (SCA3)

SCA3, also known as the Machado-Joseph Disease, is the most commonly inherited SCA (Paulson, 2007). Normal CAG repeats are in the range of 12 - 43 whilst expanded repeats are 52 - 77 (Stevanin et al., 2000; Paulson, 2009; Rüb et al., 2013). The lack of overlap in the sizes of normal and pathogenic repeats suggests there is no range for reduced penetrance unlike in SCA2. The CAG expansion is found on chromosome 14q24.3-q32.2 (Kawaguchi et al., 1994; Paulson, 2007) which contains the ataxin-3 gene (ATXN3).

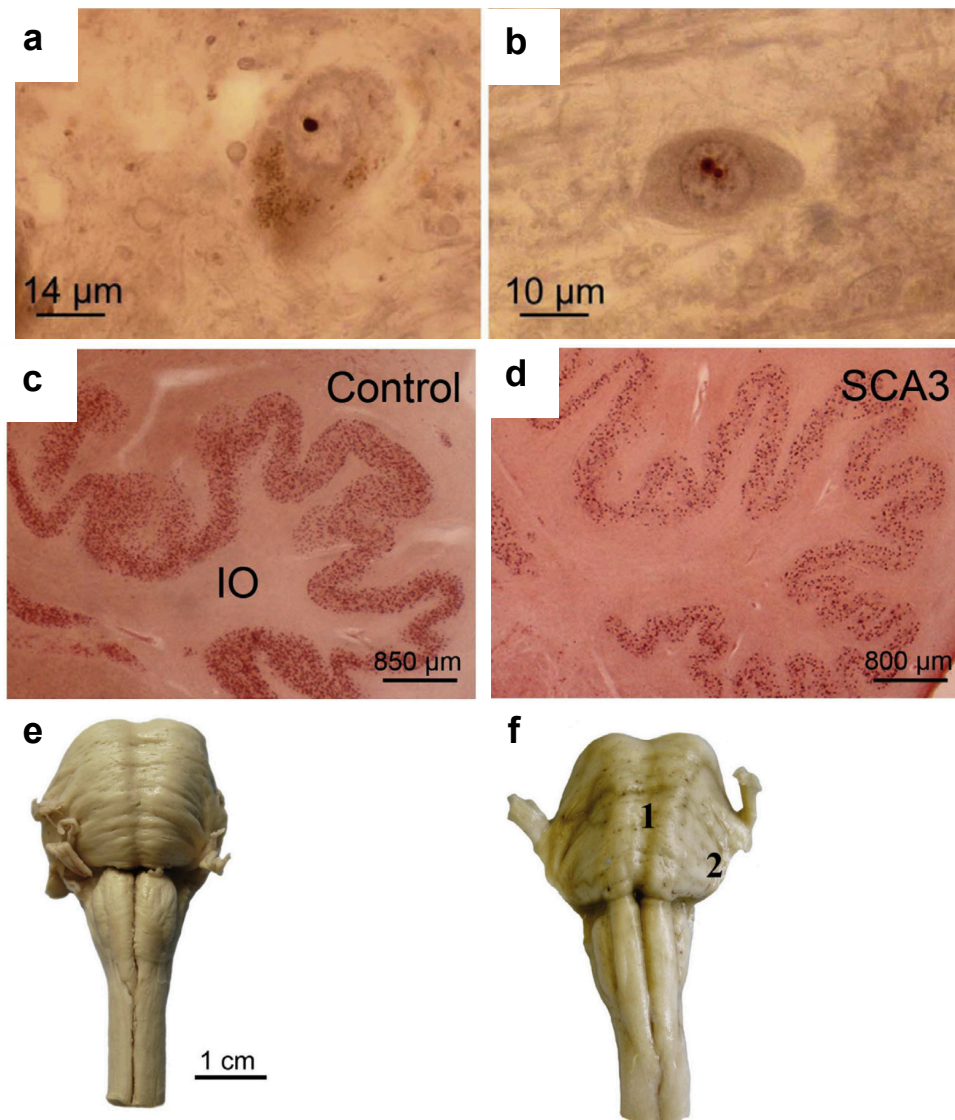
A thorough review of ataxin-3 protein has shown that it is localized to the cytoplasm, nucleus and mitochondria of peripheral and neuronal tissues. In addition, its normal function has been linked to the ubiquitin-proteasome activity that checks short-lived and misfolded proteins and degrade them (Costa Mdo & Paulson, 2012). It may also possess neuroprotective properties, aid in cellular response to heat stress, interact with shuttle proteins, influence aging process, regulate transcription by binding to transcriptional factors (Costa Mdo & Paulson, 2012). The

mutant protein alters the ubiquitin-proteasome activity and hence reduces the degradation of short-lived and misfolded proteins. This leads to the accumulation of proteins including aggregates of mutant ataxin-3 in affected tissues. Furthermore, the mutant protein leads has low neuroprotective features, impaired transcriptional regulation and shuttling of materials (Costa Mdo & Paulson, 2012). Impaired intracellular calcium signaling has also been linked to mutant ataxin-3 (Chen et al., 2008).

Cerebellum, brainstem, basal ganglia and other brain regions have been reported to show atrophy in SCA3 (Figure 7) (Paulson, 2007). There is widespread neuronal loss in the Purkinje cell layers. The dopaminergic, cholinergic, noradrenergic and GABAergic neurotransmitter systems also show neuronal loss (Rüb et al., 2013). Neuronal intranuclear inclusions are also present in affected tissues (Paulson, 2007; Yamada et al., 2008; Rüb et al., 2013). SCA3 mutation carriers have perturbed glucose utilization in cerebellum, brainstem and cerebral cortex even before symptoms onset (Soong & Liu, 1998).

Clinical presentations are dependent on the size of the CAG repeat with larger repeats leading to more severe and early onset SCA3 (Paulson, 2007). SCA3 is characterized by progressive cerebellar ataxia, muscle atrophy, dystonia, and spasticity. Very small repeats lead to the rare very late onset SCA3 that can have parkinsonian symptoms. Eye-lid retraction and infrequent blinking are peculiar features of SCA3. Patients can also have speech impairment and difficulty in swallowing (Paulson, 2007; Durr, 2010; Rüb et al., 2013).





**Figure 7: Neuropathological observations in SCA3.** Neuronal intranuclear inclusion bodies in the (a) substantia nigra and (b) pontine nuclei in SCA3. Degeneration of the inferior olives in (d) SCA3 compared to (c) healthy controls. (f) SCA3 brain shows atrophy of the brainstem compared to (e) healthy controls (Rüb et al., 2013).

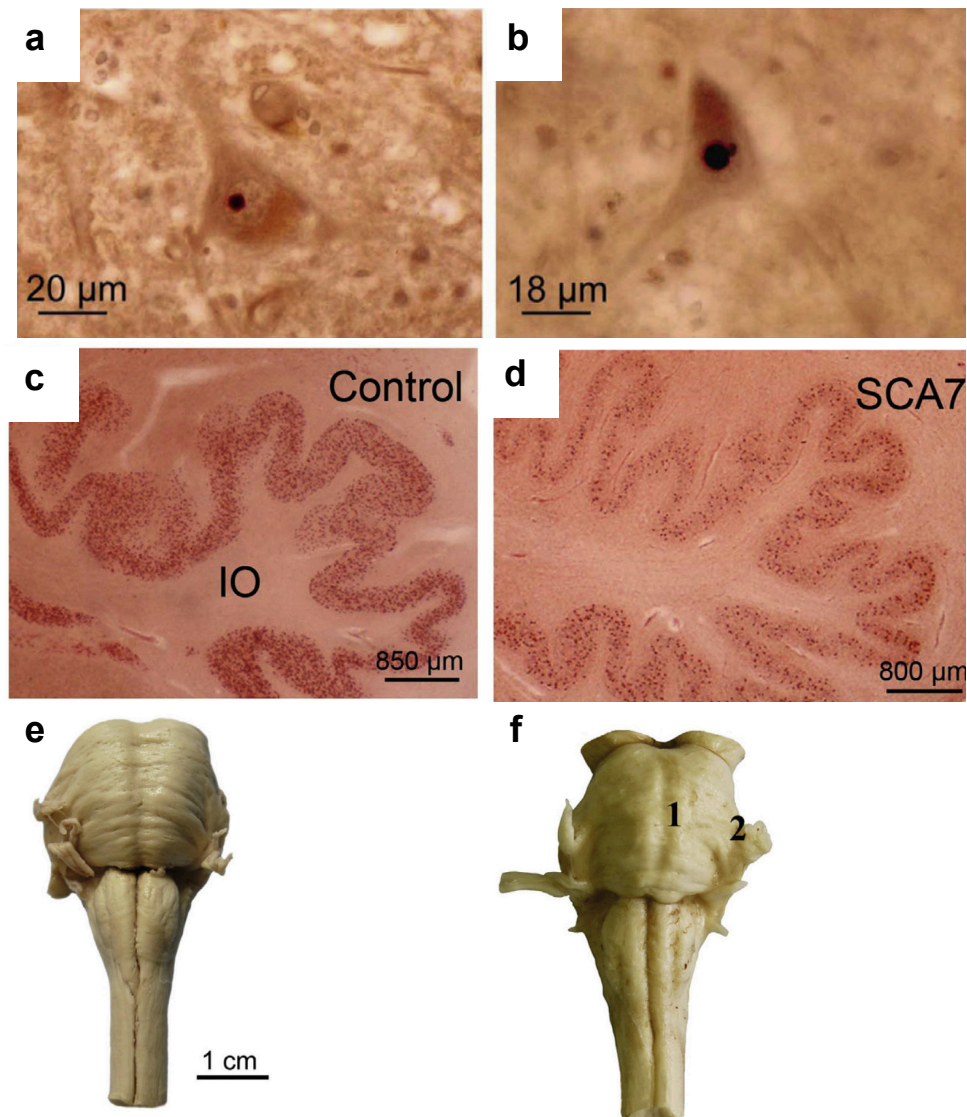
#### 1.2.4 Spinocerebellar ataxia type 7 (SCA7)

Among the dominantly inherited SCAs, SCA7 is uniquely differentiable as the only SCA with retina involvement that may lead to blindness. It is caused by expanded CAG repeats in the short arm of chromosome 3p12–13 where the ataxin-7 gene (ATXN7) gene is located (David et al., 1997). Whilst CAG repeats of more than 37 are considered pathologic, some

individuals can have over 300 repeats, and hence SCA7 has the most unstable CAG repeats (Stevanin et al., 2000; Paulson, 2009; Rüb et al., 2013). Anticipation is therefore exceptionally severe in SCA7, since the very large expansions can cause early onset disease in newborns (Paulson, 2009).

Ataxin-7 is ubiquitously expressed and localized in the cytoplasm and nucleus of neuronal and non-neuronal tissues (Cancel et al., 2000). Some studies have suggested that like other SCAs, it plays a role in transcriptional regulation by functioning as part of transcriptional repressor complexes (Palhan et al., 2005; Strom et al., 2005). In addition, it is associated with histone deubiquitination and mRNA export from the nucleus (Rüb et al., 2013). CAG expansion in ataxin-7 interferes with the normal transcription complexes such as the STAGA transcription coactivator complex. This complex interacts with the cone-rod homeobox (CRX) transactivator that is responsible for the normal function of photoreceptor genes (La Spada et al., 2001). Mutant ataxin-7 impairs the function of glial which may in turn induce degeneration in Purkinje cells (Orr & Zoghbi, 2007). The N-terminal of the mutant protein contains a stretch of polyalanine that is elongated in birth defects and oculopharyngeal muscular dystrophy (Rüb et al., 2013) and hence may play a role in the retinal degeneration observed in SCA7. A study on a SCA7 transgenic mouse model created by inserting 92 polyglutamine cDNA flanked by loxP at the start site of translation in the murine PrP gene in a bacterial artificial chromosome (BAC), led to cerebellar degeneration and loss of Bergmann glia (Furrer et al., 2011). Removal of the 92 polyglutamine ataxin-7 by crossing the transgenic mice with driver lines expressing Cre-recombinase in the Purkinje cells and inferior olive protected against cerebellar atrophy and Bergmann glia pathology. Meanwhile, when the transgenic mice were crossed with driver lines expressing Cre-recombinase in the Bergmann glia, the pathological features were not prevented (Furrer et al., 2011) and thus signify the importance of glia in SCA7 pathology. To understand the mechanism by which mutant ataxin-7 influences retinal degeneration and neurological dysfunction, transgenic mice (SCA7-D266N) with second-site mutation to prevent caspase-7 proteolysis were generated (Guyenet et al., 2015). It was reported that by inhibiting caspase-7 cleavage of the mutant ataxin-7, toxicity and aggregation of ataxin-7 were diminished and the mice lived twice as long with reduced retinal degeneration and neurological dysfunction compared to SCA7 mice (Guyenet et al., 2015). Hence proteolytic cleavage is critical to SCA7 pathology.

Retinal degeneration is unique to SCA7 with characteristic photoreceptors degeneration and damage to the retinal pigment epithelium (Durr, 2010; Rüb et al., 2013). Histopathological examinations have revealed atrophy of the optic pathways, loss of bipolar cells and ganglion cells, degeneration in the cerebellum, brainstem and pyramidal pathway (Yamada et al., 2008). Like the other SCAs, degeneration of the inferior olive is another common occurrence in the SCA7 (Figure 8).

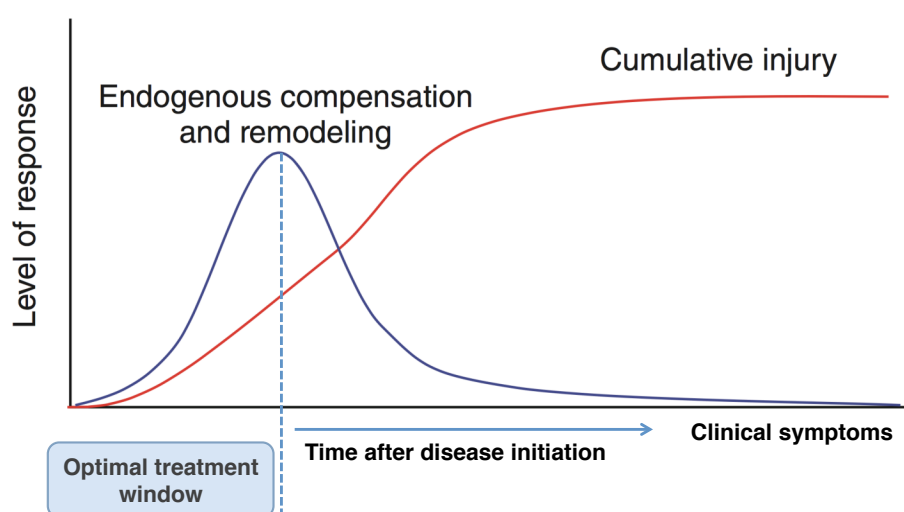


**Figure 8: Neuropathological observations in SCA7.** Intranuclei inclusion bodies are found in the (a) facial nuclei and (b) hypoglossal nuclei. (d) The inferior olives are degenerated in SCA7 compared to (c) healthy controls. (f) SCA7 pons are atrophied with loss of traversing pontocerebellar fibers and reduced medial cerebellar peduncle (Rüb et al., 2013).

Affected individuals tend to have decreased visual (83%) and auditory (24%) acuity (Durr, 2010). Affected individuals also present progressive cerebellar ataxia, dysarthria, dysphagia, slow saccades, somatosensory deficits and neuropsychological deficits (Yamada et al., 2008; Durr, 2010; Rüb et al., 2013). Patients with very large CAG repeats are also prone to cardiac failure (Durr, 2010).

### 1.3 Diagnosis and treatment of polyglutamine diseases

Diagnosis becomes easy when there is a family history of the disease. Persons at risk of HD and SCA might opt to perform genetic testing in order to make critical life decisions such as marriage, career and procreation. At risk individuals with no known family history of the disease might be caught off guard when the symptoms start appearing later on in life and when they have already started a family. The chance for children to inherit the disease with increased early onset is increased by 50% when the disease is inherited from the father (Myers, 2004). Other individuals might opt out of genetic testing due to the lack of treatment for the disease and the emotional burden that accompanies positive results. Anxiety, stress and suicidal tendencies are common with positive test results (Walker, 2007). Extensive genetic counseling could however help at risk individuals overcome the burden with the test. Genetic testing in at risk individuals may open a therapeutic window for potential therapies that could treat the disease (Figure 9).



**Figure 9: Genetic testing may offer an opportunity to take advantage of the therapeutic window before symptoms onset.** Modified from (Lo, 2010).

Currently, supportive management and symptomatic treatments are given to individuals with HD or SCA. There are treatments for some of symptoms manifested by the disease but there is still the lack of effective treatment for the disease itself. Physiotherapy must be advocated (Ilg et al., 2014; Synofzik & Ilg, 2014), and speech therapy to patients with dysarthria. Anti-choreic and mostly neuroleptic drugs have also been used to treat involuntary movements as well as anxiety and irritability (Walker, 2007; Videnovic, 2013). Such symptomatic treatment and supportive management are helpful and shall be initiated soon when symptoms develop.

In the search for disease modifying therapies, most of the studies have been focused on HD. This may be because HD is more common, but since it shares common pathophysiology with SCAs, drugs that are found to be beneficial in HD can become potential candidates for SCAs. Several treatments for HD have been explored but some showed no benefit at all, while in others the risks outweighed the benefits (Lauterbach et al., 1998; Walker, 2007). These standard clinical trials however take several years to perform and many patients are needed in order to see sufficient therapeutic effect (Tabrizi et al., 2012). Since these diseases are rare, enrolling large numbers of patients may not be feasible.

Potential treatments for polyglutamine disorders may either fall under targeting the polyglutamine protein such as gene therapy to reduce or modify the mutated protein (Labbadia et al., 2012; Olson et al., 2012) or reversing cellular defects such as compensation of key downstream cellular alterations through anaplerotic therapy (Mochel et al., 2010). In order to be able to test potential therapies that seek to amend metabolic dysfunction, methods with high effect sizes are needed to identify robust biomarkers of metabolism. As such, MRI/MRS techniques are the go to methods for exploring HD and SCA biomarkers.

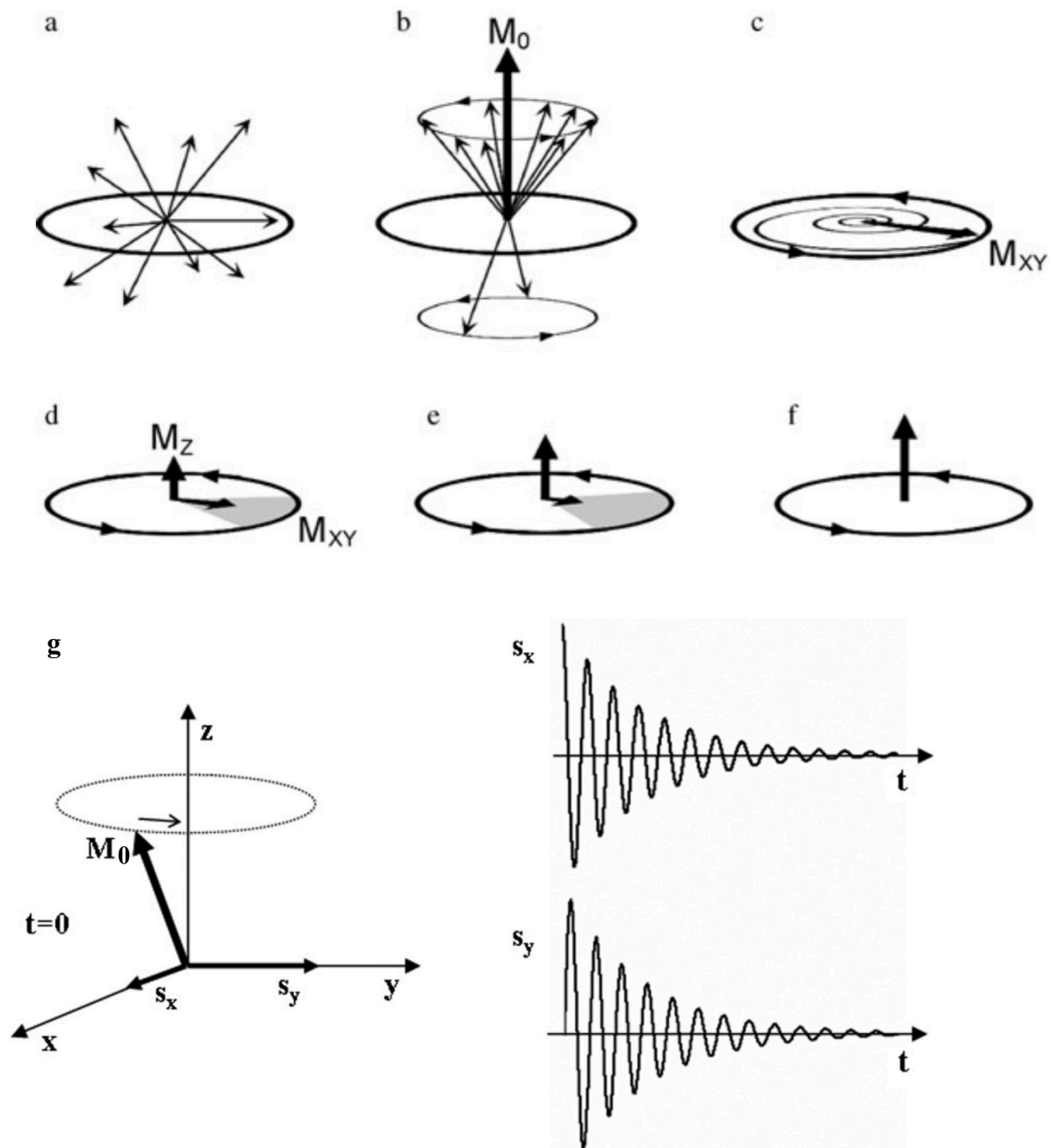
## **Magnetic resonance (MR) approaches to biomarker identification**

### **1.4.1 Principles of MR**

Several macroscopic and microscopic changes occur prior to and after symptoms onset. These changes are easily assessable with MR modalities. MR uses non-ionizing radiation to generate three-dimensional (3D) high-resolution images with high spatial and temporal resolution unlike positron emission tomography or ultrasound. In addition, structural, physiological and metabolic information can be measured using MR techniques (Sosnovik & Weissleder, 2007). Due to its effectiveness and ease of use, the past decades have seen an exponential rise in its development (Edelman, 2014).

The human body is made up of different atoms, the most abundant of which is hydrogen atoms (protons,  $^1\text{H}$ ) due to the body being composed of almost 75% water ( $\text{H}_2\text{O}$ ). These protons are in constant motion as they spin around their axis generating an electromagnetic field and therefore they act as magnets that possess North and South poles (dipole). Naturally, these spins are randomly oriented and hence they cancel each other out and no net magnetization is observed. However, due to their spin and charge, they will align and rotate or precess at a given frequency (resonance or Larmor frequency) along the magnetic field of a large external magnet ( $B_0$ ) (Hunt & Thomas, 2008; Plewes & Kucharczyk, 2012; Vijayalaxmi et al., 2015). While all magnetic substances align in one direction in the presence of an external magnetic field, protons may either align parallel to the  $B_0$  (spin-up) or opposite to the  $B_0$  (spin-down) (Edelman & Warach, 1993), which represent the lower energy state and higher energy state respectively. At this point the net magnetization is very low and not readily observed. However, when a radiofrequency (RF) energy generated from an additional oscillating magnetic field ( $B_1$ ) is applied perpendicular to the  $B_0$ , the spin-up protons absorb the energy and move into the higher energy state (Bloch, 1946). This energy is released when the spins return to their original state and this induces current in a receiver coil or antenna placed near the measured region. The current induced is the magnetic resonance signal. During the absorption of the RF energy, the net precession is pushed away from the  $B_0$  (Figure 10) depending on the amplitude and duration of the RF pulse ( $B_1$ ) and the angle between the precessing spins and the  $B_0$  field is known as flip angle. With time the net magnetization ( $M_0$ ) along the  $B_0$  begins to recover or relax as the absorbed energy is being released.  $M_0$  increases gradually until a steady state is reached and this recovery process is

known as relaxation. The time taken to recover 63% of its equilibrium value is known as the longitudinal relaxation time ( $T_1$ ) (Plewes & Kucharczyk, 2012). Another important relaxation time that is influenced by the interaction between the spins is the  $T_2$  relaxation time. The applied RF rotates the  $M_0$  into the transverse plane (XY plane). The magnetization that is observed in the transverse plane ( $M_{xy}$ ) reflects how much  $M_0$  has been pushed and the degree at which the spins are in phase (Hunt & Thomas, 2008). The precession of the spins in the XY plane induces local currents in receiver coils. A strong signal is generated when the spins are in phase and also when a large flip angle is used, preferably at  $90^\circ$ . When the RF is turned off, the interaction of the spins with each other causes them to spin out of phase which leads to a decline in  $M_{xy}$  (Figure 10). The process of dephasing or fading of the transverse signal is known as free induction decay and the time it takes for  $M_{xy}$  to completely dephase is called the transverse relaxation time ( $T_2$ ). Relaxation times are specific to each tissue type thus producing contrast between different tissue types.



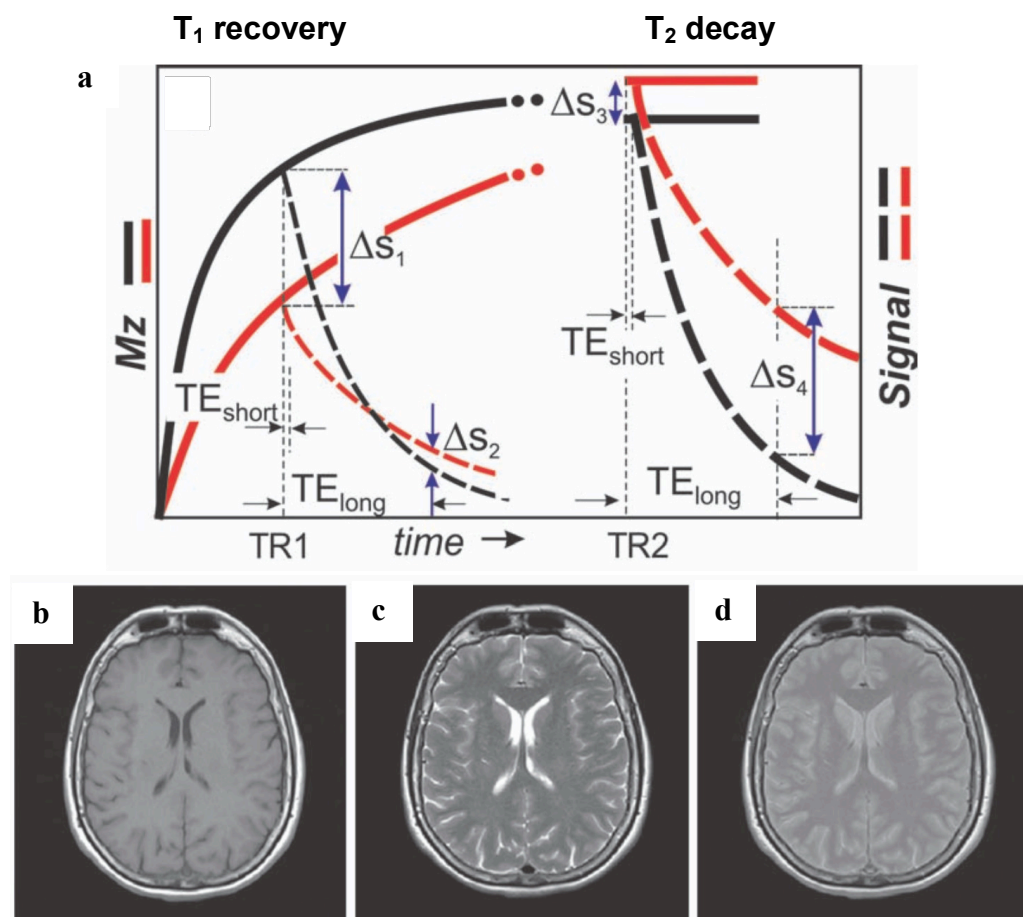
**Figure 10: Dipole moment and free induction decay.** (a) The spins are randomly oriented and hence generate no net magnetization. (b) They align and rotate at a unique frequency along an external magnetic field to generate a net magnetization ( $M_0$ ). (c) A RF pulse of same frequency flips the  $M_0$  in the transverse plane and the portion of the  $M_0$  in this plane is the  $M_{xy}$ . (d) When the RF is stopped, the spin-spin interaction causes them to precess out of phase leading to (e) a decrease in the  $M_{xy}$  whilst the magnetization along the  $B_0$  ( $M_z$ ) is recovered. (f)  $M_{xy}$  decreases faster than the recovery of  $M_z$  (Hunt & Thomas, 2008). (g) Real ( $S_x$ ) and imaginary ( $S_y$ ) parts of FID that correspond to x and y components of the rotating magnetization vector  $M_0$  (Jiru, 2008).



## 1.4.2 Evaluating atrophy and axonal damage

### *Brain volumetry*

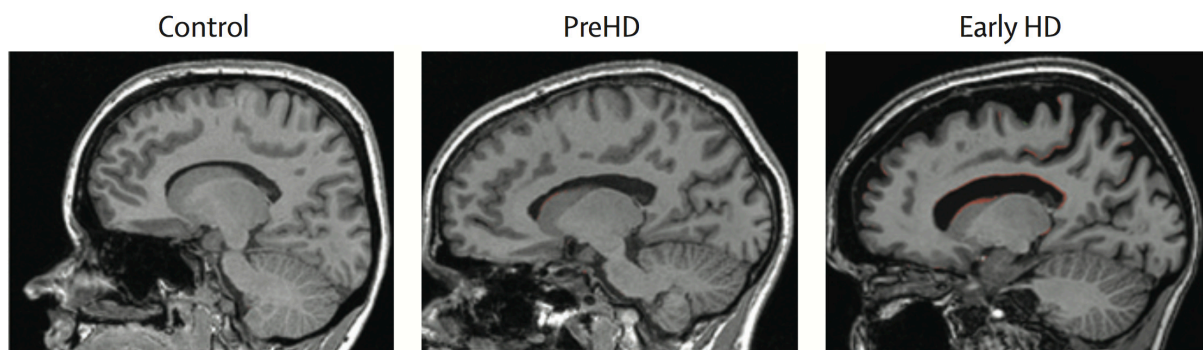
Advances in MR hardware has enabled the rapid acquisition of data with great resolution and high signal to noise ratio (SNR). Images are formed by spatial localization of signal intensities.  $T_1$  and  $T_2$  relaxation times influence the type of image that can be acquired (Figure 11). For atrophy characterization, it is imperative to have enough contrast between different tissues types that allow separation of white matter (WM), gray matter (GM) and cerebrospinal fluid (CSF) in order to determine their respective volumes in regions of interest (ROI).  $T_1$ -weighted images are thus preferred as they provide such contrast.



**Figure 11: Relaxation times introduce endogenous contrast between tissue types.** Long  $T_1$  and  $T_2$  generate a  $T_1$ -weighted image with darker CSF (b) and a short  $T_1$  and  $T_2$  generates a  $T_2$ -weighted image with brighter CSF (c). A combination of varying  $T_1$  and  $T_2$  generates proton density image (Plewes & Kucharczyk, 2012).

Segmentation can be achieved either by manually delineating ROIs or using automatic segmentation tools such as SPM (Ashburner & Friston, 2005), Freesurfer (Fischl et al., 2002) or FSL (Smith et al., 2002). Each of these has their strengths and weaknesses (Heinen et al., 2016). Importantly, they reduce segmentation time significantly and are the method of choice when large sets of data are to be analyzed. Preferably, the volumes of the ROIs should be normalized to the total intracranial volume to remove the bias introduced by different skull sizes.

Another promising approach is the boundary shift integral (BSI) which can be used to determine whole brain atrophy and atrophy of specific regions such as the caudate (Freeborough & Fox, 1997; Hobbs et al., 2009). The added advantage of BSI is that instead of looking at the whole volume of ROIs, it measures the change in the boundary between the tissue and CSF and determines how much it has changed over time. The boundary change might be very minimal and hence whole volume analysis might not be sensitive to the change whereas BSI can easily identify these changes. Therefore, BSI is more sensitive to atrophy than whole volume analysis. It uses probabilistic segmentations to estimate the change between serial MRI scans at different time points. The process is semi-automatic and hence manual corrections can be performed to improve the estimation process. It has been applied in in large cohorts of early stage HD patients and presymptomatic individuals and showed a marked atrophy of the striatum that is present at the presymptomatic stage and worsens as the disease progresses (Figure 12) (Tabrizi et al., 2011). The limitation is that the software is not generally available.



**Figure 12: Brain boundary shift integral application in HD.** The image shows regions of atrophy (red) in presymptomatic individuals (PreHD) and early stage HD patients. Source (Tabrizi et al., 2011).

## *Diffusion-weighted imaging*

Diffusion imaging provides an avenue to probe white matter integrity without the need for invasive biopsy and histological analysis.

Diffusion is the random movement of molecules in thermal equilibrium. In diffusion imaging, the principal focus is on the movement of water in tissues. Diffusion in the brain is affected by the tissue properties. In the CSF for example, diffusion is not restricted and hence can be equal in all directions and this is known as isotropic diffusion. In axons however, especially in the WM, the myelin restricts movement perpendicular to the axons and favors parallel diffusion, a phenomenon termed anisotropic diffusion. The anisotropy helps to understand the tissue structure and alterations in relation to pathology. Previously, in order to measure the anisotropy, knowledge of the axonal orientation was needed and thus was limited to fixed samples (O'Donnell & Westin, 2011). Applications to complex structures such as the brain fibers were made possible through the introduction of the diffusion tensor (DTI) model (Basser et al., 1994a, 1994b; Pierpaoli & Basser, 1996).

In order to measure diffusion in the brain, a first gradient pulses is used to change the phase of the water molecules whilst a second gradient pulse is applied after a short period of time to refocus the phase. Therefore, in the absence of diffusion, no signal is lost and the image appears brighter, whilst in the presence of diffusion, the refocusing pulse is not able to rewind the phase-shift from the first gradient and hence leads to signal loss and the image appears darker (Mori & Zhang, 2006). Unlike volumetric images, it is impossible to extract diffusion orientation from a single intensity value (Mori & Zhang, 2006). Hence, a minimum of 6 diffusion images with one non-diffusion encoded image is needed to estimate the DTI model. A 3 x 3 matrix is used to represent the diffusion model of the anisotropy. Decomposition of this matrix generates the three eigenvalues ( $\lambda_1, \lambda_2, \lambda_3$ ) with their corresponding eigenvectors. The principal eigenvalue ( $\lambda_1$ ) corresponds to the principal diffusion along the axons (axial diffusivity) whilst the average of the remaining eigenvalues represents diffusion perpendicular to the axons and known as radial diffusivity. The anisotropy of the axons is represented in a metric called the fractional anisotropy (FA) that is scaled from 0 (isotropic) to 1 (anisotropic) (Pierpaoli & Basser, 1996).

$$FA = \sqrt{\frac{1}{2} \frac{\sqrt{(\lambda_1 - \lambda_2)^2 + (\lambda_2 - \lambda_3)^2 + (\lambda_3 - \lambda_1)^2}}{\lambda_1^2 + \lambda_2^2 + \lambda_3^2}}$$

Interpretation of diffusion metrics remains complicated. Generally, however, reduced FA is thought to reflect loss of white matter integrity with a possible damage to the myelin or a disruption in the organization of the fibers (Samartzis et al., 2014). Increased RD has also been linked to alterations in the axonal diameter (Concha et al., 2010), which may in turn reflect demyelination. Despite its use in several pathologies (Alexander et al., 2007), DTI has many limitations that could complicate the interpretation of results. First of all, DTI metrics are sensitive to noise from the hardware and patient movements so that the noise might contribute to poorly estimated eigenvalues. Furthermore, DTI metrics are not capable of resolving fiber populations in regions with crossing-fibers (Wiegell et al., 2000; Tuch et al., 2002) and hence changes in the metrics cannot be attributed to specific structural changes. To resolve this, high order diffusion models for fiber tracking or tractography have been proposed (Tuch et al., 2002). Tractography technique with the non-negativity constrained spherical deconvolution (CSD) approach that has low fiber orientation error rate and high fiber detection rates is the most suitable for fiber tracking (Tournier et al., 2007; Wilkins et al., 2015). It allows the estimation of different fiber populations within a given voxel and attributes changes to specific structural changes.

### **1.4.3 Determination of brain metabolic alterations with MRS**

Metabolic dysfunction and weight loss is a commonly shared pathophysiological mechanism in HD and SCAs (Weber et al., 2014). Estimating the degree to which neurochemical are perturbed due to a pathology provides an important source of information on metabolic biomarkers. A detailed review of the physics behind MRS can be found in (de Graaf, 2007).

Some few additional steps separate MRS from MRI. As a reminder, the signal that is induced in the coil is spatially localized to generate MRI images. However, in MRS, this signal is mathematically transformed using Fourier Transform (FT) to separate the frequency components and determine the intensity or proportion of each metabolite. Metabolites are easily separated from each other due to a condition referred to as chemical shift. The interactions of the spins create small variations in the  $B_0$  and therefore protons in different molecules resonate at slightly different frequencies from their Larmor frequency. The variations are expressed in parts per million and are dependent on the position of the atom in the molecule and the neighboring spins.

MRS is often performed in a demarcated region of interest known as a spectroscopic volume of interest (VOI). The static magnetic field ( $B_0$ ) does not have a truly homogenous magnetic field along all points. Hence, one of the most important steps in MRS is to map the  $B_0$  field variations and correct them with gradient coils in the VOI. The process of producing homogenous magnetic fields in the VOI is known as a shimming. FASTMAP shimming is an automatic method of shimming with minimal time constraints that generates highly resolved spectral linewidth with excellent shim values (Gruetter & Tkac, 2000). Another important step is the calibration of the RF pulse to determine the exact amplitude needed to excite the nucleus and generate spectra with good SNR.

MRS can be performed on any nucleus with a magnetic moment (Table 1)(de Graaf, 2007). The most abundant with high sensitivity is  $^1\text{H}$ . *In vivo* studies have focused on  $^1\text{H}$ ,  $^{31}\text{P}$  (phosphorus) and  $^{13}\text{C}$  (carbon) nuclei.

**Table 1: Properties of nuclei that can be used in MRS** (de Graaf, 2007).

Isotope	Spin	Gyromagnetic ratio ( $10^7 \text{ rad T}^{-1} \text{ s}^{-1}$ )	NMR frequency at 2.35 T (MHz)	Natural abundance (%)	Relative sensitivity <sup>a</sup>
$^1\text{H}$	1/2	26.752	100.000	99.985	1.00
$^2\text{H}$	1	4.107	15.351	0.015	$1.45 \times 10^{-6}$
$^3\text{He}$	1/2	-20.380	76.181	$1.4 \times 10^{-4}$	$5.75 \times 10^{-7}$
$^7\text{Li}$	3/2	10.398	38.866	92.58	0.272
$^{13}\text{C}$	1/2	6.728	25.145	1.108	$1.76 \times 10^{-4}$
$^{14}\text{N}$	1	1.934	7.228	99.630	$1.00 \times 10^{-3}$
$^{15}\text{N}$	1/2	-2.712	10.137	0.370	$3.86 \times 10^{-6}$
$^{17}\text{O}$	5/2	-3.628	13.562	0.037	$1.08 \times 10^{-5}$
$^{19}\text{F}$	1/2	25.181	94.094	100.000	0.834
$^{23}\text{Na}$	3/2	7.080	26.466	100.000	$9.27 \times 10^{-2}$
$^{31}\text{P}$	1/2	10.841	40.481	100.000	$6.65 \times 10^{-2}$
$^{39}\text{K}$	3/2	1.250	4.672	93.100	$4.75 \times 10^{-4}$
$^{129}\text{Xe}$	1/2	-7.452	27.856	26.44	$5.71 \times 10^{-3}$

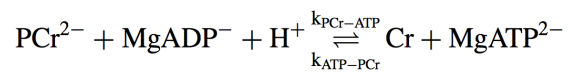
He: helium; Li: lithium, N: Nitrogen, O: oxygen, F: fluorine, Na: sodium, K: potassium, Xe: xenon.

$^1\text{H}$  MRS detects a wide range of metabolites including *N*-acetylaspartate (NAA), glutamate (Glu), choline (Cho) and creatine (Cr). Water is very abundant in the body and hence its signal overshadows those of other metabolites whose concentrations are about 24 times smaller than water. Active water suppression is therefore needed in order to observe the

spectra from metabolites. This can be coupled with outer volume suppression pulses (OVS) in order to attenuate the signal from outside the VOI and suppress signal from lipids. In addition, the VOI can be placed away from the scalp and fat-enriched bone marrow to limit the contribution of lipids and improve the shimming. In the acquisition of the spectra, one important factor to consider is the echo time ( $T_E$ ).  $T_E$  is the time between the initial  $90^\circ$  excitation of the nuclei with the RF and the sampling of the signal induced in the coil. Short  $T_E$  is optimum for  $^1\text{H}$  MRS as it allows metabolites with short and long  $T_2$  to be measured. In contrast, long  $T_E$  experiments allow the detection of the major metabolites that have long  $T_2$  including NAA, Cho and Cr.

Asides measuring static concentrations, diffusion weighted spectroscopy (DWS) can be performed by coupling diffusion sensitizing gradients to MRS to allow the extraction of cell specific information. Practically, MRI measures such as DTI and functional imaging are indirect indicators of biological events in the brain. Direct physiological monitoring of cell-specific activities is achieved when the diffusion properties of metabolites are determined. Compartment specific information directly relates to the cell types, glial or neuronal, that are implicated in neurodegenerative disorders (Ronen & Valette, 2015).

$^{31}\text{P}$  MRS is used to measure the metabolites that are directly related to brain bioenergetics. It is used to determine the concentration of phosphorus-containing metabolites such as ATP, Pi and PCr. Due to the relatively high abundance of  $^{31}\text{P}$  good quality spectra can be acquired over a short period of time. Furthermore, by utilizing their endogenous magnetization properties, reaction rates or fluxes of metabolic processes can be evaluated such as the rate of creatine-kinase (CK) that modulates the exchange of high-energy phosphate group between PCr and ATP in the following equilibrium reaction (Figure 13) (de Graaf, 2007). This process is called magnetization transfer (MT). The most common form of MT utilizes RF with specific bandwidth to selectively saturate resonances such as that of  $\gamma$ -ATP. The exchange between  $\gamma$ -ATP and PCr will cause an indirect reduction of the PCr peak and the degree of attenuation will determine the rate of CK. In order to prevent RF bleed over, which is the direct effect of the saturation pulse on the PCr signal, a symmetric saturation is performed on the opposite side of PCr and this is used to correct for RF bleed over. Understanding the rate of CK can shed light on the mechanisms underlying altered static measures of energetic metabolites such as Cr and PCr.



**Figure 13: Equation of equilibrium reaction of the exchange of high-energy phosphate group between ATP and PCr (de Graaf, 2007).**

## Objectives

The objective of this project was to combine several neuroimaging modalities to identify biomarkers in HD and SCAs. Specifically, this project aimed at:

- Using  $^{31}\text{P}$  MRS to validate Pi/PCr ratio as functional biomarker of brain energy metabolism in HD.
- Evaluating the efficacy of an anaplerotic therapy in HD using Pi/PCr ratio as a functional biomarker.
- Evaluating the underlying cause of altered energy metabolism in HD by evaluating the rate of the CK.
- Identifying additional dynamic biomarkers of metabolism in HD.
- Standardizing the acquisition and quantification process for  $^1\text{H}$  MRS in SCAs.
- Determining the metabolic and structural changes associated with SCAs.
- Integrating the multimodal data of SCAs into a model to explain the pathology.

The thesis is thus organized based on the methodologies that answer the specific aims of the project.



## Chapter 2

### Organisation:

<b>Study 1: Validation of a functional biomarker and its use to evaluate an anaplerotic therapy in HD. ....</b>	<b>35</b>
2.1 Introduction and objectives .....	35
2.2 Materials and methods.....	35
2.3 Principal results .....	36
2.4 Published article .....	37
2.6 Perspective.....	44
2.6.1 TRIHEP3 .....	44
2.6.2 REVHD .....	46
2.6.3 Key role of MRI-MRS evaluations in both studies.....	48

# **Study 1: Validation of a functional biomarker and its use to evaluate an anaplerotic therapy in HD.**

## **2.1 Introduction and objectives**

Metabolic dysfunction is an important contributor to the pathophysiology of HD. A previous study in HD patients showed that  $^{31}\text{P}$  MRS was able to detect bioenergetic alterations in the muscle of HD patients during exercise (Mochel et al., 2010). The study also reported that patients who had muscle acidosis and reduced Cr recovery saw a normalization in their pH and Cr recovery time after one week of anaplerotic therapy with triheptanoin. In order to perform therapeutic interventions seeking to amend metabolic dysfunction especially in the brain, there was the need to identify biomarkers of brain energy metabolism. A  $^{31}\text{P}$  MRS study in 15 HD patients and 15 age- and sex-matched controls reported alterations in the Pi/PCr ratio in patients during visual stimulation (Mochel et al., 2012) and suggested to use such ratio as a functional biomarker of brain energy metabolism.

Therefore, this study (ClinicalTrials.gov Identifier: NCT01696708) sponsored by the Institut national de la santé et de la recherche médicale (Inserm) was designed to i) reproduce and validate the use of Pi/PCr ratio as a functional biomarker of brain energy metabolism; ii) and evaluate the therapeutic effect of triheptanoin in the brain of HD patients.

## **2.2 Materials and methods**

$^{31}\text{P}$  MRS coupled with visual stimulation was performed on a 3-Tesla (3T) Siemens Magnetom Trio (Siemens Medical Solutions, Erlangen, Germany) scanner in the visual cortex of 13 healthy controls and 9 patients at the early stage of HD. UHDRS was used for neurological assessment of patients. Using the pulse acquire sequence, FIDs were collected with a transmit/receive surface coil (RAPID Biomedical GmbH, Rimpar, Germany) for 4 minutes whilst subjects closed their eyes (rest), 8 minutes during visual stimulation (activation), and 8 minutes after visual stimulation (recovery) with subject's eyes closed. Patients were rescanned after a month to determine if their metabolic profile changed with time. The data were analyzed with the java-based graphical user interface for the magnetic

resonance user interface (jMRUI) with the AMARES quantification method. The Pi/PCr ratios of controls were then compared to the patients.

Five of the patients used for the validation phase were recruited with 5 new patients to evaluate the anaplerotic properties of triheptanoin, a carbon-7 (C7) fatty acid, on the brain metabolic profile of HD patients. The patients had  $^{31}\text{P}$  MRS performed on them before and after one month of treatment.

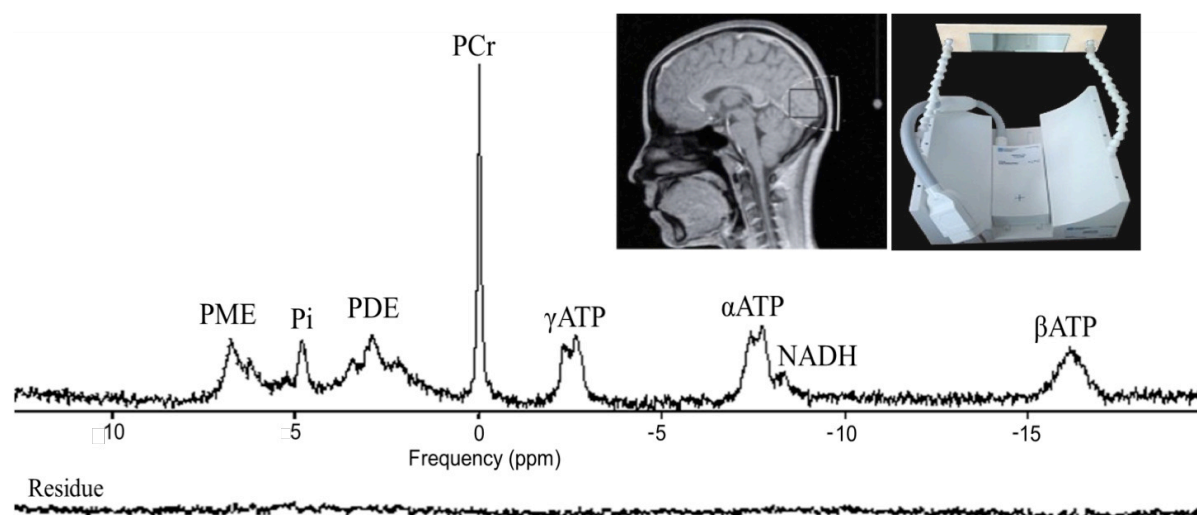
### 2.3 Principal results

We obtained good quality data from the visual cortex and the quantification method was efficient to detect all the metabolites (Figure 14). We observed similar findings as reported previously (Mochel et al., 2012) with a significant increase in Pi/PCr ratio in controls during visual stimulation. In contrast, patients showed no change in the Pi/PCr ratio during visual stimulation and this profile remained stable over one month period. This can be attributed to the underlying metabolic dysfunction in HD. Patients who were recruited to evaluate the efficacy of triheptanoin also showed no increase in the Pi/PCr ratio before treatment. After one month of treatment however, their profile was improved with an increase in Pi/PCr ratio during visual stimulation.

In another unrelated paper (Annex A, ClinicalTrials.gov Identifier: NCT02014883), we showed that this functional  $^{31}\text{P}$  biomarker can be used in other disorders related to primary metabolic dysfunction. The glucose transporter 1 (GLUT1) is an integral membrane protein responsible for the transport of glucose across plasma membrane (Olson & Pessin, 1996). Glucose is an important energy source for ATP synthesis through glycolysis. The higher energy demand of the brain means that a continuous delivery of glucose from the blood is essential for normal brain function. Mutations in *GLUT1* in brain capillaries cause the impairment of glucose transport across the blood-brain-barrier and lead to cerebral energy deficiency in the rare autosomal dominant GLUT1 deficiency syndrome (GLUT1-DS) (De Vivo et al., 1991). GLUT1-DS is characterized by seizures, permanent and paroxysmal movement disorders, and delayed development (Gras et al., 2014). Ketogenic diets used to treat this syndrome require very high fat contents that make them hard to tolerate for patients on the long term. Ketogenic diets are made up of even-chain fatty acids that are precursors of

acetyl-CoA only, whilst odd-chain fatty acids like triheptanoin are precursors of both acetyl-CoA and propionyl-CoA, a key substrate for the Krebs cycle (Roe et al., 2002; Mochel, 2017).

In this study (Annex A), we showed that triheptanoin was able to replenish the substrates needed to fuel the Krebs cycle, which led to a dramatic improvement (90%) of patient's movement disorders (Mochel et al., 2016). We also showed that  $^{31}\text{P}$  MRS was able to capture the brain energy profile of GLUT1 deficient patients at baseline. Importantly, the  $^{31}\text{P}$  MRS profile normalized with triheptanoin along with clinical improvement. Therefore, this study showed that our  $^{31}\text{P}$  MRS protocol can be a good clinical predictor of brain energy homeostasis.



**Figure 14: Representative spectra and the coil and region of interest for the  $^{31}\text{P}$  experiment.** The surface coil was adjusted to the center of the visual cortex with the aid of a water-filled tube (white sphere on the image of the head) beneath the coil. Good quality spectra were obtained and the AMARES quantification method allowed the detection of the metabolites with no residue after the model fitting. PME: phosphomonoester, PDE: phosphodiester, NADH: nicotinamide adenine dinucleotide.

## 2.4 Published article

# Triheptanoin improves brain energy metabolism in patients with Huntington disease



Isaac Mawusi Adanyeguh, MS  
Daisy Rinaldi, PhD  
Pierre-Gilles Henry, PhD  
Samantha Caillet, MS  
Romain Valabregue, PhD  
Alexandra Durr, MD, PhD  
Fanny Mochel, MD, PhD

Correspondence to  
Dr. Mochel:  
fanny.mochel@upmc.fr

## ABSTRACT

**Objective:** Based on our previous work in Huntington disease (HD) showing improved energy metabolism in muscle by providing substrates to the Krebs cycle, we wished to obtain a proof-of-concept of the therapeutic benefit of triheptanoin using a functional biomarker of brain energy metabolism validated in HD.

**Methods:** We performed an open-label study using  $^{31}\text{P}$  brain magnetic resonance spectroscopy (MRS) to measure the levels of phosphocreatine (PCr) and inorganic phosphate (Pi) before (rest), during (activation), and after (recovery) a visual stimulus. We performed  $^{31}\text{P}$  brain MRS in 10 patients at an early stage of HD and 13 controls. Patients with HD were then treated for 1 month with triheptanoin after which they returned for follow-up including  $^{31}\text{P}$  brain MRS scan.

**Results:** At baseline, we confirmed an increase in Pi/PCr ratio during brain activation in controls—reflecting increased adenosine triphosphate synthesis—followed by a return to baseline levels during recovery ( $p = 0.013$ ). In patients with HD, we validated the existence of an abnormal brain energy profile as previously reported. After 1 month, this profile remained abnormal in patients with HD who did not receive treatment. Conversely, the MRS profile was improved in patients with HD treated with triheptanoin for 1 month with the restoration of an increased Pi/PCr ratio during visual stimulation ( $p = 0.005$ ).

**Conclusion:** This study suggests that triheptanoin is able to correct the bioenergetic profile in the brain of patients with HD at an early stage of the disease.

**Classification of evidence:** This study provides Class III evidence that, for patients with HD, treatment with triheptanoin for 1 month restores an increased MRS Pi/PCr ratio during visual stimulation. *Neurology*® 2015;84:490-495

## GLOSSARY

**ANOVA** = analysis of variance; **ATP** = adenosine triphosphate; **BCAA** = branched-chain amino acid; **CoA** = coenzyme A; **fMRS** = functional magnetic resonance spectroscopy; **HD** = Huntington disease; **MRS** = magnetic resonance spectroscopy; **PCr** = phosphocreatine; **Pi** = inorganic phosphate; **UHDRS** = Unified Huntington's Disease Rating Scale.

Huntington disease (HD) is characterized by autosomal dominant inheritance and motor, behavioral, and psychiatric symptoms.<sup>1</sup> There is strong evidence for hypometabolism in the brain of patients with HD. For example, glucose consumption is reduced, especially in the basal ganglia, even in presymptomatic mutation carriers.<sup>2-4</sup> Studies in animal models have revealed decreased adenosine triphosphate (ATP) concentrations in the brain of HD mouse models.<sup>5</sup> There are also nonneurologic symptoms at the early stage of the disease, such as weight loss despite enhanced caloric intake, which suggest a hypercatabolism in HD.<sup>6</sup> Reduced concentrations of branched-chain amino acids (BCAAs)—valine, leucine, and isoleucine—have been found in plasma samples of patients with HD as early as in presymptomatic carriers even when they were on a high-caloric diet.<sup>6</sup> We hypothesized that decreased circulating levels of BCAAs reflect their mitochondrial oxidation in order to provide 2 key intermediates for the Krebs cycle: acetyl coenzyme A (acetyl-CoA) and succinyl-CoA.<sup>6</sup> Consequently, therapies aiming at

From Inserm U 1127 (I.M.A., D.R., R.V., A.D., F.M.), CNRS UMR 7225, Sorbonne Universités, UPMC University Paris 06, UMR S 1127, Institut du Cerveau et de la Moelle épinière, ICM, Paris, France; Center for Magnetic Resonance Research (P.-G.H.), University of Minnesota, Minneapolis; Departments of Dietetics (S.C.) and Genetics (A.D., F.M.), AP-HP, Pitié-Salpêtrière University Hospital, Paris; and Center for Neuroimaging Research (R.V.), Institut du Cerveau et de la Moelle épinière, Paris, France.

Go to [Neurology.org](http://Neurology.org) for full disclosures. Funding information and disclosures deemed relevant by the authors, if any, are provided at the end of the article.

providing substrates to the Krebs cycle may be of special interest in HD. We previously showed that dietary anaplerotic therapy—replenishing the pool of metabolic intermediates in the Krebs cycle—was able to improve peripheral energy metabolism in HD using  $^{31}\text{P}$  magnetic resonance spectroscopy (MRS) in muscle.<sup>7</sup> Recently, we have identified the inorganic phosphate (Pi)/phosphocreatine (PCr) ratio as an outcome measure of brain metabolic dysfunction in patients with HD.<sup>8</sup> We therefore aimed at obtaining a proof-of-concept of the effect of anaplerotic therapies on brain energy metabolism in HD using our  $^{31}\text{P}$  functional MRS (fMRS) biomarker.

**METHODS** MRS data were acquired on a 3T whole-body Siemens Magnetom Trio (Siemens Medical Solutions, Erlangen, Germany). Motor dysfunction was evaluated with the total motor score of the Unified Huntington's Disease Rating Scale (UHDRS) with a maximal-worth score of 124. Eligibility criteria included patients 18 years and older with UHDRS score between 5 and 50, and who had the ability to undergo magnetic resonance scanning. The research was performed at the Pitié-Salpêtrière University Hospital.

The study was designed to answer 2 primary research questions: (1) Can the initial findings of abnormal Pi/PCr ratio be reproduced in the same patient population and how stable is the profile over a 1-month interval? and (2) Is triheptanoin able to correct the abnormal bioenergetic profile in the brain of patients with HD at an early stage of the disease?

This study therefore falls under Class III evidence because of the absence of a concurrent control group.

**Standard protocol approvals, registrations, and patient consents.** Participants were enrolled in an observational (NCT01696708) and an interventional (NCT01882062) clinical protocol promoted by INSERM and approved by the local ethical committee. All participants were older than 18 years and signed a written informed consent before participating in the studies.

**Recruitment of participants. Observational phase: Validation of functional biomarker.** Thirteen healthy individuals (mean age  $45 \pm 15$  years) and 9 patients with HD (mean age  $41 \pm 12$  years) at an early stage of the disease with a mean UHDRS motor score of  $10 \pm 3$  (table 1) were recruited within 3 months to validate the functional biomarker: Pi/PCr ratio. Patients with HD had 2 MRS scans at a month interval to assess the stability of the  $^{31}\text{P}$  profile.

**Interventional phase: Evaluation of the anaplerotic therapy.** Ten patients (5 females and 5 males) at the early stage of HD with a mean age of  $46 \pm 10$  years (range 22–61 years) and a mean UHDRS motor score of  $14 \pm 6$  (range 5–27) (table 2) were recruited within 2 months for the TRIHEP2 Study. Five of these patients (P1–P5) were recruited from the observational study. The dietitian determined the caloric intake of all patients and adapted their daily menus so that their diet remained isocaloric despite the addition of triheptanoin. At baseline, patients were evaluated for their UHDRS scores and MRS was performed to assess their brain energy profile. Each participant was then required to ingest 1 g/kg body weight of triheptanoin oil per day, divided in 3 to 4 intakes

per day during meals. All patients came for follow-up after 1 month of triheptanoin therapy and underwent neurologic examination with UHDRS scoring and scanning with MRS profile. Blood samples were collected after an overnight fast for standard analyses, as well as plasma C3-carnitine concentrations that reflect the proper metabolism of triheptanoin<sup>7</sup> (table 2).

**$^{31}\text{P}$  fMRS.** The  $^{31}\text{P}$  fMRS protocol has been previously described.<sup>8</sup> We targeted the visual cortex for the  $^{31}\text{P}$  fMRS because it has higher energy metabolism, is easily stimulated, and is close to the scalp allowing an increased sensitivity to small surface coils. In addition, occipital volume loss has been reported in patients with HD.<sup>9–11</sup> T1-weighted  $^1\text{H}$  images of the head were acquired to position our voxel. A 6-cm  $^{31}\text{P}$  transmit/receive surface coil (RAPID Biomedical GmbH, Rimpfing, Germany) was used to collect free induction decays for 4 minutes at rest, 8 minutes during visual activation with 6-Hz red/black checkerboard flashes, and 8 minutes after stimulation. Subjects were able to focus on the flashes with a nonmagnetic mirror mounted above their eyes while all lights in the room were turned off.

**Metabolite quantification.** The spectra were analyzed in the time domain using AMARES in jMRUI, a Java-based graphical user interface for the magnetic resonance user interface. The spectra were preprocessed to include removal of dummy scans at the beginning of acquisition, zero-order and first-order phase correction, and apodization. AMARES allows the inclusion of prior knowledge about relations between peaks and was used to obtain metabolite concentrations.<sup>8</sup> The ratio of Pi/PCr was calculated to determine the brain response to cortical activation.

**Statistics.** Paired  $t$  tests were used to compare UHDRS scores and plasma C3-carnitine before and after treatment with triheptanoin. Last observation carried forward imputation approach was used on the 2 UHDRS missing data. For the Pi/PCr ratio, repeated-measures analysis of variance (ANOVA) were used to test the global hypothesis that all time points—rest, activation, and recovery—are equal. If significant with an  $\alpha$  of 0.05, paired  $t$  tests were used to make pairwise time comparisons with an  $\alpha$  of 0.05 and Bonferroni multiple-testing corrections. Pearson correlation coefficients were computed to evaluate the relationship between Pi/PCr ratio and UHDRS scores and CAG repeats length with Bonferroni correction. Probability values  $<0.05$  were considered significant.

**RESULTS Tolerance and metabolism of triheptanoin.** Triheptanoin was well tolerated in all patients with HD except one patient who had episodes of diarrhea. This was due to the ingestion of triheptanoin only once or twice a day, usually as shots instead of mixing it with food as recommended. At posttreatment, we observed an increased plasma C3-carnitine ( $p = 0.002$ ) reflecting the proper metabolism of triheptanoin (table 2).

**Motor functions.** For 2 patients, UHDRS scores could not be evaluated after treatment because of a twisted ankle and a broken arm. Nonetheless, paired  $t$  test with last observation carried forward imputation approach showed a decrease in the UHDRS motor score of patients with HD treated for 1 month with triheptanoin ( $p = 0.012$ ) (table 2).

**Table 1** Characteristics of patients with Huntington disease from the observational phase of the study

ID	Sex	Age at exam, y	CAG P	CAG N	BMI, kg/m <sup>2</sup>	UHDRS visit 1	UHDRS visit 2
P1	F	42	46	17	21	13	13
P2	M	21	55	19	23	11	11
P3	M	52	44	ND	24	6	5
P4	F	45	41	16	20	13	8
P5	M	39	44	16	26	14	14
P6	F	52	39	ND	44	13	14
P7	M	59	40	ND	23	6	6
P8	M	31	48	16	22	10	9
P9	F	29	44	ND	19	7	7

Abbreviations: BMI = body mass index; exam = examination; ID = identification; UHDRS = Unified Huntington's Disease Rating Scale.

The CAG repeat lengths reported are the pathologic repeat sizes (CAG P) and the normal allele sizes (CAG N). ND represents CAG repeat lengths that could not be evaluated. A paired *t* test was used to compare visit 1 and visit 2 (paired *t* test on UHDRS scores [ $p = 0.282$ ]).

**<sup>31</sup>P fMRS in validation of functional biomarker.** In controls, repeated-measures ANOVAs were significant for Pi/PCr ( $p = 0.029$ ). We observed an increase in Pi/PCr ratio during activation, which was followed by a significant decrease during recovery using the Bonferroni-corrected paired *t* tests ( $p = 0.013$ ). Conversely, no change in Pi/PCr ratio was detected during activation in patients with HD. In addition, the brain MRS profile of patients with HD remained abnormal after 1 month (figure 1), as well as their UHDRS score (table 1). We found no correlation between the UHDRS or the CAG repeat length and the changes in Pi/PCr ratio during brain activation.

**<sup>31</sup>P fMRS in evaluating anaplerotic therapy.** At baseline, <sup>31</sup>P fMRS studies were repeated and reconfirmed an abnormal brain energy profile in patients with HD, i.e., the absence of an increased Pi/PCr ratio during visual stimulation. After 1 month of triheptanoin therapy, the profile was greatly improved and repeated-measures ANOVAs were significant for Pi/PCr ratio ( $p = 0.035$ ). We observed an increase in Pi/PCr ratio during visual stimulation and a decrease during recovery using the Bonferroni-corrected paired *t* tests ( $p = 0.005$ ) (figure 2). We found no correlation between the UHDRS or the CAG repeat length and the changes in Pi/PCr ratio during brain activation.

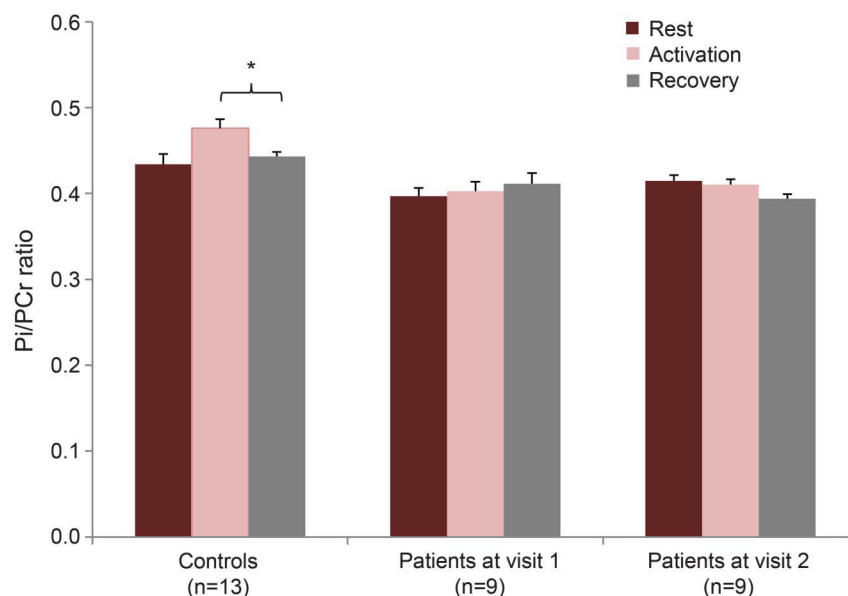
**Table 2** Characteristics of patients with Huntington disease from the interventional phase of the study

ID	Sex	Age at exam, y	BMI, kg/m <sup>2</sup>	CAG P	CAG N	UHDRS score		Plasma C3-carnitine, μmol/L	
						Pretreatment	Posttreatment	Pretreatment	Posttreatment
P1	F	51	22	41	17	5	ND	0.21	2.73
P2	M	49	24	42	19	27	ND	0.50	3.81
P3	F	42	21	46	ND	13	11	0.38	1.45
P4	F	61	21	42	16	18	9	0.36	0.48
P5	M	22	23	55	16	15	14	0.48	1.51
P6	M	52	24	44	19	5	4	0.68	2.67
P7	F	45	20	41	18	10	7	0.39	1.36
P8	F	52	18	43	23	14	11	0.35	4.09
P9	M	39	26	44	15	13	8	0.30	3.39
P10	M	46	29	45	29	16	13	0.56	0.47

Abbreviations: BMI = body mass index; exam = examination; ID = identification; UHDRS = Unified Huntington's Disease Rating Scale.

P1 to P5 were recruited from the observational phase of the study. The CAG repeat lengths reported are the pathologic repeat sizes (CAG P) and the normal allele sizes (CAG N). ND represents CAG repeat lengths that could not be evaluated and the UHDRS scores that could not be evaluated at posttreatment for 2 patients with acute motor problems. Last observation carried forward (LOCF) imputation approach was used on the missing data. The *p* values for UHDRS scores (paired *t* test with LOCF imputation approach for UHDRS [ $p = 0.012$ ]) and levels of plasma C3-carnitine (paired *t* test on plasma C3-carnitine [ $p = 0.002$ ]) were obtained using paired *t* test to compare pre- and posttreatment.

**Figure 1** Pi/PCr ratios in controls and patients



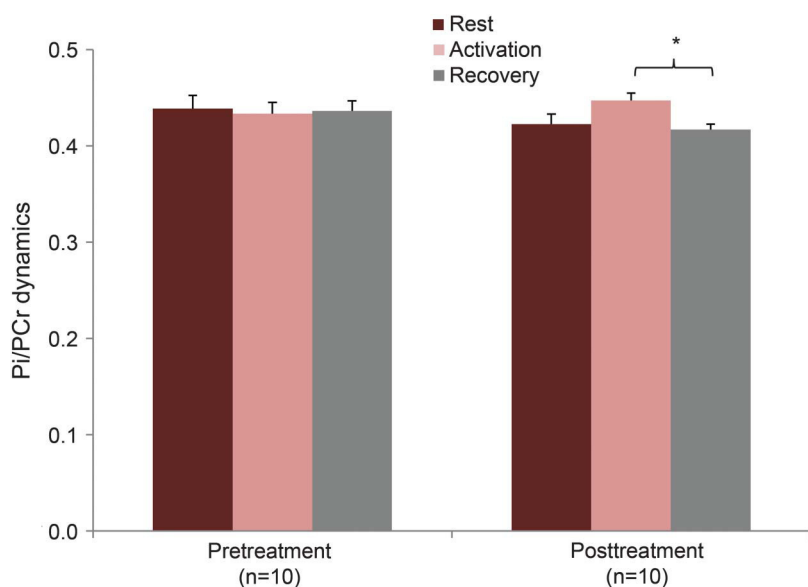
An increase in Pi/PCr ratio was observed in controls during activation, followed by a decrease during recovery ( $p = 0.013$ ). Patients with Huntington disease showed an abnormal profile characterized by the absence of changes in Pi/PCr ratio during brain activation. This abnormal profile remained stable over 1 month. Error bars represent SEM of within-subject differences using the method of Morey<sup>30</sup> to apply a correction factor to the SEM of the standardized data.<sup>31</sup> PCr = phosphocreatine; Pi = inorganic phosphate.

**DISCUSSION** This study assesses the benefit of an anaplerotic therapy on brain energy metabolism in HD. We observed an abnormal energy response to

brain activation before treatment that was improved after 1 month under triheptanoin therapy.

In the search for treatment-related biomarkers with high sensitivity to metabolic changes in the brain of patients with HD, an initial study using <sup>31</sup>P fMRS showed an 11% increase in Pi/PCr ratio in controls during activation, followed by a return to baseline levels during recovery while no such difference was found in patients.<sup>8</sup> The Pi/PCr ratio has been linked to mitochondrial activation, and metabolic deficiency has been found to lead to an unusual change in Pi/PCr in response to work.<sup>12</sup> The ratio is directly related to the ADP levels, which regulate mitochondrial oxidative metabolism. Pi/PCr ratio thus provides an index of mitochondrial oxidative regulation.<sup>13</sup> We have successfully reproduced the initial findings in newly recruited healthy individuals as well as in patients with HD. In addition, we observed that the abnormal profile of patients with HD is stable over time, which buttresses the fact that, without therapeutic intervention, metabolic dysfunction in patients with HD does not improve. This study also emphasizes the robustness of <sup>31</sup>P fMRS to capture brain energy profiles. However, the small number of patients recruited here constitutes a limitation to this study. In addition, reproducibility of MRS protocols has been an issue and thus <sup>31</sup>P MRS should be validated in a multicentric study just as it has been done recently for <sup>1</sup>H MRS.<sup>14</sup> To better understand the dynamics of ATP, Pi, and PCr in the brain, metabolic

**Figure 2** Pi/PCr dynamics after 1 month of triheptanoin therapy



At visit 1 (pretreatment), <sup>31</sup>P functional magnetic resonance spectroscopy studies confirmed an abnormal brain energy profile in patients with Huntington disease, as previously shown. After 1 month of triheptanoin therapy, the profile was corrected and we observed an increase in Pi/PCr ratio during visual stimulation with a decrease during recovery ( $p = 0.005$ ). Error bars represent SEM of within-subject differences using the method of Morey<sup>30</sup> to apply a correction factor to the SEM of the standardized data.<sup>31</sup> PCr = phosphocreatine; Pi = inorganic phosphate.



imaging tools such as  $^{31}\text{P}$  magnetization transfer techniques may be utilized to measure the dynamics of creatine kinase and ATP synthase in the brain of patients with HD.<sup>15</sup>

When triheptanoin (C7 fatty acid) oil is ingested, it is hydrolyzed to 1 glycerol molecule and 3 molecules of heptanoate (C7) that are metabolized by the liver.<sup>16</sup> The catabolism of heptanoate produces acetyl-CoA and propionyl-CoA, which fuel the Krebs cycle.<sup>17</sup> Heptanoate is more effective in fueling the Krebs cycle than even-chain fatty acids such as octanoate, which are metabolized to acetyl-CoA only.<sup>17</sup> The effectiveness of heptanoate over even-chain fatty acids is therefore attributable to the importance of propionyl-CoA in serving as a substrate for gluconeogenesis in the liver and kidneys and as an anaplerotic substrate to fill the Krebs cycle in all tissues.<sup>16</sup> In addition, oxidation of heptanoate in the liver leads to the export of C5 ketone bodies, which can be metabolized in peripheral tissues or in the brain to produce acetyl-CoA and propionyl-CoA.<sup>16</sup> Likewise, the anaplerotic property of triheptanoin has been used in several preclinical and clinical trials. Besides its effect on peripheral energy metabolism, especially fatty acid  $\beta$ -oxidation,<sup>18</sup> triheptanoin has been shown to exert anticonvulsant effects in mouse models of epilepsy<sup>19,20</sup> and affect neurotransmitter concentrations in patients with pyruvate carboxylase deficiency.<sup>21</sup>

In HD, the therapeutic effect of triheptanoin may be mediated by its ability to provide Krebs cycle intermediates. Indeed, we showed that the reduced levels of BCAAs in the plasma of patients with HD likely reflect a critical need in the brain for Krebs cycle substrates provided by peripheral organ metabolism.<sup>6</sup> Furthermore, ketone bodies have the ability to cross the blood-brain barrier<sup>20</sup> and can be used as alternative substrates to glucose in the brain.<sup>22</sup> Therefore, the C5 ketone bodies derived from triheptanoin may compensate for glucose hypometabolism in the brain of patients with HD.<sup>23</sup> Ketone bodies have also been shown to significantly increase brain bioenergetic substrates such as ATP and PCr.<sup>24,25</sup> Thus, improving mitochondrial metabolism using triheptanoin may lead to the mobilization of high-energy phosphates in the brain as suggested by our findings of increased Pi/PCr ratios after treatment with triheptanoin. Finally, triheptanoin may affect the glutamate-glutamine cycling that is altered in HD<sup>26</sup> through the provision of Krebs cycle intermediates such as  $\alpha$ -ketoglutarate, which undergo transamination for the synthesis of glutamate.<sup>27</sup> Newly developed techniques that have the potential to establish brain map of glutamate levels, such as chemical exchange saturation transfer,<sup>28</sup> may be able to further elucidate

the mechanisms of action of triheptanoin on the brain of patients with HD.

Our proof-of-concept study strongly suggests that triheptanoin is able to improve the brain metabolic profile of patients with HD at an early stage of the disease. Although it has to be interpreted with caution because of a possible placebo effect in this open-label study, we also observed an improvement of motor functions in patients with HD after 1 month of anaplerotic therapy. Besides the short-term effect of triheptanoin on brain energy metabolism, its effect on surrogate markers such as caudate atrophy or motor functions, which have been reported as prominent in a multicentric HD study,<sup>29</sup> needs now to be evaluated. Overall, this study shows the significance of functional or metabolic biomarkers such as the Pi/PCr ratio in establishing proof-of-concepts for candidate drugs, especially when they target brain metabolism.

### AUTHOR CONTRIBUTIONS

Mr. Adanyeguh was involved in acquisition of data, analysis and interpretation of data, statistical analysis of data, and drafting/revising the manuscript. Dr. Rinaldi was involved in study supervision and coordination and drafting/revising the manuscript. Dr. Henry was involved in study concept and design, analysis and interpretation of data, and drafting/revising the manuscript. Ms. Caillet was involved in the dietary management of the patient and analysis and interpretation of data. Dr. Valabregue was involved in acquisition of data and drafting/revising the manuscript. Dr. Durr was involved in patient recruitment, analysis and interpretation of data, and drafting/revising the manuscript. Dr. Mochel was involved in study concept and design, obtaining funding, study supervision and coordination, analysis and interpretation of data, statistical analysis, and drafting/revising the manuscript.

### ACKNOWLEDGMENT

The authors thank the patients and controls who participated in the study and the Centre d'Investigation Clinique Pitié Neurosciences, CIC-1422, Département des Maladies du Système Nerveux, Hôpital Pitié-Salpêtrière, Paris, France.

### STUDY FUNDING

The observational study was funded by Ipsen (NCT01696708) and the interventional study by the Institut National de la Santé et de la Recherche Médicale (NCT01882062). Ultragenyx Pharmaceutical Inc. provided the investigational drug triheptanoin. The research leading to these results has received funding from the program Investissements d'avenir ANR-10-IAIHU-06. The authors are grateful to the collaborators from the Center for Neuroimaging Research, France, and the Center for Magnetic Resonance Research, USA (NIH grants P41 EB015894 and P30 NS076408 to Center for Magnetic Resonance Research).

### DISCLOSURE

I. Adanyeguh and D. Rinaldi report no disclosures. P. Henry is supported by grants from NIH (P41 EB015894 and P30 NS076408), Bob Allison Research Center at the University of Minnesota, and Friedreich's Ataxia Research Alliance. S. Caillet and R. Valabregue report no disclosures. A. Durr holds a patent on the use of triheptanoin in Huntington disease (BIO06353). F. Mochel holds a patent on the use of triheptanoin in Huntington disease (BIO06353). Go to [Neurology.org](http://Neurology.org) for full disclosures.

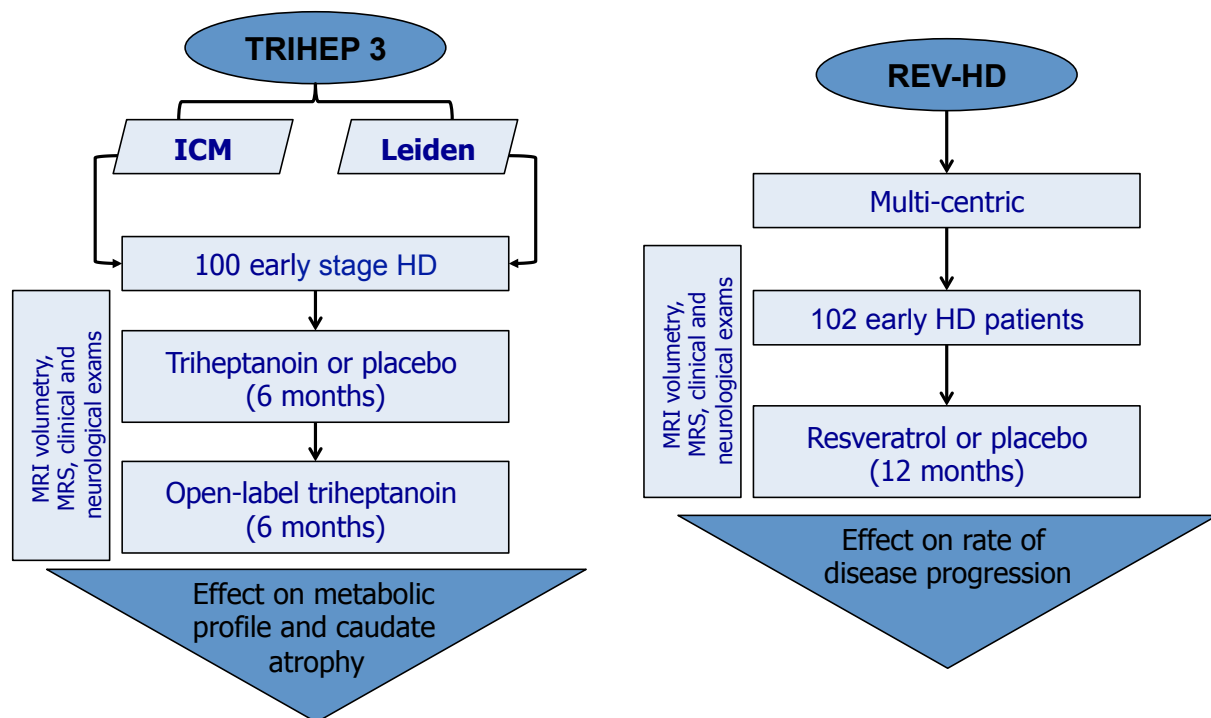
Received June 4, 2014. Accepted in final form October 3, 2014.

## REFERENCES

1. Roos RAC. Huntington's disease: a clinical review. *Orphanet J Rare Dis* 2010;5:40.
2. Grafton ST, Mazziotta JC, Pahl JJ, et al. Serial changes of cerebral glucose metabolism and caudate size in persons at risk for Huntington's disease. *Arch Neurol* 1991;49:1161–1167.
3. Kuwert T, Lange HW, Boecker H, et al. Striatal glucose consumption in chorea-free subjects at risk of Huntington's disease. *J Neurol* 1993;241:31–36.
4. Antonini A, Leenders KL, Spiegel R, et al. Striatal glucose metabolism and dopamine D2 receptor binding in asymptomatic gene carriers and patients with Huntington's disease. *Brain* 1996;119:2085–2095.
5. Mochel F, Durant B, Meng X, et al. Early alterations of brain cellular energy homeostasis in Huntington disease models. *J Biol Chem* 2012;287:1361–1370.
6. Mochel F, Charles P, Seguin F, et al. Early energy deficit in Huntington disease: identification of a plasma biomarker traceable during disease progression. *PLoS One* 2007;2:e647.
7. Mochel F, Duteil S, Marelli C, et al. Dietary anaplerotic therapy improves peripheral tissue energy metabolism in patients with Huntington's disease. *Eur J Hum Genet* 2010;18:1057–1060.
8. Mochel F, N'Guyen TM, Deelchand D, et al. Abnormal response to cortical activation in early stages of Huntington disease. *Mov Disord* 2012;27:907–910.
9. Tabrizi SJ, Reilman R, Ross RAC, et al. Potential endpoints for clinical trials in premanifest and early Huntington's disease in the TRACK-HD study: analysis of 24 month observational data. *Lancet Neurol* 2012;11:42–53.
10. Scahill RI, Hobbs NZ, Say MJ, et al. Clinical impairment in premanifest and early Huntington's disease is associated with regionally specific atrophy. *Hum Brain Mapp* 2013;34:519–529.
11. Wolf RC, Sambatro F, Vasic N, et al. Visual system integrity and cognition in early Huntington's disease. *Eur J Neurosci* 2014;40:2417–2426.
12. Chance B, Eleff S, Leigh JS, Sokolow D, Sapega A. Mitochondrial regulation of phosphocreatine/inorganic phosphate ratios in exercising human muscle: a gated <sup>31</sup>P NMR study. *Proc Natl Acad Sci USA* 1981;78:6714–6718.
13. Weiner DH, Fink LI, Maris J, Jones RA, Chance B, Wilson JR. Abnormal skeletal muscle bioenergetics during exercise in patients with heart failure: role of reduced muscle blood flow. *Circulation* 1986;73:1127–1136.
14. Deelchand DK, Adanyeguh IM, Emir UE, et al. Two-site reproducibility of cerebellar and brainstem neurochemical profiles with short-echo, single-voxel MRS at 3T. *Magn Reson Med Epub* 2014 Jun 19.
15. Chen W, Zhu XH, Adriany G, Ugurbil K. Increase of creatine kinase activity in the visual cortex of human brain during visual stimulation: a <sup>31</sup>P magnetization transfer study. *Magn Reson Med* 1997;38:551–557.
16. Roe CR, Mochel F. Anaplerotic diet therapy in inherited metabolic disease: therapeutic potential. *J Inherit Metab Dis* 2006;29:332–340.
17. Roe CR, Sweetman L, Roe DS, David F, Brunengraber H. Treatment of cardiomyopathy and rhabdomyolysis in long-chain fat oxidation disorders using an anaplerotic odd-chain triglyceride. *J Clin Invest* 2002;110:259–269.
18. Roe CR, Yan BZ, Brunengraber H, Roe DS, Wallace M, Garritson BK. Carnitine palmitoyltransferase II deficiency: successful anaplerotic diet therapy. *Neurology* 2008;71:260–264.
19. Willis S, Stoll J, Sweetman L, Borges K. Anticonvulsant effects of a triheptanoin diet in two mouse chronic seizure models. *Neurobiol Dis* 2010;40:565–572.
20. Borges K, Sonnewald U. Triheptanoin—a medium chain triglyceride with odd chain fatty acids: a new anaplerotic anticonvulsant treatment? *Epilepsy Res* 2012;100:239–244.
21. Mochel F, DeLonlay P, Touati G, et al. Pyruvate carboxylase deficiency: clinical and biochemical response to anaplerotic diet therapy. *Mol Genet Metab* 2005;84:305–312.
22. Stanley JC. The glucose–fatty acid–ketone body cycle: role of ketone bodies as respiratory substrates and metabolic signals. *Br J Anaesth* 1981;53:131–136.
23. Feigin A, Leenders KL, Moeller JR, et al. Metabolic network abnormalities in early Huntington's disease: an [<sup>18</sup>F]FDG PET study. *J Nucl Med* 2001;42:1591–1595.
24. DeVivo DC, Lecki MP, Ferrendelli JS, McDougal DB Jr. Chronic ketosis and cerebral metabolism. *Ann Neurol* 1978;3:331–337.
25. Bough KJ, Wetherington J, Hassel B, et al. Mitochondrial biogenesis in the anticonvulsant mechanism of the ketogenic diet. *Ann Neurol* 2006;60:223–235.
26. Behrens PF, Franz P, Woodman B, Lindenberg KS, Landwehrmeyer GB. Impaired glutamate transport and glutamate–glutamine cycling: downstream effects of the Huntington mutation. *Brain* 2002;125:1908–1922.
27. Owen OE, Kalhan SC, Hanson RW. The key role of anaplerosis and cataplerosis for citric acid cycle function. *J Biol Chem* 2002;277:30409–30412.
28. Cai K, Haris M, Singh A, et al. Magnetic resonance imaging of glutamate. *Nat Med* 2012;18:302–306.
29. Tabrizi SJ, Scahill RI, Owen G, et al. Predictors of phenotypic progression and disease onset in premanifest and early-stage Huntington's disease in the TRACK-HD study: analysis of 36-month observational data. *Lancet Neurol* 2013;12:637–649.
30. Morey RD. Confidence intervals from normalised data: a correction to Cousineau (2005). *Tutor Quant Methods Psychol* 2008;4:61–64.
31. Cousineau D. Confidence intervals in within-subject designs: a simpler solution to Loftus and Masson's method. *Tutor Quant Methods Psychol* 2005;1:42–45.

## 2.6 Perspective

The promising results from the proof-of-concept anaplerotic therapy with triheptanoin has led to the start of two new studies to test in a randomized, blinded, placebo-controlled trials, the efficacy of triheptanoin (TRIHEP3) and resveratrol (REVHD) on regulating brain metabolic functions in HD. The studies are designed as follows (Figure 15)



**Figure 15: Design of the multi-centric studies to test the efficacy of two therapeutic agents in improving metabolic dysfunction and slowing caudate atrophy in HD.**

### 2.6.1 TRIHEP3

TRIHEP3 is a randomized, double-blind, controlled and bi-centric study between France and the Netherlands, sponsored by Inserm (ClinicalTrials.gov Identifier: NCT02453061). The study started in 2015 and plans to recruit 100 early stage HD patients ( $5 \leq \text{UHDRS} \leq 40$ ). The project is structured such that patients receive 1g/kg of body weight per day of either triheptanoin ( $n = 50$ ) or a placebo ( $n = 50$ ) for six months. After six months, all patients will receive triheptanoin in the open-label-phase of the study for an additional six months. Triheptanoin (UX007; Ultragenyx Pharmaceuticals Inc; Novato; USA) is a medium odd-chain

triglyceride containing three 7-carbon fatty acids. Its metabolism yields appropriate substrates for both fatty acid metabolism and anaplerosis. A trained dietician determines the daily calorie intake for each patient and adjusts his or her daily menu to ensure both proper treatment administration and an isocaloric diet. The patients are asked to ingest a treatment dose (triheptanoin or placebo) representing around 30% of their usual daily calorie intake.

The primary objectives are to evaluate the efficacy of triheptanoin in:

- i. Increasing the short-term energy response in the metabolic profile of the brain of early affected HD patients.
- ii. Slowing atrophy in the caudate of early affected HD patients as measured with volumetric magnetic resonance imaging.

The secondary objectives are to:

- Assess the impact of triheptanoin on brain diffusion metrics
- Assess the clinical benefit of triheptanoin on motor function in HD.
- Assess the clinical benefit of triheptanoin on cognitive function and psychiatric symptoms in HD.
- Confirm long-term clinical and biological tolerance of triheptanoin in HD.
- Find correlations between neuroimaging volumetric parameters, brain energy profiles and clinical scores, before and after treatment.

Patients are evaluated at baseline and every three months for a year. The UHDRS and Total Functional Capacity (TFC) scores are used for the clinical assessment of patients. Neuropsychological tests include symbol digit modality (visuomotor integration), trail making parts A and B (attention, processing speed and mental flexibility), forward and backward digit span (short-term and working memory), stroop (attention and capacity for inhibition), sustained attention to response task (attention and inhibitory processes of attention control) and a self-report questionnaire (SF36) to obtain self-ratings of physical and emotional health. Psychiatric evaluations with Problem Behaviors Assessment for HD Short Version (PBA-S) allows the assessment of the severity and frequency of different behavioral symptoms in HD. Dietary consultations with the dietician help participants to incorporate triheptanoin or the placebo into their daily food. Biochemical assessments are performed on plasma and urine

samples to test for plasma acylcarnitines, plasma C5-ketone bodies and urine organic acids – which give information on the metabolism of triheptanoin.

<sup>31</sup>P MRS is used to assess the metabolic profile of patients at baseline and during treatment with triheptanoin or placebo using the Pi/PCr ratio biomarker. The MRI protocol consists of a 3D T<sup>1</sup>-weighted anatomical sequence (1 mm isotropic, T<sub>R</sub> = 2300 ms, T<sub>E</sub> = 2.98 ms, field of view (FOV) = 240 x 256). The brain image is analyzed using the whole brain and caudate boundary shift integral (BSI) approach (Freeborough & Fox, 1997; Hobbs et al., 2009) to determine rate of atrophy over time. Finally, DTI and tractography are performed on diffusion-weighted data (*b* value = 1500 s/mm<sup>2</sup>, T<sub>R</sub> = 14400 ms, T<sub>E</sub> = 93 ms, slice thickness = 2 mm isotropic, matrix = 128 x 128, flip angle = 90°) acquired in 30 directions.

Currently, the first phase of the study (n= 50 patients) has been completed in both centers and the study is now on the second phase (n= 50 patients). The data are still blinded and statistical analysis are awaiting the end of the study.

## **2.6.2 REVHD**

Resveratrol is a non-toxic polyphenol present in certain foods (grape, blackberry, red wine, peanuts) showing anti-inflammatory and anti-oxidant properties. Studies in mice showed that resveratrol enhances mitochondrial number and function at the peripheral level, as well as mouse aerobic skills (Lagouge et al., 2006). Many preclinical studies have also demonstrated a neuroprotective effect of resveratrol in HD (Quincozes-Santos & Gottfried, 2011). But until now, the use of resveratrol in therapeutic trials in humans has been limited due to a short half-life in plasma resulting in a poor bioavailability. In this study, a newly formulated resveratrol, which has prolonged absorption and no risk of toxicity, is given in capsules that contain 20 mg of purified resveratrol, with a maximum given daily dose of 80 mg.

REVHD is a French multi-centric randomized, double-blind, controlled study, sponsored by the Assistance Publique des Hôpitaux de Paris (APHP, ClinicalTrials.gov Identifier: NCT02336633), that plans to recruit 102 early affected HD patients. Patients receive either resveratrol at 80 mg (n = 51), or placebo (n = 51) for 12 months.

The primary objective of REVHD is to evaluate the ability of resveratrol to slow down disease progression in early affected HD patients reflected by a decrease in the rate of caudate atrophy.

The secondary objectives are to:

- Assess the impact of resveratrol on brain energy metabolism.
- Assess the impact of resveratrol on brain diffusion metrics.
- Assess the clinical benefit of resveratrol on motor function in HD.
- Assess the clinical benefit of resveratrol on cognitive function and psychiatric symptoms in HD.
- Confirm the clinical and biological tolerance of resveratrol in HD.
- Determine correlations between the neuroimaging volumetric parameters, brain energy profile and clinical scores, before and after treatment.

The total participation period for each patient is 13 months (12 months of treatment and 1 month follow-up). All neuroimaging is performed in Paris at the Institut du cerveau et de la moelle (ICM) whilst other tests including neuropsychological, clinical and biochemical tests are performed in the co-investigator site (Angers, Bordeaux, Marseille, Montpellier, Paris) nearest to the patient. After a pre-screening phase participants visit their co-investigator site for inclusion (V1). Immediately afterwards, the second visit (V2) is made to ICM in Paris for neuroimaging before receiving either resveratrol or placebo. Patients receive their treatment (placebo or resveratrol at 80 mg/day, i.e. two 20 mg capsules in the morning and in the evening) for three months. Every three months, patients return to their nearby hospital in order to have neurological (UHDRS, TFC) and clinical examination. Neuropsychiatric and cognitive evaluations consist of Starkstein apathy scale (relating to apathy), hospital anxiety and depression scale (depression and anxiety symptoms), frontal systems behavior inventory (behavior associated with damage to frontal systems of the brain), forward and backward digit span, stroop, trail making parts A and B, SF36, and symbol digit modality. A nurse performs fasting blood sampling 30 minutes after pill intake at visits 3 (V3) and 5 (V5) and before pill intake at visit 4 (V4) in order to get information on the metabolism of resveratrol. After a year of treatment, patients return to ICM for neuroimaging, as described for TRIHEP3 – i.e. <sup>31</sup>P MRS, 3D T<sub>1</sub>-weighted anatomical sequence and diffusion weighted imaging.

Currently, more than 70 patients have been enrolled in REVHD. The data are still blinded and statistical analysis are awaiting the end of the study.

### **2.6.3 Key role of MRI-MRS evaluations in both studies**

MR is used as the primary outcome measures of both studies. I did set-up the protocol on the newly installed Siemens Magnetom Prisma (Siemens Medical Solutions, Erlangen, Germany) scanner at ICM (TRIHEP3 and REVHD) and on the Philips scanner in Leiden (TRIHEP3). This entailed performing phantom and volunteer tests to ensure that similar sequences, acquisition approaches and visual stimulations were being applied at both centers.

I perform the image and spectra acquisitions in Paris whilst dedicated doctoral students are responsible for data acquisition in Leiden. One of the main challenges to MR data is poor shimming. I therefore perform quality control on all the MRS datasets to ensure that we reported values are reliable. I also ensure that all data are well preprocessed to include zero and first order phase correction as well as shot-to-shot frequency correction.

In order to eliminate bias, I am the only one responsible for whole brain and caudate BSI analysis of volumetric data from both study sites. I have also setup an analytical pipeline for the analysis of diffusion weighted data.

# Chapter 3

## Organisation:

<b>Study 2a: Understanding the biochemical basis of altered bioenergetics in HD using <sup>31</sup>P MT .....</b>	<b>50</b>
3.1.1 Introduction and objectives.....	50
3.1.2 Materials and methods.....	50
3.1.3 Results.....	51
<b>Study 2b: Proton spectroscopy in the visual cortex and striatum of HD.....</b>	<b>53</b>
3.2.1 Introduction and objectives.....	53
3.2.2 Materials and methods.....	53
3.2.3 Principal results .....	54
3.2.4 Submitted paper for publication .....	54
3.3 Perspective: Identifying biomarkers of dynamic energy metabolism (HDeENERGY).....	79
3.3.1 <sup>31</sup> P magnetization transfer .....	79
3.3.2 Diffusion weighted spectroscopy .....	80
3.3.3 Resting state functional MRI (rsfMRI) .....	82
3.3.4 Structural analysis .....	85
3.3.5 Protocol setup .....	86



## **Study 2a: Understanding the biochemical basis of altered bioenergetics in HD using $^{31}\text{P}$ MT**

### **3.1.1 Introduction and objectives**

We showed in study 1 that metabolic dysfunction persists in HD patients in the absence of therapeutic intervention. The altered Pi/PCr ratio could be attributed to underlying enzymatic disturbances. Indeed, creatine kinase (CK) is responsible for the equilibrium reactions involving the donation of high-energy phosphate group from one phosphate-containing molecule to the other such as from PCr to adenosine diphosphate (ADP) to form ATP (Figure 13). As an energy transport system between site of ATP synthesis and ATP utilization (de Graaf, 2007), we hypothesized that decreased CK activity may explain the altered Pi/PCr ratio observed in study 1.

In this study, sponsored by Inserm (ClinicalTrials.gov Identifier: NCT01696708), we chose to focus on the CK rate that regulates PCr and ATP interaction. We did not look at Pi and ATP flux since the small Pi peak is prone to noise in MT experiments making quantification and interpretation of results difficult at 3T.

### **3.1.2 Materials and methods**

Ten early stage HD patients (UHDRS  $15 \pm 11$ ) and 10 age and sex-matched controls were recruited for the study. The rate of CK was measured using  $^{31}\text{P}$  MT (pulse-acquire, TR 15s). A  $25 \times 25 \times 25 \text{ mm}^3$  voxel placed in the visual cortex and covering most of the calcarine was used for shimming. Frequency calibration was performed for each subject in order to determine the voltage needed to achieve maximum signal. Saturation of the  $\gamma\text{ATP}$  resonance was performed using 8 cycles of B1-insensitive train to obliterate signal (BISTRO) (Luo et al., 2001) pulse (duration 3.5 s). Phantom and volunteer tests were first performed to calibrate the flip angle at which complete saturation of  $\gamma\text{ATP}$  resonance is achieved with minimal to no direct effect on the PCr resonance. The transmit-receive frequency was set at -50 Hz, a region of noise, to avoid contamination of resonances by the direct current artifact. A symmetric saturation was performed at the opposite side of the PCr resonance to correct for RF bleed

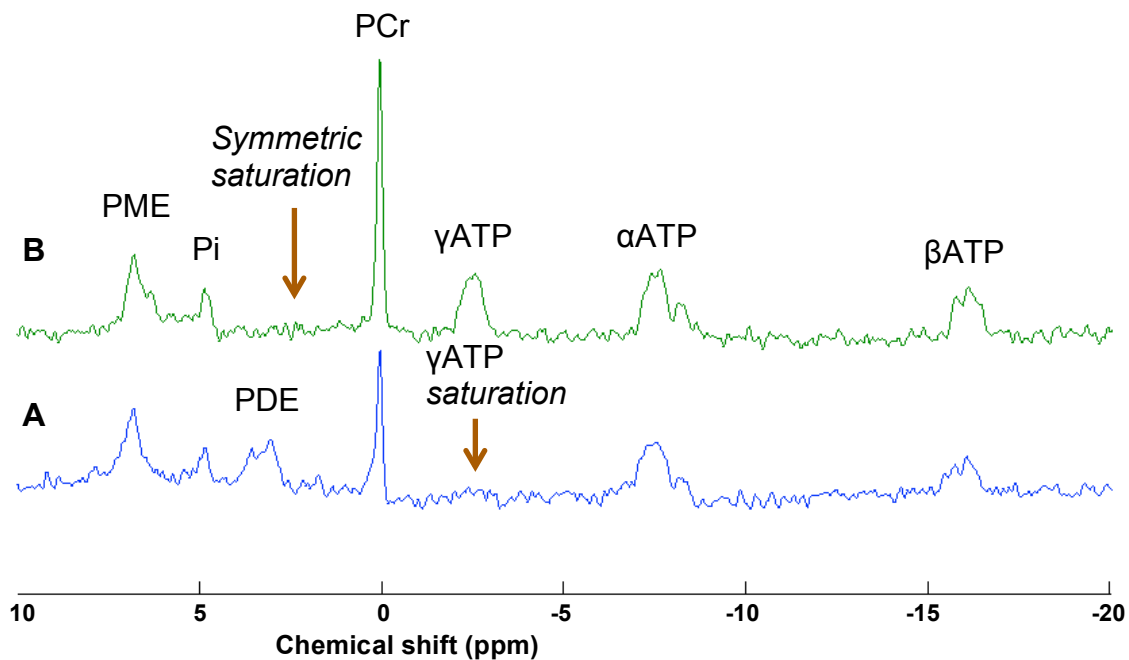
over. Data were collected for 8 min each at rest, activation and recovery. The rate of PCr was then calculated assuming  $T_1 = 2.4$  s using the formula:

$$k_{ck} = \frac{1}{T_1} \times \left( \frac{M_o}{M_s} - 1 \right)$$

Where  $M_s$  and  $M_o$  are the steady-state magnetization with and without saturation of  $\gamma$ ATP respectively.

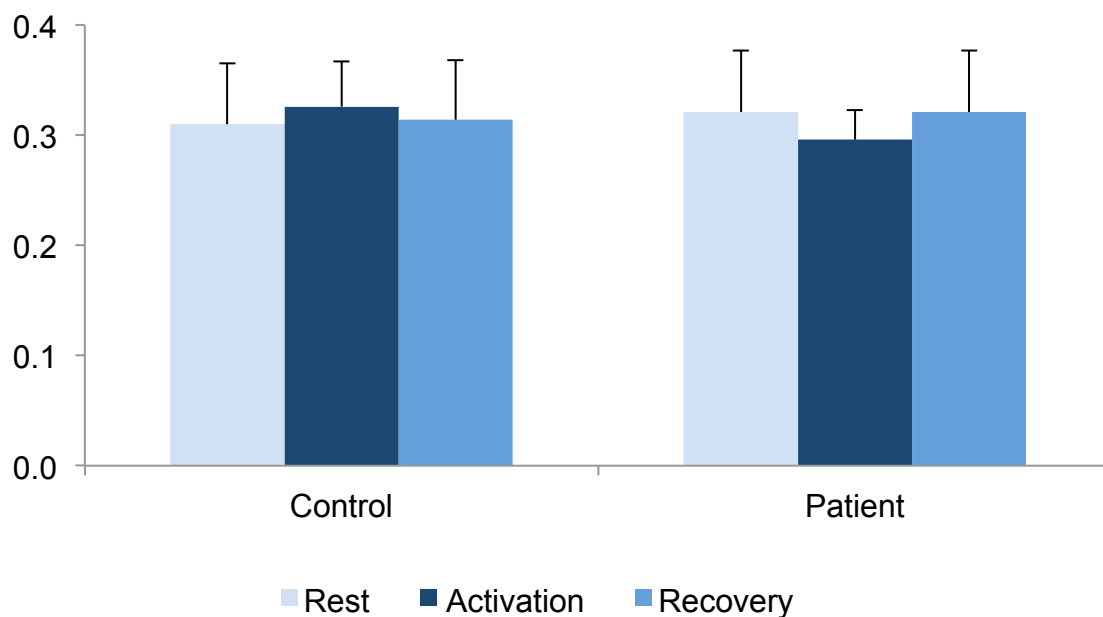
### 3.1.3 Results

We achieved complete attenuation of the  $\gamma$ ATP signal with the BISTRO pulse with no effect on the PCr resonance (Figure 16).



**Figure 16:**  $^{31}\text{P}$  MT spectra from the visual cortex. (A) Saturation applied on the  $\gamma$ ATP achieves complete attenuation of the signal. (B) Symmetric saturation does not have an effect on the PCr resonance; hence any decrease in the PCr signal reflects the chemical exchange between PCr and  $\gamma$ ATP through the CK reaction. PME: phosphomonoester, PDE: phosphodiester.

The symbolic error propagation calculation in MATLAB was used to estimate the error in our CK calculations. The rate of CK was observed to be similar in controls and patients at rest. During visual stimulation, however, the rate of CK showed a 5% increase in controls ( $k = 0.326 \pm 0.041 \text{ s}^{-1}$ ) compared to patients ( $k = 0.296 \pm 0.027 \text{ s}^{-1}$ ) ( $p = 0.07$ ) (Figure 18) but did not reach significance. This however could suggest an abnormal energy metabolism in the visual cortex during functional activation in patients at early stage of HD. Although not significant, possibly due to the small sample size, this reduced CK rate could explain the lack of increase in Pi/PCr ratio during visual activation that we observed previously. However, this study should be validated in a larger cohort of patients and presymptomatic individuals.



**Figure 17: Rate of CK measured with  $^{31}\text{P}$  MT in the visual cortex of patients and controls.** No change was observed at rest but a trend of 5% increase in CK was observed in controls during visual stimulation ( $p = 0.07$ ).

## **Study 2b: Proton spectroscopy in the visual cortex and striatum of HD**

### **3.2.1 Introduction and objectives**

The previous studies focused on the phosphate containing-molecules that are limited in the number of metabolites that can be reported. Several studies have used  $^1\text{H}$  MRS to identify neurochemical alterations in different parts of brain (Clarke et al., 1998; Ruocco et al., 2007; van den Bogaard et al., 2011). Whilst metabolite ratios were reported in some studies, it is unreliable and interpretation of ratios are complicated since changes cannot be attributed to particular metabolites. Even though the visual cortex is also affected in HD, most MRS studies have focused on the striatum.

One of the major challenges of MRS studies is results reproducibility. This often leads to studies reporting different results from the same brain region. Having a standardized protocol with similar acquisition and analytical procedure could bridge this gap.

In this study sponsored by Inserm (ClinicalTrials.gov Identifier: NCT01696708), we sought to use a validated  $^1\text{H}$  MRS sequence (described in Chapter 4) to identify more metabolites in the striatum and visual cortex of patients at the early stage of HD.

### **3.2.2 Materials and methods**

This study was performed on the subjects recruited in study 2a. The  $^1\text{H}$  MRS protocol consisted of a validated semi-LASER protocol ( $T_R = 5000$  ms,  $T_E = 28$  ms, averages = 64, vector size = 2048, acquisition time = 6 min). A  $34 \times 19 \times 23$  mm<sup>3</sup> VOI and a  $25 \times 25 \times 25$  mm<sup>3</sup> VOI were placed in the striatum and visual cortex respectively. Calibrations were performed in each VOI to include FASTMAP shimming and RF power calibration for the 90° excitation pulse. Water suppression and outer volume suppression were performed for each VOI to attenuate signal from the more abundant water and quell signals from lipids and regions outside the VOI respectively. We corrected for CSF contributions as well as partial volume fractions during quantification with LCModel. In addition to  $^1\text{H}$  MRS, we compared the volumes of WM, GM and CSF in each VOI.

### **3.2.3 Principal results**

Significantly higher total creatine (tCr) was observed in the visual cortex of patients whilst a decrease in Glu concentration was observed in the striatum. Moreover, in patients, the GM was significantly decreased whilst CSF was significantly increased. No change in WM was observed.

### **3.2.4 Submitted paper for publication**

## **Expanded neurochemical profile in the early stage of Huntington disease using proton magnetic resonance spectroscopy**

Isaac M. Adanyeguh<sup>1</sup>, Marie-Lorraine Monin<sup>1,2</sup>, Daisy Rinaldi<sup>1</sup>, Léorah Freeman<sup>3</sup>, Alexandra Durr<sup>1,2</sup>, Stéphane Lehericy<sup>1,4</sup>, Pierre-Gilles Henry<sup>5</sup>\*, Fanny Mochel<sup>1,2,6</sup>\*

<sup>1</sup> Inserm U 1127, CNRS UMR 7225, Sorbonne Universités, UPMC Univ Paris 06 UMR S 1127, Institut du Cerveau et de la Moelle épinière, ICM, F-75013, Paris, France

<sup>2</sup> AP-HP, Pitié-Salpêtrière University Hospital, Department of Genetics, Paris, France

<sup>3</sup> Department of Neurology, McGovern Medical School at UTHealth, Houston, TX, Unites States

<sup>4</sup> Center for NeuroImaging Research (CENIR), Institut du Cerveau et de la Moelle épinière, Paris, France

<sup>5</sup> Center for Magnetic Resonance Research (CMRR), University of Minnesota, Minneapolis, MN, United States

<sup>6</sup> University Pierre and Marie Curie, Neurometabolic Research Group, Paris, France

\* These authors contributed equally to this work.

**Correspondence to:** Dr Fanny Mochel, Institut du Cerveau et de la Moelle épinière, Aile 4A, Hôpital Pitié-Salpêtrière, 75013 Paris, France; Tel: +33 (0) 1 57 27 46 82; Fax: +33 (0) 1 57 27 47 95; email: fanny.mochel@upmc.fr

**Word count:** Abstract (215), main text (2493).

**Grant support:** This study was funded by NIH grants (P41EB015894 and P30NS076408) and the Ecole des Neurosciences de Paris. The study also received funding from Ipsen

(NCT01696708) and the program “Investissements d’avenir” ANR-10-IAIHU-06 and ANR-11-INBS-0006.

**Keywords:** Huntington disease, movement disorders, <sup>1</sup>H MRS, semi-LASER, neurometabolite, neurochemical profile.

**List of abbreviations:**

AFP: Adiabatic full passage

HD: Huntington disease

CAG: Cysteine-adenine-guanine trinucleotide

UHDRS: Unified Huntington Disease Rating Scale

GM: Gray matter

WM: White matter

CSF: Cerebrospinal fluid

OVS: Outer volume suppression

VAPOR: Variable power and optimized relaxation delays

VOI: Volume of interest

RF: Radiofrequency

## ABSTRACT

**Purpose:** The striatum is a well-known region affected in Huntington disease (HD). However, other regions including the visual cortex are implicated. We previously identified an abnormal energy response in the visual cortex of patients at an early stage of HD using  $^{31}\text{P}$  magnetic resonance spectroscopy (MRS). We therefore sought to further characterize these metabolic alterations with  $^1\text{H}$  MRS using a well-validated semi-LASER sequence that minimizes J-modulation.

**Materials and methods:** Ten early affected patients (UHDRS, total motor score =  $13.6 \pm 10.8$ ) and ten healthy volunteers of similar characteristics were recruited for the study. We performed  $^1\text{H}$  MRS in the striatum – the region that is primary affected in HD – and the visual cortex.

**Results:** This allowed a reliable quantification of 10 metabolites in the visual cortex and 8 in the striatum, compared to 3-5 metabolites in prior  $^1\text{H}$  MRS studies performed in HD. We identified higher total creatine ( $p = 0.030$ ) in the visual cortex and decreased glutamate ( $p = 0.001$ ) in the striatum of HD patients compared to controls. Lower abundant neurometabolites (glutamine, GABA, lactate, glutathione, ascorbate or aspartate) showed similar concentrations in both groups.

**Conclusion:** Our study identifies early energy changes in the visual cortex of HD patients related to creatine metabolism. Decreased striatal glutamate could reflect early neuronal dysfunction or impaired glutamatergic neurotransmission.



## INTRODUCTION

Huntington disease (HD) is a polyglutamine disorder caused by expansion in the glutamine-encoding cysteine-adenine-guanine (CAG) repeats<sup>1</sup> and striatal atrophy is a prominent characteristic of the disease.<sup>2</sup> Other brain regions including the thalamus, cerebral cortex, cerebellum<sup>3,4</sup> and visual cortex<sup>5</sup> are also involved in the pathological process as the disease progresses. Positron emission tomography studies have shown metabolic alterations in the striatum<sup>6</sup> whilst <sup>31</sup>P MRS studies have revealed abnormal energy response in the visual cortex of HD patients at an early stage of the disease.<sup>7,8</sup> With the availability of genetic testing for HD, there exists a therapeutic window that can be taken advantage of before symptoms onset. However, biomarkers are critically needed to evaluate presymptomatic individuals and make use of this therapeutic window<sup>5</sup> since the Unified Huntington Disease Rating Scale (UHDRS),<sup>10</sup> the most commonly used measure to assess disease severity, is unable to evaluate pathological processes prior to motor symptoms onset. In the search for biomarkers, <sup>1</sup>H MRS has been used to study neurometabolism in HD at different field strengths.<sup>11-15</sup> Metabolic alterations start indeed in the very early stages of the disease,<sup>16</sup> and represent important targets for neuroprotective therapies.<sup>8</sup>

Previous studies with <sup>1</sup>H MRS in HD were carried out at field strengths between 0.5 T and 7 T (Table 1), with several studies performed on 3 T systems that are becoming common in hospitals.<sup>12,13,15,17</sup> In general, these studies have focused on the most prominent metabolites in the <sup>1</sup>H spectrum – total NAA (tNAA), total creatine (tCr), total choline (tCho), and to a lesser extent *myo*-inositol (*myo*Ins) and glutamate (Glu) – but not on less obvious metabolites such as gamma amino-butyric acid (GABA), glutamine (Gln), or glutathione (GSH). Some studies reported metabolite ratios only, which further complicate data interpretation.<sup>12,13</sup> Moreover, most of these studies focused mainly on the striatum, caudate or putamen, and only a few on the occipital cortex (Table 1) even though abnormal metabolic alterations are also present in

this region.<sup>6-8</sup> Furthermore, these studies used STEAM and PRESS sequences with long or short  $T_E$  without prior test of robustness or reproducibility. The present study thus sought to measure an expanded neurochemical profile in both the visual cortex and the striatum of early affected HD patients at 3 T, using a previously optimised and validated semi-LASER sequence with water as an internal concentration reference and correction of concentrations for CSF content.

## **MATERIAL AND METHODS**

### **Subjects**

The local ethics committee approved this study and all subjects signed a written informed consent after the nature of the procedure had been fully explained before participating in the study. Motor dysfunction was evaluated with the total motor score (TMS) of the Unified Huntington Disease Rating Scale (UHDRS) with a maximal worth score of 124. We recruited ten patients at the early stage of HD without medication as well as ten healthy volunteers with similar general characteristics – sex, age and BMI (Table 2).

### **MR Protocol**

MRS data were acquired on 3 T whole-body Siemens Magnetom Trio scanner (Siemens Medical Solutions, Erlangen, Germany). We used a modified semi-LASER  $^1\text{H}$  MRS protocol<sup>18</sup> that has been previously tested in healthy controls for robustness and reproducibility in a bi-centric study and demonstrated highly reproducible data.<sup>19</sup> Using a 32-channel head coil, 3D  $T_1$ -weighted volumetric images ( $T_R = 2530$  ms,  $T_E = 3.65$  ms, 1 mm isotropic, FOV = 256 x 240 mm<sup>2</sup>, matrix size = 256 x 240) were acquired for spatial normalization and localization of brain volumes and for volumetric analysis of brain regions

of interest. Shimming and spectra acquisition were performed on a  $34 \times 19 \times 23 \text{ mm}^3$  volume-of-interest (VOI) in the striatum, and a  $25 \times 25 \times 25 \text{ mm}^3$  VOI in the visual cortex (Figure 1). Automatic shimming of the voxels were achieved with FAST(EST)MAP<sup>20</sup> to generate highly resolved spectral linewidths. The calibration and acquisition steps were performed as described in prior studies.<sup>18,19,21</sup> The RF power for the asymmetric slice-selective  $90^\circ$  pulse (duration = 2 ms) of the semi-LASER sequence ( $T_R = 5000 \text{ ms}$ ,  $T_E = 28 \text{ ms}$ , averages = 64, vector size = 2048, acquisition time = 6 min) was calibrated by determining the power that produced the maximum signal. The power for the  $180^\circ$  hyperbolic secant adiabatic full passage (AFP) pulses (duration = 4 ms) was set automatically based on the  $90^\circ$  pulse. For better suppression of unwanted coherences with shorter spoiler gradients, AFP pulses were interleaved. Water suppression pulses with the variable pulse power and optimized relaxation delays (VAPOR) were adjusted by following signal intensities to determine the power with maximum water suppression. The VAPOR pulses were interleaved with outer volume suppression (OVS) pulses to reduce contamination from other brain regions outside the VOI in the visual cortex (thickness: anterior = 200 mm, posterior = 40 mm) and the striatum (thickness: anterior = 80 mm, posterior = 80 mm). A 7 mm margin was left between the VOI and the OVS slices in order to avoid signal loss in the VOI due to the transition band of the OVS pulse profile. Two preparation scans were performed at the beginning of spectra acquisition to balance the initial fluctuation of the readout on Siemens systems. Additionally, unsuppressed water spectra were acquired for eddy current correction (VAPOR off) and another (VAPOR and OVS off) was used as an internal water reference for metabolite quantification.<sup>19,21</sup> The total scan time for each VOI that included shimming, calibration and spectra acquisition was approximately 10 minutes. To evaluate the cerebrospinal fluid (CSF) contribution to VOI, we segmented the brain and estimated the %CSF content in the VOI as explained below. Metabolite concentrations were then corrected for regional CSF content.

## Metabolite quantification

Pre-processing of data that included eddy current, phase and frequency correction and quantification of spectra with LCModel were performed in MATLAB as previously described.<sup>19,21</sup> The basis set was simulated for all metabolites – alanine, ascorbate, aspartate, creatine,  $\gamma$ -aminobutyric acid (GABA), glycerophosphorylcholine (GPC), phosphocholine (PCho), phosphocreatine (PCr), glucose (Glc), glutamine (Gln), glutamate (Glu), glutathione (GSH), myoinositol (*myo*-Ins), scyllo-inositol (sIns), lactate, *N*-acetylaspartate (NAA), *N*-acetylaspartylglutamate (NAAG), phosphorylethanolamine (PE) and taurine. The basis set also included macromolecule spectra that were acquired in healthy volunteers.<sup>19</sup> Phase and frequency correction were performed on each subject spectra. The unsuppressed water spectra were used for eddy current correction. By using water from the same VOI as an internal concentration reference, we limited errors that otherwise could arise from the use of an external reference such as those related to  $B_1$  homogeneities and coil loading. Metabolite concentrations were corrected for CSF content and GM/WM partial volume fraction assuming 100% water content in CSF, 78% water content in GM and 65% water content in WM as recommended in the LCModel manual. Even though atrophy is observed in HD, tissue water content seems to remain fairly similar.<sup>22</sup> We thus assumed identical tissue water content in GM and WM in controls and patients. Metabolites were considered reliably quantified when Cramér-Rao lower bounds (CRLB)  $\leq 20\%$  were observed in at least half the subject population as this threshold allows the selection of the most reliably quantified metabolites as recommended in the LCModel manual. However, in order to avoid quantification bias, we reported the average of all concentration values for each reliably quantified metabolite, including those with CRLB  $< 999\%$ . For metabolites exhibiting high cross-correlation (correlation coefficient  $< -0.7$ ) – e.g. Cr and PCr; and NAA and NAAG – only the sum was reported (e.g. tCr for Cr and PCr; tNAA for NAA and NAAG). Spectra with water linewidth

> 10 Hz were excluded from the analysis. Pre-processing and quantification steps took approximately 3 minutes to complete.

### **Brain tissue volume estimation**

We first extracted the coordinates used for spectroscopy measurements in the visual cortex and the striatum in order to reconstruct this volume of interest (VOI) for each subject using in-house scripts developed in MATLAB. To obtain reliable volume estimates, 3D T1 images were automatically segmented using Freesurfer v5.3 (<https://surfer.nmr.mgh.harvard.edu/>). The gray matter (GM)/white matter (WM) interface as well as the GM volume segmentations were examined and reprocessed if corrections were needed. For each subject, VOIs were registered to their respective 3D T1 image and the volume fractions of the GM, WM and cerebrospinal fluid (CSF) within each VOI were extracted and quantified using tools available from Freesurfer.

### **Statistical analysis**

We applied a student *t*-test to compare neurometabolite concentrations between patients and controls. Pearson correlations were performed between neurometabolite concentrations and TMS, CAG repeat length and brain volume fractions in the VOI with Holm-Bonferroni multiple comparison correction. Probability values of  $p < 0.05$  were considered significant.

## **RESULTS**

Reduced GM volume fractions and increased CSF fractions were observed in HD patients compared to controls (Figure 2). Each subject's volume fractions were used to correct for partial volume effects.

We could not acquire one dataset from the visual cortex of a patient due to scanning time constraints. Hence nine datasets were reported for the visual cortex of patients. In the visual cortex, HD patients displayed higher tCr than controls ( $p = 0.032$ ) (Figure 3A). All other neurometabolites (Gln, Glu, GSH, *myo*Ins, tCho and tNAA) had similar concentrations in both groups. In the striatum, HD patients showed decreased Glu concentrations ( $p = 0.001$ ) whilst the other metabolites were comparable to controls (Figure 3B). In contrast to the striatum, Glu levels showed a trend to increase in the visual cortex. Similarly, tCr showed a trend to decrease in the striatum in contrast to the visual cortex.

In order to analyse more neurometabolites (aspartate, ascorbic acid, *scyllo*-inositol, lactate and taurine), the CRLB threshold was increased to 50%. These additional metabolites did not show any significant differences between patients and controls (data not shown). Overall, neurometabolite levels did not correlate with TMS, CAG repeat length or age.

## DISCUSSION

We showed increased tCr in the visual cortex and decreased Glu in the striatum at an early stage of HD, but no significant changes in less prominent metabolites such as GABA, Gln or GSH. While the striatum is at the center of structural and metabolic changes in HD, we confirmed that the visual cortex is also involved in the early stage of the disease. The extended analysis of 10 neurometabolites in the visual cortex and 8 in the striatum was possible due to a previously validated semi-LASER sequence providing high SNR and minimal *J*-modulation. The difference in lower number of metabolites reported for the striatum is due to the higher cross-correlation observed in this region.

Most clinical protocols use PRESS and STEAM sequences, which are vendor provided sequences. In the previous studies compiled in Table 1, long  $T_E$  protocols<sup>23,24</sup> provide a

limited number of metabolites that can be reported since metabolites with short  $T_2$  cannot be measured. Other studies used short  $T_E$  STEAM<sup>12,15,25</sup> and PRESS<sup>14,26,27</sup> protocols to report absolute concentrations or ratios of metabolites. However, it has been established that vendor sequences such as STEAM produces spectra with low SNR and PRESS has high chemical shift displacement artefacts.<sup>28</sup> In addition, the two pairs of  $180^\circ$  AFP pulses that we used preserve the  $J$ -modulation and provide consistency in measured  $J$ -coupled as well as singlet metabolites.<sup>19</sup>

Total creatine (tCr) serves as an energetic marker and maintains brain energy homeostasis.<sup>29</sup> Its importance may stem from the limited glucose storage capability by the brain.<sup>30</sup> Increased tCr has been reported in the brain of HD mouse models<sup>31</sup> and this increase preceded the depletion of ATP.<sup>32</sup> Patients with spinocerebellar ataxia type 1, 2 and 3, another group of polyglutamine disorders that share common pathophysiological pathways with HD,<sup>33</sup> also displayed increased tCr in the vermis and the pons.<sup>21</sup> In addition, the relative concentrations of components of energy metabolism – ATP, PCr and inorganic phosphate (Pi) – were previously measured using  $^{31}\text{P}$  MRS in the visual cortex of HD patients before, during and after visual stimulation.<sup>7,8</sup> Healthy controls exhibited a normal profile, with increased Pi/PCr ratio during visual stimulation, followed by a return to baseline levels during recovery. In contrast, HD patients displayed no significant change in Pi/PCr ratio in two independent studies.<sup>7,8</sup> The increase in tCr in the visual cortex reported here is in agreement with these studies. Altogether, these studies underlie that creatine metabolism is modified in the visual cortex of HD patients, a region that is particularly enriched in mitochondria,<sup>7,8</sup> at an early stage of the disease and may signify a compensatory mechanism. In the striatum however, there was no difference in tCr concentration but there was a trend to decreased tCr. This trend is similar to studies performed on HD patients in the striatum,<sup>12</sup> caudate<sup>15</sup> and putamen.<sup>14,15,34</sup>

The significant decrease in the neuronal marker Glu in the striatum is in agreement with previous reports from the putamen.<sup>14,15</sup> Decreased Glu could be due in part to the lower GM content in the striatal VOI. However, assuming that Glu was two-fold higher in GM than in WM,<sup>35</sup> we calculated that the measured decrease in GM content would have resulted in a less than 5% decrease in Glu concentration in the VOI, and therefore did not explain the 18% decrease observed in our study. Since it has been shown that the striatum is highly affected in HD, even at the presymptomatic stage,<sup>2</sup> decreased Glu concentrations could reflect neuronal dysfunction as a result of atrophy. Furthermore, Glu levels have been linked to metabolic activity.<sup>29</sup> Twenty percent of brain glucose metabolism is directed to Glu synthesis through the Gln-Glu cycle.<sup>36</sup> As HD patients display glucose hypometabolism in the striatum and cortex,<sup>37</sup> decreased Glu levels could reflect decreased metabolic activity in HD patients.

We did not find a difference in tNAA between patients and controls, which could be due to the fact that our cohort was at a very early stage of the disease. Previous studies reported no change in tNAA but a decrease in NAA.<sup>12,14,15,34</sup> However, we have observed high cross-correlation between NAA and NAAG, which indicates that reporting tNAA is more reliable than individual concentrations. It might be argued that the much smaller NAAG contribution should not offset any observable differences with NAA. Still, such high cross-correlations among the individual metabolites might lead to underestimation or overestimation of their actual individual values. Furthermore, GABA is another important metabolite in HD since the medium-sized spiny neurons that contain GABA undergo selective degeneration in the striatum.<sup>38</sup> In <sup>1</sup>H MRS experiments, however, special editing sequences are needed to extensively quantify the peaks at 3 T due to its overlap with other larger signals.<sup>36</sup> This study is therefore limited in its quantification of the GABA signal and it is possible that our reported values might not be a true reflection of the actual GABA concentration.



In conclusion, this study used an optimized semi-LASER protocol to help understand the early neurometabolic alterations that occur in HD. We reported absolute metabolite concentrations and not ratios,<sup>11,23,27,34,39</sup> in order to be able to analyse the impact of each individual metabolite. Unlike all the aforementioned studies summarized in Table 1, we obtained an expanded neurochemical profile of up to 10 metabolites. Our main finding is that creatine metabolism is affected at an early stage of HD, which supports the use of therapies aiming at improving brain energy metabolism.

## **Acknowledgements**

The authors wish to thank warmly the patients and volunteers who participated in this study.

The authors are also grateful to collaborators from the Center for Neuroimaging Research, France, and the Center for Magnetic Resonance Research, USA.

## **DISCLOSURE/CONFLICT OF INTEREST**

**No disclosure:** Adanyeguh, Monin, Rinaldi.

**Freeman:** Research support by grants from the National Multiple Sclerosis Society.

**Durr:** Research support by grants from the French Agency for Research, Fondation pour la recherche médicale (FRM), and Pfizer Inc.

**Lehericy:** Received grants from Agence Nationale de la Recherche (ANRMNP 2009, Nucleipark), DHOS-Inserm (2010, Nucleipark), France Parkinson (2008), Ecole Neurosciences de Paris, 'Investissements d'avenir' [grant number ANR-10-IAIHU-06 and ANR-11-INBS-0006] during the conduct of the study. Outside of this study, he received commercial research support from Servier and Pfizer, funding for travel from Siemens and General Electric and honoraria from Pileje, Lundbeck and Roche.

**Henry:** Research support by grants from NIH (P41 EB015894, P30 NS076408) and Friedreich's Ataxia Research Alliance.

**Mochel:** Research support by grants from INSERM, Carnot Institutes, ASL Foundation and Ultragenyx Pharmaceutical.

## REFERENCES

1. Kremer B, Goldberg P, Andrew SE, et al. A worldwide study of the Huntington's disease mutation. The sensitivity and specificity of measuring CAG repeats. *N Engl J Med* 1994;330(20):1401-1406.
2. Tabrizi SJ, Scahill RI, Owen G, et al. Predictors of phenotypic progression and disease onset in premanifest and early-stage Huntington's disease in the TRACK-HD study: analysis of 36-month observational data. *Lancet Neurol* 2013;12:637-649.
3. Rosas HD, Koroshetz WJ, Chen YI, et al. Evidence for more widespread cerebral pathology in early HD: an MRI-based morphometric analysis. *Neurology* 2003;60:1615-1620.
4. Waldvogel HJ, Kim EH, Tippett LJ, Vonsattel JP, Faull RL. The Neuropathology of Huntington's Disease. *Curr Top Behav Neurosci* 2015;22:33-80.
5. Rub U, Seidel K, Vonsattel JP, et al. Huntington's Disease (HD): Neurodegeneration of Brodmann's Primary Visual Area 17 (BA17). *Brain Pathol* 2015;25(6):701-711.
6. Feigin A, Leenders KL, Moeller JR, et al. Metabolic network abnormalities in early Huntington's disease: an [(18)F]FDG PET study. *J Nucl Med* 2001;42(11):1591-1595.
7. Mochel F, N'Guyen TM, Deelchand D, et al. Abnormal response to cortical activation in early stages of Huntington disease. *Mov Disord* 2012;27:907-910.
8. Adanyeguh IM, Rinaldi D, Henry PG, et al. Triheptanoin improves brain energy metabolism in patients with Huntington disease. *Neurology* 2015;84:490-495.
9. Corvol JC. Neuroprevention: a new challenge? *Rev Neurol (Paris)* 2012;168:796-801.
10. Huntington Study Group. Unified Huntington's disease rating scale: Reliability and consistency. *Mov Disord* 1996;11:136-142.

11. Jenkins BG, Rosas HD, Chen YC, et al. <sup>1</sup>H NMR spectroscopy studies of Huntington's disease: correlations with CAG repeat numbers. *Neurology* 1998;50:1357-1365.
12. Clarke CE, Lowry M, Quarrell OWJ. No change in striatal glutamate in Huntington's disease measured by proton magnetic resonance spectroscopy. *Parkinsonism Relat Disord* 1998;4:123-127.
13. Ruocco HH, Lopes-Cendes I, Li LM, Cendes F. Evidence of thalamic dysfunction in Huntington disease by proton magnetic resonance spectroscopy. *Mov Disord* 2007;22:2052-2056.
14. Sturrock A, Laule C, Decolongo J, et al. Magnetic resonance spectroscopy biomarkers in premanifest and early Huntington disease. *Neurology* 2010;75:1702-1710.
15. van den Bogaard SJ, Dumas EM, Teeuwisse WM, et al. Exploratory 7-Tesla magnetic resonance spectroscopy in Huntington's disease provides in vivo evidence for impaired energy metabolism. *J Neurol* 2011;258:2230-2239.
16. Liot G, Valette J, Pépin J, Flament J, Brouillet E. Energy defects in Huntington's disease: Why "in vivo" evidence matters. *Biochem Biophys Res Commun* 2017;483:1084-1095.
17. Tkáč I, Öz G, Adriany G, et al. In vivo <sup>1</sup>H NMR spectroscopy of the human brain at high magnetic fields: metabolite quantification at 4T vs. 7T. *Magn Reson Med* 2009;62:868-879.
18. Öz G, Tkáč I. Short-echo, single-shot, full-intensity proton magnetic resonance spectroscopy for neurochemical profiling at 4 T: Validation in the cerebellum and brainstem. *Magn Reson Med* 2011;65:901-910.

19. Deelchand DK, Adanyeguh IM, Emir UE, et al. Two-site reproducibility of cerebellar and brainstem neurochemical profiles with short-echo, single-voxel MRS at 3T. *Magn Reson Med* 2014;73:1718-1725.
20. Gruetter R, Tkac I. Field mapping without reference scan using asymmetric echo-planar techniques. *Magn Reson Med* 2000;43(2):319-323.
21. Adanyeguh IM, Henry PG, Nguyen TM, et al. In vivo neurometabolic profiling in patients with spinocerebellar ataxia types 1, 2, 3, and 7. *Mov Disord* 2015;30:662-670.
22. Zacharoff L, Tkac I, Song Q, et al. Cortical metabolites as biomarkers in the R6/2 model of Huntington's disease. *J Cereb Blood Flow Metab* 2012;32:503-514.
23. Taylor-Robinson SD, Weeks RA, Bryant DJ, et al. Proton magnetic resonance spectroscopy in Huntington's disease: evidence in favour of the glutamate excitotoxic theory. *Mov Disord* 1996;11:167-173.
24. van Oostrom JC, Sijens PE, Roos RA and Leenders KL. <sup>1</sup>H magnetic resonance spectroscopy in preclinical Huntington disease. *Brain Res* 2007;1168:67-71.
25. van den Bogaard SJ, Dumas EM, Teeuwisse WM, et al. Longitudinal metabolite changes in Huntington's disease during disease onset. *J Huntingtons Dis* 2014;3:377-386.
26. Sturrock A, Laule C, Wyper K, et al. A longitudinal study of magnetic resonance spectroscopy Huntington's disease biomarkers. *Mov Disord* 2015;30:393-401.
27. Padowski JM, Weaver KE, Richards TL, et al. Neurochemical correlates of caudate atrophy in Huntington's disease. *Mov Disord* 2014;29:327-335.

28. Boer VO, van Lier AL, Hoogduin JM, Wijnen JP, Luijten PR, Klomp DW. 7-T 1H MRS with adiabatic refocusing at short TE using radiofrequency focusing with a dual-channel volume transmit coil. *NMR Biomed* 2011;24:1038-1046
29. Rae CD. A guide to the metabolic pathways and function of metabolites observed in human brain 1H magnetic resonance spectra. *Neurochem Res* 2014;39:1-36.
30. Brewer GJ, Wallimann TW. Protective effect of the energy precursor creatine against toxicity of glutamate and beta-amyloid in rat hippocampal neurons. *J Neurochem* 2000;74:1968-1978.
31. Tkac I, Dubinsky JM, Keene CD, et al. Neurochemical changes in Huntington R6/2 mouse striatum detected by in vivo 1H NMR spectroscopy. *J Neurochem* 2007;100:1397-1406.
32. Mochel F, Durant B, Meng X, et al. Early alterations of brain cellular energy homeostasis in Huntington disease models. *J Biol Chem* 2012;287:1361-1370.
33. Gatchel JR and Zoghbi HY. Diseases of unstable repeat expansion: mechanisms and common principles. *Nat Rev Genet* 2005;6:743-755.
34. Hoang TQ, Bluml S, Dubowitz DJ, et al. Quantitative proton-decoupled 31P MRS and 1H MRS in the evaluation of Huntington's and Parkinson's diseases. *Neurology* 1998;50:1033-1040.
35. Hassel B, Dingledine R. Glutamate. In: Siegel GJ, Albers RW, Brady S, Price D, editors. *Basic neurochemistry: molecular, cellular and medical aspects*. 7th edition. San Diego: Elsevier Academic Press; 2005:267-290.

36. Maddock RJ, Buonocore MH. MR spectroscopic studies of the brain in psychiatric disorders. *Curr Topics Behav Neurosci* 2012;11:199-251.
37. Pagano G, Niccolini F, Politis M. Current status of PET imaging in Huntington's disease. *Eur J Nucl Med Mol Imaging* 2016;43:1171-1182.
38. Vonsattel JP, DiFiglia M. Huntington disease. *J Neuropathol Exp Neurol* 1998;57(5):369-384.
39. Jenkins BG, Koroshetz WJ, Beal MF, Rosen BR. Evidence for impairment of energy metabolism in vivo in Huntington's disease using localized <sup>1</sup>H NMR spectroscopy. *Neurology* 1993;43:2689-2695.
40. Gómez-Ansón B, Alegret M, Muñoz E, et al. Decreased frontal choline and neuropsychological performance in preclinical Huntington disease. *Neurology* 2007;68:906-910.
41. Sánchez-Pernaute R, García-Segura JM, del Barrio Alba A, et al. Clinical correlation of striatal <sup>1</sup>H MRS changes in Huntington's disease. *Neurology* 1999;53:806-812.

**Table 1:** Summary of previous 1H MRS studies in the striatum and occipital cortex

	<b>Striatum</b>	<b>Caudate</b>
<b>Presymptomatic vs controls</b>		
<b>NAA/tNAA</b>		
<b>No change in any metabolite</b>	Gomez-Anson 2007 (n=19) <sup>40</sup>	Van den Bogaard 2011 (n=11 reported) <sup>15</sup>
<b>Patients vs controls</b>		
<b>NAA/tNAA</b>	<ul style="list-style-type: none"> <li>↘ Jenkins 1993 (tNAA/Cr, n=15)<sup>39</sup></li> <li>↘ Jenkins 1998 (tNAA/Cr, n=31)<sup>11</sup></li> <li>↘ Clarke 1998 (NAA, n=6)<sup>12</sup></li> </ul>	<ul style="list-style-type: none"> <li>↘ Van den Bogaard 2011 (n=5 reported)<sup>15</sup></li> </ul>
<b>mIns</b>		
<b>tCr</b>	<ul style="list-style-type: none"> <li>↘ Clarke 1998 (Cr) (n=6)<sup>12</sup></li> <li>↗ Glx Taylor-Robinson 1996 (Glx/tCr, n=5)<sup>23</sup></li> </ul>	<ul style="list-style-type: none"> <li>↘ Van den Bogaard 2011 (n=5 reported)<sup>15</sup></li> </ul>
<b>Glu</b>	<ul style="list-style-type: none"> <li>↗ Jenkins 1993 (tCho/tCr, n=15)<sup>39</sup></li> <li>↗ Jenkins 1998 (tCho/tCr, n=31)<sup>11</sup></li> </ul>	
<b>Cho/tCho</b>	<ul style="list-style-type: none"> <li>↗ Clarke 1998 (Cho/Cr, n=6)<sup>12</sup></li> <li>↗ Jenkins 1993 (n=15)<sup>39</sup></li> <li>↗ Jenkins 1998 (n=31)<sup>11</sup></li> </ul>	
<b>Lac</b>	<ul style="list-style-type: none"> <li>↗ Jenkins 1998 (n=31)<sup>11</sup></li> </ul>	
<b>No change in any metabolite</b>		
<b>Mixed presymptomatic/patients vs controls</b>		
<b>NAA/tNAA</b>		<ul style="list-style-type: none"> <li>↘ Sanchez-Pernaute 1999 (n=4 PMC, n=6 MC)<sup>41</sup></li> </ul>
<b>mIns</b>		
<b>tCr</b>		<ul style="list-style-type: none"> <li>↘ Sanchez-Pernaute 1999 (n=4 PMC, n=6 MC)<sup>41</sup></li> <li>↘ Padowski 2014 (only when considering ratios) (n=6 PMC, n=4 MC)<sup>27</sup></li> </ul>
<b>Glu</b>		
<b>Mixed presymptomatic/patients longitudinal changes</b>		
<b>NAA/tNAA</b>		
<b>mIns</b>		<ul style="list-style-type: none"> <li>↘ van den Bogaard 2014 (n=7 PMC, n=2 MC)<sup>25</sup></li> </ul>
<b>Cr</b>		<ul style="list-style-type: none"> <li>↘ van den Bogaard 2014 (n=7 PMC, n=2 MC)<sup>25</sup></li> </ul>
<b>Cho</b>		
<b>No change in any metabolite</b>		



Table 1 continued

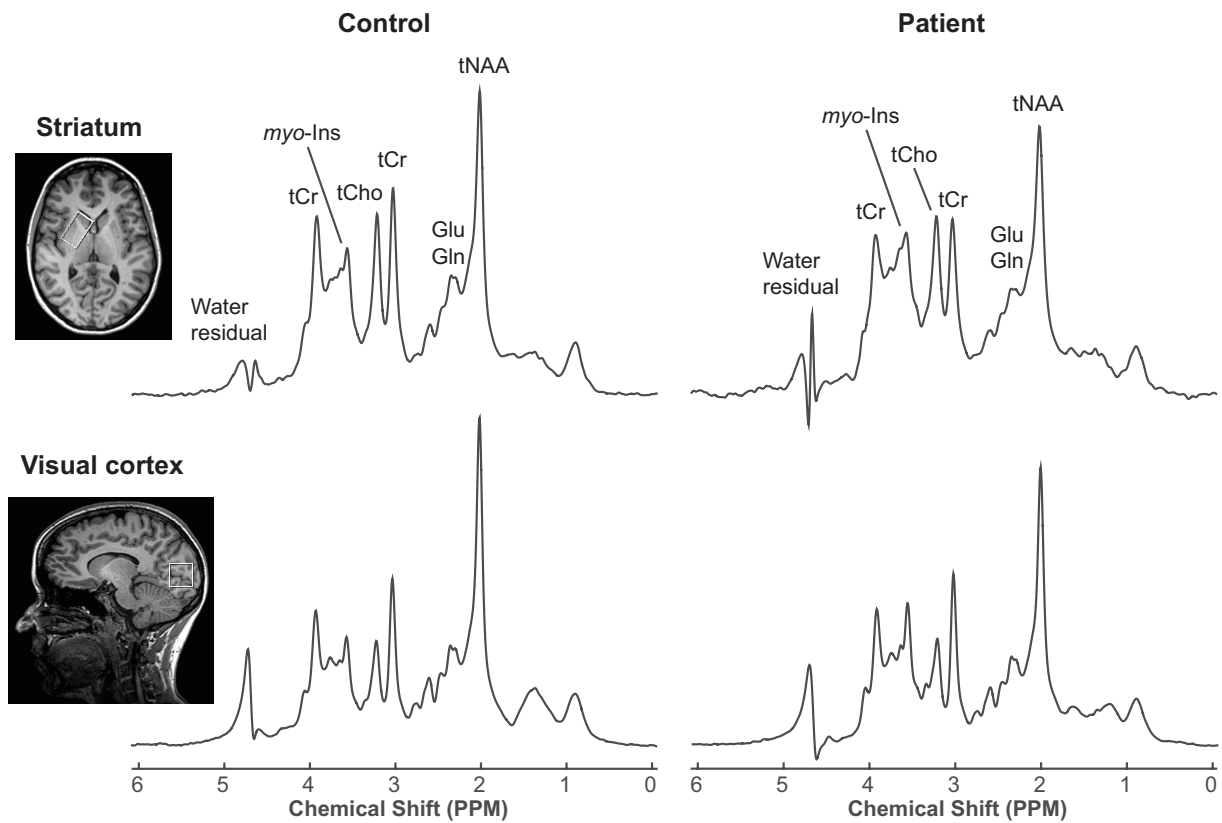
	Putamen	Occipital cortex
<b>Presymptomatic vs controls</b>		
NAA/tNAA	<p>⬇ NAA -8% but not tNAA Sturrock 2010 (n=25)<sup>14</sup></p> <p>No change in NAA but ⬇tNAA Sturrock 2015 (n=25)<sup>26</sup></p>	
No change in any metabolite	<p>Van den Bogaard 2011 (n=9 reported)<sup>15</sup></p> <p>Van Oostrom 2007 (n=19) (34)</p>	
<b>Patients vs controls</b>		
NAA/tNAA	<p>⬇ -17%/-15% Sturrock 2010 (n=29)<sup>14</sup></p> <p>⬇ Van den Bogaard 2011 (n=5 reported)<sup>15</sup></p> <p>⬇ NAA Hoang 1998 (n=15)<sup>34</sup></p> <p>⬇ Sturrock 2015 (n=23/24)<sup>26</sup></p>	<p>⬇ NAA/Cr Hoang 1998<sup>34</sup></p>
mIns	<p>↗ Hoang 1998 (n=15)<sup>34</sup></p> <p>↗ ~50% Sturrock 2010 (n=29)<sup>14</sup></p> <p>↗ Sturrock 2015 (n=23/24)<sup>26</sup></p>	
tCr	<p>⬇ Van den Bogaard 2011 (n=5 reported)<sup>15</sup></p> <p>⬇ Hoang 1998 (n=15)<sup>34</sup></p> <p>⬇ -18% Sturrock 2010 (n=29)<sup>14</sup></p>	
Glu	<p>⬇ Van den Bogaard 2011 (n=5 reported)<sup>15</sup></p> <p>⬇ ~10% Sturrock 2010 (n=29)<sup>14</sup></p>	
Cho/tCho	<p>↗ ~10% Sturrock 2010 (n=29)<sup>14</sup></p> <p>↗ Hoang 1998 (n=15)<sup>34</sup></p>	<p>↗ Jenkins 1998 (n=31)<sup>11</sup></p> <p>↗ Jenkins 1993 (n=15)<sup>39</sup></p> <p>↗ Jenkins 1998 (n=31)<sup>11</sup></p>
Lac		<p>Taylor-Robinson 1996<sup>23</sup></p> <p>Hoang 1998 (abs conc)<sup>34</sup></p>
No change in any metabolite		
<b>Mixed presymptomatic/patients vs controls</b>		
mIns	Trend ↗ Padowski 2014 (n=6 PMC, n=4 MC) <sup>27</sup>	
<b>Mixed presymptomatic/patients longitudinal changes</b>		
NAA/tNAA	<p>⬇ van den Bogaard 2014 (n=6 PMC, n=1 MC)<sup>25</sup></p> <p>Trend mIns/NAA ↗ Sturrock 2015 (n = 23/24 MC)<sup>26</sup></p>	
mIns		
Cho	<p>⬇ van den Bogaard 2014 (n=6 PMC, n=1 MC)<sup>25</sup></p>	
No change in any metabolite	Sturrock 2015 (n=25/22 PMC, n= 23/24 MC) <sup>26</sup>	

NAA: *N*-acetylaspartate, tNAA: total *N*-acetylaspartate. Cr: creatine, tCr: total creatine, Glu: glutamate, Glx: glutamine and glutamate, tCho: total choline, Lac: lactate, *myo*-Ins: *myo*-inositol, PMC: premanifest carrier; MC: manifest carrier, abs conc: absolute concentration; ↗: increased concentration; ⬇: decreased concentration

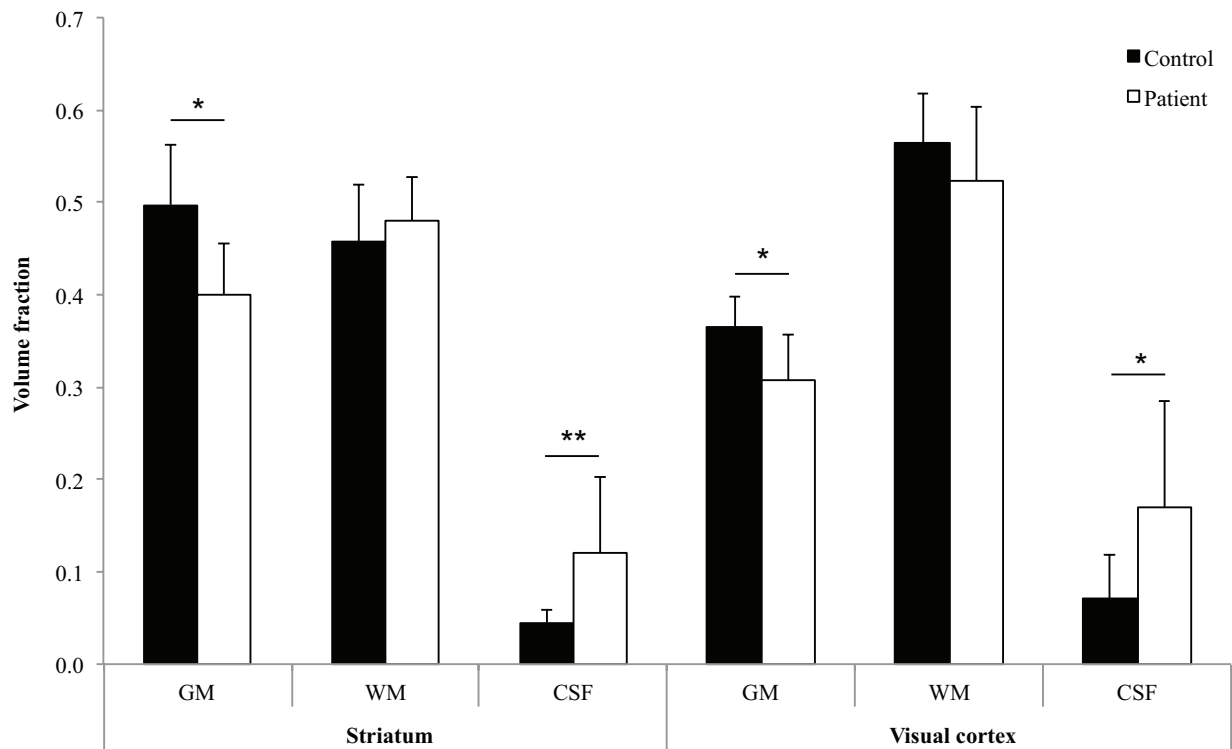
**Table 2:** Demographic and spectroscopic parameters of participants.

<b>Variable</b>	<b>Controls</b>	<b>HD patients</b>
<b>N<sup>o</sup> of participants</b>	10.0	10.0
<b>Gender (M/F)</b>	3/7	3/7
<b>Age (years)</b>	38.9 ± 13.8	45.6 ± 12.7
<b>BMI (kg/m<sup>2</sup>)</b>	21.1 ± 1.7	21.6 ± 3.3
<b>TMS (UHDRS)</b>	0.9 ± 1.0	13.6 ± 10.8 <sup>#</sup>
<b>CAG length</b>		44.1 ± 4.2
<b>Lw striatum (Hz)</b>	10.0 ± 1.0	8.3 ± 2.6
<b>Lw visual cortex (Hz)</b>	7.8 ± 0.7	6.6 ± 1.1 *
<b>SNR striatum</b>	46.7 ± 11.3	39.0 ± 16.7
<b>SNR visual cortex</b>	65.6 ± 19.4	57.1 ± 14.5
<b>%CSF striatum</b>	4.5 ± 1.4	12.0 ± 8.4 *
<b>%CSF visual cortex</b>	7.0 ± 4.8	17.0 ± 11.5 *

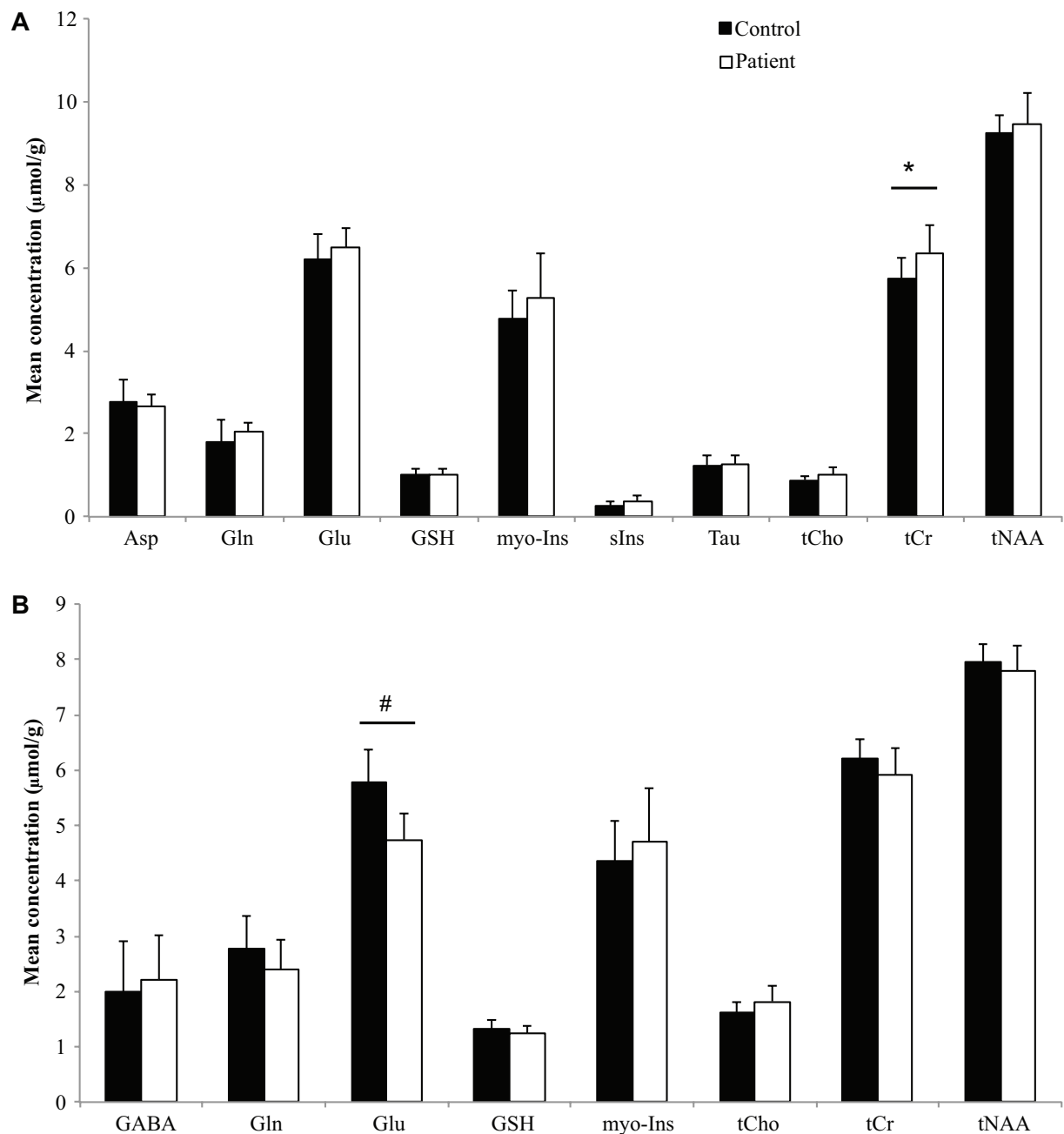
Data are presented as mean ± standard deviation and compared by *t*-test. BMI: body mass index; TMS: total motor score; SNR: signal-to-noise ratio estimated by LCModel; Lw: water linewidth estimated by LCModel; CSF: cerebrospinal fluid. \**p*<0.05 and <sup>#</sup>*p*≤0.01 represent significant differences between HD patients and controls.



**Figure 1:** Voxel positioning and spectra acquired from the striatum and visual cortex of controls and patients. Spectra were acquired in an acquisition voxel of  $34 \times 19 \times 23 \text{ mm}^3$  in the striatum and  $25 \times 25 \times 25 \text{ mm}^3$  in the visual cortex using the modified semi-LASER sequence ( $T_R = 5000 \text{ ms}$ ,  $T_E = 28 \text{ ms}$ , averages = 64). tNAA: total *N*-acetylaspartate, Glu: glutamate, Gln: glutamine, tCr: total creatine, tCho: total choline, *myo*-Ins: *myo*-Inositol.



**Figure 2:** Brain tissue volume fraction in VOI in the striatum and visual cortex. Gray matter (GM) was markedly reduced in the striatum and visual cortex whilst cerebrospinal fluid (CSF) was significantly increased. \* $p < 0.05$  and \*\* $p \leq 0.01$  represent significant differences between HD patients and controls.



**Figure 3:** Mean metabolite concentrations obtained in the A) visual cortex and B) striatum. Fewer metabolites are reported for the striatum since they did not meet the quality control threshold unlike in the visual cortex. Asp: aspartate, Gln: glutamine, Glu: glutamate, GSH: glutathione, myo-Ins: *myo*-inositol, sIns: *scyllo*-inositol, Tau: taurine, tCho: total choline, tCr: total creatine, tNAA: total *N*-acetylaspartate. Error bars represent standard deviations. \* $p < 0.05$ , # $p < 0.01$ .

### **3.3 Perspective: Identifying biomarkers of dynamic energy metabolism (HDeENERGY)**

This project aims at measuring dynamic parameters of brain energy metabolism in order to decipher the mechanisms underlying brain energy deficit in HD and identify novel functional biomarkers to be used in clinical trials such as those targeting the Krebs cycle. This study seeks to recruit 20 patients at the early stage of HD, 20 presymptomatic individuals and 20 healthy controls. Each subject's participation in this study spans half a day. HDeENERGY is sponsored by APHP (ClinicalTrials.gov Identifier: NCT02639871). The project also comprises preclinical studies that are being conducted at MIRCen by Emmanuel Brouillet's team in a rat model of HD. Besides the determination of the synthesis rate of phosphocreatine using saturation transfer  $^{31}\text{P}$  MRS in the BACHD rat, methodological breakthroughs at MIRCen includes evaluating the turnover of the Krebs cycle using  $^{13}\text{C}$  MRS, and the establishment of brain maps of pH and glutamate using chemical exchange saturation transfer.

The clinical study was split into two phases; the first phase was the validation phase where 10 healthy volunteers were recruited to setup and optimize the protocol. The second phase is the implementation of the optimized protocols in the subjects recruited for the study. Preliminary results from the 10 volunteers and 8 patients are presented.

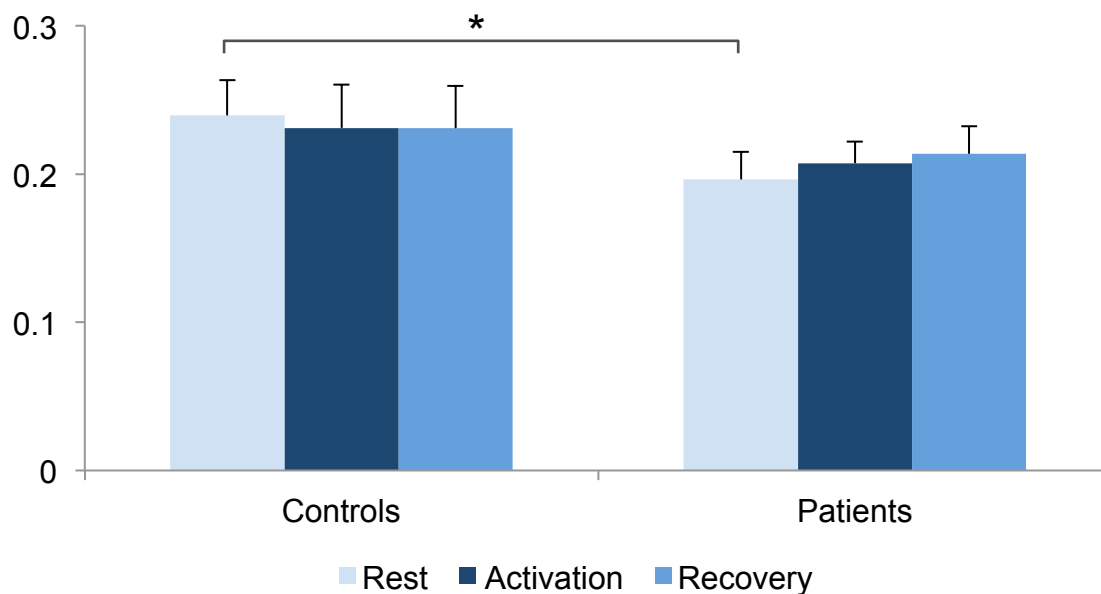
The MRS protocol includes several modalities to determine metabolic, functional and structural biomarkers of dynamic energy metabolism.

#### **3.3.1 $^{31}\text{P}$ magnetization transfer**

$^{31}\text{P}$  MT is performed in the visual cortex as described in study 2a. Study 2a showed a trend of 5% increase in CK in controls during visual stimulation contrary to patients. Hence we would like to determine the CK in a larger cohort of HD patients. CK rate calculations are made by assuming intrinsic  $T_1$  of PCr to be 5.03 (Du et al., 2014). A correction factor of 0.83 is applied assuming that steady-state intensity of PCr is not reached during  $\gamma\text{ATP}$  saturation (Chen et al., 1997).

Preliminary analysis of data has not yielded yet the expected results observed in study 2a. Here we observed a 4% increase in CK rate in controls compared to patients, but only at rest

( $p = 0.02$ ). We did not find any differences during visual stimulation and recovery between the two groups. Unfortunately, the change of our MR system to Siemens Prisma, which occurred after the conduct of study 2a, led to a reduced field of view of the projected visual stimulation regardless of the different changes in stimulation setups that we performed. This might account for the no observable increase in CK in controls during visual stimulation. We are now pursuing the acquisition of data in patients, controls and premanifest individuals in order to reach 20 per group and see whether we can obtain similar results as reported in study 2a, but with significant differences between controls and patients.



**Figure 18: Preliminary results of the rate of CK measured with  $^{31}\text{P}$  MT in the visual cortex of patients and controls.** Controls had higher rate of CK at rest (4%) compared to patients ( $p = 0.02$ ). No change was observed during visual stimulation and recovery phase.

### 3.3.2 Diffusion weighted spectroscopy

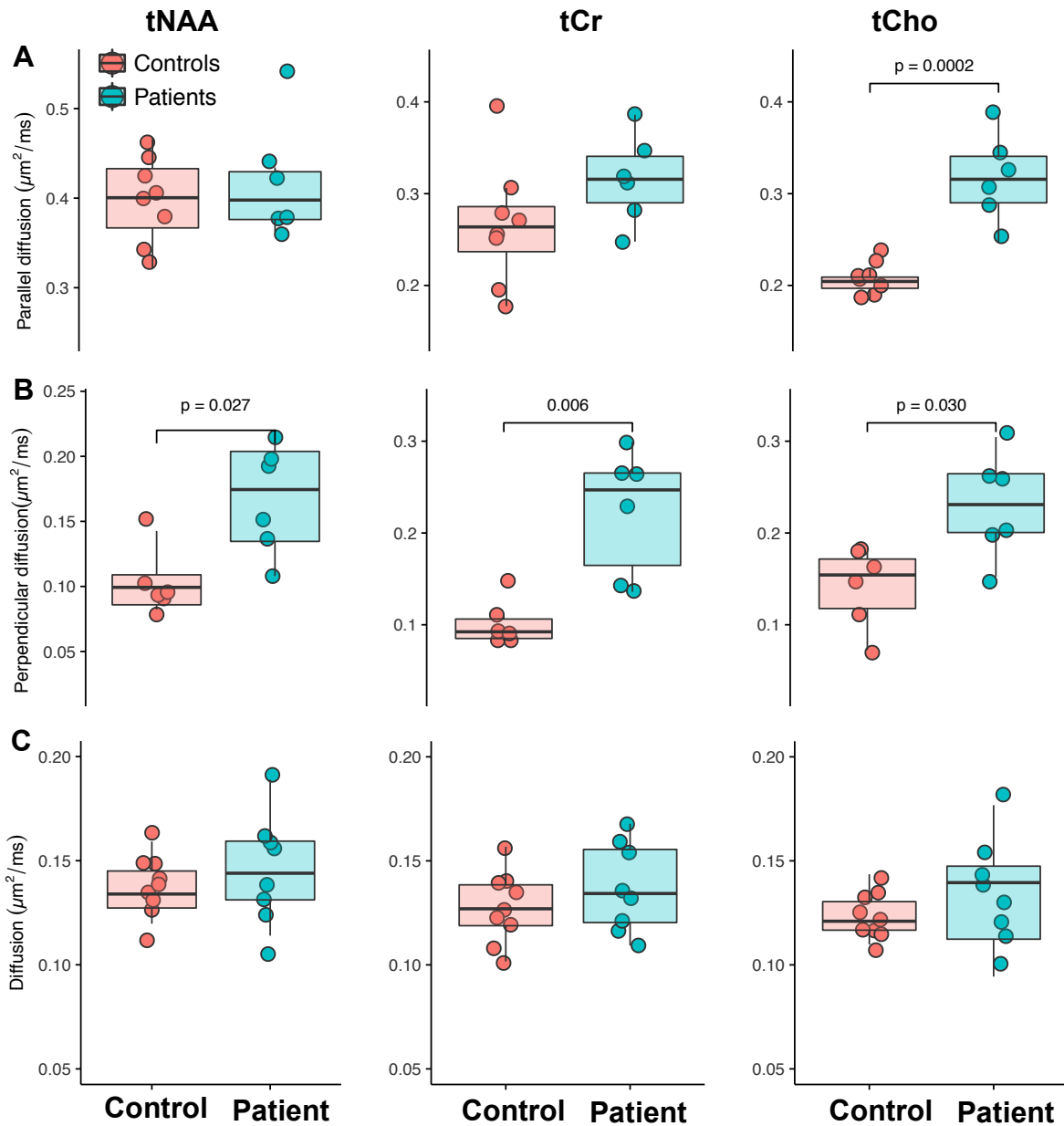
Diffusion imaging of brain water diffusion has been used over the years to detect indirect indicators of biological processes. DWS provides an alternate approach to directly probe cellular and extracellular compartments for their immediate link to biological events. By measuring the apparent diffusion coefficient (ADC) of certain metabolites, we can directly infer the level of activation of certain neurons, the microstructural properties of tissues and

the processes involved in particular disease processes such as inflammation or axonal damage (Branzoli et al., 2013; Ronen & Valette, 2015; Ercan et al., 2016). The principle of DWS is similar to that of DTI where diffusion sensitizing encoding gradients are coupled to the MRS protocol. Unlike water, metabolites are of very low concentrations and high  $b$ -values are needed to observe their diffusion properties. A series of alternating acquisitions of spectra with no diffusion gradient applied, and spectra with applied diffusion gradient, are acquired several times to improve the SNR. The metabolite peaks are attenuated in the presence of diffusion gradients. Due to this attenuation, reliable quantification can only be reported on the most prominent metabolites, i.e. total creatine (tCr), total *N*-acetylaspartate (tNAA) and total choline (tCho).

In the HDENERGY study, DWS is performed in the visual cortex (VOI = 25 x 25 x 25 mm<sup>3</sup>,  $b$  value = 0, 3550 s/mm<sup>2</sup>) and the corpus callosum (VOI = 8 x 15 x 32 mm<sup>3</sup>, parallel diffusion:  $b$  values = 0, 482, 772, 1737, 3088 s/mm<sup>2</sup>; perpendicular diffusion:  $b$  values = 0, 964, 1544, 3474, 6176 s/mm<sup>2</sup>). We chose the visual cortex due to its reported altered metabolism in our <sup>31</sup>P MRS studies. The corpus callosum was chosen for its highly defined white matter structures and reported atrophy in some patients, as well as preclinical data showing altered glutamate concentrations (using CEST) in the corpus callosum of BACHD rats compared to wild types (team of E. Brouillet at MIRCen).

We identified increased parallel and perpendicular diffusion of tCho in the corpus callosum, which may reflect increased gliosis. We found increased parallel diffusion of tCr, and a trend to increased perpendicular diffusion of tCr, in the corpus callosum of patients that may indicate an energetic compensatory mechanism. Perpendicular diffusion of tNAA was also significantly higher in patients than controls. Axonal damage could be an underlying reason for this increase (Ercan et al., 2016). We have not observed any differences yet in the visual cortex (Figure 19).





**Figure 19: Preliminary results of DWS analysis.** There was an increased parallel diffusion of tCho in patients (A) and increased perpendicular diffusion of tCho, tCr and tNAA in patients (B). No change was observed in the visual cortex (C).

### 3.3.3 Resting state functional MRI (rsfMRI)

RsfMRI has been included in this study to capture the impact of functional connectivity on neurometabolism and *vice versa*. RsfMRI relies on the blood oxygen level (BOLD) to determine regions of the brain that are activated during a resting state. The hemoglobin in

blood possesses different magnetic properties depending on whether it is oxygenated or deoxygenated (Pauling & Coryell, 1936). Oxygenated blood is diamagnetic, meaning it does not affect the MR signal. Meanwhile, deoxygenated blood is paramagnetic meaning that it introduces susceptibilities that cause dephasing of the nuclei spins leading to a decrease in the MR signal or darker images. Increase in neural activity leads to a high consumption of energy leading to an increase in deoxygenated blood. However, the increase in cerebral blood flow leads to a faster clearance of deoxygenated blood and hence increase in signal is observed.

rsfMRI measures the brain's spontaneous activity in the absence of external stimuli. At rest, low frequency fluctuations of the BOLD signal correlates with functional connections of different brain regions (Biswal et al., 1995). The advantage of rsfMRI over task related fMRI is that, rsfMRI can be used in all individuals, even patients who are physically incapable of performing certain tasks. Furthermore, network identification with rsfMRI has been shown to be reproducible over time except for the visual and sensorimotor networks that may be influenced by laboratory conditions such as the temperature in the examination room (Choe et al., 2015). Its reproducibility makes it a good biomarker in neurodegenerative diseases such as HD.

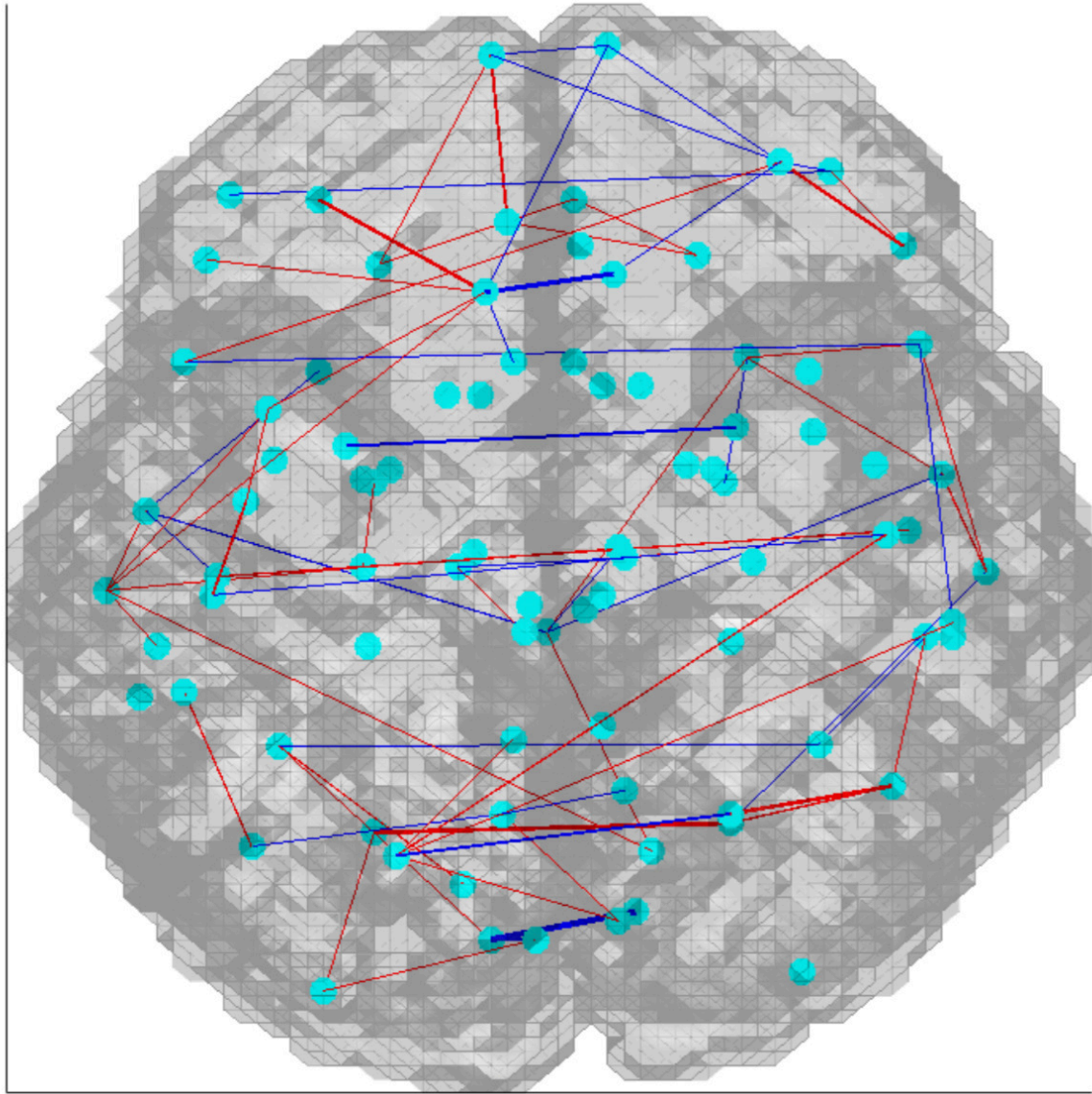
Functional connectivity is a dynamic process and hence static correlation analysis that are currently used to analyze rsfMRI data are inadequate in capturing the full dynamic process of functional connectivity (Cole et al., 2010). The seed-based correlation analysis that was originally proposed (Biswal et al., 1995) is biased by the choice of seed region and size, and it under-represents the actual networks as it ignores other networks than the seed region being considered even when coupled with principal component analysis (Leonardi et al., 2013) or independent component analysis (Beckmann et al., 2005). This approach is also unable to distinguish spurious or indirect spatial correlations; that is, it is unable to tell if two nodes are directly correlated or their correlation is as a result of their individual correlations with a third node. To resolve this, partial correlation (Marrelec et al., 2006) has been proposed to account for spurious correlations where two nodes are considered to be linked only if their partial correlation is non-zero. Another problem that partial correlation fails to address is temporal correlations that exist in brain activity time series (Smith, 2012). Partial coherence methods (Salvador et al., 2005) have been used to address this issue. To extract biologically meaningful information, graph analysis methods (Achard et al., 2006) have been used to identify networks that reflect underlying anatomical connectivity. One major disadvantage of

these methods is that the number of components that are generated significantly influence the result and physiological noise components can contribute to the true neural components (Cole et al., 2010). More importantly, these methods rely on group analysis and do not allow individual network identification.

Our collaborators at the Neuroscience Research Australia, Sydney, Australia (PI: Caroline Rae) have developed algorithm (Cassidy et al., 2015) that overcomes the problems of associated with current analytical methods. It uses autoregressive models coupled with frequency domain coherence to tackle the problem of temporal correlations. It incorporates partial coherence to solve spurious spatial correlation problems. In addition, it incorporates sparsity methods from statistical signal processing to avoid problems with artifacts and allow its use on datasets with poor quality. The algorithm has been shown to be robust at identifying functional networks with repeatable and reliable results even on individual subjects (Cassidy et al., 2015).

In this study, we acquire high-resolution images (FOV = 204 x 204,  $T_R = 1000$  ms,  $T_E = 30$  ms, flip angle =  $74^\circ$ , slice thickness = 3 mm isotropic, number of measurements = 600, acquisition time = 10 min) with the multiband accelerated EPI sequence (multiband acceleration factor = 3). The multiband acquisition scheme enables multiple slices to be acquired simultaneously, within the same time that it would take to acquire one slice using conventional schemes. Subjects are made to fix their eyes on a cross to prevent them from sleeping and they were instructed to refrain from moving, speaking or performing cognitive tasks as much as possible. After preprocessing the data that includes parcellation of 3D  $T_1$ -weighted volumetric brain image, motion and susceptibility correction of functional data, and co-registration of functional and volumetric images, the data is sent to our collaborators at the Neuroscience Research Australia, Sydney, Australia.

Analysis of preliminary volunteer data shows that the data are of good quality and we are able to identify the networks (Figure 20). The main idea is not just detect the networks but perform statistical analysis to identify the differences between controls, patients and presymptomatic individuals.



**Figure 20: Preliminary network analysis (rsfMRI) on volunteers data.**

### 3.3.4 Structural analysis

Atrophy in presymptomatic individuals and patients will be determined by the BSI approach as previously explained. Furthermore, changes in white matter fibers will be evaluated using the fixel-based approach as detailed in study 6. In this study, however, we do not acquire diffusion data with only one  $b$  value. We acquire diffusion data with multiple  $b$  values (multi-shell) and we also utilize multiband acceleration (FOV = 208 x 208,  $T_R$  = 2920 ms,  $T_E$  = 71 ms, slice thickness = 2 mm isotropic, flip angle =  $90^\circ$ , multiband acceleration factor = 3,  $b$

values = 2500 s/mm<sup>2</sup> (60 directions), 900 s/mm<sup>2</sup> (32 directions) and 300 s/mm<sup>2</sup> (8 directions)). Acquisition of each  $b$  value is repeated but the directions are in the opposite phase to allow for susceptibility and distortion corrections. The use of multi-shell acquisition in diffusion imaging can often be time consuming. Still, this study benefits from the multiband acquisition scheme, which speeds up the acquisition protocol and thus we have a total acquisition time of 13 minutes. Furthermore, multi-shell acquisitions improve the SNR and contrast-to-noise ratio thereby improving the estimation of the fibers during tractography (Daianu et al., 2015).

### 3.3.5 Protocol setup

Setting up the protocol involved a lot of phantom tests and adjustment of several parameters. Especially with the change of MR system, the optimum flip angle for the BISTRO had to be recalibrated.

With the help of an expert in DWS, Francesca Branzoli, we determined the maximum gradient strength and orientation of the VOI for the visual cortex and the corpus callosum. We also included a provision for patients who were likely to move during scans and cause the VOI to be shifted to a different region. Interleaving the scans with shot localizer sequences allowed us to readjust the VOI in case of significant movement.

I acquire all datasets and perform quality control on all spectroscopy and imaging datasets to ensure reliable reporting of results. I perform the analyses of MT, DWS and diffusion datasets. After I preprocess rsfMRI datasets, they are then sent to Ben Cassidy from our collaborators team and he performs the identification of the functional networks. The networks are then sent back to me for statistical analysis and extraction of biologically meaningful connections.

# Chapter 4

## Organisation:

<b>Study 3: Standardization and optimization of <sup>1</sup>H MRS protocol at 3T using short-echo, single-voxel semi-LASER protocol .....</b>	<b>88</b>
4.1 Introduction and objectives .....	88
4.2 Materials and methods.....	88
4.3 Results .....	89
4.5 Published article .....	89

## **Study 3: Standardization and optimization of <sup>1</sup>H MRS protocol at 3T using short-echo, single-voxel semi-LASER protocol**

### **4.1 Introduction and objectives**

Vendor provided MR sequences – PRESS and STEAM – are mostly used for MR studies (Jissendi Tchifo & Baleriaux, 2009). Even in multi-centric trials, these sequences have been used at different field strengths to quantify and report few metabolites (Chard et al., 2002; Jessen et al., 2009). In MRS, short  $T_E$  allows the quantification of several metabolites as J-coupled spins such as Glu and glutamine (Gln) are easily detected. Additionally, STEAM sequences produce spectra with low spatial resolution whilst PRESS is prone to chemical shift artifacts.

This study, sponsored by APHP (ClinicalTrials.gov Identifier: NCT01470729), sought to test the reproducibility of metabolite concentrations using the semi-LASER sequence which has twice the SNR of STEAM and is less prone to chemical shift artifacts.

### **4.2 Materials and methods**

The study was carried out the Center for Magnetic Resonance Research (CMRR), Minnesota, USA and ICM, Paris, France. 24 healthy subjects from CMRR and 33 healthy subjects from ICM were recruited for the study. <sup>1</sup>H MRS data were collected at 3T with the semi-LASER sequence ( $T_R = 5000$  ms,  $T_E = 28$  ms, averages = 64, vector size = 2048, acquisition time = 6 min) in a  $10 \times 25 \times 25$  mm<sup>3</sup> in the cerebellar vermis,  $16 \times 16 \times 16$  mm<sup>3</sup> in the pons. Before spectra acquisition, the VOI were shimmed using FASTMAP. The RF power for the 90° asymmetric pulse and for water suppression were calibrated for each VOI. Outer volume suppression pulses were also included to eliminate contamination from other brain regions. Fully relaxed unsuppressed water signals were acquired at different  $T_E$  values in order to determine the CSF contribution to the VOI. Two unsuppressed water signals were also acquired for eddy current correction and phase correction.

Model basis sets were generated for spectra quantification with LCModel. Cramér-Rao lower bounds were used to estimate reliable metabolites to report.

### **4.3 Results**

Shimming in the pons proved to be a challenge in some instances. The semi-LASER sequence generated very good quality spectra with many metabolites. Using the same sequence and quantification procedures, we obtained similar neurochemical profiles in both control groups, which underlined the robustness of our method.

### **4.5 Published article**



# Two-Site Reproducibility of Cerebellar and Brainstem Neurochemical Profiles With Short-Echo, Single-Voxel MRS at 3T

Dinesh K. Deelchand,<sup>1\*</sup> Isaac M. Adanyeguh,<sup>2</sup> Uzay E. Emir,<sup>1</sup> Tra-My Nguyen,<sup>2</sup> Romain Valabregue,<sup>2,3,4</sup> Pierre-Gilles Henry,<sup>1</sup> Fanny Mochel,<sup>2,4,5,6</sup> and Gülin Öz<sup>1</sup>

**Purpose:** To determine whether neurochemical concentrations obtained at two MRI sites using clinical 3T scanners can be pooled when a highly optimized, nonvendor short-echo, single-voxel proton MRS pulse sequence is used in conjunction with identical calibration and quantification procedures.

**Methods:** A modified semi-LASER sequence ( $T_E = 28$  ms) was used to acquire spectra from two brain regions (cerebellar vermis and pons) on two Siemens 3T scanners using the same  $B_0$  and  $B_1$  calibration protocols from two different cohorts of healthy volunteers ( $N = 24$ – $33$  per site) matched for age and body mass index. Spectra were quantified with LCModel using water scaling.

**Results:** The spectral quality was very consistent between the two sites and allowed reliable quantification of at least 13 metabolites in the vermis and pons compared with 3–5 metabolites in prior multisite magnetic resonance spectroscopy trials using vendor-provided sequences. The neurochemical profiles were nearly identical at the two sites and showed the feasibility to detect interindividual differences in the healthy brain.

**Conclusion:** Highly reproducible neurochemical profiles can be obtained on different clinical 3T scanners at different sites, provided that the same, optimized acquisition and analysis techniques are used. This will allow pooling of multisite data in

clinical studies, which is particularly critical for rare neurological diseases. *Magn Reson Med* 73:1718–1725, 2015. © 2014 Wiley Periodicals, Inc.

**Key words:** 3 Tesla; multi-site; reproducibility; spectroscopy

## INTRODUCTION

Proton MR spectroscopy ( $^1\text{H}$  MRS) is a noninvasive tool that allows the measurement of a wide range of biochemical compounds in the brain in both health and disease. The method has been demonstrated to be valuable in the evaluation of several common disorders of the central nervous system, including tumors, neonatal hypoxia-ischemia, inherited metabolic diseases, demyelinating disorders, and infectious brain lesions (1). Because metabolic alterations are thought to precede structural changes, magnetic resonance spectroscopy (MRS) is likely to provide dynamic biomarkers of neuronal dysfunction at an earlier stage of disease progression than structural MRI. This is of even greater importance for therapeutic approaches for which a neuroprotective effect is expected. However, unlike structural MRI, MRS has not gained widespread acceptance as a routine clinical tool for diagnostic and prognostic purposes (2,3). This is partially due to the relatively large variation in metabolite concentrations or ratios reported from different sites (4–9).

As higher magnetic fields are becoming routinely available, the increased sensitivity and resolution they provide can benefit metabolite quantification (10–12) and facilitate robust clinical applications of the technique. However, with this potential, the need to standardize robust MRS acquisition and analysis methods is critical, as also emphasized by the recent MRS Consensus Group study (1). Such standardized MRS methodology would allow pooling of data from multiple sites, which is particularly important for clinical research and clinical trials in rare diseases. Prior multisite MRS trials primarily have used vendor-provided MRS sequences (PRESS and STEAM) and were able to quantify 3–5 metabolites—such as *N*-acetylaspartate (NAA), total creatine (tCr), total choline (tCho), and *myo*-inositol (Ins)—at both 1.5T and 3T (6–9).

Recently, optimized short-echo sequences such as SPECIAL (12) and semi-LASER (13) were implemented on clinical platforms, thereby allowing an extended

<sup>1</sup>Center for Magnetic Resonance Research, Department of Radiology, University of Minnesota, Minneapolis, Minnesota, USA.

<sup>2</sup>INSERM UMR S975, Brain and Spine Institute, Hospital La Salpêtrière, Paris, France.

<sup>3</sup>Institut du Cerveau et de la Moelle, Centre de Neuroimagerie de Recherche, Hôpital La Salpêtrière, Paris, France.

<sup>4</sup>University Pierre and Marie Curie, Paris, France.

<sup>5</sup>AP-HP, Department of Genetic, Hospital La Salpêtrière, Paris, France.

<sup>6</sup>Neurometabolic Unit, Hospital La Salpêtrière, Paris, France.

Grant sponsor: National Institute of Neurological Disorders and Stroke; Grant number: R01 NS070815; Grant sponsor: Assistance Publique des Hôpitaux de Paris and the program “Investissements d’avenir”; Grant number: ANR-10-IAIHU-06; Grant sponsor: National Center for Research Resources; Grant number: P41 RR008079 (CMRR); Grant sponsor: National Institute of Biomedical Imaging and Bioengineering; Grant number: P41 EB015894 (CMRR); Grant sponsor: Institutional Center Cores for Advanced Neuroimaging; Grant number: P30 NS076408 (CMRR).

\*Correspondence to: Dinesh K. Deelchand, Ph.D., Center for Magnetic Resonance Research, University of Minnesota, 2021 6<sup>th</sup> St SE, Minneapolis, MN 55455, USA. E-mail: dinesh@cmrr.umn.edu

Additional Supporting Information may be found in the online version of this article.

Current address for Uzay E. Emir: Oxford Centre for Functional MRI of the Brain, John Radcliffe Hospital, University of Oxford, Headington, Oxford OX3 9DU, UK.

Received 3 December 2013; revised 8 April 2014; accepted 25 April 2014

DOI 10.1002/mrm.25295

Published online 19 June 2014 in Wiley Online Library (wileyonlinelibrary.com).

Table 1  
Demographics and Spectroscopic Parameters Measured in Two Brain Regions

	CMRR	ICM	$P^a$
Subjects scanned ( $N$ )	24	33	
Sex (male/female)	13/11	15/18	0.52 <sup>b</sup>
Age (years)	53 ± 15	48 ± 13	0.19
BMI (kg/m <sup>2</sup> )	26 ± 6	25 ± 4	0.47
Vermis	$n = 24$	$n = 33$	
Water linewidth (Hz)	8 ± 1	7 ± 1	0.06
$T_2$ tissue water (ms)	80 ± 8	80 ± 7	0.93
CSF fraction (%)	11 ± 5	9 ± 4	0.04
SNR of NAA <sup>c</sup>	56 ± 5	59 ± 9	0.21
Pons	$n = 16$	$n = 23$	
Water linewidth (Hz)	8 ± 1	8 ± 1	0.57
$T_2$ tissue water (ms)	67 ± 4	68 ± 2	0.34
CSF fraction (%)	1 ± 1	2 ± 2	0.16
SNR of NAA <sup>c</sup>	27 ± 5	28 ± 6	0.49

Values are presented as the mean ± standard deviation.

<sup>a</sup>Unpaired, two-tailed Student's  $t$  test except when noted otherwise.

<sup>b</sup>Chi-squared test.

<sup>c</sup>SNR was measured in the frequency domain (defined as peak height divided by 2 times root mean square noise), and no apodization functions were applied to the data.

neurochemical profile consisting of both singlet and  $J$ -coupled metabolites to be measured. Therefore, there is a need to determine the between-site reproducibility of such profiles.

The aim of the present study was to examine the reproducibility of metabolite concentrations measured in two brain regions using a short-echo, single-shot, full-intensity sequence with identical experimental protocols at two different sites on clinical 3T scanners. A previously described semi-LASER sequence (14) was used to achieve lower apparent  $T_2$  relaxation, minimal  $J$ -coupling evolution, and smaller chemical shift displacement errors relative to the standard PRESS sequence. Two relatively challenging brain regions were chosen for this two-site comparison: the cerebellar vermis and pons (15).

## METHODS

Two 3T whole-body Siemens Tim Trio (Siemens Medical Solutions, Erlangen, Germany) scanners were used in this study; one located at the Center for Magnetic Resonance Research (CMRR) in Minnesota and the other one at the Institut du Cerveau et de la Moelle (ICM) in Paris. Healthy subjects who were matched for age and body mass index (Table 1) were enrolled after giving informed consent according to procedures approved by the Institutional Review Board at CMRR and by the local ethics committee at ICM. The standard body radiofrequency (RF) coil was used for RF transmission, and the 32-channel phased-array Siemens head coil was used for signal reception. Soft pads were used to hold each subject's head in place to minimize head movement in the MR system.  $T_1$ -weighted MPRAGE images (repetition time [ $T_R$ ] = 2530 ms; echo time [ $T_E$ ] = 3.65 ms; flip angle = 7°; slice thickness = 1 mm; 224 slices; field-of-view = 256 × 176 mm<sup>2</sup>; matrix size = 256 × 256) were acquired to position the volume-of-interest (VOI) for

MRS measurements.  $B_0$  shimming was achieved using an adiabatic version of FAST(EST)MAP (16), which is available as a work-in-progress (WIP) package on the Siemens system.

Proton spectra were acquired using a modified semi-LASER sequence ( $T_E = 28$  ms;  $T_R = 5$  s; 64 averages) (14) from two VOIs: the cerebellar vermis (10 × 25 × 25 mm<sup>3</sup>) and pons (16 × 16 × 16 mm<sup>3</sup>). Voxel placement was based on anatomical landmarks. The fourth ventricle, cervical spinal cord and the brainstem were used to separate the cerebellum. The surfaces, lobes, lobules, and fissures of the cerebellum were then used as landmarks in positioning the voxel in the vermis. For pons VOI placement, the midbrain, fourth ventricle, and medulla were used as landmarks.

The semi-LASER sequence (14) used in this study is a more compact version of the originally published semi-LASER sequence (17). Briefly, the sequence consisted of a 2-ms asymmetric slice-selective 90° pulse (18) followed by two pairs of slice selective adiabatic full passage pulses (4 ms duration, HS4 modulation, R25) (19), which were interleaved, rather than applied sequentially, to improve suppression of unwanted coherences with shorter spoiler gradient pulses. Water suppression was achieved with VAPOR, which was interleaved with outer volume suppression (OVS) to suppress unwanted coherences (18). A substantially lower chemical shift displacement error is obtained with the semi-LASER sequence (3.6% /ppm for the slice-selective 90° pulse and 2% /ppm for the adiabatic full passage pulses) compared with the standard PRESS sequence provided on the Siemens platform (12%–13% /ppm).

$B_1$  levels required for localization pulses and for water suppression were adjusted for each voxel. Specifically, the RF power magnitude for the 90° asymmetric pulse was calibrated by monitoring the signal intensity while increasing the RF power and choosing the RF power setting that produced the maximum signal. The power for the adiabatic full passage pulses was automatically set relative to the 90° pulse. A similar procedure was performed for the water suppression calibration.

On the scanner, signals from individual coil elements were combined after correcting for phase shifts between elements and weighting them based on the coil sensitivities (20) to generate a free induction decay. Each free induction decay was then individually saved for shot-to-shot frequency and phase correction before averaging. Two nonsuppressed water spectra were acquired: one for eddy current correction (the RF pulses of the VAPOR scheme were turned off) and one for use as reference for metabolite quantification (VAPOR and OVS schemes turned off in order to eliminate magnetization transfer effects). To evaluate the cerebrospinal fluid (CSF) contribution to each VOI, fully relaxed unsuppressed water signals were acquired at different  $T_E$ s ranging from 28–4000 ms ( $T_R = 15$  s) with the entire VAPOR and OVS scheme turned off (21).

All spectral processing was performed in MATLAB by the same investigator prior to LCModel fitting. Eddy current correction was performed first to correct for distorted line shapes and zero-order phase. Individual shots affected by subject motion (based on water suppression

efficiency) were removed. Single-shot frequency correction was performed using a cross-correlation algorithm and phase correction was performed using a least-square fit algorithm. All steps were completely automated except for the removal of free induction decays affected by motion. Finally, the summed spectrum was referenced based on NAA resonance at 2.01 ppm.

Spectra were then analyzed with LCModel (22) with the water scaling option (version 6.3-0G). The model basis set was generated based on density matrix formalism as described previously (23). The basis set also included macromolecule spectra, which were acquired using an inversion-recovery technique in four healthy subjects (total averages = 928;  $T_R = 2.5$  s; inversion time = 0.75 s; VOI = 15.6 mL; 5 ms duration HS5 inversion pulse; occipital cortex). Due to the shorter  $T_1$  relaxation time of the methylene protons of tCr at 3.93 ppm relative to other metabolite protons (24), this resonance was present in the metabolite-nulled macromolecule spectra and was removed using a Hankel singular value decomposition algorithm in MATLAB. A 12.5-Hz Gaussian line broadening was also applied to the macromolecule spectra after incorporating a reference peak at 0 ppm (Supporting Information). No baseline correction, zero-filling, or apodization functions were applied to the in vivo data prior to the analysis. LCModel fitting (Supporting Information) was performed over the spectral range from 0.5 to 4.2 ppm.

Metabolite concentrations were determined after correcting for tissue water content and CSF contributions in the selected VOI using the water-scaling option in LCModel. The transverse relaxation times ( $T_2$ ) of tissue water and percent CSF contribution to the VOI were obtained by fitting the integrals of the unsuppressed water spectra acquired in each VOI at different  $T_E$  values with a biexponential fit (21), with the  $T_2$  of CSF fixed at 740 ms based on measurement of  $T_2$  of water in a small voxel located in ventricles with the same semi-LASER sequence (four healthy subjects;  $T_R = 15$  s; VOI = 0.125–0.360 mL; 12  $T_E$  values ranging from 28 to 4000 ms), and three free parameters:  $T_2$  of tissue water, amplitude of tissue water, and amplitude of CSF water.

In order to obtain accurate metabolite concentrations, corrections must be made for  $T_2$  relaxation of both water and metabolites. In the case of semi-LASER,  $T_2$  relaxation is slowed due to the Carr-Purcell (CP) conditions, and  $T_2$  values under CP conditions must be used for quantification. For water, these values can be estimated by correcting the free precession  $T_2$  value measured for the tissue water signal at different echo times by a fixed factor to account for CP effects. A previous study compared water  $T_2$  values measured with LASER and CP-LASER sequences at 4T and 7T (25). Extrapolating from that study, we assumed that the  $T_2$  of water under CP conditions is  $1.5 \times$  longer than the measured free precession  $T_2$  at 3T. Signal loss due to  $T_2$  relaxation of metabolites was neglected, since the apparent  $T_2$  is sequence-dependent. This assumption is justified by the fact that metabolites have longer  $T_2$  such that correction factors would be small at  $T_E = 28$  ms. Nonetheless, this choice will result in somewhat underestimated metabolite concentrations relative to the true concentrations in tissue.

A water content of 82% and 72% was used for the vermis and pons, respectively (26,27).

Metabolites that were quantified with Cramér-Rao lower bounds (CRLB)  $\leq 50\%$  from at least half of the spectra from a particular brain region were included in the neurochemical profile. In addition, if the correlation between two metabolites was very high (i.e., if the correlation coefficient  $r$  was more negative than  $-0.7$ ) in the majority of the spectra from a region, then only their sum was reported (e.g., tCr [creatine + phosphocreatine] and tCho [glycerophosphorylcholine + phosphorylcholine]). If there was indication for pairwise correlation with  $r$  from  $-0.5$  to  $-0.7$ , then the concentration sum of the pair was reported in addition to the individual metabolites' concentrations (e.g., NAA, NAAG and total NAA [tNAA, NAA + NAAG]), as recommended by the LCModel manual (22). Moreover, spectra with the associated water reference linewidth greater than 10 Hz were excluded due to trends observed in overestimating aspartate and ascorbate and underestimating glutamate in these spectra. Water linewidths  $>10$  Hz only occurred for spectra acquired from the pons region.

## RESULTS

Using the modified semi-LASER sequence with identical parameters and identical  $B_0$  and  $B_1$  calibration protocols on two 3T scanners, consistently high quality  $^1\text{H}$  spectra with comparable peak signal-to-noise ratio (SNR) were obtained at both sites (Fig. 1A, Table 1). No noticeable baseline distortions due to insufficient water suppression or contamination by signals from outside the voxel, such as out-of-phase lipids, were observed. The peak SNR in the pons was lower than in the vermis due to the smaller voxel size and lower sensitivity of the receive coil in this particularly deep brain region. Examples of LCModel fits obtained in both regions are illustrated in Figure 1B. No obvious residual was observed around the 0.9 to 2 ppm region, suggesting that the macromolecule spectrum acquired from the occipital cortex is appropriate when fitting spectra from vermis and pons. This finding is consistent with a recent study (28), which showed that the differences in macromolecule signal between gray and white matter regions are relatively small and concluded that a general macromolecule baseline provides sufficiently accurate neurochemical profiles.

At CMRR, pons data were not collected from three subjects due to poor  $B_0$  shimming in two cases and subject movement in one case and five spectra were rejected due to the broad linewidth criteria. Similarly at ICM, pons data from eight subjects were not acquired due to poor shimming and two spectra were rejected due to broad water linewidth. This was consistent with the known challenges with shimming in the brainstem (29) due to the presence of the sphenoid sinus. All spectra from the vermis were used in the final results (Table 1). Motion effects were minimal in this cohort of healthy volunteers and only one single-shot in the vermis (out of 64) was excluded from the sum in one subject due to motion.

No statistical differences were observed in the spectral quality metrics (i.e., water peak linewidth and SNR), as

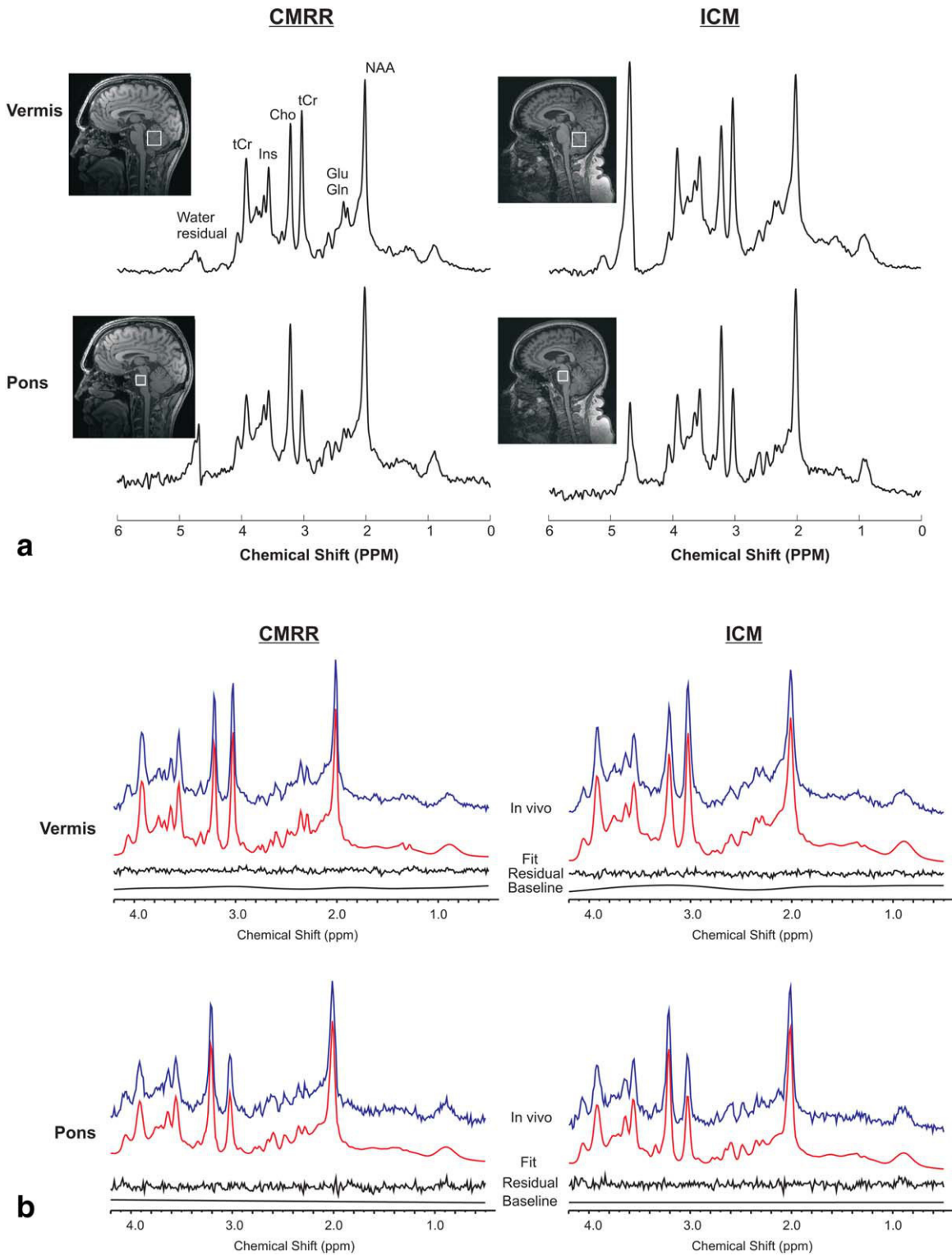


FIG. 1. **a:** Typical proton spectra obtained from the cerebellar vermis and pons in two different subjects at the two sites using semi-LASER ( $T_E = 28$  ms,  $T_R = 5$  s, 64 averages) at 3T. The locations of the VOI are shown on the  $T_1$ -weighted images. Spectra were processed with a 1-Hz exponential decay and 5-Hz Gaussian functions. Comparable spectral quality and pattern are apparent for each region at both sites. **b:** LCMODEL fits of the spectra shown in panel A without any apodization functions. Top to bottom: the in vivo spectrum, the fit, the residual after subtracting the fit from the in vivo spectrum, and the baseline.

well as tissue water  $T_2$  values between the two sites in both brain regions (Table 1). CSF fraction was found to be slightly higher in the vermis VOI from CMRR relative to

ICM ( $P = 0.04$ ). As expected, the  $T_2$  of tissue water in pons was shorter compared with that in vermis consistent with the fact that pons consists mainly of white matter (30).

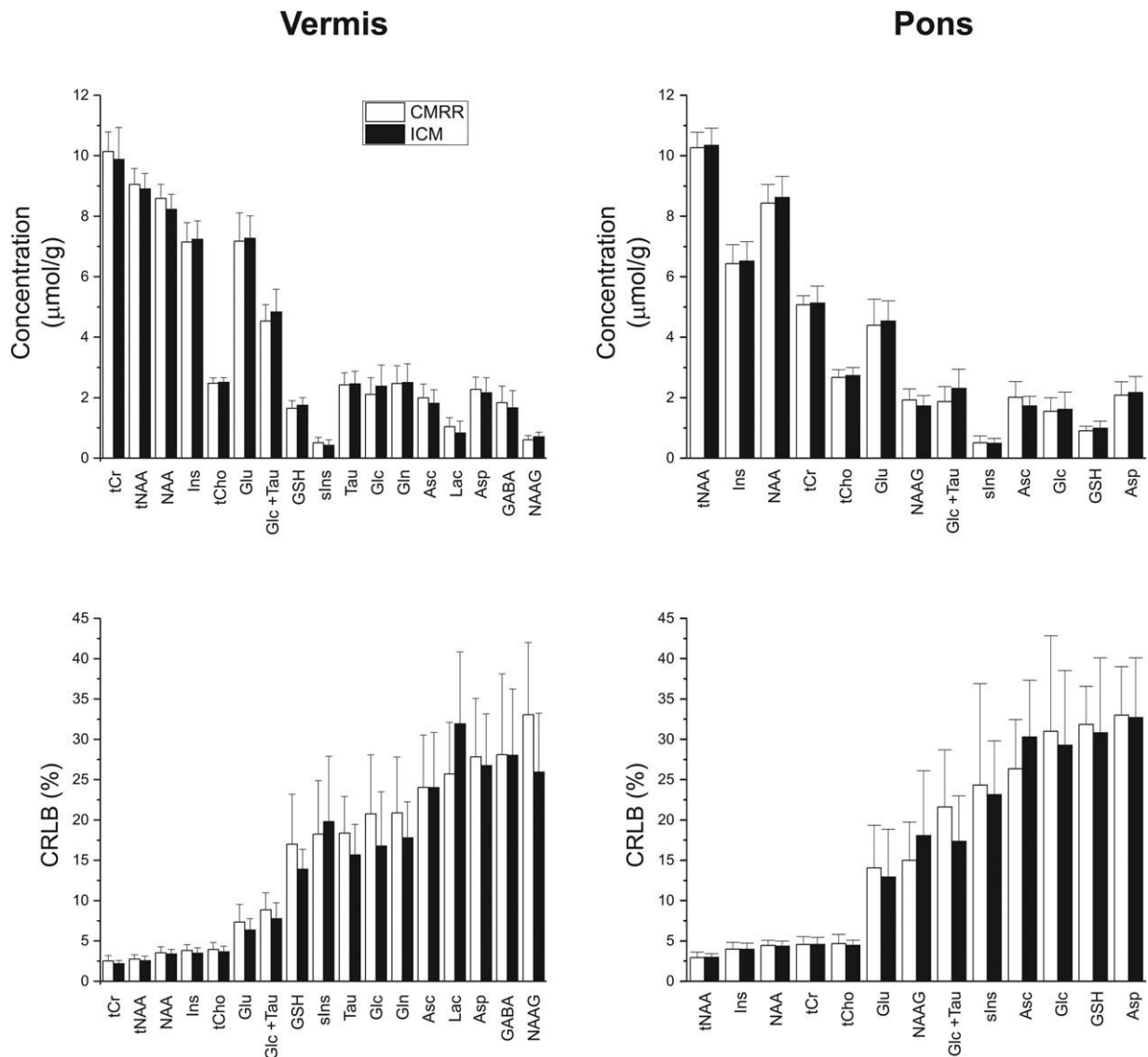


FIG. 2. Mean metabolite concentrations (in  $\mu\text{mol/g}$ ) and CRLB (in %) measured in the cerebellar vermis ( $n = 24$  at CMRR,  $n = 33$  at ICM) and pons ( $n = 16$  at CMRR,  $n = 23$  at ICM) at the two sites. Error bars represent intersubject standard deviations. Asc, ascorbate; Asp, aspartate; GABA,  $\gamma$ -aminobutyric acid; Glc, glucose; Gln, glutamine; Glu, glutamate; GSH, glutathione; Ins, *myo*-inositol; Lac, lactate; NAAG, *N*-acetylaspartylglutamate; slns, *scyllo*-inositol; Tau, taurine; tCho, total choline; tCr, total creatine; tNAA, total *N*-acetylaspartate.

Using the unsuppressed water signal as an internal concentration reference and after correcting for  $T_2$  relaxation of water, tissue water and CSF contributions, the concentrations of 17 metabolites were determined in the vermis using the reliability criteria described in the Methods. Due to lower SNR and higher cross-correlation between metabolites in the pons compared with the vermis (Supporting Information), 13 concentrations passed the same criteria in the pons (Fig. 2).

The neurochemical profiles of the two brain regions were nearly identical between the two sites (Fig. 2, Table 2). A comparison of the metabolite concentrations from ICM and CMRR in each brain region (i.e., vermis and pons) revealed no statistically significant difference between the two sites via analysis of variance. Similarly,

no differences were observed in the metabolite quantification precision (as determined by CRLB) between the sites (Fig. 2), as expected based on the similar spectral quality (Table 1). In the vermis, the mean CRLB for all singlets (NAA, tNAA, tCr, and tCho), Ins, Glu, and Glc + Tau was less than 10% with the other metabolites having mean CRLBs  $<35\%$ . In the pons, NAA, tNAA, tCr, tCho, and Ins were quantified with a mean CRLB  $<5\%$ , with other metabolites having mean CRLBs smaller than 35%.

When the relationship between the mean CRLB and between-subject coefficients of variance (CV, mean and standard deviation) was investigated for each brain region and each site (Fig. 3), the CRLBs were consistently lower than between-subject CV for the most reliably quantified metabolites (CRLB  $<12\%$ ). For example,

Table 2  
Mean  $\pm$  SD Metabolite Concentrations (in  $\mu\text{mol/g}$ ) Measured in the Cerebellar Vermis and Pons at the Two Sites

Metabolite	Vermis		Pons	
	CMRR	ICM	CMRR	ICM
tCr	10.1 $\pm$ 0.7	9.9 $\pm$ 1.1	5.1 $\pm$ 0.3	5.1 $\pm$ 0.6
tNAA	9.1 $\pm$ 0.5	8.9 $\pm$ 0.5	10.3 $\pm$ 0.5	10.3 $\pm$ 0.6
NAA	8.6 $\pm$ 0.5	8.2 $\pm$ 0.5	8.4 $\pm$ 0.6	8.6 $\pm$ 0.7
Ins	7.1 $\pm$ 0.6	7.2 $\pm$ 0.6	6.4 $\pm$ 0.6	6.5 $\pm$ 0.6
tCho	2.5 $\pm$ 0.2	2.5 $\pm$ 0.1	2.7 $\pm$ 0.3	2.7 $\pm$ 0.3
Glu	7.2 $\pm$ 0.9	7.3 $\pm$ 0.7	4.4 $\pm$ 0.9	4.5 $\pm$ 0.7
Glc+Tau	4.5 $\pm$ 0.5	4.8 $\pm$ 0.8	1.9 $\pm$ 0.5	2.3 $\pm$ 0.6
GSH	1.6 $\pm$ 0.3	1.7 $\pm$ 0.3	0.9 $\pm$ 0.2	1.0 $\pm$ 0.2
sIns	0.5 $\pm$ 0.2	0.4 $\pm$ 0.2	0.5 $\pm$ 0.2	0.5 $\pm$ 0.2
Tau	2.4 $\pm$ 0.4	2.5 $\pm$ 0.4		
Glc	2.1 $\pm$ 0.6	2.4 $\pm$ 0.7	1.5 $\pm$ 0.5	1.6 $\pm$ 0.6
Gln	2.5 $\pm$ 0.6	2.5 $\pm$ 0.6		
Asc	2.0 $\pm$ 0.5	1.8 $\pm$ 0.4	2.0 $\pm$ 0.5	1.7 $\pm$ 0.3
Lac	1.0 $\pm$ 0.3	0.8 $\pm$ 0.4		
Asp	2.3 $\pm$ 0.4	2.2 $\pm$ 0.5	2.1 $\pm$ 0.4	2.2 $\pm$ 0.5
GABA	1.8 $\pm$ 0.5	1.7 $\pm$ 0.6		
NAAG	0.6 $\pm$ 0.1	0.7 $\pm$ 0.2	1.9 $\pm$ 0.4	1.9 $\pm$ 0.4

the between-subject CVs for tCr, tNAA, tCho, NAA, and Ins were in the range of 6%–12% in both the vermis and pons, whereas their CRLBs were in the range of 2%–5%, indicating that the method has precision to detect interindividual differences in these metabolites in the healthy brain (Fig. 3, right). For other metabolites, between-subject CVs and CRLBs were more comparable (metabolites that fall around the identity line in Figure 3), indicating the measurement errors were comparable to or higher than physiological, interindividual differences.

**DISCUSSION**

This study demonstrates that nearly identical neurochemical profiles consisting of 13–17 metabolites are obtained in two different brain regions in relatively large healthy cohorts by different operators at two MR sites.

The acquisition of high-quality MRS data from the cerebellum and brainstem is particularly challenging due to their caudal location in the head and broader intrinsic linewidths relative to other cerebral VOI (14,15). We were able to obtain high-quality MRS data in a dual-site setting due the consistency of obtaining artifact-free short  $T_E$  spectra using an in-house developed and highly optimized pulse sequence and identical  $B_0$  and  $B_1$  adjustment protocols.

The relative metabolite concentrations within and between the two VOIs were consistent with previous publications (14,31–34). Note that the concentrations reported are slightly underestimated relative to their true tissue values since the effects of  $T_2$  relaxation for metabolites were not taken into account. This approach was chosen since apparent  $T_2$ s are pulse sequence-dependent (35), brain region-dependent (24) (see also water  $T_2$ s in Table 1), and metabolite-dependent (36). While it is relatively straightforward to measure the water  $T_2$  in each VOI from all volunteers, acquisition of region-specific  $T_2$ s for all metabolites in the reported profiles was both outside the scope of this project and is not feasible in routine clinical applications. Alternatively, a single correction factor could be identified based on literature values for a different pulse sequence; however, this would almost certainly be inaccurate for most metabolites reported. Note, however, that the systematic bias in metabolite concentrations resulting from omission of the metabolite  $T_2$  correction is inconsequential for multisite investigations provided that the same assumptions are used in the analysis of all data.

Almost all multisite trials on clinical scanners so far have only reported the concentrations or concentration ratios of tNAA, tCr, tCho, and Ins (the latter only measured at short  $T_E$ ) using  $^1\text{H}$  spectra measured at short or long echo-times (6–9). Although the  $T_E$  of semi-LASER used in this study is comparable to that of the vendor-provided PRESS sequence (shortest  $T_E$  of 30 ms), the presence of the two pairs of  $180^\circ$  adiabatic pulses, which act as a Carr-Purcell pulse train, helps to preserve the  $J$ -modulation and signal intensity of metabolites (37). As such, the semi-LASER sequence enabled the

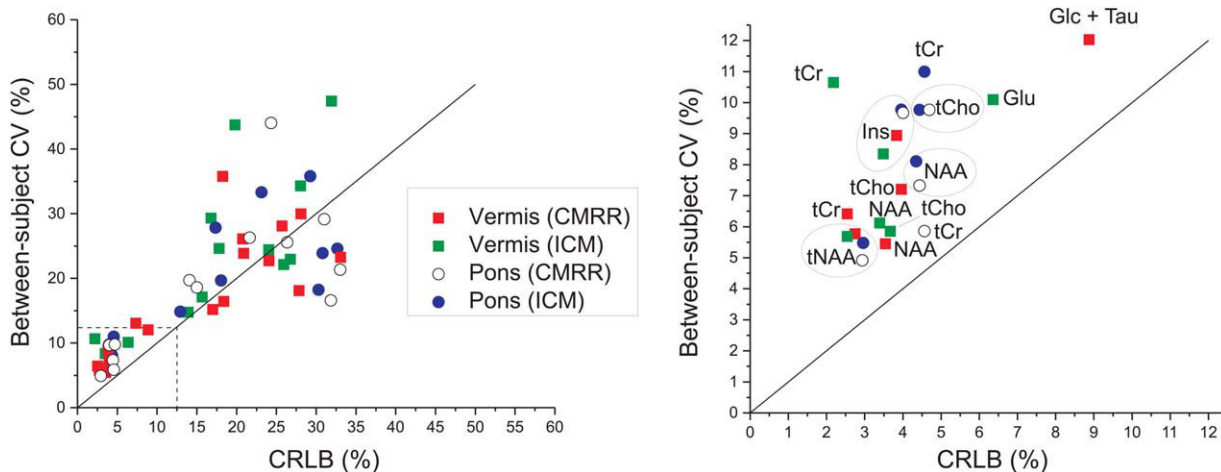


FIG. 3. Relationship between mean CRLB and between-subject CV for all metabolites reported in Figure 2: CV and CRLB  $\leq$ 50% (left) and zoomed CV and CRLB between 0 and 12.5% (right). The solid line represents the identity line.

quantification of at least 13 metabolites in the pons and vermis at each site, thereby showing the feasibility of consistently measuring *J*-coupled metabolites in addition to singlet metabolites between different sites.

Multisite trials utilizing  $^1\text{H}$  MRS have been challenging due to large variations in reported metabolite concentrations between sites, even within each site. In such investigations the within-site CVs ranged between 2% and 30% and between-site CVs were between 2% and 35% for singlet metabolites (5,6,9). These reproducibility issues might be related to various factors such as the quality of the raw spectral data, number of subjects studied, reference used for quantification, or the stability of the MR scanner. On the other hand, multisite studies that have used metabolite ratios (e.g., tNAA/tCr or tNAA/tCho) have reported lower within-site CV of less than 10% (38,39). Although quantifying ratios does not require corrections for  $T_2$  and water content and therefore is easier, it does not provide a clear understanding on how individual metabolites change under different pathological conditions. For instance, tCr concentration, which is generally used as an internal reference, was reported to change in various neurological conditions (40,41).

In the present study, we took the more challenging approach of water scaling (also referred to as “absolute” quantification). The within-site CV for singlet metabolite concentrations was between 6% and 12% (Fig. 3), which lies in the lower end of the CV range reported in prior multisite investigations. Furthermore, the mean CRLBs, which indicate quantification precision, were substantially lower (3%–5%) than CVs for these metabolites, indicating that the CV is dominated by between-subject differences rather than measurement errors. This demonstrates the feasibility of detecting interindividual differences in the healthy brain at high field, consistent with our prior experience at 4T and 7T (11). Similarly, a recent two-site 3T MRS imaging study using semi-LASER reported mean CRLBs of  $\leq 6\%$  for tNAA, tCr, tCho, and Ins in selected gray and white matter VOI in the cerebrum and also demonstrated lower within-subject variation in these metabolites than between-subject variation (13). No between-site CVs are reported in the present study, since different subjects were scanned at each site. However, since the percent difference in metabolite concentrations between sites was very small, the between-site CV is also expected to be low.

The semi-LASER sequence was developed and optimized (i.e., spoiler gradients and OVS parameters) at CMRR prior to the transfer to the ICM site. The only requirements to successfully run the spectroscopy sequence was to adjust the first- and second-order shims using FAST(EST)MAP and to calibrate the RF power required for the  $90^\circ$  and water suppression pulses. This step was done in each study for each VOI location because the standard slice-based voltage adjustment done by the scanner once at the beginning of the scanning session often under/overestimates the RF power required in the selected VOI. The MRS data acquired at the two sites using widely available commercial hardware demonstrates that nonvendor, ready-to-use MRS

sequences can be shared among sites, generating highly reproducible spectral quality. This is expected to facilitate robust, multisite MRS trials where large numbers of datasets can be acquired in a relatively short time.

The main limitation of the current study was that the reproducibility of neurochemical profiles was tested at two sites using an MR scanner and hardware from the same vendor. For more generalized conclusions, it is critical to investigate across-vendor reproducibility of neurochemical profiles in larger multisite investigations. Such efforts were reported recently in abstract form (42). Another limitation was the need to manually initiate the voxel-specific  $B_1$  calibrations; automating these steps as done in standard vendor-provided packages is feasible and will be important for seamless application in the clinical environment.

## CONCLUSION

This dual-site study shows that a wide range of metabolites (singlet and *J*-coupled) can be quantified on clinical 3T scanners with highly reproducible neurochemical profiles using an in-house developed and highly optimized pulse sequence. These profiles can be pooled in multisite investigations provided that the same acquisition and analysis techniques are used at all sites.

Furthermore, within each site, the between-subject coefficients of variance for singlet resonances and *myo*-inositol were substantially higher than their CRLBs, indicating precision to detect interindividual differences in the healthy brain.

## ACKNOWLEDGMENTS

We thank Diane Hutter for assistance with subject recruitment; Petr Bednařik for providing the measured  $T_2$  value of CSF; Ivan Tkáč for discussions about the LCMoDel control parameter choices; Lynn Eberly for chi-square statistics; and the staff of the Center for MR Research for maintaining and supporting the MR systems. Dinesh K. Deelchand, Isaac M. Adanyeguh, Fanny Mochel, and Gülin Öz contributed equally to the study.

## REFERENCES

1. Öz G, Alger J, Barker P, et al. Clinical proton MR spectroscopy in central nervous system disorders: the MRS Consensus Group. *Radiology* 2014;270:658–679.
2. Wattjes MP. Structural MRI. *International Psychogeriatrics* 2011; 23(Supplement S2):S13–S24.
3. Hentschel F, Kreis M, Damian M, Krumm B, Frolich L. The clinical utility of structural neuroimaging with MRI for diagnosis and differential diagnosis of dementia: a memory clinic study. *Int J Geriatr Psychiatry* 2005;20:645–650.
4. Komoroski RA, Kotrla KJ, Lemen L, Lindquist D, Diaz P, Foundas A. Brain metabolite concentration ratios in vivo: multisite reproducibility by single-voxel  $^1\text{H}$  MR spectroscopy. *Magn Reson Imaging* 2004; 22:721–725.
5. Traber F, Block W, Freymann N, et al. A multicenter reproducibility study of single-voxel  $^1\text{H}$ -MRS of the medial temporal lobe. *Eur Radiol* 2006;16:1096–1103.
6. Jessen F, Gur O, Block W, et al. A multicenter  $^1\text{H}$ -MRS study of the medial temporal lobe in AD and MCI. *Neurology* 2009;72:1735–1740.
7. Chard DT, Parker GJM, Griffin CMB, Thompson AJ, Miller DH. The reproducibility and sensitivity of brain tissue volume measurements derived from an SPM-based segmentation methodology. *J Magn Reson Imaging* 2002;15:259–267.

8. Keevil SF, Barbiroli B, Brooks JCW, et al. Absolute metabolite quantification by in vivo NMR spectroscopy: II. A multicentre trial of protocols for in vivo localised proton studies of human brain. *Magn Reson Imaging* 1998;16:1093–1106.
9. Vavasour I, Laule C, Meyers S, Mädler B, Harris T, Li D, Traboulsee A, MacKay A. Cross-site reproducibility of 1H-MRS. *Proc Intl Soc Mag Reson Med* 2010;18:2008.
10. Deelchand DK, Iltis I, Henry P-G. Improved quantification precision of human brain short echo-time 1H magnetic resonance spectroscopy at high magnetic field: a simulation study. *Magn Reson Med* 2014;72:20–25.
11. Tkac I, Oz G, Adriany G, Ugurbil K, Gruetter R. In vivo <sup>1</sup>H NMR spectroscopy of the human brain at high magnetic fields: metabolite quantification at 4T vs. 7T. *Magn Reson Med* 2009;62:868–879.
12. Mekle R, Mlynárik V, Gambarota G, Hergt M, Krueger G, Gruetter R. MR spectroscopy of the human brain with enhanced signal intensity at ultrashort echo times on a clinical platform at 3T and 7T. *Magn Reson Med* 2009;61:1279–1285.
13. Wijnen JP, van Asten JJA, Klomp DWJ, Sjobakk TE, Gribbestad IS, Scheenen TWJ, Heerschap A. Short echo time 1H MRSI of the human brain at 3T with adiabatic slice-selective refocusing pulses; reproducibility and variance in a dual center setting. *J Magn Reson Imaging* 2010;31:61–70.
14. Öz G, Tkac I. Short-echo, single-shot, full-intensity proton magnetic resonance spectroscopy for neurochemical profiling at 4 T: validation in the cerebellum and brainstem. *Magn Reson Med* 2011;65:901–910.
15. Öz G. MR spectroscopy in health and disease. In: Manto M, Gruol DL, Schmahmann JD, Koibuchi N, Rossi F, eds. *Handbook of the Cerebellum and Cerebellar Disorders*. Vol 1. New York, NY: Springer Dordrecht; 2013:713–733.
16. Gruetter R, Tkac I. Field mapping without reference scan using asymmetric echo-planar techniques. *Magn Reson Med* 2000;43:319–323.
17. Scheenen TWJ, Klomp DWJ, Wijnen JP, Heerschap A. Short echo time 1H-MRSI of the human brain at 3T with minimal chemical shift displacement errors using adiabatic refocusing pulses. *Magn Reson Med* 2008;59:1–6.
18. Tkac I, Starcuk Z, Choi IY, Gruetter R. In vivo <sup>1</sup>H NMR spectroscopy of rat brain at 1 ms echo time. *Magn Reson Med* 1999;41:649–656.
19. Tannus A, Garwood M. Improved performance of frequency-swept pulses using offset-independent adiabaticity. *J Magn Reson Series A* 1996;120:133–137.
20. Natt O, Bezkorovaynyy V, Michaelis T, Frahm J. Use of phased array coils for a determination of absolute metabolite concentrations. *Magn Reson Med* 2005;53:3–8.
21. Ernst T, Kreis R, Ross BD. Absolute quantitation of water and metabolites in the human brain. I. Compartments and water. *J Magn Reson Series B* 1993;102:1–8.
22. Provencher SW. Estimation of metabolite concentrations from localized in vivo proton NMR spectra. *Magn Reson Med* 1993;30:672–679.
23. Deelchand DK, Henry P-G, Ugurbil K, Marjanska M. Measurement of transverse relaxation times of J-coupled metabolites in the human visual cortex at 4 T. *Magn Reson Med* 2012;67:891–897.
24. Traber F, Block W, Lamerichs R, Gieseke J, Schild HH. <sup>1</sup>H metabolite relaxation times at 3.0 Tesla: measurements of T<sub>1</sub> and T<sub>2</sub> values in normal brain and determination of regional differences in transverse relaxation. *J Magn Reson Imaging* 2004;19:537–545.
25. Bartha R, Michaelis S, Merkle H, Adriany G, Andersen P, Chen W, Ugurbil K, Garwood M. In vivo <sup>1</sup>H<sub>2</sub>O T<sub>2</sub><sup>+</sup> measurement in the human occipital lobe at 4T and 7T by Carr-Purcell MRI: detection of microscopic susceptibility contrast. *Magn Reson Med* 2002;47:742–750.
26. Siegel GJ (ed.). *Basic neurochemistry: molecular, cellular and medical aspects*. Lippincott-Raven Publishers: Philadelphia, PA, 1999.
27. Randall L. Chemical topography of the brain. *J Biol Chem* 1938;124:481–488.
28. Schaller B, Xin L, Gruetter R. Is the macromolecule signal tissue-specific in healthy human brain? A 1H MRS study at 7 Tesla in the occipital lobe. *Magn Reson Med* 2014;72:934–940.
29. Pouwels PJW, Frahm J. Regional metabolite concentrations in human brain as determined by quantitative localized proton MRS. *Magn Reson Med* 1998;39:53–60.
30. Frahm J, Bruhn H, Gyngell ML, Merboldt KD, Hanicke W, Sauter R. Localized proton NMR spectroscopy in different regions of the human brain in vivo. Relaxation times and concentrations of cerebral metabolites. *Magn Reson Med* 1989;11:47–63.
31. Öz G, Hutter D, Tkac I, Clark HB, Gross MD, Jiang H, Eberly LE, Bushara KO, Gomez CM. Neurochemical alterations in spinocerebellar ataxia type 1 and their correlations with clinical status. *Mov Disord* 2010;25:1253–1261.
32. Baker EH, Basso G, Barker PB, Smith MA, Bonekamp D, Horska A. Regional apparent metabolite concentrations in young adult brain measured by 1H MR spectroscopy at 3 Tesla. *J Magn Reson Imaging* 2008;27:489–499.
33. Michaelis T, Merboldt KD, Bruhn H, Hanicke W, Frahm J. Absolute concentrations of metabolites in the adult human brain in vivo: quantification of localized proton MR spectra. *Radiology* 1993;187:219–227.
34. Mascalchi M, Brugnoli R, Guerrini L, Belli G, Nistri M, Politi LS, Gavazzi C, Lolli F, Argenti G, Villari N. Single-voxel long TE 1H-MR spectroscopy of the normal brainstem and cerebellum. *J Magn Reson Imaging* 2002;16:532–537.
35. Michaelis S, Garwood M, Zhu XH, DelaBarre L, Andersen P, Adriany G, Merkle H, Ugurbil K, Chen W. Proton T<sub>2</sub> relaxation study of water, N-acetylaspartate, and creatine in human brain using Hahn and Carr-Purcell spin echoes at 4T and 7T. *Magn Reson Med* 2002;47:629–633.
36. Xin L, Gambarota G, Mlynarik V, Gruetter R. Proton T<sub>2</sub> relaxation time of J-coupled cerebral metabolites in rat brain at 9.4 T. *NMR Biomed* 2008;21:396–401.
37. Allerhand A. Analysis of Carr-Purcell spin-echo NMR experiments on multiple-spin systems. I. The effect of homonuclear coupling. *J Chem Phys* 1966;44:1–9.
38. Currie S, Hadjivassiliou M, Wilkinson I, Griffiths P, Hoggard N. Magnetic resonance spectroscopy of the normal cerebellum: what degree of variability can be expected? *The Cerebellum* 2013;12:205–211.
39. Lee PL, Yiannoutsos CT, Ernst T, et al. A multi-center 1H MRS study of the AIDS dementia complex: validation and preliminary analysis. *J Magn Reson Imaging* 2003;17:625–633.
40. Vrenken H, Barkhof F, Uitdehaag BMJ, Castelijns JA, Polman CH, Pouwels PJW. MR spectroscopic evidence for glial increase but not for neuro-axonal damage in MS normal-appearing white matter. *Magn Reson Med* 2005;53:256–266.
41. Öz G, Iltis I, Hutter D, Thomas W, Bushara KO, Gomez CM. Distinct neurochemical profiles of spinocerebellar ataxias 1, 2, 6, and cerebellar multiple system atrophy. *The Cerebellum* 2011;10:208–217.
42. van de Bank BL, Emir UE, Boer VO, van Asten JJA, Wijnen JP, Kan HE, Öz G, Klomp DWJ, Scheenen TWJ. Multi-center reproducibility of short echo time single voxel 1H MRS of the human brain at 7T with adiabatic slice-selective refocusing pulses. *Proc Intl Soc Mag Reson Med* 2013:3982.



# Chapter 5

## Organisation:

<b>Study 4: Application of the validated <math>^1\text{H}</math> MRS protocol in SCAs.....</b>	<b>99</b>
5.1 Introduction and objectives .....	99
5.2 Materials and methods.....	99
5.4 Principal results .....	99
5.5 Published article .....	100

## **Study 4: Application of the validated <sup>1</sup>H MRS protocol in SCAs**

### **5.1 Introduction and objectives**

Many of the published MRS studies in SCAs were performed on 1.5T MR systems. Currently, 3T systems are becoming widely available in many hospitals. High field MR systems have the advantage of increasing the SNR of the spectra and enhancing the resolution of J-coupled metabolites. Furthermore, most studies focused on only one SCA type due to the rarity of the diseases. In addition, none of these studies with the exception of (Oz et al., 2010) used a validated protocol that is robust and proven to have high reproducibility.

In this BIOSCA study sponsored by APHP (ClinicalTrials.gov Identifier: NCT01470729), we sought to use the modified semi-LASER sequence to identify neurochemical changes in SCAs.

### **5.2 Materials and methods**

This study was conducted in subjects with similar age, sex and BMI: 33 healthy controls, 16 SCA1, 12 SCA2, 21 SCA3 and 12 SCA7 patients. Three-dimensional T<sub>1</sub>-weighted volumetric images (T<sub>R</sub> = 2530 ms, T<sub>E</sub> = 3.65 isotropic, field-of-view (FOV) = 256 x 240 mm<sup>2</sup>) for spatial normalization and localization of brain volumes. The choice of performing spectroscopy on the vermis and pons is due to the prominent atrophy of these two regions in SCAs. The acquisition, calibration and quantification steps are as described in study 3. The CRLB threshold was set at 20% and spectra with water linewidth > 10 Hz were excluded from the analysis.

### **5.4 Principal results**

We observed a decrease of the neuronal marker (NAA and Glu) and an increase of the glial marker (*myo*-Inositol; *myo*-Ins) and energetic marker (tCr). The increase in these metabolites may signify a compensatory mechanism in response to neuronal loss. Some neurochemicals correlated with the SARA score. Plotting the neurochemicals against each other allowed the

separation between patients with SCAs and controls. Principal component analysis was able to separate the metabolites and draw out the link between the significantly different neurometabolites and clinical parameters.

## **5.5 Published article**

## In Vivo Neurometabolic Profiling in Patients With Spinocerebellar Ataxia Types 1, 2, 3, and 7

Isaac M. Adanyeguh, MS,<sup>1</sup> Pierre-Gilles Henry, PhD,<sup>2</sup> Tra M. Nguyen, MS,<sup>1</sup> Daisy Rinaldi, PhD,<sup>1</sup> Celine Jauffret, MS,<sup>1</sup> Romain Valabregue, PhD,<sup>3</sup> Uzay E. Emir, PhD,<sup>2</sup> Dinesh K. Deelchand, PhD,<sup>2</sup> Alexis Brice, MD, PhD,<sup>1</sup> Lynn E. Eberly, PhD,<sup>4</sup> Gülin Öz, PhD,<sup>2</sup> Alexandra Durr, MD, PhD,<sup>1,5</sup> and Fanny Mochele, MD, PhD<sup>1,5\*</sup>

<sup>1</sup>INSERM U 1127, Sorbonne Universités, UPMC Univ Paris Institut du Cerveau et de la Moelle épinière, ICM, Paris, France

<sup>2</sup>Center for Magnetic Resonance Research, University of Minnesota, Minneapolis, MN, United States

<sup>3</sup>Center for Neuroimaging Research, Institut du Cerveau et de la Moelle épinière, Paris, France

<sup>4</sup>Division of Biostatistics, School of Public Health, University of Minnesota, Minneapolis, MN, USA

<sup>5</sup>Assistance Publique-Hôpitaux de Paris, Fédération de Génétique, La Pitié-Salpêtrière University Hospital, Paris, France

**ABSTRACT:** Spinocerebellar ataxias (SCAs) belong to polyglutamine repeat disorders and are characterized by a predominant atrophy of the cerebellum and the pons. Proton magnetic resonance spectroscopy (<sup>1</sup>H MRS) using an optimized semiadiabatic localization by adiabatic selective refocusing (semi-LASER) protocol was performed at 3 T to determine metabolite concentrations in the cerebellar vermis and pons of a cohort of patients with SCA1 (n = 16), SCA2 (n = 12), SCA3 (n = 21), and SCA7 (n = 12) and healthy controls (n = 33). Compared with controls, patients displayed lower total *N*-acetylaspartate and, to a lesser extent, lower glutamate, reflecting neuronal loss/dysfunction, whereas the glial marker, myoinositol (*myo*-Ins), was elevated. Patients also showed higher total creatine as reported in Huntington's disease, another polyglutamine repeat disorder. A strong correlation was found between the Scale for the Assessment and Rating of Ataxia and the neuro-metabolites in both affected regions of patients. Principal component analyses confirmed that neuronal metabo-

lites (total *N*-acetylaspartate and glutamate) were inversely correlated in the vermis and the pons to glial (*myo*-Ins) and energetic (total creatine) metabolites, as well as to disease severity (motor scales). Neurochemical plots with selected metabolites also allowed the separation of SCA2 and SCA3 from controls. The neurometabolic profiles detected in patients underlie cell-specific changes in neuronal and astrocytic compartments that cannot be assessed by other neuroimaging modalities. The inverse correlation between metabolites from these two compartments suggests a metabolic attempt to compensate for neuronal damage in SCAs. Because these biomarkers reflect dynamic aspects of cellular metabolism, they are good candidates for proof-of-concept therapeutic trials. © 2015 International Parkinson and Movement Disorder Society

**Key Words:** spinocerebellar ataxia; biomarker; movement disorders; NMR spectroscopy; neurochemical profile

Spinocerebellar ataxias (SCAs 1, 2, 3, 7) are polyglutamine repeat disorders inherited as an autosomal dominant trait. The cerebellum and the brainstem are

mainly affected in SCAs,<sup>1</sup> their atrophy being detectable several years before the predicted onset of motor symptoms.<sup>2</sup> Progressive ataxia is the prominent

\*Correspondence to: Dr. Fanny Mochele, Institut du Cerveau et de la Moelle épinière—Aile 4A, La Pitié-Salpêtrière University Hospital, 47 Bd de l'Hôpital—75013 Paris, France, E-mail: fanny.mochel@upmc.fr

**Funding agencies:** This study was supported by the Programme Hospitalier de Recherche Clinique (PHRC, AOM10094, NCT01470729) and the program "Investissements d'avenir" ANR-10-IAIHU-06. The Center for Magnetic Resonance Research is funded by the National Institute of Biomedical Imaging and Bioengineering (NIBIB) grant P41 EB015894 and the Institutional Center Cores for Advanced Neuroimaging award P30 NS076408. Additional support was received from the National Institute of Neurological Diseases and Stroke grant R01 NS070815.

**Relevant conflicts of interest/financial disclosures:** Nothing to report. Full financial disclosures and author roles may be found in the online version of this article.

**Received:** 12 September 2014; **Revised:** 28 December 2014; **Accepted:** 8 January 2015

Published online 15 March 2015 in Wiley Online Library (wileyonlinelibrary.com). DOI: 10.1002/mds.26181

**TABLE 1.** Demographic and spectroscopic parameters of all subjects

Variable	Control	SCA1	SCA2	SCA3	SCA7
No of participants	33	16	12	21	12
Sex (M/F)	15/18	9/7	7/5	9/12	6/6
Age (y)	48 ± 13	44 ± 16	45 ± 13	51 ± 12	46 ± 14
BMI (kg/m <sup>2</sup> )	25 ± 4	24 ± 6	26 ± 5	24 ± 4	23 ± 3
SARA score	0.7 ± 0.9	11.1 ± 6.2 <sup>c</sup>	12.6 ± 6.0 <sup>c</sup>	13.2 ± 7.1 <sup>c</sup>	9.2 ± 7.2 <sup>c</sup>
CAG length		47 ± 7	40 ± 3	69 ± 6	42 ± 5
Disease duration (y)		7 ± 7	10 ± 6	9 ± 5	9 ± 5
Lw vermis (Hz)	7.3 ± 0.6	6.4 ± 1.1 <sup>a</sup>	5.6 ± 1.1 <sup>c</sup>	6.6 ± 1.5 <sup>a</sup>	6.7 ± 1.2
Lw pons (Hz)	8.1 ± 0.9	8.0 ± 1.6	6.0 ± 1.5 <sup>c</sup>	7.6 ± 1.1	7.7 ± 0.8
SNR vermis	33 ± 6	31 ± 6	27 ± 5 <sup>b</sup>	31 ± 4	29 ± 4
SNR pons	21 ± 3	19 ± 3	16 ± 3 <sup>b</sup>	16 ± 3 <sup>c</sup>	18 ± 4
% CSF vermis	9 ± 4	20 ± 8 <sup>c</sup>	33 ± 10 <sup>c</sup>	22 ± 8 <sup>c</sup>	19 ± 8 <sup>c</sup>
% CSF pons	2 ± 2	2 ± 2	8 ± 5 <sup>c</sup>	3 ± 2	2 ± 1

SNR, signal-to-noise ratio; Lw, water linewidth; CSF, cerebrospinal fluid.

Data are presented as mean ± SD and compared by 1-way ANOVA with Dunnett correction.

<sup>a</sup>*P* < 0.05, represents significant difference between SCAs and controls.

<sup>b</sup>*P* < 0.01.

<sup>c</sup>*P* < 0.001.

symptom of all SCAs. In SCA1, SCA2, SCA3, and SCA7, ataxia is often accompanied by pyramidal signs, sensory disturbances, muscle wasting, and brainstem oculomotor signs.<sup>3</sup> Spinocerebellar ataxia 7 is clearly distinguished from all other SCAs by the invariable presence of pigmentary retinal dystrophy. Several scales exist to assess disease state, but the Scale for the Assessment and Rating of Ataxia (SARA) is the best studied and validated so far.<sup>4</sup> The SARA is, however, of no use in presymptomatic individuals and is also not able to identify subtle differences that can serve as endpoints in future therapeutic trials.<sup>5</sup> Because SCAs are rare, studying a large cohort with adequate power for clinical trials is a major hindrance.<sup>6</sup> Magnetic resonance spectroscopy (MRS) offers a non-ionizing and noninvasive approach for quantitative information on the relationship between metabolism and clinical function in patients with neurodegenerative diseases.<sup>7</sup> Moreover, MRS allows the identification of *in vivo* alterations in brain metabolite concentrations that are likely to occur before brain atrophy<sup>8</sup> and may be amended by early therapeutic intervention.

Changes in brain metabolites in SCAs have been previously studied with MRS but mainly on a 1.5-Tesla MR system, with smaller cohorts, and none included SCA7 patients.<sup>9-12</sup> Most of these studies only reported metabolite ratios, which complicate data interpretation.<sup>13,14</sup> A few MRS studies also have been implemented on a 4-Tesla MR system but only in SCA1, SCA2, and SCA6.<sup>15,16</sup> Furthermore, 4-Tesla systems are uncommon, and MRS data obtained in patients with SCAs on clinical 3 Tesla scanners, such as those now widely available in hospitals, are lacking. In this context, the purpose of our study was to identify *in vivo* metabolic biomarkers in a large cohort of patients with SCA1, SCA2, SCA3, and SCA7 on a 3-Tesla MR system commonly used in hospitals.

## Methods

Experimental procedures were approved by the local ethics committee (AOM10094, CPP Ile de France VI, Ref: 105-10). The MRS data were acquired on a 3-Tesla whole-body Siemens Magnetom Trio scanner (Siemens Medical Solutions, Erlangen, Germany). All participants were older than 18 y and signed a written informed consent before participating in the study.

### Patients and Controls

We recruited 16 patients with SCA1, 12 patients with SCA2, 21 patients with SCA3, and 12 patients with SCA7 as part of the BIOSCA study (NCT01470729). All patients underwent neurological examinations. Thirty-three healthy volunteers with no history of neurological diseases and with a median age, sex, and body mass index (BMI) similar to the patient groups were also recruited (Table 1). The SARA was used to evaluate the severity of the cerebellar ataxia.<sup>4</sup> The scale ranges from 0 (no cerebellar symptoms) to 40 (most severe cerebellar symptoms).

### MR Protocol

A modified semiadiabatic localization by adiabatic selective refocusing (semi-LASER) sequence was used for <sup>1</sup>H MRS.<sup>17</sup> This sequence provides approximately twice the signal-to-noise ratio (SNR) compared with the stimulated-echo acquisition mode (STEAM) sequence, is less prone to motion artifacts compared with the spin echo full-intensity-acquired localization (SPECIAL) sequence, and has the lowest chemical shift displacement artefact.<sup>18</sup> Three-dimensional *T1*-weighted volumetric images (*T<sub>R</sub>* = 2530 ms, *T<sub>E</sub>* = 3.65 ms, 1 mm isotropic, field-of-view (FOV) = 256 × 176 mm<sup>2</sup>, matrix size = 256 × 256) were acquired for spatial

normalization and localization of brain volumes. Shimming was performed on a  $25 \times 10 \times 25 \text{ mm}^3$  volume-of-interest (VOI) in the vermis, and a  $16 \times 16 \times 16 \text{ mm}^3$  VOI in the pons, using a fast automatic shimming technique with echo-planar signal trains using mapping along projections, FAST(EST)MAP.<sup>19</sup> The radiofrequency (RF) power for the  $90^\circ$  asymmetric pulse of the semi-LASER sequence and the variable pulse power and optimized relaxation delays (VAPOR) water suppression pulses were calibrated for each VOI. The power for the  $90^\circ$  excitation pulse also served as the basis for setting the power for the outer volume suppression (OVS) pulses. A Siemens 32-channel head coil was used to collect signals from the VOI in the vermis and pons of participants using the semi-LASER sequence ( $T_R = 5000 \text{ ms}$ ,  $T_E = 28 \text{ ms}$ , Averages = 64). The VAPOR water suppression pulses in combination with three-dimensional OVS pulses allowed for improved localization and water suppression performance. Two unsuppressed water spectra were acquired: one for eddy current correction (the radiofrequency pulses of the VAPOR scheme were turned off) and one for use as reference for metabolite quantification (VAPOR and OVS schemes turned off to eliminate magnetization transfer effects). Unsuppressed water spectra were also acquired at a series of  $T_E$  values ( $T_E = 28 - 4000 \text{ ms}$ ;  $T_R = 15,000 \text{ ms}$  for full relaxation) to evaluate the cerebrospinal fluid (CSF) contribution to the VOI.<sup>20</sup> The total acquisition time per voxel, including power calibrations, metabolite spectrum acquisition, and water reference acquisition for quantification and CSF evaluation, was approximately 20 min.

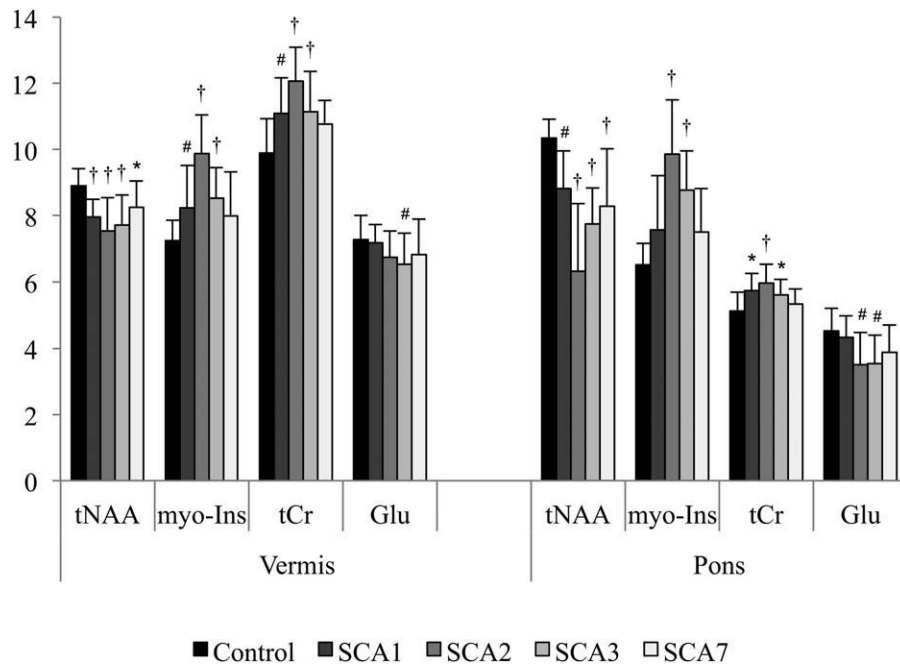
### Metabolite Quantification

Spectral processing and metabolite quantification were performed in the frequency domain using LCModel<sup>21</sup> as described previously.<sup>22</sup> The model spectra (basis set) were generated to include the following metabolites: alanine, ascorbate, aspartate, creatine,  $\gamma$ -aminobutyric acid, glycerophosphorylcholine, phosphorylcholine, phosphocreatine (PCr), glucose, glutamine, glutamate (Glu), glutathione (GSH), myoinositol (*myo*-Ins), *scyllo*-inositol, lactate, *N*-acetylaspartate (NAA), *N*-acetylaspartylglutamate (NAAG), phosphorylethanolamine (PE), taurine, and experimentally measured macromolecules, as illustrated in Supplemental Data eFigure 1. Preprocessing steps included shot-to-shot phase and frequency correction as well as eddy-current compensation using the unsuppressed water spectra acquired from the same VOI. Metabolite concentrations were obtained using water as an internal concentration reference. Concentrations were corrected for cerebrospinal fluid (CSF) content, determined by fitting the integrals of the unsuppressed water spectra at different  $T_E$  values with a bi-exponential fit.<sup>20</sup> Tissue water content was assumed at

82% for vermis and 72% for pons.<sup>23,24</sup> The  $T_2$  of CSF was fixed at 740 ms based on experimental measurement. The water signal at  $T_E = 28 \text{ ms}$  used as a concentration reference was corrected for signal loss caused by  $T_2$  relaxation. Because metabolites have longer  $T_2$  than water, the loss of signal caused by  $T_2$  relaxation of metabolites at  $T_E = 28 \text{ ms}$  was neglected.<sup>22</sup> Tissue concentrations of glucose and lactate were corrected for CSF contribution to the VOI assuming 3.2 mM glucose and 1.8 mM lactate in CSF.<sup>15</sup> Only metabolites quantified with mean Cramér-Rao lower bounds (CRLB), which are estimated errors of metabolite quantification, of 20% or less are reported. The 20% CRLB threshold allows the selection of the most reliably quantified metabolites, as outlined by the LCModel manual and the MRS Consensus Group.<sup>25,26</sup> We calculated and reported the average of all concentration values of reliably quantified metabolites, including values with high CRLB but excluding metabolites with CRLB = 999%. Only the sum of metabolites was reported if the correlation between two metabolites was consistently high (correlation coefficient  $< -0.7$ ) in a given region (eg, total creatine,  $tCr = Cr + PCr$ ). Similarly, when the correlation coefficient was in the range of  $-0.5$  to  $-0.7$ , the sum of the two correlated metabolites was reported in addition to the individual metabolites (eg, NAA, NAAG, and  $tNAA = NAA + NAAG$ ). Spectra with water linewidth greater than 10 Hz were excluded from data analysis. Approximately 3 min were required for preprocessing and quantification of each spectrum.

### Statistical Analysis

Participant characteristics, spectral quality, and metabolite concentrations—separately for the vermis and the pons—were analyzed using analysis of variance with a Dunnett multiple comparison test to compare each SCA type with the controls. For each SCA type separately, using those regions and metabolites showing significant SCA versus control differences, Pearson correlation was performed between the metabolite and SARA score, CAG repeat length, and disease duration; these *P* values were corrected for multiple testing using the step-down Bonferroni procedure,<sup>27</sup> separately for pons and vermis. Using patient data only, clinical characteristics and concentrations of metabolites that were significantly different in patients compared with controls were grouped into two principal components using principal component analysis (PCA). Principal component analysis was performed to investigate the global interaction between the selected metabolites and the clinical parameters across patient groups using XLSTAT. In addition, the metabolites that showed the largest differences between patients and controls were plotted against



**FIG. 1.** Mean concentrations of metabolites that showed significant differences in the vermis and the pons of patients with SCA1, 2, 3, 7 versus controls. *P* values represent Dunnett-corrected statistically significant differences between patients and controls differences (\**P* < 0.05; #*P* < 0.01; †*P* < 0.001). Lower neuronal markers tNAA and Glu in patients are associated with higher glial marker *myo*-Ins and higher-energy marker tCr. Error bars represent standard deviations (SDs). SCA, spinocerebellar ataxia; tNAA, *N*-acetylaspartate and *N*-acetylaspartylglutamate; Glu, glutamate; tCr, creatine + phosphocreatine.

each other to find ratios that could separate patient groups from the control group. A partial least squares discriminant analysis was also performed on the entire set of metabolites to identify the variables with class separation information using XLSTAT.

## Results

### Data Quality Control

Good quality spectra with a high SNR and excellent resolution were consistently obtained from both controls and patients. The SNR was 6% to 24% lower and water linewidth 1 to 2 Hz narrower in some patient groups than controls, likely because of the higher CSF fraction in patients' vermis and pons, especially in patients with SCA2 in whom cerebellar and brainstem atrophy was the most severe and percent CSF highest (Table 1). Pons data were rejected in one patient with SCA1, one patient with SCA2, one patient with SCA7, four patients with SCA3, and two healthy control subjects because of broad water linewidth (>10 Hz). Alanine, aspartate, ascorbate,  $\gamma$ -aminobutyric acid, lactate, phosphorylcholine, and PE did not meet the mean CRLB criterion of 20% or greater in both the vermis and pons. In addition, NAAG did not meet this criterion in the vermis, whereas creatine, glucose, glutamine, GSH, PCr, and taurine did not meet the criterion in the pons. Our control data were also part of a two-site reproducibil-

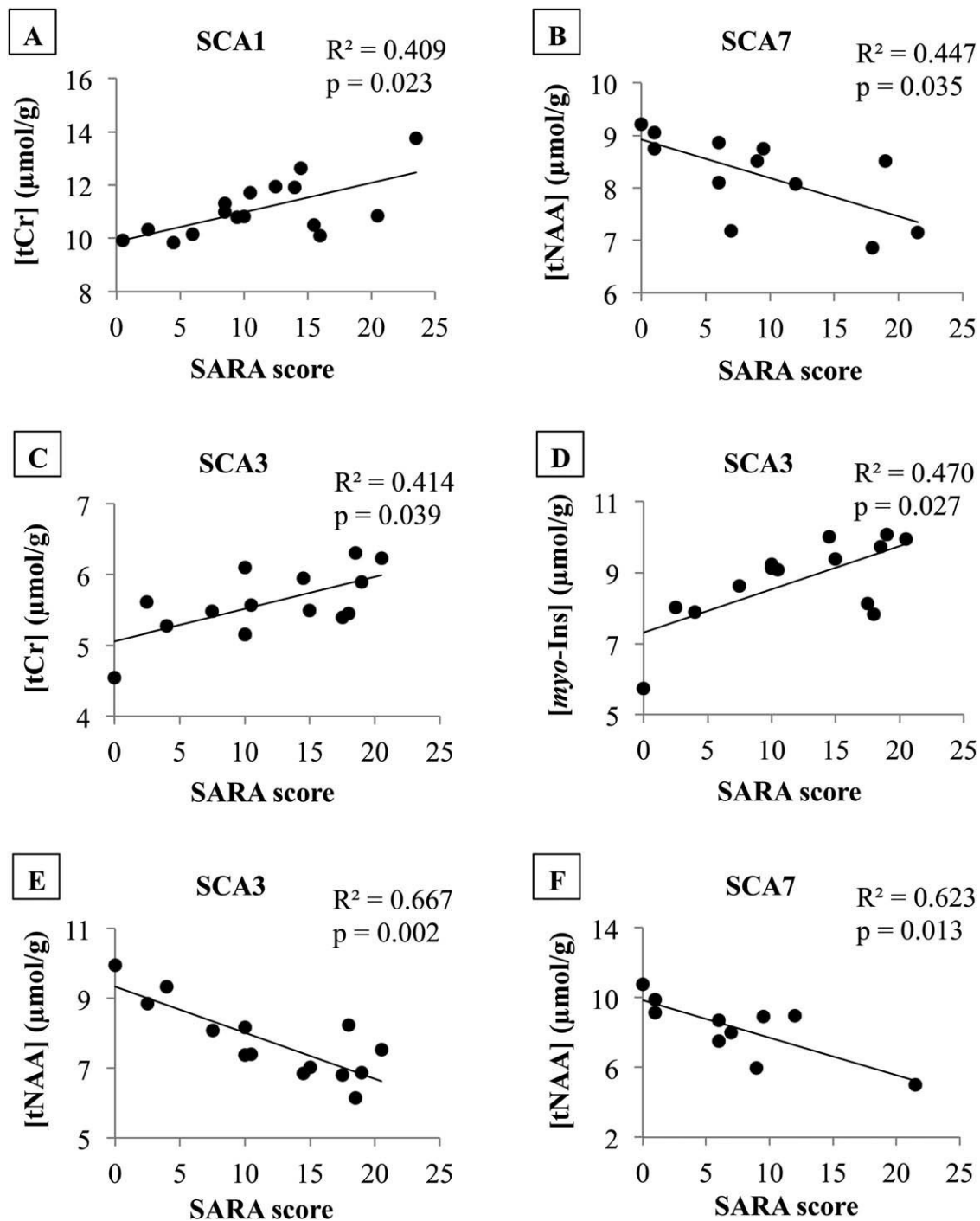
ity study previously published in which the two participating centers obtained consistent spectral quality and similar neurochemical concentrations in controls by using the same MRS pulse sequence (semi-LASER) in conjunction with identical calibration and quantification procedures.<sup>22</sup>

### Neurochemical Alterations in Patients With SCAs

In patients with SCAs, NAA and tNAA were significantly lower than in controls in both the vermis and the pons (Fig. 1). Glu was also significantly lower in the vermis of patients with SCA3 and the pons of patients with SCA2 and SCA3 (Fig. 1). Lower NAA, a marker of neuronal loss/dysfunction, in the vermis and the pons of patients was associated with significantly higher concentrations of *myo*-Ins, a putative glial marker, and tCr, a marker of energy metabolism (Fig. 1). Neurochemical alterations tended to be more pronounced in patients with SCA2 and SCA3 (Fig. 1 and Supplemental Data eFig. 2 and eFig. 3).

### Correlation Between Disease Parameters and Neurochemical Concentrations

A strong negative correlation was found between SARA scores and tNAA in the vermis of patients with SCA7 and in the pons of patients with SCA3 and SCA7 (Fig. 2). Total creatine also strongly correlated with SARA scores in the vermis of patients with SCA1

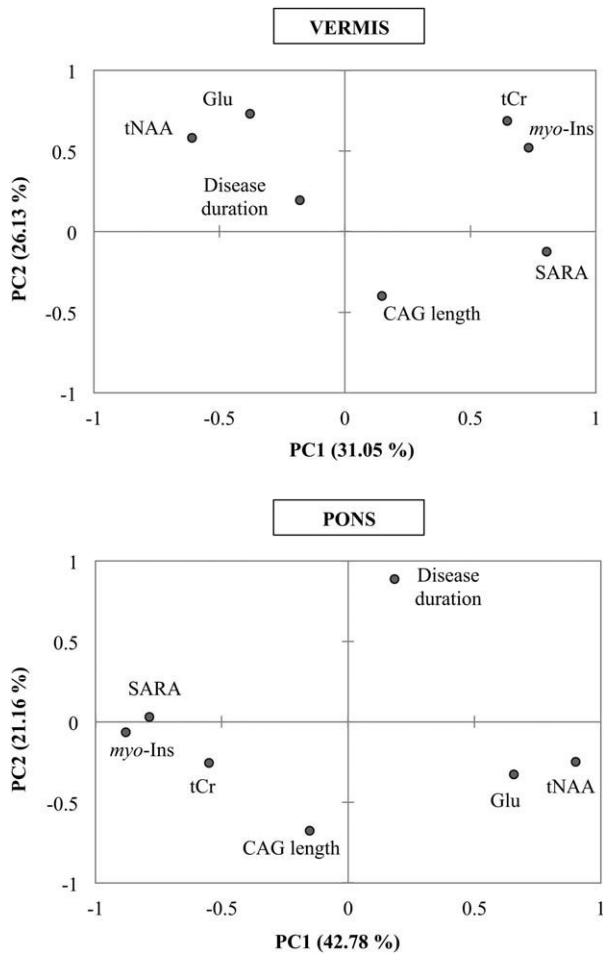


**FIG. 2.** Correlation between clinical scores and neurochemical concentrations in the vermis and the pons of patients with SCAs. SARA scores correlated with (A) tCr in SCA1 vermis, (B) tNAA in SCA7 vermis, (C) *myo*-Ins in SCA3 pons, (D) tCr in SCA3 pons, (E) tNAA in SCA3 pons, and (F) tNAA in SCA7 pons. Metabolites that showed Dunnett significance when each SCA type was compared with controls were included in the correlation analysis. *P* values of the correlations have been corrected for multiple testing with step-down Bonferroni method. SCA, spinocerebellar ataxia; SARA, Scale for the Assessment and Rating of Ataxia; tCr, creatine + phosphocreatine; tNAA, *N*-acetylaspartate and *N*-acetylaspartylglutamate; *myo*-Ins, myoinositol.

and in the pons of patients with SCA3 (Fig. 2). Furthermore, SARA scores correlated with *myo*-Ins in the pons of patients with SCA3 (Fig. 2). However, CAG repeat length and disease duration did not correlate with the concentration of any neurochemical (Supplemental Data eTable).

Using patient data only, PCA was used for metabolites with significant differences between patients and controls—tNAA, *myo*-Ins, tCr, and Glu—as well as for disease parameters of interest in SCAs—SARA, CAG repeat length, and disease duration. The first two principal components explained 57.18% and





**FIG. 3.** Principal component analysis (PCA) of metabolites of interest and disease characteristics of patients with SCAs. The first two components accounted for 57.4% and 64% variation in the vermis and the pons, respectively. PCA was able to separate the neuronal markers—tNAA and Glu—from the energetic marker (tCr), the glial marker (*myo*-Ins) and the SARA score. SCA, spinocerebellar ataxia; tNAA, *N*-acetylaspartate and *N*-acetylaspartylglutamate; Glu, glutamate; tCr, creatine + phosphocreatine; *myo*-Ins, myoinositol; SARA, Scale for the Assessment and Rating of Ataxia.

63.94% of the variance in the vermis and the pons, respectively (Fig. 3). Principal component analysis separated the neuronal markers—tNAA and Glu—from the glial (*myo*-Ins) and energetic markers (tCr) in both vermis and pons (Fig. 3). Among the disease parameters, PC1 further showed that the motor score (SARA) was the only one inversely correlated with the neuronal markers and correlated with the glial and energetic markers in both vermis and pons (Fig. 3). Of note, PCA showed a negative correlation between CAG repeat length and disease duration (Fig. 3).

### Separation Between Patients and Controls Using Neurochemical Concentrations

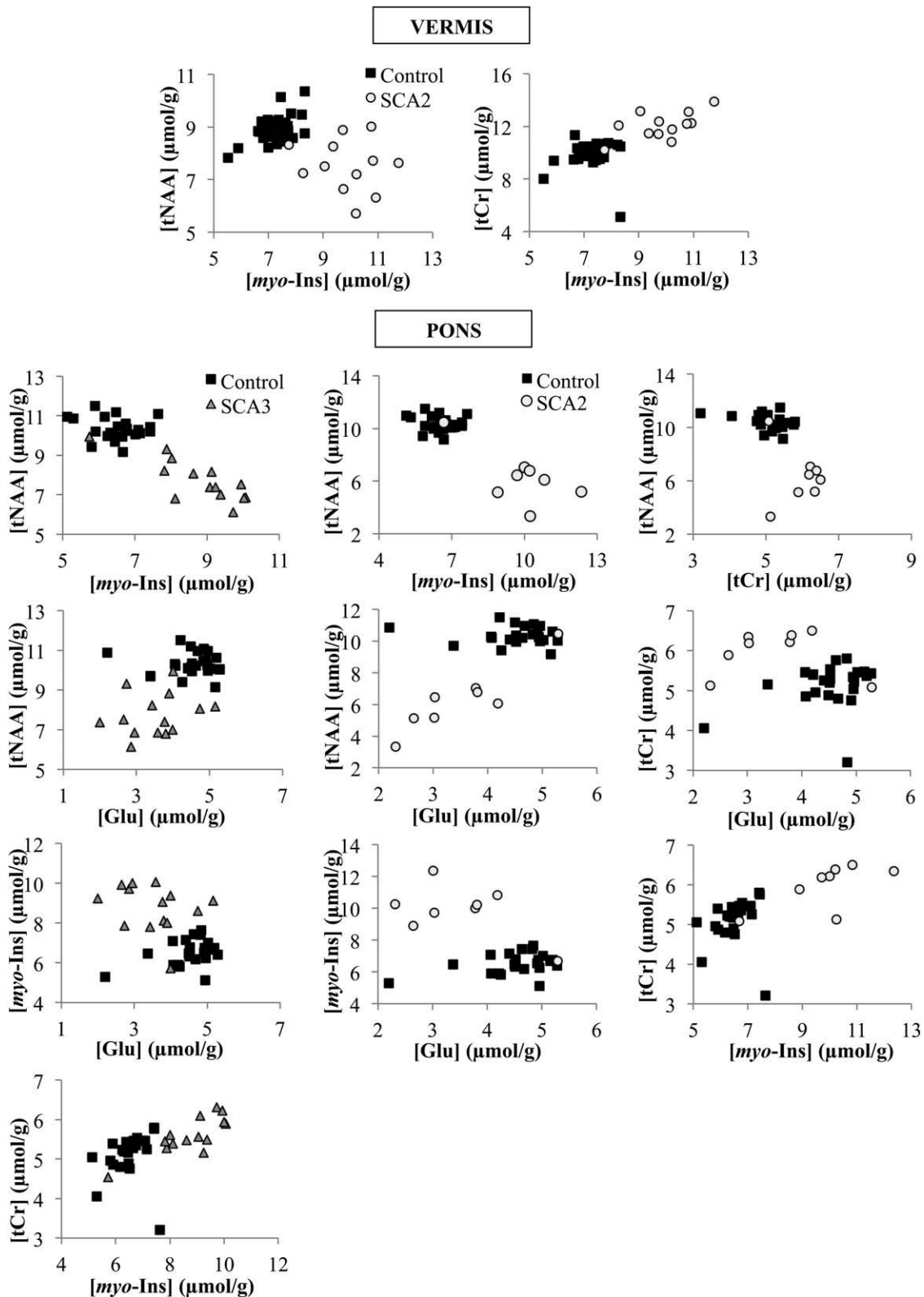
The concentrations of metabolites that showed the largest differences between patients and controls—tNAA, tCr, *myo*-Ins, and Glu—were plotted against

each other to determine the separation between patient and control groups. These neurochemical plots demonstrated the separation of patients with SCA2 and SCA3 from controls in both vermis and pons (Fig. 4). However, we could not clearly separate patients with SCA1 and SCA7 from controls (data not shown). In addition, we used partial least squares discriminant analysis to identify the variables with class separation information, but we were unable to obtain a good separation between the different SCAs (data not shown). Likewise, although MRS allowed discriminating metabolic profiles from patients and controls as well as correlating patients' metabolic profile with clinical status, it did not reveal metabolic profiles characteristic of any of the SCA types.

## Discussion

This is the first study reporting neurochemical profiling on a large cohort of patients with SCAs (SCA 1, 2, 3, and 7), using a 3 Tesla clinical MR system. In the vermis and the pons, patients displayed lower NAA, a neuronal marker, higher *myo*-Ins, a glial marker, and higher total Cr compared with controls. Glu, another neuronal marker, was also lower in patients' vermis (SCA3) and pons (SCA2 and SCA3). Our control data also have been part of a two-site study to establish the reproducibility of our methods, which underscores the robustness of our findings.<sup>22</sup> Although the CRLB of 20% or less criterion is fairly conservative, quantification of some metabolites such as GSH from short-TE spectra still requires caution, because their quantification may be sensitive to small changes in the baseline, even with the excellent spectral quality achieved in this study. However, all of the main findings reported here focus on metabolites (NAA, *myo*-Ins, tCr, Glu) that have the most prominent resonances and are therefore visually apparent in spectra.

The significant decrease in NAA and Glu observed in patients with SCAs, likely reflecting neuronal loss/dysfunction in those structures,<sup>1</sup> is in agreement with prior MRS studies in SCAs.<sup>28</sup> We also observed the decrease of NAA in the pons to be more substantial than that in the vermis. This is similar to the observations in SCA1 studies<sup>15</sup> and may be attributable to a more pronounced pathological involvement and atrophy in the pons.<sup>29</sup> Conversely, the increase in *myo*-Ins, a six-carbon sugar that serves as an intermediate in the metabolism of membrane and myelin phospholipids,<sup>30</sup> can indicate damage to myelin sheaths as a result of neurodegeneration resulting in increased concentration of free *myo*-Ins. As a glial marker, the increase in *myo*-Ins levels in response to neuronal loss also may be an attempt to improve glial proliferation to modulate vascular and metabolic activities and



**FIG. 4.** Separation between patients with SCAs and controls by plotting the concentrations of neurochemicals against each other. The concentrations of metabolites that showed significant differences in patients—tNAA, tCr, *myo*-Ins, and Glu—were plotted against each other to determine the ratio that could separate subjects into patient and control groups, with almost no overlap. SCA2 has the best separation with at most one dataset overlapping with controls. SCA, spinocerebellar ataxia; tNAA, *N*-acetylaspartate and *N*-acetylaspartylglutamate; Glu, glutamate; tCr, creatine + phosphocreatine; *myo*-Ins, myo-inositol.

therefore to compensate for neuronal loss.<sup>31</sup> This pinpoints the important role of non-neuronal cells in SCAs, especially astrocytes that play key roles in brain homeostasis through their neurovascular and neuro-metabolic coupling with neurons—ie, neurotransmitter recycling and provision of energy substrates.<sup>32</sup>

Furthermore, we observed a significant increase in tCr, an energetic marker often used in prior studies as a concentration reference in MRS,<sup>29</sup> in both the vermis<sup>33</sup> and the pons of patients. Because of the limited ability of the brain to store glucose, the creatine kinase/PCr system is important to keep up with the high energy demands of neurons.<sup>34</sup> Because mitochondrial creatine kinase activity suppresses formation of free radicals within the mitochondria,<sup>35,36</sup> the increase in tCr might be an attempt to increase Cr levels to suppress formation of free radicals and increase neuro-protection. Changes in creatine and PCr have been reported in Huntington's disease (HD), another polyglutamine disease that shares pathophysiological commonalities with SCAs.<sup>37</sup> Using microwave fixation techniques, which instantaneously inactivate brain enzymatic activities and preserve in vivo levels of analytes, increased levels of creatine and PCr were reported in HD mice brain. The increase of tCr preceded decreased adenosine triphosphate levels as early as 4 weeks of age in presymptomatic mice.<sup>38</sup> Similarly, increased tCr<sup>39</sup> and significant changes in [PCr]/[Cr] ratio<sup>40</sup> have been reported in the brains of HD mouse models at an early age using <sup>1</sup>H MRS techniques. Recently, we also described abnormal ratios of inorganic phosphate/PCr using <sup>31</sup>P MRS during brain activation in patients with HD at an early stage of the disease, confirming altered brain bioenergetics in HD.<sup>41</sup> Therefore, the increase of tCr in patients with SCAs is comparable to the dysregulation of the tCr pool that we observed in patients and animal models with HD. Accordingly, determining whether the above-mentioned mechanisms are activated at a presymptomatic stage of SCAs would be interesting.

Higher disease severity, reflected by higher SARA scores, was associated with lower tNAA concentration and higher concentrations of *myo*-Ins and tCr in both the vermis and the pons of several SCA types. Moreover, the PCA confirmed that neuronal metabolites (tNAA and Glu) varied inversely in the vermis and the pons to glial metabolites (*myo*-Ins), energetic metabolites (tCr), and disease severity (SARA score) in patients with SCAs. This inverse correlation suggests that the metabolic attempt to compensate for neuronal damage is critical to SCAs' pathophysiology, even more as the metabolic changes are associated with disease severity scores. The absence of correlations between neurochemical concentrations and CAG repeat length or disease duration may be partly

explained by the limited dynamic range in CAG and duration.

Using neurochemical plots with our metabolites of interest (tNAA, *myo*-Ins, tCr, and Glu), we were able to separate patients with SCA2 and SCA3 from controls but not SCA1, unlike what was previously reported.<sup>15</sup> Moreover, metabolic profiles could not discriminate the different SCAs from one another. Altogether, this study indicates that, rather than providing subtype-specific information about SCAs, MRS has the potential to unravel early metabolic/cellular changes in various SCAs, which are likely to occur before brain atrophy. Neurometabolic profiles also provide cell-specific information on neurons and astrocytes, which cannot be assessed in vivo by other neuroimaging modalities. Because these biomarkers reflect dynamic aspects of cellular metabolism and mirror disease severity, they also may be of special interest to establish proof-of-concepts for drugs before the evaluation of clinical outcome measures in phase III therapeutic trials. Our previous report of highly reproducible data in controls in a two-site study supports the claim that these biomarkers can be used in multicentric trials.<sup>22</sup> ■

**Acknowledgment:** We thank the patients and volunteers who participated in this study. We also thank the Centre d'Investigation Clinique Pitié Neurosciences, CIC-1422, Département des Maladies du Système Nerveux, Hôpital Pitié-Salpêtrière, Paris, France.

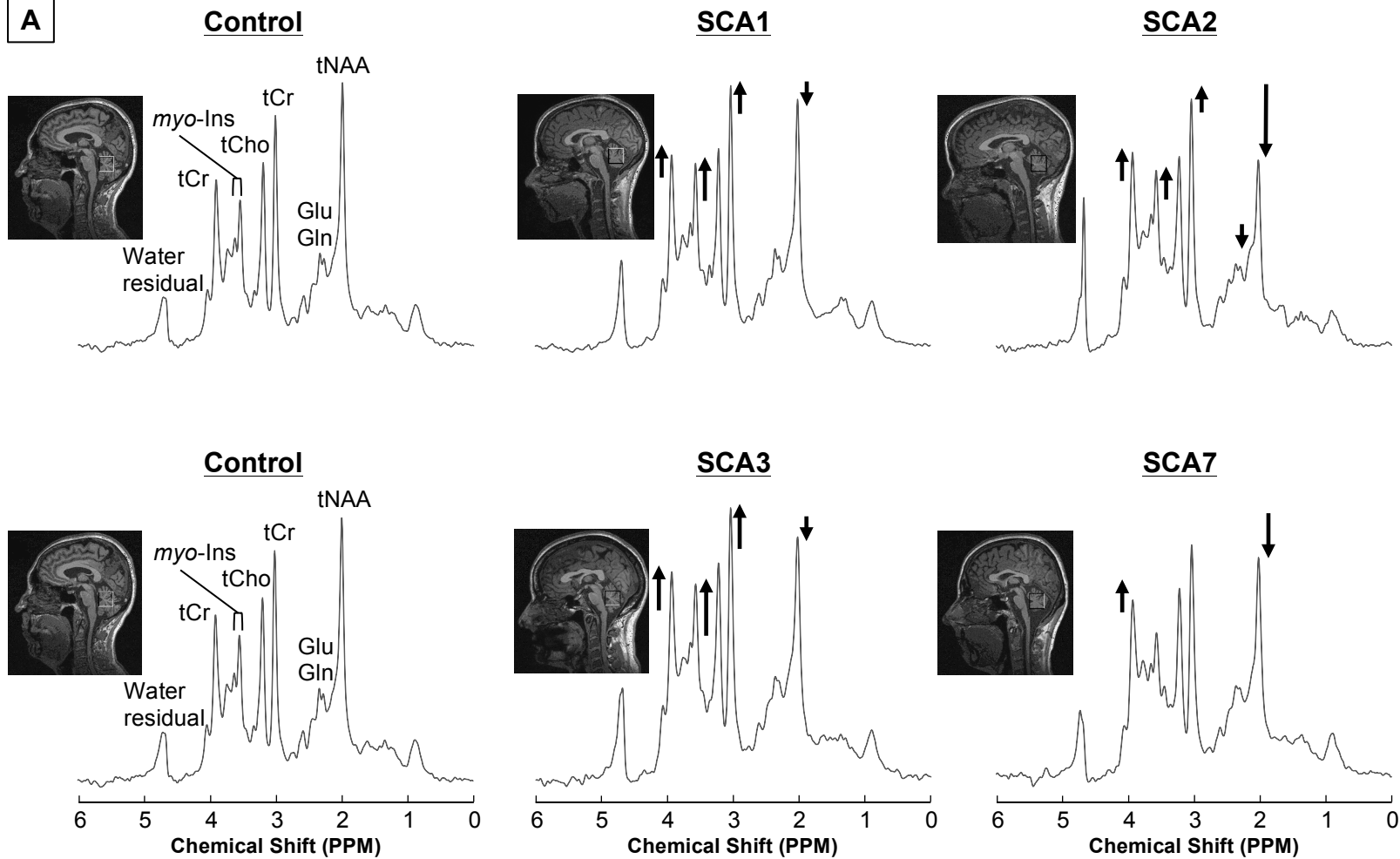
## References

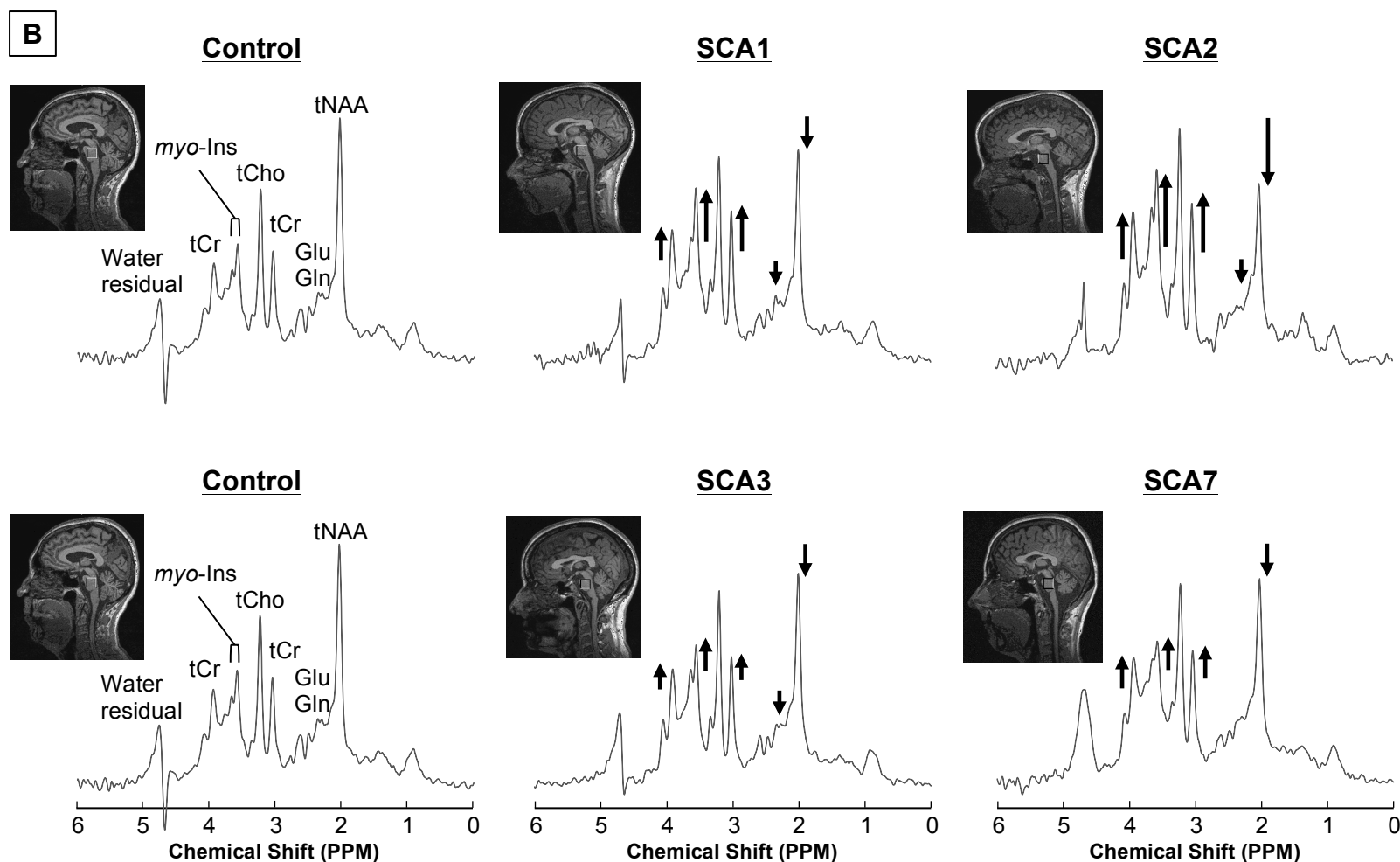
1. Yamada M, Sato T, Tsuji S, Takahashi H. CAG repeat disorder models and human neuropathology: similarities and differences. *Acta Neuropathol* 2008;115:71-86.
2. Jacobi H, Reetz K, du Montcel ST, et al. Biological and clinical characteristics of individuals at risk for spinocerebellar ataxia types 1, 2, 3, and 6 in the longitudinal RISCA study: analysis of baseline data. *Lancet Neurol* 2013;12:650-658.
3. Durr A. Autosomal dominant cerebellar ataxias: polyglutamine expansions and beyond. *Lancet Neurol* 2010;9:885-894.
4. Schmitz-Hübsch T, du Montcel ST, Baliko L, et al. Scale for the assessment and rating of ataxia: development of a new clinical scale. *Neurology* 2006;66:1717-1720.
5. Saute JA, Donis KC, Serrano-Munuera C, et al. Ataxia rating scales: psychometric profiles, natural history and their application in clinical trials. *Cerebellum* 2012;11:488-504.
6. Underwood BR, Rubinsztein DC. Spinocerebellar ataxias caused by polyglutamine expansions: a review of therapeutic strategies. *Cerebellum* 2008;7:215-221.
7. Hall H, Cuellar-Baena S, Dahlberg C, In't Zandt R, Denisov V, Kirik D. Magnetic resonance spectroscopic methods for the assessment of metabolic functions in the diseased brain. *Curr Top Behav Neurosci* 2012;11:169-198.
8. Öz G, Nelson CD, Koski DM, et al. Noninvasive detection of presymptomatic and progressive neurodegeneration in a mouse model of spinocerebellar ataxia type 1. *J Neurosci* 2010;30:3831-3838.
9. Guerrini L, Lolli F, Ginestroni A, et al. Brainstem neurodegeneration correlates with clinical dysfunction in SCA1 but not in SCA2: a quantitative volumetric, diffusion and proton spectroscopy MR study. *Brain* 2004;127:1785-1795.
10. Lirng JF, Wang PS, Chen HC, Soong BW, Guo WY, Wu HM, Chang CY. Differences between spinocerebellar ataxias and multiple system atrophy-cerebellar type on proton magnetic resonance spectroscopy. *PLoS One* 2012;7:e47925.

11. Mascalchi M, Cosottini M, Lolli F, et al. Proton MR spectroscopy of the cerebellum and pons in patients with degenerative ataxia. *Radiology* 2002;223:371-378.
12. Wang PS, Chen HC, Wu HM, Lirng JF, Wu YT, Soong BW. Association between proton magnetic resonance spectroscopy measurements and CAG repeat number in patients with spinocerebellar ataxias 2, 3, or 6. *PLoS One* 2012;7:e47479.
13. Ferguson KJ, MacLulich AMJ, Marshall I, Deary IJ, Starr JM, Seckl JR, Wardlaw JM. Magnetic resonance spectroscopy and cognitive function in healthy elderly men. *Brain* 2002;125:2743-2749.
14. Henriksen O. *In vivo* quantitation of metabolite concentrations in the brain by means of proton MRS. *NMR Biomed* 1995;8:139-148.
15. Öz G, Hutter D, Tkáč I, et al. Neurochemical alterations in spinocerebellar ataxia type 1 and their correlations with clinical status. *Mov Disord* 2010;25:1253-1261.
16. Öz G, Iltis I, Hutter D, Thomas W, Bushara KO, Gomez CM. Distinct neurochemical profiles of spinocerebellar ataxias 1,2,6, and cerebellar multiple system atrophy. *Cerebellum* 2011;10:208-217.
17. Öz G, Tkáč I. Short-echo, single-shot, full-intensity proton magnetic resonance spectroscopy for neurochemical profiling at 4 T: Validation in the cerebellum and brainstem. *Magn Reson Med* 2011;65:901-910.
18. Boer VO, van Lier AL, Hoogduin JM, Wijnen JP, Luijten PR, Klomp DW. 7-T 1H MRS with adiabatic refocusing at short TE using radiofrequency focusing with a dual-channel volume transmit coil. *NMR Biomed* 2011;24:1038-1046.
19. Gruetter R, Tkac I. Field mapping without reference scan using asymmetric echo-planar techniques. *Magn Reson Med* 2000;43:319-323.
20. Ernst T, Kreis R, Ross BD. Absolute quantitation of water and metabolites in the human brain. I. Compartments and water. *J Magn Reson* 1993;102:1-8.
21. Provencher SW. Estimation of metabolite concentrations from localized *in vivo* proton NMR spectra. *Magn Reson Med* 1993;30:672-679.
22. Deelchand DK, Adanyeguh IM, Emir UE, et al. Two-site reproducibility of cerebellar and brainstem neurochemical profiles with short-echo, single-voxel MRS at 3T. *Magn Reson Med* 2014. DOI: 10.1002/mrm.25295.
23. Randall L. Chemical topography of the brain. *J Biol Chem* 1938; 124:481-488.
24. Siegel GJ, ed. *Basic Neurochemistry: Molecular, Cellular and Medical Aspects*. 6th ed. Philadelphia: Lippincott-Raven Publishers; 1999.
25. Oz G, Alger JR, Barker PB, et al. Clinical proton MR spectroscopy in central nervous system disorders. *Radiology* 2014;270:658-679.
26. Provencher S. *LCModel and LCMgui User's Manual*. 2014. [Accessed 2014 December 20]. Available from: <http://s-provencher.com/pub/LCModel/manual/manual.pdf>.
27. Holm S. A simple sequentially rejective multiple test procedure. *Scand J Statist* 1979;6:65-70.
28. Viau M, Boulanger Y. Characterization of ataxias with magnetic resonance imaging and spectroscopy. *Parkinsonism Relat Disord* 2004;10:335-351.
29. Reetz K, Costa AS, Mirzazade S, et al. Genotype-specific patterns of atrophy progression are more sensitive than clinical decline in SCA1, SCA3 and SCA6. *Brain* 2013;136:905-917.
30. Maddock RJ, Buonocore MH. MR spectroscopic studies of the brain in psychiatric disorders. *Curr Top Behav Neurosci* 2012;11: 199-251.
31. Brand A, Richter-Landsberg C, Leibfritz D. Multinuclear NMR studies on the energy metabolism of glial and neuronal cells. *Dev Neurosci* 1993;15:289-298.
32. Allaman I, Bélanger M, Magistretti PJ. Astrocyte-neuron metabolic relationships: for better and for worse. *Trends Neurosci* 2011;34: 76-87.
33. Guerrini L, Belli G, Mazzoni L, et al. Impact of cerebrospinal fluid contamination on brain metabolites evaluation with 1 H-MR Spectroscopy: a single voxel study of the cerebellar vermis in patients with degenerative ataxias. *J Magn Reson Imaging* 2009; 30:11-17.
34. Brewer GJ, Wallimann TW. Protective effect of the energy precursor creatine against toxicity of glutamate and beta-amyloid in rat hippocampal neurons. *J Neurochem* 2000;74: 1968-1978.
35. Genius J, Geiger J, Bender A, Moller HJ, Klopstock T, Rujescu D. Creatine protects against excitotoxicity in an *in vitro* model of neurodegeneration. *PLoS One*. 2012;7:e30554.
36. Meyer LE, Machado LB, Santiago APSA, et al. Mitochondrial creatine kinase activity prevents reactive oxygen species generation: antioxidant role of mitochondrial kinase-dependent ADP re-cycling activity. *J Biol Chem* 2006;281:37361-37371.
37. Gatchel JR, Zoghbi HY. Diseases of unstable repeat expansion: mechanisms and common principles. *Nat Rev Genet* 2005;6:743-755.
38. Mochel F, Durant B, Meng X, et al. Early alterations of brain cellular energy homeostasis in Huntington disease models. *J Biol Chem* 2012;287:1361-1370.
39. Zacharoff L, Tkáč I, Song Q, et al. Cortical metabolites as biomarkers in the R6/2 model of Huntington's disease. *J Cereb Blood Flow Metab* 2012;32:502-514.
40. Tkáč I, Henry PG, Zacharoff L, et al. Homeostatic adaptations in brain energy metabolism in mouse models of Huntington disease. *J Cereb Blood Flow Metab* 2012;32:1977-1988.
41. Mochel F, N'Guyen TM, Deelchand D, et al. Abnormal response to cortical activation in early stages of Huntington disease. *Mov Disord* 2012;27:907-910.

Supplementary eFigure 1

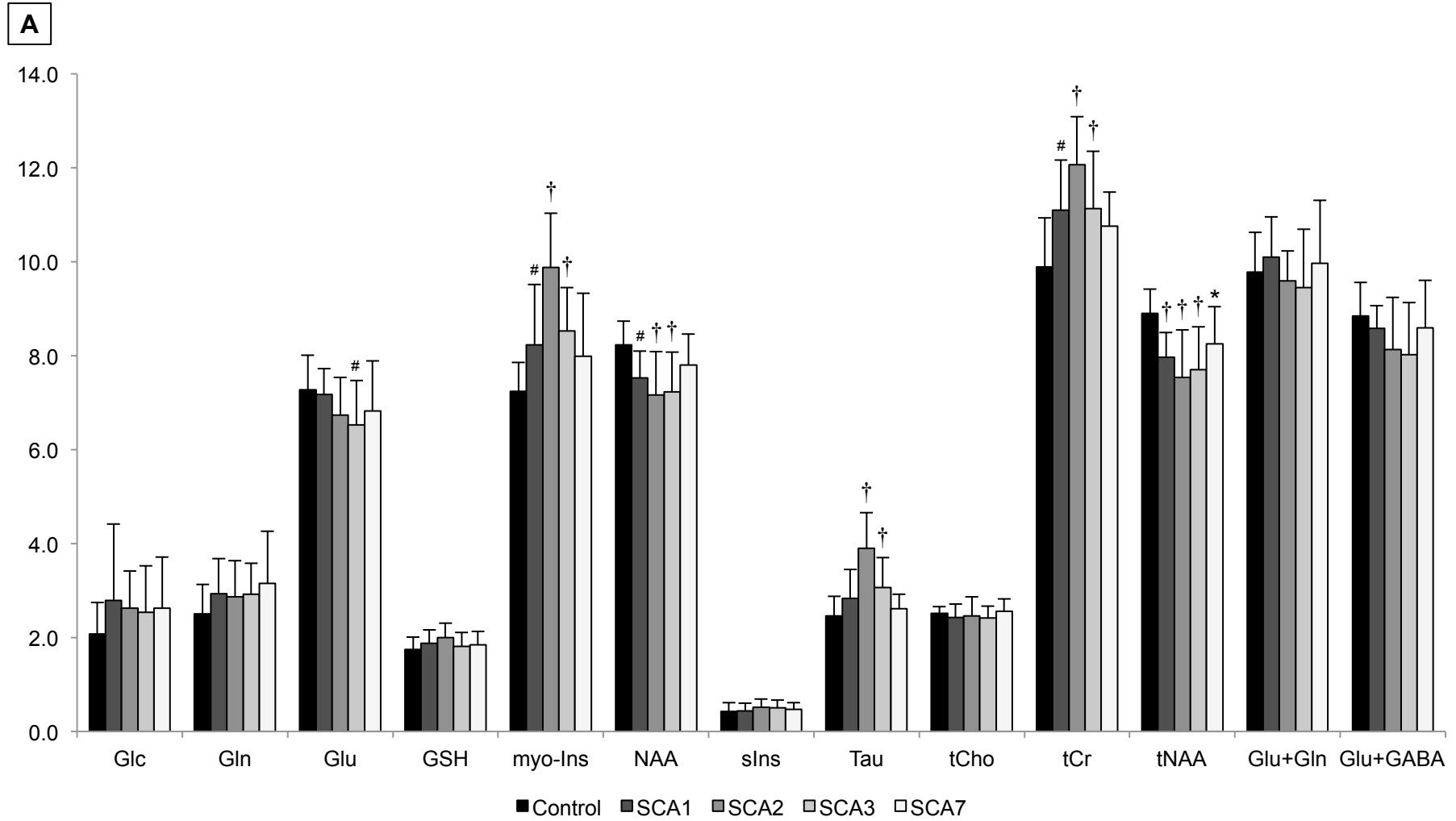
**A**

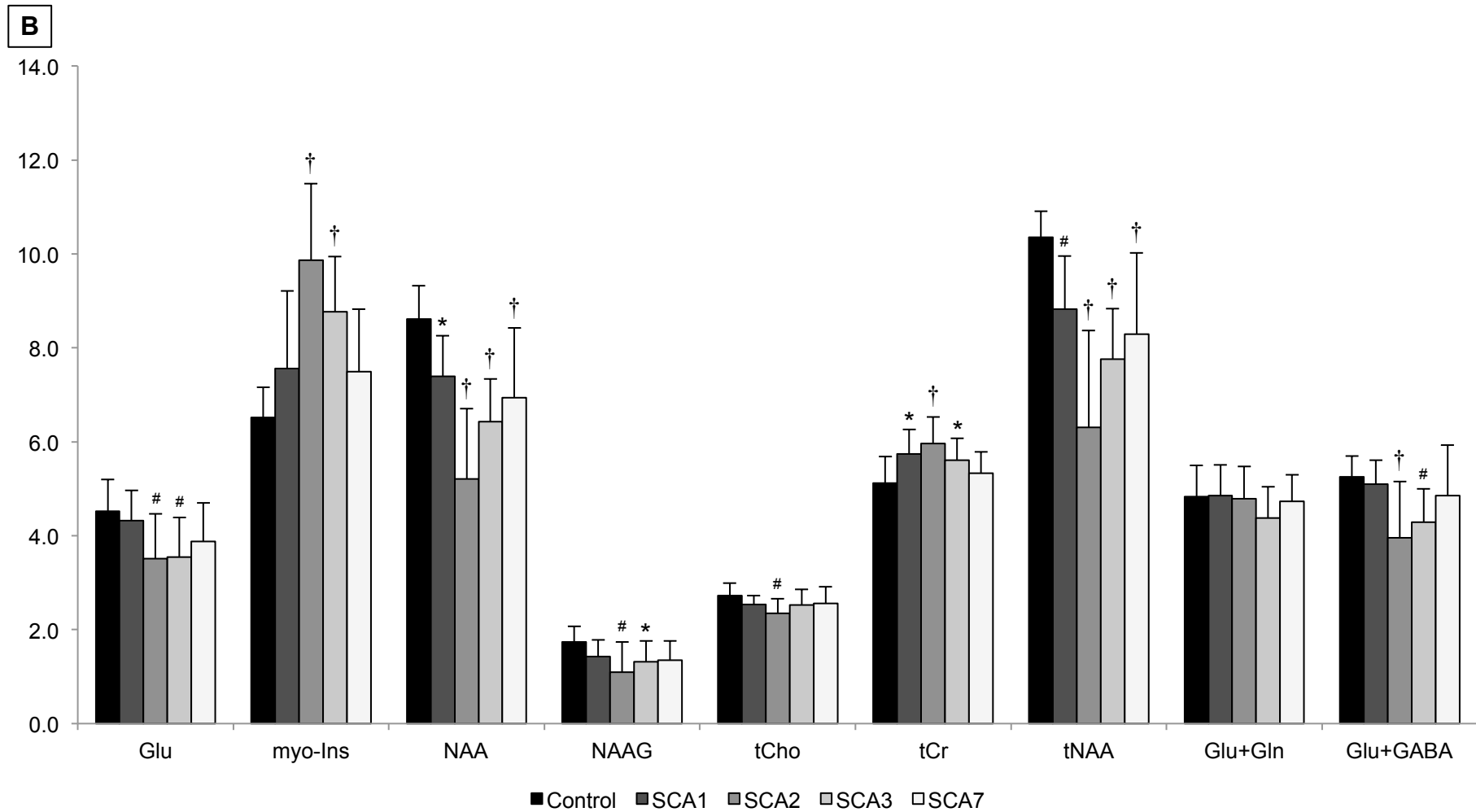




Alterations in neurochemicals in localized proton MR spectra obtained from healthy controls and patients. Arrows show increase or decrease in metabolites in patient brain compared to control. Ala, Asp, Asc, GABA, Lac, PCho and PE did not meet the mean CRLB criterion of  $\leq 20\%$  in both the vermis and pons. In addition, NAAG did not meet this criterion in the vermis, whilst Cr, Glc, Gln, GSH, PCr and Tau did not meet the criterion in the pons **A**: Proton spectra were obtained in the vermis of subjects using semi-LASER sequence ( $TE = 28$  ms,  $TR = 5$  s, 64 averages) at 3 T. Alterations are pronounced in the vermis of patients with SCA compared to healthy controls. **B**: Proton spectra obtained in the pons of subjects using semi-LASER sequence ( $TE = 28$  ms,  $TR = 5$  s, 64 averages) at 3 T. Changes in neurochemicals are evident in the pons of patients with SCA compared to controls.

Supplementary eFigure 2





Neurochemical profiles in controls and patients with SCA at 3 T. **A:** Mean metabolite concentrations ( $\mu\text{mol/g}$ ) measured in the vermis of healthy controls ( $n = 33$ ) and patients with SCA (SCA1,  $n = 16$ ; SCA2,  $n = 12$ ; SCA3,  $n = 21$ ; SCA7,  $n = 12$ ). **B:** Mean metabolite concentrations ( $\mu\text{mol/g}$ ) measured in the pons of healthy controls ( $n = 23$ ) and patients with SCA (SCA1,  $n = 10$ ; SCA2,  $n = 8$ ; SCA3,  $n = 14$ ; SCA7,  $n = 10$ ).  $p$  values represent Dunnett-corrected statistically significant differences between patients and controls (\*  $p < 0.05$ ; #  $p < 0.01$ ; †  $p < 0.001$ ). Error bars represent standard deviations (SDs).



**Supplementary eTable:** Correlations of metabolites in the vermis and pons of each SCA type with SARA score, CAG repeat length and disease duration (DD)

Region	Group	Variable	SARA_corr	Raw_p	Holm_p	CAG_corr	Raw_P	Holm_P	DD_corr	Raw_P	Holm_p
VERMIS	SCA1	myo-Ins	0.254	0.342	0.683	0.339	0.199	0.597	-0.110	0.708	1.000
	SCA1	tCr	0.639	0.008	0.023	0.313	0.238	0.597	0.227	0.435	1.000
	SCA1	tNAA	-0.113	0.677	0.683	-0.271	0.309	0.597	0.011	0.971	1.000
	SCA2	GSH	0.422	0.172	0.780	0.341	0.278	0.690	0.177	0.582	1.000
	SCA2	myo-Ins	0.336	0.285	0.780	0.547	0.066	0.330	0.122	0.706	1.000
	SCA2	Tau	0.365	0.245	0.780	0.509	0.091	0.364	0.169	0.599	1.000
	SCA2	tCr	0.189	0.557	1.000	-0.118	0.715	0.715	0.316	0.317	1.000
	SCA2	tNAA	-0.437	0.156	0.780	-0.375	0.230	0.690	0.065	0.842	1.000
	SCA3	Glu	-0.390	0.08	0.160	-0.064	0.801	1.000	-0.182	0.443	0.886
	SCA3	myo-Ins	0.482	0.027	0.135	-0.231	0.356	1.000	0.362	0.117	0.468
	SCA3	Tau	0.461	0.036	0.144	-0.159	0.529	1.000	0.544	0.013	0.065
	SCA3	tCr	0.455	0.038	0.144	-0.158	0.532	1.000	0.259	0.269	0.807
	SCA3	tNAA	-0.356	0.114	0.160	0.156	0.536	1.000	-0.056	0.813	0.886
	SCA7	Gln	0.454	0.138	0.138	-0.066	0.838	0.838	-0.214	0.552	0.552
	SCA7	tNAA	-0.668	0.0175	0.035	-0.412	0.183	0.366	-0.416	0.231	0.462
PONS	SCA1	tCr	0.603	0.065	0.130	-0.265	0.459	0.918	0.529	0.178	0.356
	SCA1	tNAA	-0.436	0.208	0.208	-0.094	0.796	0.918	-0.319	0.442	0.442
	SCA2	Glu	-0.701	0.053	0.212	-0.491	0.216	0.471	-0.090	0.832	1.000
	SCA2	Ins	0.383	0.349	1.000	0.796	0.018	0.090	-0.165	0.696	1.000
	SCA2	tCho	0.206	0.624	1.000	-0.550	0.157	0.471	0.335	0.417	1.000
	SCA2	tCr	-0.077	0.856	1.000	0.301	0.469	0.471	-0.317	0.444	1.000
	SCA2	tNAA	-0.802	0.017	0.083	-0.607	0.110	0.440	-0.201	0.633	1.000
	SCA3	Glu	-0.263	0.365	0.365	0.081	0.784	1.000	-0.379	0.202	1.000
	SCA3	myo-Ins	0.685	0.007	0.021	-0.178	0.542	1.000	0.277	0.360	1.000
	SCA3	tCr	0.644	0.013	0.026	-0.320	0.265	0.795	0.119	0.699	1.000
	SCA3	tNAA	-0.817	<0.001	0.002	0.368	0.195	0.780	-0.278	0.358	1.000
	SCA7	tNAA	-0.791	0.007	0.007	-0.272	0.447	0.447	-0.468	0.242	0.484

ANOVA was used to compare each SCA type to control group and adjusted for multiple comparison with Dunnett correction. Only SCA types that were Dunnett significant from controls were included in the correlation analysis. The correlation is presented under SARA\_corr, CAG\_corr and DD\_corr. The uncorrected p value and the Holm corrected p value are presented under Raw\_p and Holm\_p respectively.

# Chapter 6

## Organisation:

<b>Study 5: Autosomal dominant ataxia: identification of imaging biomarkers with high effect size .....</b>	<b>116</b>
6.1 Introduction and objectives .....	116
6.2 Materials and methods.....	117
6.2.1 Participants .....	117
6.2.2 Imaging protocol .....	118
6.2.3 Volumetric analysis .....	118
6.2.4 Rate of atrophy .....	119
6.2.5 Diffusion tensor imaging.....	119
6.2.6 Tractography - Fixel based analysis.....	120
6.2.7 Statistical analysis .....	121
6.3 Results .....	122
6.3.1 Clinical score.....	122
6.3.2 Volumetric analysis.....	122
6.3.3 Diffusion tensor imaging.....	123
6.3.4 Fixel Based Analysis .....	123
6.3.5 Effect size .....	123
6.4 Discussion.....	135

## **Study 5: Autosomal dominant ataxia: identification of imaging biomarkers with high effect size**

### **6.1 Introduction and objectives**

Currently, the most common clinical scores for rating disease severity in patients with SCA are the Scale for the Assessment and Rating of Ataxia (SARA) (Schmitz-Hübsch et al., 2006) and the Composite Cerebellar Functional Severity Score (CCFS) (du Montcel et al., 2008). However, in therapeutic trials of very rare disorders like SCAs, the low effect sizes of clinical scores would likely require a large number of patients making these trials hardly feasible. Clinical scores are not able either to detect macro- and microstructural changes such as atrophy and metabolic alterations that may occur before, during and after symptoms onset. Another important caveat of clinical scales is that, by definition, they cannot be used to evaluate premanifest individuals. Hence, there is a need for biomarkers with effect sizes greater than clinical scores that can be used on small sample sizes of patients with SCA. Magnetic resonance imaging (MRI) techniques provide a unique way to probe changes occurring before symptoms onset and were shown in Huntington disease, another polyglutamine repeat disorder, to be more sensitive than any motor or cognitive task to track disease progression once symptoms have developed (Tabrizi et al., 2012; Tabrizi et al., 2013). Still, most of the volumetric studies performed in SCAs (Yamada et al., 2008; Durr, 2010; Schulz et al., 2010; Rüb et al., 2013) have not investigated the rate of atrophy over time. Other imaging studies in SCAs have looked at the brain diffusion properties, which give information on the microstructural changes related to the disease (Della Nave et al., 2004; Guerrini et al., 2004; Mandelli et al., 2007; Prakash et al., 2009; Alcauter et al., 2011; Guimarães et al., 2013; Kang et al., 2014; Hernandez-Castillo et al., 2015; Mascalchi et al., 2015; Rozenfeld et al., 2015; Hernandez-Castillo et al., 2016; Yoo & Oh, 2017). Unfortunately, most of these studies only reported diffusion metrics such as fractional anisotropy (FA) that is not able to account for different fiber populations within a voxel.

This study was a follow-up of study 4. In this study (ClinicalTrials.gov Identifier: NCT01470729), we focused on imaging biomarkers of SCA. We compared manual and automatic segmentation of brain volume for their effectiveness to capture atrophy in a unique cohort of patients with SCA1, SCA2, SCA3 and SCA7. Furthermore, we investigated white matter microstructural changes in SCA using, not only conventional diffusion tensor imaging

(DTI) metrics – FA and radial diffusivity (RD) –, but also a novel tractography method to determine differences in the fiber density (FD) and fiber cross-section (FC) called whole brain fixel (i.e. specific fiber population in a voxel) based analysis (FBA) (Raffelt et al., 2012b; Raffelt et al., 2015; Raffelt et al., 2017). Likewise, we looked at the correlation between clinical scores, atrophy, DTI and FBA metrics.

## **6.2 Materials and methods**

The local ethics committee (AOM10094, CPP Ile de France VI, Ref: 105-10) approved the study. All participants were over 18 years and signed a written informed consent after the experimental procedure was fully explained before they participated in the study. In addition, participants had to have the ability to undergo an MRI. MRI acquisitions were performed on a 3 T whole-body Siemens MAGNETOM Trio scanner (Siemens Medical Solutions, Erlangen, Germany). The MRI system was upgraded during the study period and hence twelve datasets were acquired on a 3 T whole-body Siemens MAGNETOM Prisma scanner (Siemens Medical Solutions, Erlangen, Germany).

### **6.2.1 Participants**

Participants were recruited as part of the BIOSCA study (NCT01470729) and only those who could perform MRI and complete the follow-up imaging protocol were reported. Despite the scarcity of SCAs, we were able to enroll a large cohort of patients so that the pooled dataset included 15 patients with SCA1, 12 patients with SCA2, 20 patients with SCA3 and 10 patients with SCA7. Twenty-four healthy individuals of similar general characteristics – median age, sex and BMI – were also included (Table 2). Ataxia severity was evaluated with the SARA score, which ranges from 0 (no cerebellar symptoms) to 40 (most severe cerebellar symptoms) (Schmitz-Hübsch et al., 2006), and the CCFS, a composite score obtained from a nine-hole pegboard test and a click test (du Montcel et al., 2008).

### 6.2.2 Imaging protocol

The Siemens volume-transmit 32-receive coil array was used for the imaging protocol. 3D T1-weighted volumetric images ( $T_R = 2530$  ms,  $T_E = 3.65$  ms, slice thickness = 1 mm isotropic, field of view (FOV) =  $256 \times 256$  mm<sup>2</sup>, matrix =  $256 \times 256$ ) were acquired for volumetric analyses of brain regions of interest. Images were inspected immediately after acquisition and those with motion artifacts were reacquired immediately. Each participant had two time points of acquisition at baseline and at 24 months in order to evaluate the rate of atrophy.

Due to method development, diffusion imaging was only performed at 24-month. DTI data were acquired along 60 isotropic directions with echo-planar spin-echo sequence ( $T_R = 10000$  ms,  $T_E = 89$  ms, slice thickness = 2 mm isotropic, FOV =  $220 \times 220$  mm<sup>2</sup>, matrix =  $110 \times 110$ , flip angle =  $90^\circ$ , 34 reference lines,  $b$  value =  $1500$  s/mm<sup>2</sup>). The directions were interleaved with five non-diffusion weighted reference images (b0 images,  $b$  value =  $0$  s/mm<sup>2</sup>) at every 12 directions. Another b0 image with opposite phase-encode blip was acquired. The b0 images were used for correcting motions, eddy currents geometric distortions, and susceptibility-induced off-resonance field distortions.

### 6.2.3 Volumetric analysis

The 3D T1-weighted volumetric images were processed to evaluate the rate of atrophy. The images were first manually segmented by hand using ITK-SNAP (Yushkevich et al., 2006). Manual segmentation was performed because it remains the gold standard. It is however time consuming and very laborious. Hence, it was performed only on the cerebellar vermis that is the region mostly affected in this pathology, and a region from which neurometabolic findings were previously reported (Oz et al., 2010; Adanyeguh et al., 2015). The images were first linearly aligned along the midline using the FMRIB's Linear Image Registration Tool (Jenkinson et al., 2002). The mid-sagittal slice was located and, starting from the apex of the fourth ventricle, the vermis lobules (Courchesne et al., 1988) were delineated whilst excluding the cerebellar tonsils. This was repeated on eight more slices – four slices each to the right and left of the mid-sagittal slice. The number of slices was limited to nine due to the poor contrast in the subsequent slices when the vermis could not be clearly separated from the

tonsils and the cerebellar hemispheres. In order to limit bias, only one rater performed the delineation to extract the volume of the cerebellar vermis. The volume was normalized to the total intracranial volume estimated from the next step.

Freesurfer version 5.3 was used to automatically segment the brain including the subcortical structures (Fischl et al., 2002). Segmentation of the pons was based on probabilistic atlas and Bayesian inference approach (Iglesias et al., 2015) implemented in Freesurfer version 6. The segmented images were visually inspected to detect segmentation errors and the need for manual editing. The segmentation process was however very good and there was no need for manual correction.

#### **6.2.4 Rate of atrophy**

The volumes of the cerebellum and the pons estimated from automatic segmentation and normalized to the intracranial volume were used to evaluate the rate of atrophy. The two regions were chosen because they are primarily affected in SCAs (Yamada et al., 2008). Atrophy was calculated as the percentage change relative to baseline and normalized by the duration (time between visits in months) as represented in the equation below (Reetz et al., 2013).

$$\text{Rate of atrophy} = \frac{\left( \frac{\text{followup value} - \text{baseline value}}{\text{baseline value}} \right)}{\text{visit interval (months)}}$$

#### **6.2.5 Diffusion tensor imaging**

The DTI datasets were visually inspected for head movements, missing volumes and spike noise. Data with extensive artifacts were excluded from the analyses. The diffusion data were also denoised (Veraart et al., 2016a; Veraart et al., 2016b) to improve the signal to noise ratio (SNR). Tools available in FMRIB Software Library (FSL) version 5.0.8 (<http://www.fmrib.ox.ac.uk>) were used for processing the data. The FSL brain extraction tool (BET) (Smith, 2002) was used to strip the skull and create a DTI mask. Eddy current correction was performed to correct for motion and geometric distortions. A combination of topup (Andersson et al., 2003; Smith et al., 2004) and eddy (Andersson & Sotiropoulos, 2016)

were applied to achieve optimal eddy current and motion correction as well as susceptibility-induced off-resonance field distortion correction. The diffusion tensor model was then fitted to generate diffusion metrics such as FA and RD. FA indicates fiber integrity and decreased FA usually reflects reduced fiber bundle. RD represents diffusion across the fibers and increased RD often correlates with changes in axonal diameter, demyelination or myelin injury. Tract based spatial statistics with threshold-free cluster enhancement (Smith et al., 2006) were performed on the diffusion metrics – FA and RD – to compare the SCA groups with controls using FSL randomise (Winkler et al., 2014) at  $p < 0.05$ . FSL randomise was also used to evaluate the correlation between FA and cerebellar and pontine atrophy. All statistical tests with FSL randomise were performed with 5000 permutations and family-wise error correction of significance at  $p < 0.05$ .

### **6.2.6 Tractography - Fixel based analysis**

Tractography, also known as fiber tracking, provides a way to extract complex white matter pathways, which otherwise are underestimated using the diffusion tensor model. Though the DTI model is widely used, it is limited in its ability to distinguish between different fiber populations within a voxel (Alexander et al., 2001; Alexander et al., 2002). In this study, we reported whole brain statistical analysis on specific fiber populations in a voxel known as fixel (Raffelt et al., 2015; Raffelt et al., 2017). The processing steps have previously been fully detailed (Raffelt et al., 2012b; Raffelt et al., 2015; Raffelt et al., 2017) and were performed using the MRtrix software version 0.3.15. The diffusion data were denoised (Veraart et al., 2016a; Veraart et al., 2016b) to improve the SNR and upsampled by a factor of 2 to improve the contrast. FSL BET (Smith, 2002) was used to create the brain mask since the mask creation process suggested by MRtrix left holes in the mask, which affected subsequent steps. Motion artifacts, eddy current and susceptibility-induced off-resonance field distortion were corrected with FSL tools as described. The data were then corrected for field inhomogeneity (Tustison et al., 2010) and the image intensity was normalized across all subjects. The constrained spherical deconvolution (CSD) approach that accounts for non-white matter tissue composition (Dhollander et al., 2016) was used to estimate the fiber orientation distribution (FOD) (Jeurissen et al., 2014) from the averaged response function of all subjects. An equal number of controls ( $n = 20$ ) and SCA patients ( $n = 20$ ) was used to generate a population template for the FOD to which all subjects' FOD was registered

(Raffelt et al., 2011; Raffelt et al., 2012a). The FODs in the template space were segmented to estimate FD, FC and a combination of both, FDC (Raffelt et al., 2017). FD relates to the volume of the intra-axonal compartment for a specific fiber population (fixel) whilst FC refers to the volume perpendicular to the fiber bundle. Following the recommendations from the MRtrix manual, whole brain tractogram (Tournier et al., 2010) of the template image was generated with 20 million tracts after which it was filtered to 2 million tracts to reduce biases and generate an anatomically meaningful tractogram (Smith et al., 2013). The connectivity-based fixel enhancement (Raffelt et al., 2015) was used to perform statistical analysis between the SCA groups and controls on FD, FC and FDC with 5000 permutations and family-wise error corrected significance at  $p < 0.05$ . For each SCA group, a mask was created from regions that showed significant differences in FDC and this was used to extract the fixel values that were then used for correlation analysis with clinical parameters and the rate of atrophy.

### 6.2.7 Statistical analysis

The effect size for clinical scores, manual segmentation and automatic segmentation by Freesurfer was calculated as the mean change to the standard deviation of the change (Reetz et al., 2013).

$$Effect\ size = \frac{\Sigma \left( \frac{\left( \frac{followup\ value - baseline\ value}{baseline\ value} \right)}{visit\ interval\ (months)} \right)}{SD(change\ in\ value)}$$

Where SD represents standard deviation.

Since diffusion and tractography metrics were measured at one time point, the effect size for FA and FDC were calculated between the SCA groups and the controls using Cohen's  $d$  represented in the following equation (Cohen, 1988):

$$d = \frac{(M_1 - M_2)}{\sqrt{((SD_1^2 + SD_2^2)/2)}}$$



where  $M_1$  = mean value for controls,  $M_2$  = mean value for a specific SCA,  $SD_1$  = standard deviation of controls and  $SD_2$  = standard deviation of the specific SCA group.

The scale for the effect size was set at 0.2, 0.5, 0.8, 1.2 and 2.0 as small, medium, large, very large and huge changes, respectively (Cohen, 1988; Sawilowsky, 2009).

Within group difference in clinical parameters between baseline and follow-up were evaluated with paired *t*-test. One way ANOVA with Bonferroni multiple test correction was used to determine between group differences of clinical parameters at each time point. The rate of atrophy was evaluated with ANOVA and when significant, Dunnett test was performed to correct for multiple comparison between each SCA group and the control group. For each SCA group separately, Pearson correlation was performed between FDC values, the rate of atrophy and clinical parameters with the step-down Bonferroni multiple correction approach (Holm, 1979); *p* values of  $< 0.05$  were considered significant.

## **6.3 Results**

### **6.3.1 Clinical score**

Patients with SCA showed decreased motor performance abilities with increased SARA scores and CCFS after 24 months (Figure 21). There was no difference, though, in the SARA scores and CCFS across the SCA groups at baseline and after 24 months.

### **6.3.2 Volumetric analysis**

Manual segmentation only focused on the vermis and no change in volume was observed after 24 months except in SCA7 (Figure 22a). However, automatic segmentation with Freesurfer showed decreased cerebellar and pontine volume after 24 months in all SCA groups, and even among healthy controls ( $p < 0.05$ ) (Figure 22b and 22c). With its sensitivity to change over time, the rate of atrophy performed on the values obtained from Freesurfer segmentation showed a faster rate of atrophy in patients with SCA compared to controls in both the cerebellum and the pons ( $p < 0.05$ ) (Figure 23).

### **6.3.3 Diffusion tensor imaging**

Diffusion data were not acquired for 2 patients with SCA1, 2 patients with SCA3, 3 patients with SCA7 and 2 healthy controls. Datasets that did not meet the quality control criteria and had to be rejected for one patient with SCA1, 2 patients with SCA2, 2 patients with SCA3 and one healthy control. All SCA groups displayed decreased FA compared to controls, except for patients with SCA7 (Figure 24a). Additionally, RD was increased across all SCA groups compared to controls ( $p < 0.05$ ) (Figure 24b). Most of the changes in diffusion metrics were localized to the cerebellar and cerebral peduncles, as well as the pontine crossing tracts. However, the corticospinal tract (CST), corona radiata and internal capsule were also affected in patients with SCA1 and SCA2. Furthermore, the corpus callosum was altered in patients with SCA2. Of note, atrophy in the cerebellum and the pons correlated with FA in patients with SCA1 (Figure 24c and 24d).

### **6.3.4 Fixel Based Analysis**

The preprocessing steps yielded improved SNR and contrast in the datasets (Figure 25). A visual inspecting the FODs already shows some differences between controls and SCAs, with controls having more fiber distributions in the CST than SCAs (Figure 26). Using the template fixel mask and template tractogram and performing connectivity-based fixel enhancement statistics on the subject groups revealed decreased FD, FC and FDC in the CST of all SCA patients compared to controls ( $p < 0.05$ ). A significant decrease of FD was also observed in the corpus callosum of SCA7 patients ( $p < 0.05$ ) (Figure 27). FDC correlated with the SARA score and CCFS in patients with SCA1 and SCA3. Furthermore, FDC correlated with cerebellar atrophy in patients with SCA1 (Figure 28).

### **6.3.5 Effect size**

Clinical scores and brain volume were assessed at baseline and follow-up so that effect sizes could be calculated using the method proposed by Reetz et al. (Reetz et al., 2013). Clinical scores showed low effect size ( $<0.8$ ) whilst segmentation with Freesurfer showed high effect size ( $>1.2$ ) (Table 3) in patients with SCA. Manual segmentation showed low effect size

(<0.5). Using the Cohen's *d* (Cohen, 1988), FA, the most common DTI metric, and FDC, a tractography metric, also showed high effect sizes (>1.2 and >2.0, respectively). Likewise, the effect sizes of FDC were on average 1.2 times higher than those of FA (Table 3).

**Table 2: Demographic parameters of participants.**

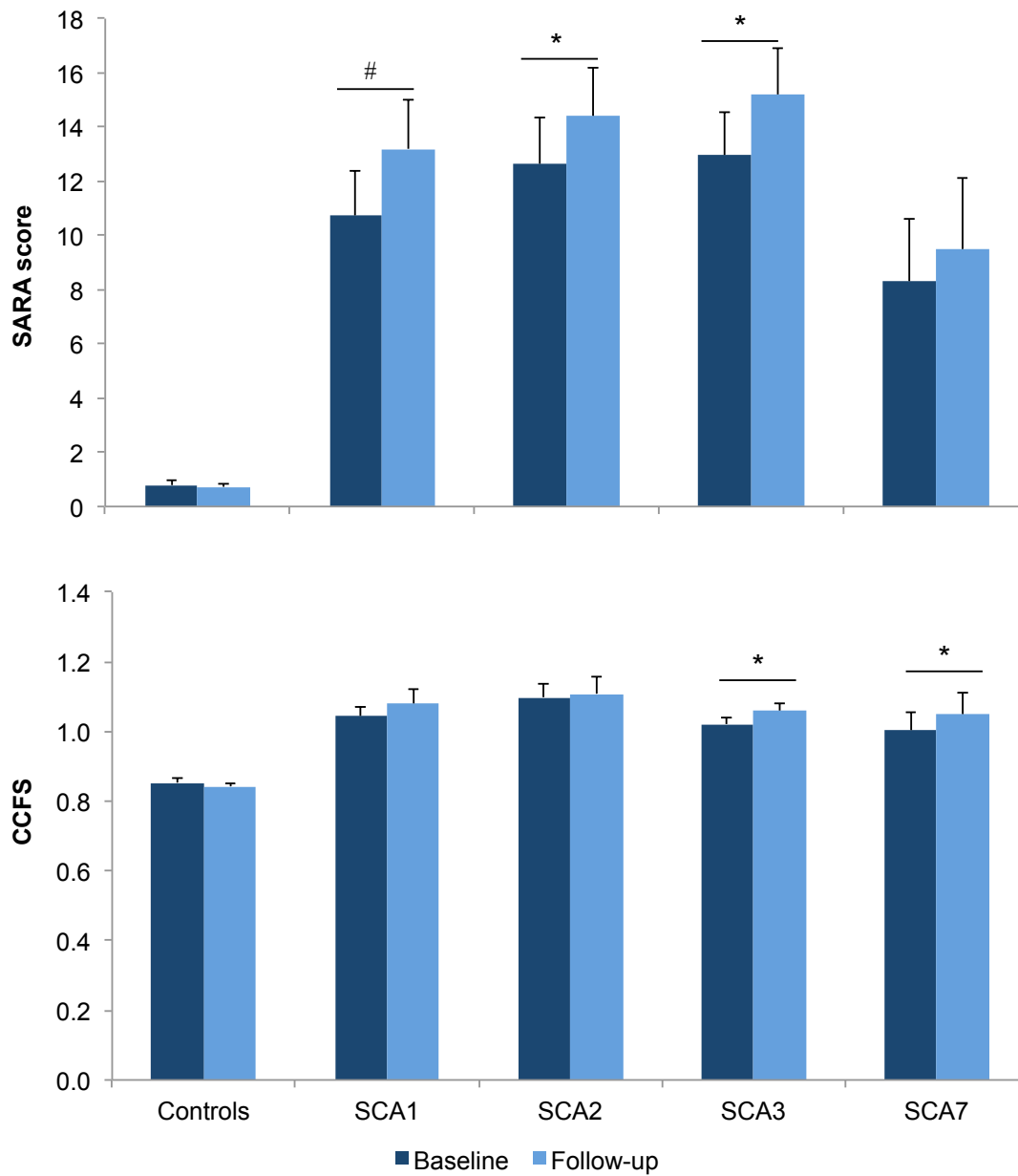
<b>Variable</b>	<b>Control</b>	<b>SCA1</b>	<b>SCA2</b>	<b>SCA3</b>	<b>SCA7</b>
<b># Participants</b>	24	15	12	20	10
<b>Sex (M/F)</b>	11/13	9/6	7/5	8/12	5/5
<b>Age (yr)<sup>a</sup></b>	50±13	43±15	45±13	51±12	48±14
<b>Age (yr)<sup>b</sup></b>	52±13	45±15	47±13	53±12	50±14
<b>BMI (Kg/m<sup>2</sup>)<sup>a</sup></b>	25.3±3.9	23.6±6.3	25.7±4.6	23.7±4.5	22.1±1.8
<b>BMI (Kg/m<sup>2</sup>)<sup>b</sup></b>	25.3±3.6	23.6±6.7	26.6±4.4	24.1±4.8	22.7±2.6
<b>SARA score<sup>a</sup></b>	0.8±0.8	10.7±6.3 <sup>†</sup>	12.6±6.0 <sup>†</sup>	13.0±7.2 <sup>†</sup>	8.3±7.4 <sup>†</sup>
<b>SARA score<sup>b</sup></b>	0.7±0.7	13.2±7.0 <sup>†</sup>	14.4±6.3 <sup>†</sup>	15.2±7.5 <sup>†</sup>	9.5±8.3 <sup>†</sup>
<b>CCFS<sup>a</sup></b>	0.9±0.1	1.0±0.1 <sup>†</sup>	1.1±0.1 <sup>†</sup>	1.0±0.1 <sup>†</sup>	1.0±0.2 <sup>#</sup>
<b>CCFS<sup>b</sup></b>	0.8±0.0	1.1±0.2 <sup>†</sup>	1.1±0.2 <sup>†</sup>	1.1±0.1 <sup>†</sup>	1.0±0.2 <sup>#</sup>
<b>CAG length</b>		47±7	40±3	69±6	41±3
<b>Disease duration<sup>a</sup></b>		7±6	10±6	9±5	9±6
<b>Disease duration<sup>b</sup></b>		9±6	12±6	11±5	11±5

<sup>a</sup>Parameters at baseline; <sup>b</sup>parameters at follow-up. Data are presented as mean ± standard deviation. <sup>†</sup>p ≤ 0.001 and <sup>#</sup>p ≤ 0.01 represent significant differences between SCAs and controls. There was no difference in the other demographic parameters between the SCAs. p values were obtained with one-way ANOVA and Bonferroni correction.

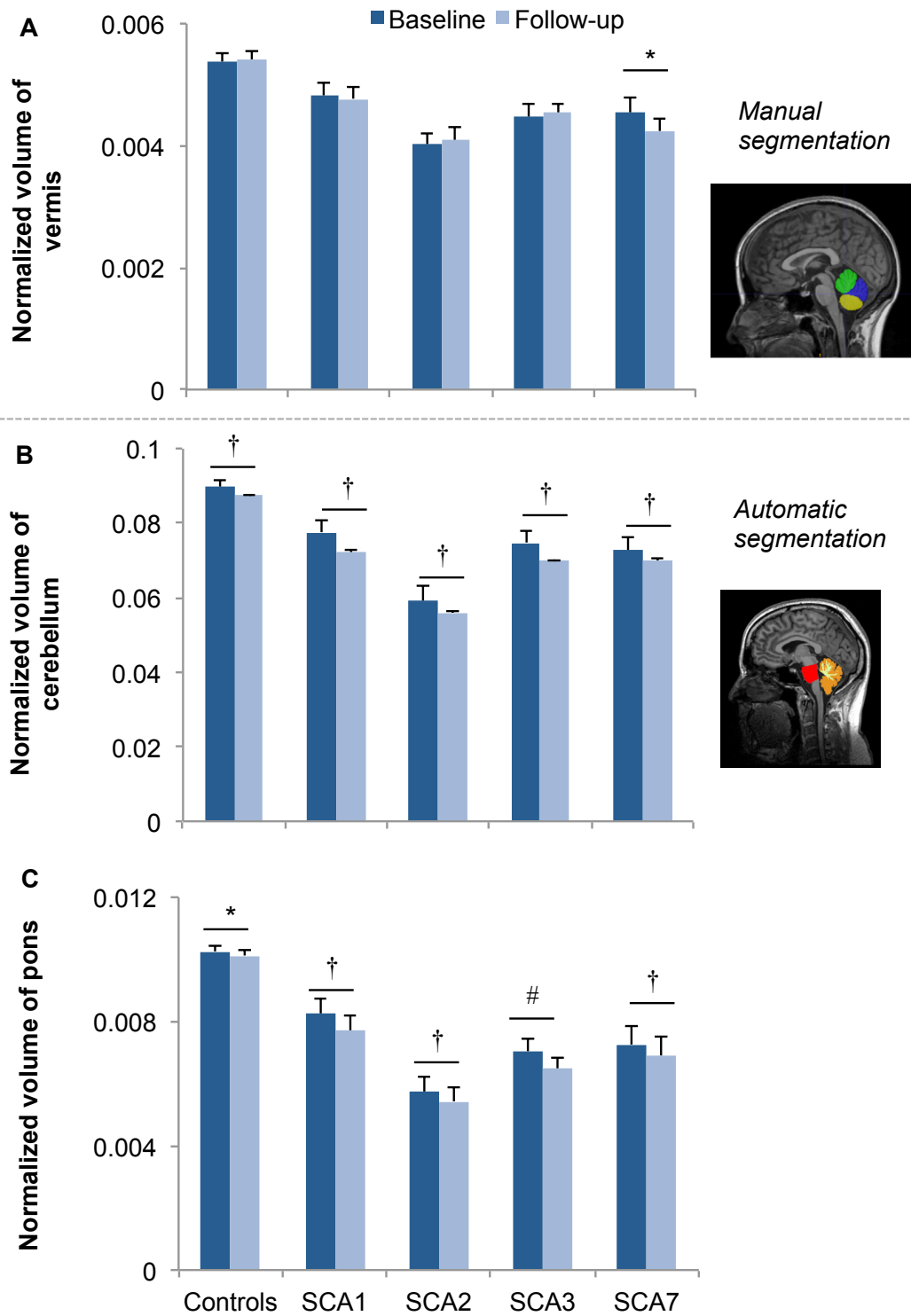
**Table 3: Effect size of clinical scores and brain imaging parameters**

	Clinical scores		Brain volumetry			Diffusion imaging	
	SARA	CCFS	FS cerebellum	FS pons	MN vermis	FA	FDC
<b>SCA1</b>	0.75	-0.40	-1.49	-1.43	-0.11	1.76	1.87
<b>SCA2</b>	0.77	0.17	-1.45	-1.77	0.18	1.88	2.36
<b>SCA3</b>	0.82	0.67	-1.15	-1.29	0.31	2.42	3.16
<b>SCA7</b>	0.05	0.82	-1.66	-3.43	-0.70	2.10	2.65
<b>Control</b>	-0.10	-0.21	-0.83	-0.44	0.16	-	-

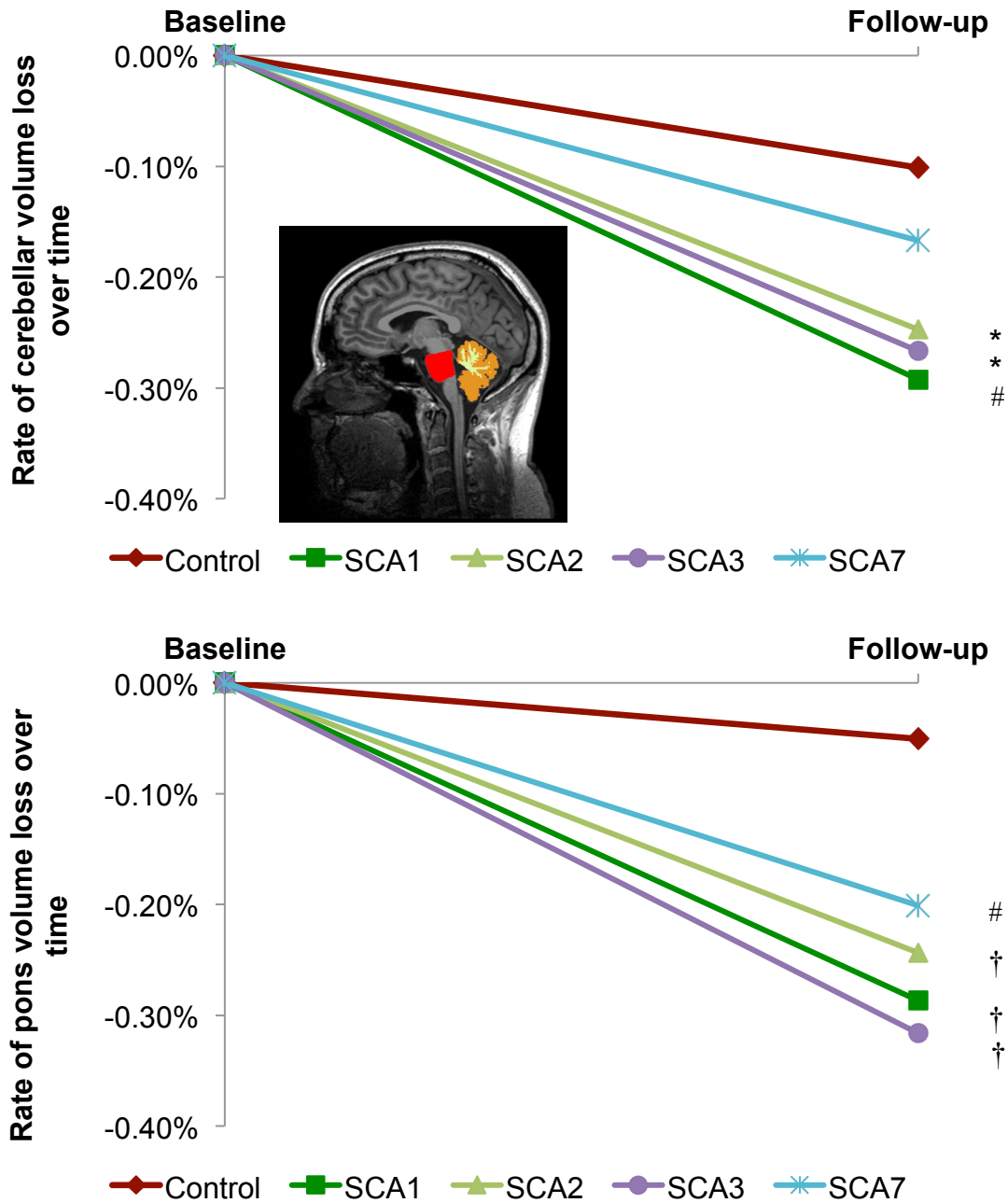
FS cerebellum and FS pons: Automatic Freesurfer segmentation of cerebellum and pons; Manual vermis: manual segmentation of the vermis. The following key represents the effect size: 0.2: small, 0.5: medium, 0.8: large, 1.2: very large, 2.0: huge changes (Cohen, 1988; Sawilowsky, 2009).



**Figure 21: Change in clinical scores after 24 months.** All SCAs showed an increase in SARA scores that reached significance in SCA1, SCA2 and SCA3. CCFS was also significantly increased in SCA3 and SCA7. Error bars represent standard error of mean (SEM) (\*  $p < 0.05$ , #  $p \leq 0.01$ ).

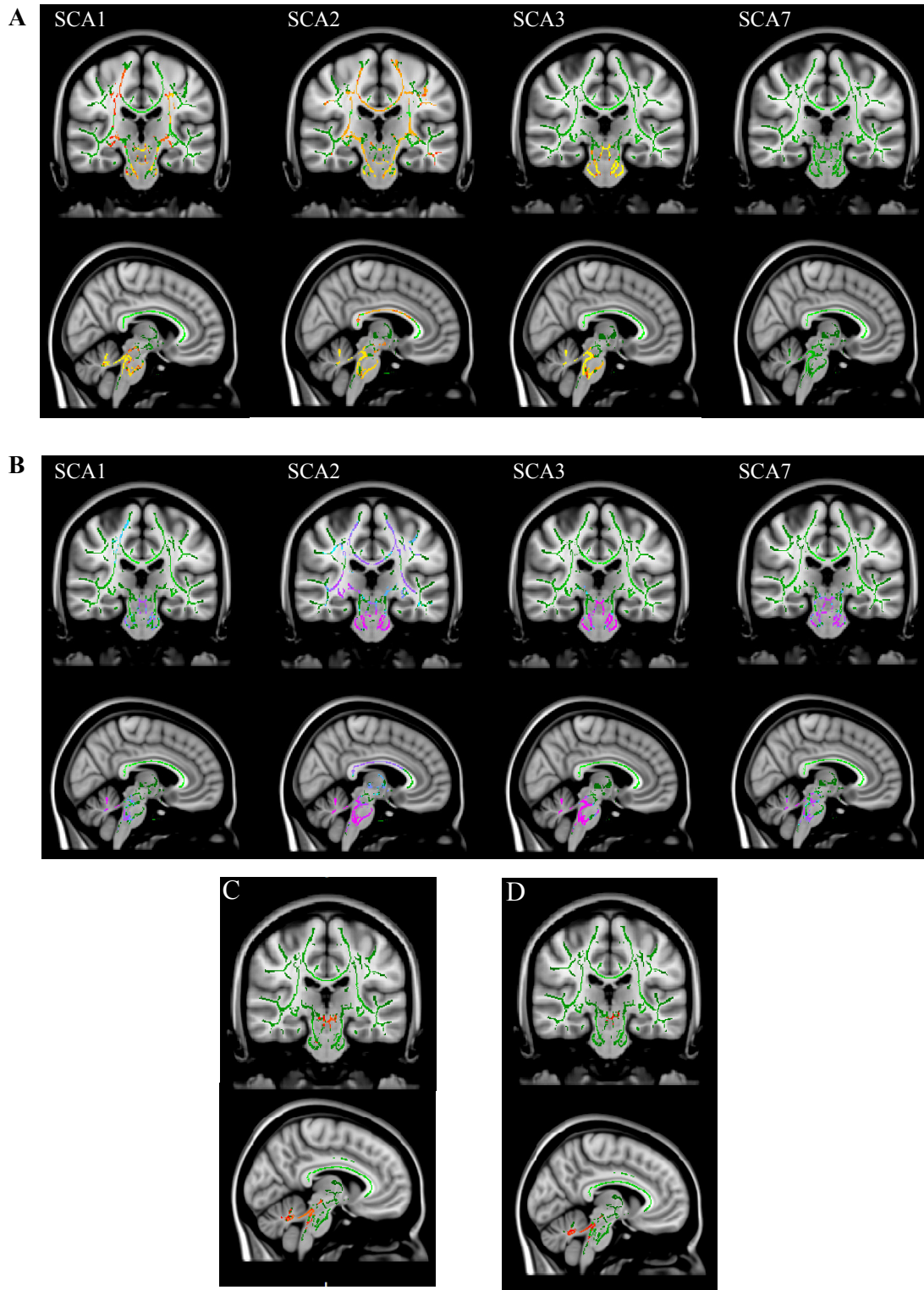


**Figure 22: Change in regional volume after 24 months.** A) Manual segmentation of the vermis showed a significant change in volume only in SCA7. Freesurfer segmentation showed that there is a decrease in the B) cerebellum and C) pons in the controls and patients with SCA over 24 months. Error bars represent standard error of mean (\*  $p < 0.05$ , #  $p \leq 0.01$ , †  $p \leq 0.001$ ).

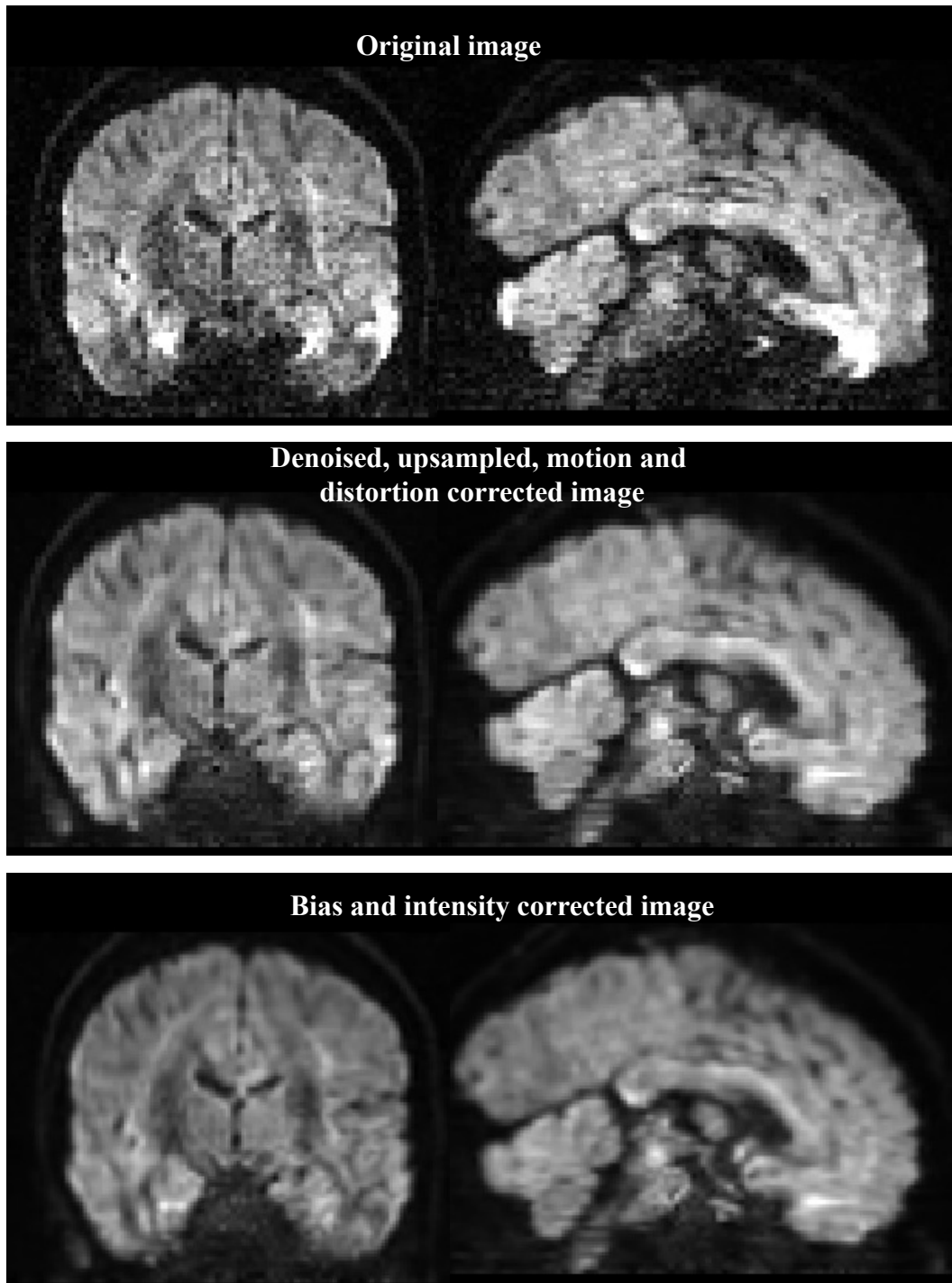


**Figure 23: Rate of atrophy in the cerebellum and pons.** A faster rate of atrophy is observed in patients with SCA compared to controls in both the cerebellum and pons with a faster rate in the pons (\*  $p < 0.05$ , #  $p \leq 0.01$ , †  $p \leq 0.001$ ).

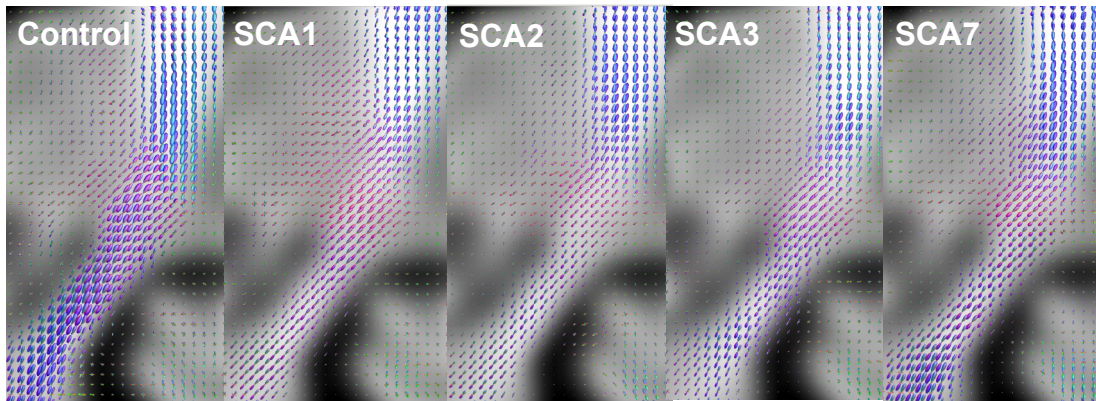
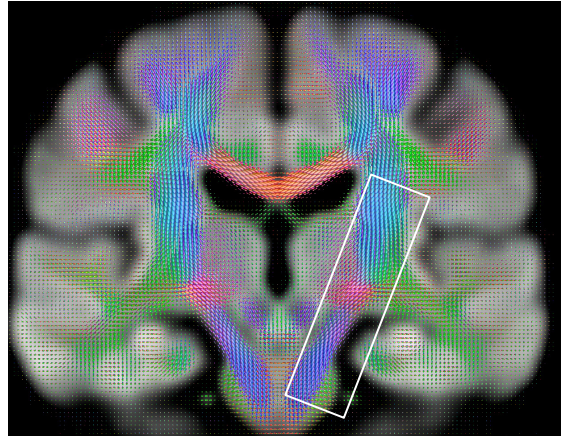




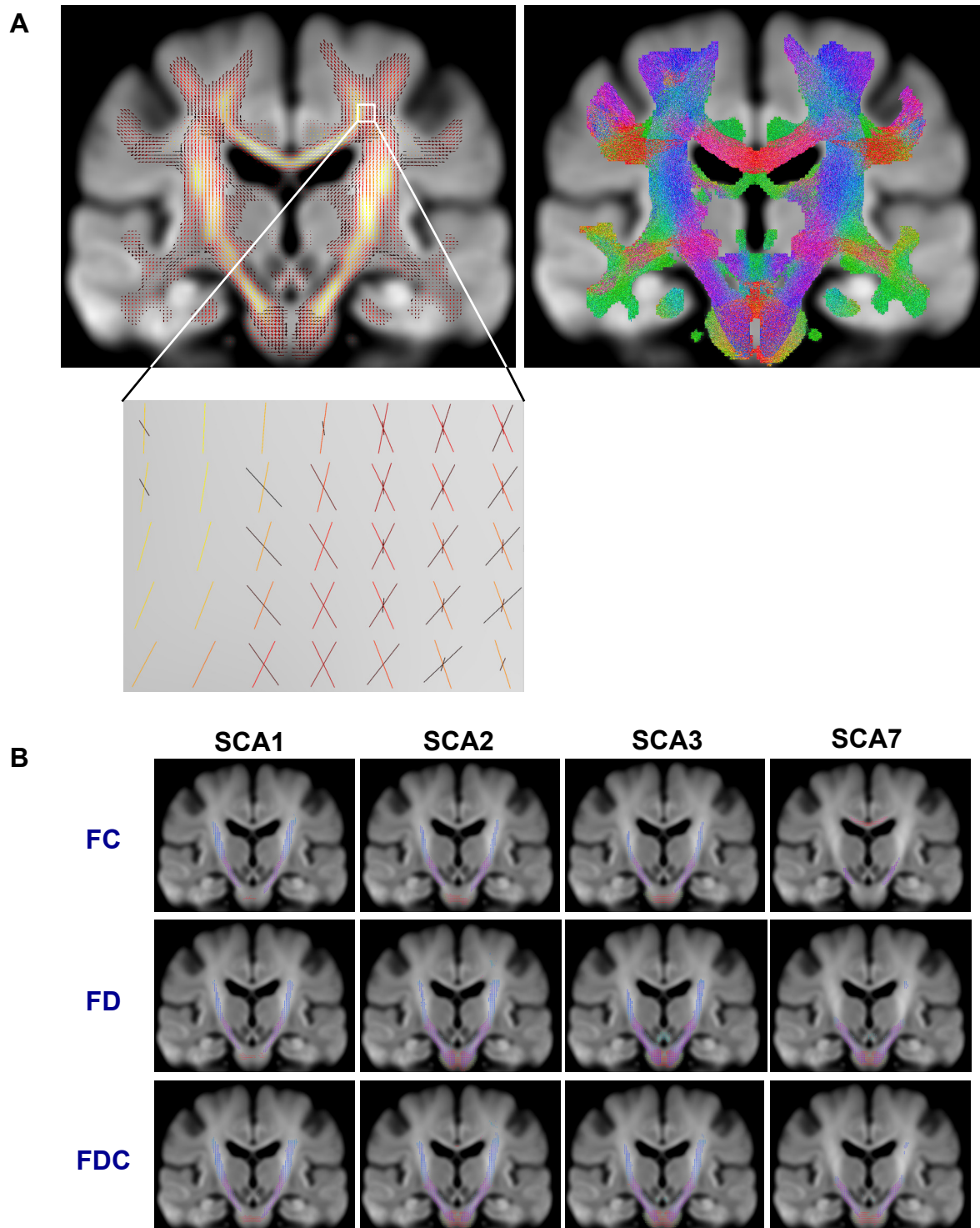
**Figure 24: Tract based statistical analysis of FA and RD in SCAs and controls.** (A) Red-yellow highlights show areas of decreased FA in SCAs ( $p < 0.05$ ). (B) Pink regions show areas of increased RD in SCAs ( $p < 0.05$ ). FA correlated with (C) cerebellar atrophy and (D) pontine atrophy in SCA1 ( $p < 0.05$ ) (Red highlights).



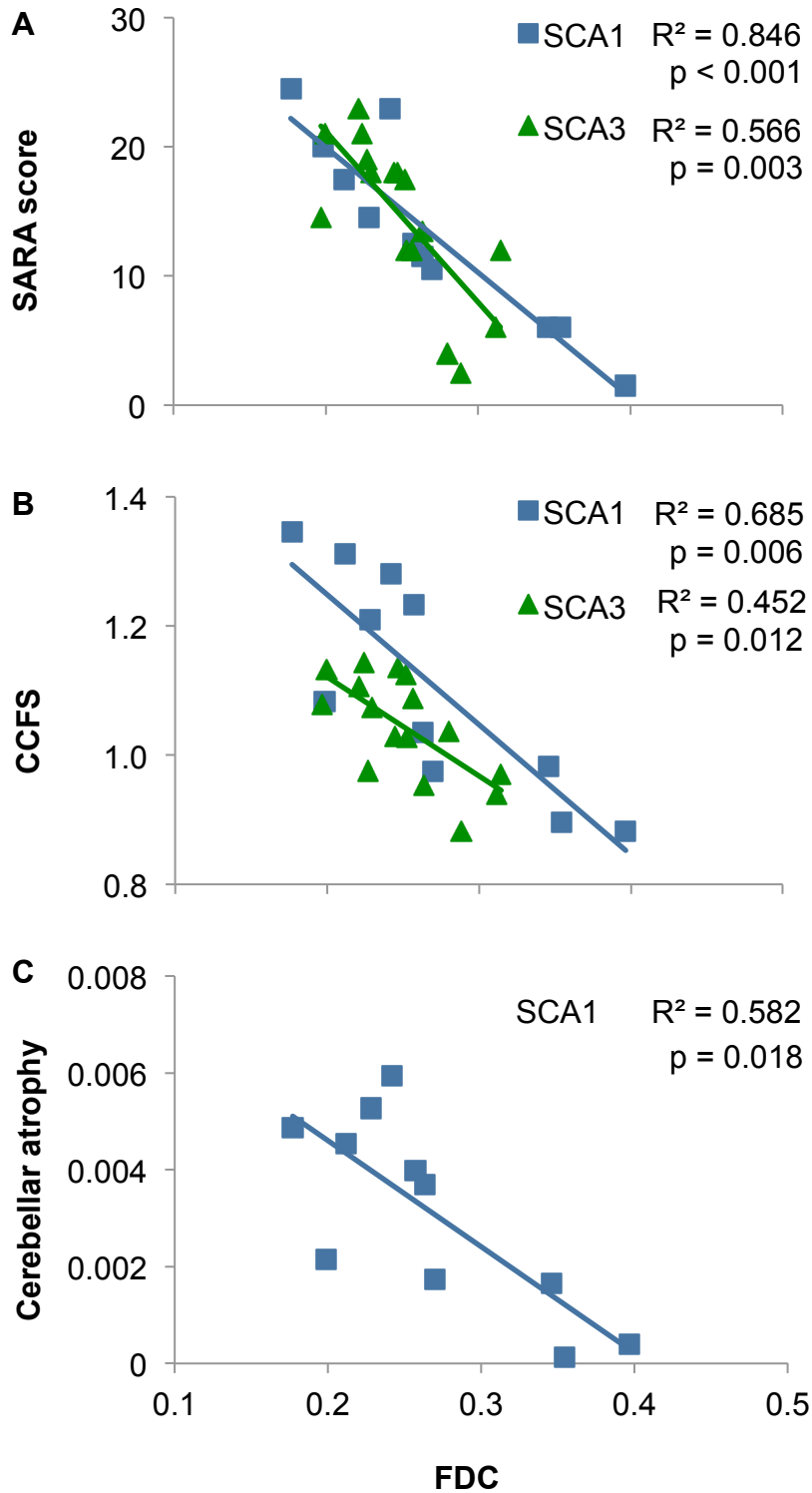
**Figure 25: The preprocessing steps of the diffusion data for FBA.** The diffusion data were denoised (Veraart et al., 2016a; Veraart et al., 2016b) and upsampled by a factor of two to improve SNR and contrast. The upsampled data were then corrected for motion, eddy current and susceptibility distortions as well as bias and intensity correction using FSL and MRtrix.



**Figure 26: Distribution of fibers in the CST in SCAs and controls.** Visual inspection of the FODs seems to show that controls have more fiber distributions than SCAs.



**Figure 27: Connectivity-based fixel enhancement on FD, FC and FDC.** A) The fixel mask and tractogram used for the statistics. (B) FD, FC and FDC are significantly reduced in the CST of SCAs ( $p < 0.05$  with family-wise error correction). Fiber colors are directional: blue = superior-inferior direction; red = left-right direction; green = anterior-posterior direction.



**Figure 28: FDC correlation with clinical scores and cerebellar atrophy.** FDC correlated negatively with (A) SARA score and (B) CCFS in SCA1 and SCA3. (B) FDC correlated negatively with cerebellar atrophy in SCA1.

## 6.4 Discussion

This study compared clinical scores and imaging parameters in terms of sensitivity to change in a unique cohort of patients with SCA1, SCA2, SCA3 and SCA7. We identified high effect sizes for volumetric and tractography parameters compared to clinical scores. Likewise, we advocate to use these imaging parameters in upcoming clinical trials in SCAs. In addition, we report a new approach (FBA) to probe white matter fiber integrity in SCAs. FBA allows the analysis of individual fibers in each voxel making it more sensitive and robust compared to FA, the conventional DTI metric. We showed that FA may not be a reliable metric for use in clinical trials as it detected no microstructural change in SCA7. Instead, using FBA analyses, we identified white matter fiber changes in the CST of all SCAs, including SCA7.

Volumetric studies performed in SCA have reported smaller brain regions compared to controls, including the cerebellum, brainstem and cerebellar peduncles (Yamada et al., 2008; Durr, 2010; Schulz et al., 2010; Rüb et al., 2013). The rate of volumetric change, though, has only been reported by Reetz et al. (Reetz et al., 2013) who compared the rate of atrophy across patients with SCA1, SCA3 and SCA6, but not with controls. They reported greater atrophy in the brainstem and left cerebellar hemisphere in patients with SCA1 compared to SCA3 (Reetz et al., 2013). In patients with SCA1 and SCA3, Reetz et al. also reported large effect sizes for the SARA scores ( $>1.2$ ) and the pons atrophy ( $>0.8$ ) but low effect sizes ( $<0.8$ ) for the cerebellum (Reetz et al., 2013). In contrast, we reported atrophy rates in patients with SCA1, SCA2, SCA3 and SCA7 in reference to healthy controls. Our data were acquired on a 3 T MR system that gives twice the image resolution and contrast compared to the 1.5 T system used in the study by Reetz et al. In our estimation of brain volumes, we also used a fully automated method without user interference whilst Reetz et al. used a semi-automated method that included user defined regions of interest. Although our findings need to be confirmed in an independent cohort using the same methodologies and high spatial resolution, we found high effect sizes for the rate of atrophy of the cerebellum and the pons compared to the SARA and CCFS. The discrepancy between the rate of clinical progression and brain atrophy was especially striking for patients with SCA7. This may be, in part, explained by the small sample size of this patient group ( $n = 10$ ) and their relative early symptomatic stage. Nonetheless, SCA7 is a severe disease, as outlined by the common occurrence of additional non-neurological symptoms (retina, heart), so that a fast rate of brain atrophy is expected.

Using diffusion tensor metrics, we observed decreased FA across several tracts, with the exception of SCA7, associated with increased RD in all SCA groups, including SCA7. Decreased FA in the corpus callosum of patients with SCA2 is in agreement with previous studies (Hernandez-Castillo et al., 2015; Mascalchi et al., 2015). In contrast to Kang et al. (Kang et al., 2014), we did not find any change in FA and RD in the corpus callosum, internal capsule and corona radiata in patients with SCA3. These previous DTI studies conducted in SCAs did not make mention of the quality control process used to include or reject data with missing volumes or spikes. It is therefore possible that the noise in their dataset contributed to the statistically significant differences found in many brain regions.

Even though TBSS is highly favored due to its elimination of user drawn regions of interest and reasonable control on misalignments that may arise when different images are registered together, it is still limited as it is highly dependent on FA. But FA cannot differentiate between different fiber populations in a voxel (Alexander et al., 2001; Alexander et al., 2002), hence the need for higher-order models. To resolve the limitations of FA, Rozenfeld et al. performed fiber tracking using the deterministic approach that assumes that fibers have a single orientation within each voxel, and requires prior knowledge of the orientation of fibers before its application (Rozenfeld et al., 2015). However, one cannot be certain of the orientation of the fibers as each voxel contains several populations of axons that may be oriented in different directions. With high uncertainty in estimating the fiber direction and evaluating crossing fibers, the deterministic approach is therefore less robust and less sensitive as compared to the probabilistic approach (Petersen et al., 2016; Schlaier et al., 2017) that overcomes the problem of uncertainty in fiber orientation and accounts for multiple fibers in each voxel. Kang et al. (Kang et al., 2014) and Prakash et al. (Prakash et al., 2009) used the probabilistic approach but with algorithms that have more fiber orientation error rate and low fiber detection rate as compared to the non-negativity CSD approach (Tournier et al., 2007; Wilkins et al., 2015). This is why we chose to implement fiber tract specific analysis, i.e. FBA, in our SCA cohort. FBA has been successfully applied in traumatic brain injury (Wright et al., 2017) and in motor neuron disease (Raffelt et al., 2015; Raffelt et al., 2017). In our study, FBA revealed decreased FD in the pontine crossing, CST, cerebral peduncle, internal capsule and corona radiata in patients with SCA1, SCA2 and SCA3. In patients with SCA7, contrary to the results obtained with FA, FD was decreased in the corpus callosum and cerebral peduncles. Decreased FD could either be a result of atrophy leading to a decrease in the volume, or dense packing of the axons leading to reduced axonal volume. However,

decreased FC suggested a reduced number of axons in these regions in patients with SCA. Furthermore, FDC correlated with cerebellar atrophy in patients with SCA1 and the clinical scores in patients with SCA1 and SCA3. Hence, we can attribute the combined effect of FD and FC to brain atrophy and reduction in the number of fibers in SCAs.

In conclusion, clinical scores such as the SARA and the CCFS are widely used to evaluate ataxia, but their low effect sizes make them less suited for therapeutic trials in very rare disorders like SCAs. Furthermore, they cannot be of use in presymptomatic individuals. Using volumetry methods that limit user interference, and tractography techniques with CSD approach (i.e. FBA) that are sensitive to subtle changes otherwise overlooked by DTI metrics (e.g. FA), we identified biomarkers with very large effect sizes in SCAs, making them suitable for therapeutic trials. Since a single biomarker is likely to fail reflecting the complexity of the neurodegenerative cascades leading to the onset and progression of SCAs, a multimodal biomarkers approach, aiming at the integration and visualization of multivariate datasets, can also be applied, as recently shown in our SCA cohort at baseline (Garali et al., 2017).



# Chapter 7

## Organisation:

<b>Study 6: A strategy for multimodal data integration: application to biomarkers identification in spinocerebellar ataxia .....</b>	<b>139</b>
7.1 Introduction and objectives .....	139
7.2 Materials and methods.....	139
7.3 Principal results .....	140
7.4 Perspective.....	140
7.5 Published article .....	140

## **Study 6: A strategy for multimodal data integration: application to biomarkers identification in spinocerebellar ataxia**

### **7.1 Introduction and objectives**

Using individual methods can help answering questions pertaining to specific areas of a disease. For example, MRS benefits from identifying alterations to metabolites due to the disease whilst DTI gives information on the structural integrity of white matter fibers in the brain. However, in order to fully understand the biochemical basis of the disease, a process that is capable of integrating multi-datasets from different modalities is crucial. Likewise, to understand the pathophysiology of polyglutamine diseases and identify robust biomarkers, several modalities including imaging, metabolomics, transcriptomics, lipidomics, among others, have been used to obtain measures that could best explain the underlying disease mechanisms. In light of these growing number of modalities, new statistical approaches are needed of data integration to relate the modalities to i) better explain the disease and ii) identify biomarkers with high effect sizes.

This study presents a statistical approach of data integration using reported – MRS and volumetric data – and unreported data – metabolomics, lipidomics and calorimetric data – from studies 5 and 6 performed at baseline on the SCA dataset (ClinicalTrials.gov Identifier: NCT01470729).

### **7.2 Materials and methods**

This study was performed using data collected at baseline from studies 5 and 6. In addition to the MRS and volumetric data presented in the previous studies, other modalities such as calorimetry, metabolomics and lipidomics datasets were included.

Multivariate analyses were performed using the regularized generalized canonical correlation analysis (RGCCA). RGCCA works to reduce the number of blocks (modalities) into variables that summarize the information between and within each block. RGCCA was coupled with its sparse generalized canonical correlation analysis (SGCCA), a variable selection procedure that can identify most relevant features that are linked between and within each block. Since in SCA the atrophy of the pons progresses faster than in the cerebellum, we

chose to identify the link between the pons atrophy and changes observed with the other modalities (MRS, volumetry, calorimetry, metabolomics and lipidomics).

### **7.3 Principal results**

This method of RGCAA/SGCAA was able to take into account the heterogeneous nature and sizes of the datasets obtained from different modalities in patients with SCA and controls. Separation between patients and controls was best achieved with the MRS modality. Among patients with SCA, SCA7 was separated from the other SCAs due to the possible influence of certain lipid species (sphingolipids and phospholipids) detected in plasma by lipidomic analyses.

### **7.4 Perspective**

The next step is to apply this statistical method on the longitudinal dataset (baseline and 24 months) of the BIOSCA study, as well as on the multimodal datasets from the ongoing studies conducted in HD (TRIHEP3, REVHD, HDeENERGY).

### **7.5 Published article**

# A strategy for multimodal data integration: application to biomarkers identification in spinocerebellar ataxia

Imene Garali, Isaac M. Adanyeguh,\* Farid Ichou,\* Vincent Perlberg, Alexandre Seyer, Benoit Colsch, Ivan Moszer, Vincent Guillemot, Alexandra Durr, Fanny Mochel\* and Arthur Tenenhaus\*

\* These authors contributed equally to this work.

Corresponding author: Arthur Tenenhaus, Laboratoire des Signaux et Systèmes at CentraleSupélec Gif-sur-Yvette, France. Tel.: +33 (0)169851422; E-mail: arthur.tenenhaus@centralesupelec.fr

## Abstract

The growing number of modalities (e.g. multi-omics, imaging and clinical data) characterizing a given disease provides physicians and statisticians with complementary facets reflecting the disease process but emphasizes the need for novel statistical methods of data analysis able to unify these views. Such data sets are indeed intrinsically structured in blocks, where each block represents a set of variables observed on a group of individuals. Therefore, classical statistical tools cannot be applied without altering their organization, with the risk of information loss. Regularized generalized canonical correlation analysis (RGCCA) and its sparse generalized canonical correlation analysis (SGCCA) counterpart are component-based methods for exploratory analyses of data sets structured in blocks of variables. Rather than operating sequentially on parts of the measurements, the RGCCA/SGCCA-based integrative analysis method aims at summarizing the relevant information between and within the blocks. It processes a priori information defining which blocks are supposed to be linked to one another, thus reflecting hypotheses about the biology underlying the data blocks. It also requires the setting of extra parameters that need to be carefully adjusted.

**Imene GARALI** obtained her PhD degree from Aix-Marseille University in 2015 in image processing. Since 2016, she is a postdoctoral researcher at the Bioinformatics and Biostatistics Core Facility of the Brain and Spine Institute, La Pitié-Salpêtrière Hospital, Paris, France.

**Isaac Adanyeguh** is PhD student at the Pierre and Marie Curie University whose research focuses on biomarker identification and disease modelling in polyglutamine disorders using multimodal neuroimaging approaches.

**Farid Ichou** is currently working as metabolomic core manager and researcher at ICANalytics department, institute of cardiometabolism and nutrition, Paris, France. His research interests include study of gut-derived metabolite, discovery approach and translational research in preclinical and clinical studies for cardiometabolic and neurodegenerative diseases.

**Vincent Perlberg** is a research engineer at the Bioinformatics and Biostatistics Core Facility of the Brain and Spine Institute, La Pitié-Salpêtrière Hospital, in charge of biomarkers identification in neuroimaging.

**Alexandre Seyer** is currently researcher at the SpectMet platform of the MedDay Pharmaceuticals company, Paris, France. His research focus on the identification of new therapeutic targets for nervous system disorders through metabolomic and lipidomic analysis in preclinical and clinical studies.

**Benoit Colsch** is currently research scientist in the LEMM Laboratory at CEA-Saclay, France. His research interests are based on the development of qualitative and quantitative methods using LC-MS in lipidomics and metabolomics projects in the field of neurosciences.

**Ivan Moszer** is currently managing the Bioinformatics and Biostatistics Core Facility of the Brain and Spine Institute, La Pitié-Salpêtrière Hospital (Paris, France), which provides scientists and clinicians with expert support in omics data processing and high-dimensional heterogeneous data analysis.

**Vincent Guillemot** is currently a research engineer at Institut Pasteur, in the Statistical Genetics group, and in the Bioinformatics / Biostatistics Core Facility.

**Alexandra Durr** is full professor and consultant in genetics at the Pitié-Salpêtrière University Hospital in Paris, developing translational neurogenetics at the Brain and Spine Institute.

**Fanny Mochel** is an associate professor of genetics at the University Pierre and Marie Curie (UPMC) and the Pitié-Salpêtrière university hospital. She runs the French reference center for Neurometabolic diseases in adults. Her research is focused on the characterization and treatment of brain energy deficiencies using both in vitro (metabolomics) and in vivo (nuclear magnetic resonance spectroscopy) approaches.

**Arthur Tenenhaus** is currently associate professor in the L2S Laboratory at CentraleSupélec, France, and researcher at the Bioinformatics and Biostatistics Core Facility of the Brain and Spine Institute, La Pitié-Salpêtrière Hospital.

**Submitted:** 18 November 2016; **Received (in revised form):** 27 April 2017

© The Author 2017. Published by Oxford University Press. All rights reserved. For Permissions, please email: journals.permissions@oup.com

Here, we provide practical guidelines for the use of RGCCA/SGCCA. We also illustrate the flexibility and usefulness of RGCCA/SGCCA on a unique cohort of patients with four genetic subtypes of spinocerebellar ataxia, in which we obtained multiple data sets from brain volumetry and magnetic resonance spectroscopy, and metabolomic and lipidomic analyses. As a first step toward the extraction of multimodal biomarkers, and through the reduction to a few meaningful components and the visualization of relevant variables, we identified possible markers of disease progression.

**Key words:** data integration; Regularized Generalized Canonical Correlation Analysis; biomarker discovery; spinocerebellar ataxia

## Introduction

The growing number of modalities (e.g. multi-omics, imaging and clinical data) characterizing a given disease provides physicians and statisticians with complementary facets of the disease process. However, novel statistical methods of data analysis are needed to unify these views. This data set is indeed intrinsically structured in blocks, where each block represents a set of variables observed on a group of individuals. The number and the nature of the variables can differ from one block to another. Therefore, classical statistical tools cannot be applied without altering the structure of the multiblock data set. The integration and visualization of these multivariate data sets is also challenging, explaining the need of dedicated modeling algorithms able to cope with the inherent properties of these structured data sets.

In this article, we present the principles of regularized generalized canonical correlation analysis (RGCCA) [1, 2], and its sparse generalized canonical correlation analysis (SGCCA) counterpart [3], a component-based framework for the integrative exploration of multimodal and high-dimensional data sets. We apply it to an original multiblock data set generated from a unique, considering the rarity of these diseases, cohort of patients with spinocerebellar ataxia (SCA) and controls. We show how the obtained results are useful, as SGCCA allows both the extraction of biomarkers and the reduction of the multiblock data sets into a few meaningful components that can be easily described as a set of graphical representations. The main objectives of the article are thus to provide users with practical guidelines for the application of RGCCA and SGCCA, and to illustrate their versatility and relevance on the SCA data set.

This article is organized as follows. In ‘Multiblock component methods’ section, the RGCCA and SGCCA optimization problems are briefly presented, and a synthetic overview of methods, which are special cases of RGCCA/SGCCA, is given. In ‘Practical guidelines for using RGCCA and SGCCA’ section, practical guidelines defining how to use RGCCA/SGCCA are provided. ‘Case study: the SCA data set’ section illustrates on a real and challenging multiblock data set, the usefulness of RGCCA/SGCCA for data integration.

## Multiblock component methods

The following section describes a general framework for multiblock component methods, RGCCA and variations, that was previously published [1–3] and assessed [4–6]. For the sake of comprehension of the use of these methods, their theoretical bases will be briefly described in the next subsections. In short, RGCCA is a rich technique that encompasses several important multivariate analysis methods (see Table 1 for the overview). The objective of RGCCA is to find, for each block, a weighted composite of variables (called block component) summarizing the relevant information between and within the blocks. The

block components are obtained such that (i) block components explain well their own block and/or (ii) block components that are assumed to be connected are highly correlated. Indeed, RGCCA can process a priori information defining which blocks are supposed to be linked to one another, thus reflecting hypotheses about the biology underlying the data blocks. In addition, RGCCA integrates a variable selection procedure, called SGCCA, allowing the identification of the most relevant features. Finally, as a component-based method, RGCCA/SGCCA can provide users with graphical representations to visualize the sources of variability within blocks and the amount of correlation between blocks.

## Regularized generalized canonical correlation analysis

We consider  $J$  data matrices  $\mathbf{X}_1, \dots, \mathbf{X}_j, \dots, \mathbf{X}_J$ . Each  $n \times p_j$  data matrix  $\mathbf{X}_j = [\mathbf{x}_{j1}, \dots, \mathbf{x}_{jp_j}]$  is called a block and represents a set of  $p_j$  variables observed on  $n$  individuals. The number and the nature of the variables may differ from one block to another, but the individuals must be the same across blocks. We assume that all variables are centered. The objective of multiblock component methods is to find block components  $\mathbf{y}_j = \mathbf{X}_j \mathbf{w}_j$ ,  $j = 1, \dots, J$  (where  $\mathbf{w}_j$  is a column vector with  $p_j$  elements) summarizing the relevant information between and within the blocks. The second-generation RGCCA [2] subsumes 50 years of multiblock component methods (see [2] for a complete review). It provides important improvements to the initial version of RGCCA [1] and is defined as the following optimization problem:

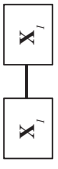
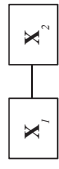

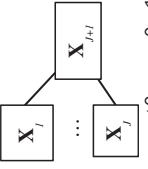
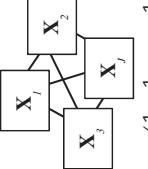
$$\max_{\mathbf{w}_1, \dots, \mathbf{w}_J} \sum_{j,k=1}^J c_{jk} g(\text{cov}(\mathbf{X}_j \mathbf{w}_j, \mathbf{X}_k \mathbf{w}_k)) \quad , \quad (1)$$

$$\text{s.t. } (1 - \tau_j) \text{var}(\mathbf{X}_j \mathbf{w}_j) + \tau_j \|\mathbf{w}_j\|_2^2 = 1, \quad j = 1, \dots, J$$

where:

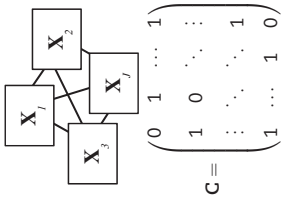
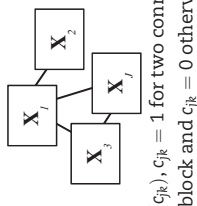
- The scheme function  $g$  is any continuous convex function and allows to consider different optimization criteria. Typical choices of  $g$  are the identity (leading to maximizing the sum of covariances between block components), the absolute value (yielding maximization of the sum of the absolute values of the covariances) or the square function (thereby maximizing the sum of squared covariances).
- The design matrix  $\mathbf{C} = \{c_{jk}\}$  is a symmetric  $J \times J$  matrix of non-negative elements describing the network of connections between blocks that the user wants to take into account. Usually,  $c_{jk} = 1$  for two connected blocks and 0 otherwise.
- The  $\tau_j$  are called shrinkage parameters ranging from 0 to 1. Setting the  $\tau_j$  to 0 will force the block components to unit variance ( $\text{var}(\mathbf{X}_j \mathbf{w}_j) = 1$ ), in which case the covariance criterion boils down to the correlation. The correlation criterion is better

Table 1. Special cases of RGCCA in a situation of  $J$  blocks

Method	Scheme function $g(x)$	Shrinkage constants $(\tau_j, j = 1, \dots, J)$	Design matrix (C)
PCA [7]	$x$	$\tau_1 = 1$	 $C = \begin{pmatrix} 0 & 1 \\ 1 & 0 \end{pmatrix}$
Canonical Correlation Analysis (CCA) [8]	$x$	$\tau_1 = 0$ and $\tau_2 = 0$	 $C = \begin{pmatrix} 0 & 1 \\ 1 & 0 \end{pmatrix}$
Interbattery Factor Analysis [9] (or PLS [10])	$x$	$\tau_1 = 1$ and $\tau_2 = 1$	 $C = \begin{pmatrix} 0 & 1 \\ 1 & 0 \end{pmatrix}$
Redundancy analysis of $X_1$ with respect to $X_2$ (RR) [11]	$x$	$\tau_1 = 1$ and $\tau_2 = 0$	
GGCA [12]	$x^2$	$\tau_j = 0, j = 1, \dots, J+1$	 $C = \begin{pmatrix} 0 & \dots & 0 & 1 \\ \vdots & \ddots & \vdots & \vdots \\ 0 & \dots & 0 & 1 \end{pmatrix}$
GGCA [13]	$x^2$	$\tau_j = 0, j = 1, \dots, J_1, J+1$ $\tau_j = 1, j = J_1+1, \dots, J$	
HPCA [14]	$x^4$	$\tau_j = 1, j = 1, \dots, J$ $\tau_{J+1} = 0$	
MCOA [15], CPCA [16], CPCA-W [17] and MFA [18]	$x^2$	$\tau_j = 1, j = 1, \dots, J$ $\tau_{J+1} = 0$	$c_j, j+1 = 1, j = 1, \dots, J$ and 0 otherwise
SUM of CORrelations method (SUMCOR) [19]	$x$	$\tau_j = 0, j = 1, \dots, J$	 $C = \begin{pmatrix} 1 & 1 & \dots & 1 \\ 1 & 1 & \dots & \vdots \\ \vdots & \vdots & \ddots & \vdots \\ 1 & \dots & \dots & 1 \end{pmatrix}$
Sum of Squared CORrelations method (SSQCOR) [20]	$x^2$	$\tau_j = 0, j = 1, \dots, J$	
Sum of Absolute value CORrelations method (SABCOR) [21]	$ x $	$\tau_j = 0, j = 1, \dots, J$	
SUM of COVariances method (SUMCOV-1). SUMCOV-1 is the 'one component per block' version of MAXBET [22]	$x$	$\tau_j = 1, j = 1, \dots, J$	
Sum of Squared COVariances method (SSQCOV-1). SSQCOV-1 is the 'one component per block' version of MAXBET B [23]	$x^2$	$\tau_j = 1, j = 1, \dots, J$	
Sum of Absolute value COVariances method (SABCOV) [1, 24]	$ x $	$\tau_j = 1, j = 1, \dots, J$	

(continued)

Table 1. Continued

Method	Scheme function $g(x)$	Shrinkage constants $(\tau_j, j = 1, \dots, J)$	Design matrix (C)
SUMCOV-2. SUMCOV-2 is the 'one component per block' version of MAXDIFF [22]	$x$	$\tau_j = 1, j = 1, \dots, J$	 $C = \begin{pmatrix} 0 & 1 & \dots & 1 \\ 1 & 0 & \dots & \vdots \\ \vdots & \vdots & \ddots & \vdots \\ 1 & \dots & \vdots & 1 & 0 \end{pmatrix}$
SSQCOV-2. SSQCOV-2 is the 'one component per block' version of MAXDIFF B [23]	$x^2$	$\tau_j = 1, j = 1, \dots, J$	 $C = (c_{jk}), c_{jk} = 1 \text{ for two connected block and } c_{jk} = 0 \text{ otherwise}$
PLS path modeling—Mode B [25]	$ x $	$\tau_j = 0$	

Note:  $\mathbf{X}_{j+1} = \mathbf{X}_1, \dots, \mathbf{X}_j$  is called superblock and is defined as the concatenation of the  $J$  blocks.  $(j + 1)$ th block defined as a superblock, the concatenation of the  $J$  blocks.

in explaining the correlated structure across data sets, thus discarding the variance within each individual data set. Setting  $\tau_j$  to 1 will normalize the block weight vectors ( $\mathbf{w}_j^T \mathbf{w}_j = 1$ ), which applies the covariance criterion. A value between 0 and 1 will lead to a compromise between the two first options and correspond to the following constraint  $\mathbf{w}_j^T (\tau_j \mathbf{I} + (1 - \tau_j)(1/n)\mathbf{X}_j^T \mathbf{X}_j) \mathbf{w}_j = 1$  in Equation (1). The choices  $\tau_j = 1$ ,  $\tau_j = 0$  and  $0 < \tau_j < 1$  are, respectively, referred as Modes A, B and Ridge.

From optimization problem in Equation (1), the term 'generalized' in the acronym of RGCCA embraces at least three notions. The first one relates to the generalization of two-block methods—including Canonical Correlation Analysis [8], Interbattery Factor Analysis [9] and Redundancy Analysis [10]—to three or more sets of variables. The second one relates to the ability of taking into account some hypotheses on between-block connections: the user decides which blocks are connected and which ones are not. The third one relies on the choices of the shrinkage parameters allowing to capture both correlation or covariance-based criteria.

### Variable selection in RGCCA: SGCCA

The quality and interpretability of the RGCCA block components  $\mathbf{y}_j = \mathbf{X}_j \mathbf{w}_j$ ,  $j = 1, \dots, J$  are likely affected by the usefulness and relevance of the variables of each block. Accordingly, it is an important issue to identify within each block a subset of significant variables that are active in the relationships between blocks. SGCCA extends RGCCA to address this issue of variable selection. Specifically, RGCCA with all  $\tau_j$ ,  $j = 1, \dots, J$  equal to 1 is combined with an L1 penalty that gives rise to SGCCA [3]. The SGCCA optimization problem is defined as follows:

$$\max_{\mathbf{w}_1, \dots, \mathbf{w}_J} \sum_{j,k=1}^J c_{jk} g(\text{cov}(\mathbf{X}_j \mathbf{w}_j, \mathbf{X}_k \mathbf{w}_k)) \quad \text{s.t.} \quad \begin{cases} \|\mathbf{w}_j\|_2 = 1 \\ \|\mathbf{w}_j\|_1 \leq s_j \end{cases}, \quad j = 1, \dots, J, \quad (2)$$

where  $s_j$  is a user-defined positive constant that determines the amount of sparsity for  $\mathbf{w}_j$ ,  $j = 1, \dots, J$ . The smaller the  $s_j$ , the larger the degree of sparsity for  $\mathbf{w}_j$ .

### Higher stage block components

It is possible to obtain more than one block component per block for RGCCA and SGCCA. Higher stage block components can be obtained using a deflation strategy [1]. This strategy forces all the block components within a block to be uncorrelated. This deflation procedure can be iterated in a flexible way. It is not necessary to keep all the blocks in the procedure at all stages: the number of components summarizing a block can vary from one block to another [2].

### Implementation

The function `rgcca()` of the RGCCA package [26] implements a monotonically convergent algorithm for the optimization problem in Equation (1), i.e. the bounded criterion to be maximized increases at each step of the iterative procedure, which hits at convergence a stationary point of Equation (1). Two numerically equivalent approaches for solving the RGCCA optimization problem are available. A primal formulation described in [1] requires the handling of matrices of dimension  $p_j \times p_j$ . A dual formulation described in [27] requires the handling of matrices of

dimension  $n \times n$ . Therefore, the primal formulation of the RGCCA algorithm will be used when  $n \geq p_j$ , and the dual form will be preferred when  $n < p_j$ . The `rgcca()` function of the RGCCA package implements these two formulations and selects automatically the best one. The SGCCA algorithm is similar to the RGCCA algorithm and keeps the same convergence properties. The algorithm associated with the optimization problem in Equation (2) is available through the function `sgcca()` of the RGCCA package.

Moreover, multiblock data faces two types of missing data structure: (i) if an observation  $i$  has missing values on a whole block  $j$  and (ii) if an observation  $i$  has some missing values on a block  $j$  (but not all). For these two situations, it is possible to exploit the algorithmic solution proposed for partial least squares (PLS) regression path modeling to deal with missing data ([28], p. 171). Work is in progress to implement this missing data solution within the RGCCA package.

### Special cases of RGCCA

Many different multiblock methods were published for 50 years. The choice of the ‘best’ multiblock method must be in line with the nature of the data set and the objective of the analysis. The introduction of the design matrix  $\mathbf{C}$ , the shrinkage parameters  $\tau_j$ s’ and the scheme function  $g$  makes RGCCA highly versatile. A practical guideline for appropriately specifying these extra parameters is proposed in the next two sections. From a statistical data analysis perspective, RGCCA subsumes a remarkably large number of well-known methods as particular cases—including principal component analysis (PCA) [7], generalized Canonical Correlation Analysis (GCCA) [12], PLS regression [10], consensus PCA (CPCA) [16], hierarchical PCA (HPCA) [14], multiple co-inertia analysis (MCOA) [15], etc. For an exhaustive list of methods, see [2]. All the methods cited above (and many others) are recovered with RGCCA by appropriately defining the triplet  $(\mathbf{C}, \tau_j, g)$ . Table 1 gives the correspondence between the triplet  $(\mathbf{C}, \tau_j, g)$  and the associated methods. SGCCA offers a sparse counterpart to all the covariance-based methods of RGCCA. RGCCA/SGCCA provides a framework for exploratory data analysis of multiblock data sets that has immediate practical consequences for a unified statistical analysis and implementation strategy. It is noteworthy that a complete review on dimension reduction approaches for simultaneous exploratory analyses of multiple data sets, and especially multi-omics data sets, has been recently published [5]. In that review, RGCCA/SGCCA is discussed and appears to occupy a key position as many of the single-block, two-block and multiblock component methods—referred as PCA (Principal Component Analysis), sPCA (sparse Principal Component Analysis), CCA (Canonical Correlation Analysis), RDA (Redundancy analysis), rCCA (Regularized canonical correlation), sCCA (sparse Regularized canonical correlation), PLS (Partial Least Squares), sPLS (sparse Partial Least Squares), sPLSDA (sparse Partial Least Squares - discriminant analysis), cPCA (consensus PCA), CIA (Co-Inertia Analysis), multiple factor analysis (MFA), MCOA (Multiple Co-Inertia Analysis) and GCCA (Generalized Canonical Correlation Analysis)—are special cases of RGCCA/SGCCA.

In the next section, we provide some guidelines to choose the triplet  $(\mathbf{C}, \tau_j, g)$  according to the objectives of the user and the nature of the data.

### Practical guidelines for using RGCCA and SGCCA

There are eight steps, discussed hereafter, that need to be applied: (i) construction of the multiblock data set, (ii)

preprocessing, (iii) definition of the between-block connections, (iv) determination of the shrinkage or sparsity parameters, (v) choice of the scheme function, (vi) determination of the number of components per block, (vii) visualization of the results and (viii) assessment of the reliability of parameter estimates.

### Construction of the multiblock data set

The variables that compose each block have to be defined carefully: not only according to their nature (e.g. one block that contains all the voxels of an image, one block for all the metabolites, etc.) but also according to external information. Nowadays, a huge amount of external information is available and can be used to define each block. For example, a block that contains all the metabolites can be divided into several data blocks; hence, metabolites belonging to one pathway are gathered within the same block. A block that contains all the voxels of an image can be grouped by regions: voxels belonging to one specific region are then gathered within the same block. This grouping strategy makes more interpretable blocks and facilitates the interpretation of the RGCCA/SGCCA model. RGCCA/SGCCA can be viewed as a ‘divide and conquer’ strategy that allows incorporating prior information when defining the blocks.

### Preprocessing

In general, and especially for the covariance-based criterion, the data might be preprocessed to ensure comparability between variables and blocks. To make variables comparable, standardization is applied (zero mean and unit variance). To make blocks comparable, a strategy is to divide each block by the square root of its number of variables [16]. This two-step procedure leads to  $\text{trace}(\mathbf{X}_j^T \mathbf{X}_j) = n$  for each block (i.e. the sum of the eigenvalues of the covariance matrix of  $\mathbf{X}_j$  is equal to 1 whatever the block). Such a preprocessing will be implicitly used throughout this article.

Another way to make blocks more comparable is to divide each block  $\mathbf{X}_j$  by the square root of the first eigenvalue of  $\frac{1}{n} \mathbf{X}_j^T \mathbf{X}_j$ . This is exactly the normalization procedure used for MFA [18]. The rationale of this normalization is the same as in PCA where variables are standardized to have the same influence in the analysis; here, it can be seen as an extension to blocks of variables where the first singular value plays the role of the standard deviation. This second strategy may be preferred in a situation where the numbers of uninformative and noisy variables are unbalanced between blocks. General guidelines for centering and scaling in component analysis are available in [29]. Several normalization strategies used in the context of simultaneous component analysis are discussed in [30].

### Definition of the design matrix $\mathbf{C}$

The between-block connections are encoded through the design matrix  $\mathbf{C} = (c_{jk})$ ; usually  $c_{jk} = 1$  for two connected blocks and 0 otherwise. The customization of the design matrix can be defined according to biological assumptions reflecting the biology underlying the data blocks. For instance, multi-omics data (transcriptomics, metabolomics, etc..) and other modalities such as neuroimaging, electrophysiological data and scores of disease severity are routinely acquired to study the complexity of the neurodegenerative cascades. It can be roughly considered that the path between omics data and behavioral data is mediated by neuroimaging data (i.e. no direct relationship between



omics and behavioral data is imposed). The prior information on the between-block connections can be injected in the design matrix.

Furthermore, from a statistical viewpoint, the design matrix is a flexible way to reach one of the methods listed in Table 1.

### Determination of the shrinkage parameters $0 < \tau_j < 1$ , $j=1, \dots, J$ and the sparsity parameter $s_j$ , $j=1, \dots, J$

The RGCCA model introduces some extra parameters, particularly a shrinkage parameter. The shrinkage parameters  $0 < \tau_j < 1$ ,  $j=1, \dots, J$  interpolate smoothly between maximizing the covariance (all  $\tau_j = 1$ ) and maximizing the correlation (all  $\tau_j = 0$ ). More precisely, we can define the choice of the shrinkage parameters by providing interpretations on the properties of the resulting block components:

- $\tau_j = 1$  yields the maximization of a covariance-based criterion. It is recommended when the user wants a stable component (large variance) while simultaneously taking into account the correlations between blocks. The user must, however, be aware that variance dominates over correlation.
- $\tau_j = 0$  yields the maximization of a correlation-based criterion. It is recommended when the user wants to maximize correlations between connected components. This option can yield unstable solutions in case of multicollinearity and cannot be used when a data block is rank deficient (e.g.  $n < p_j$ ).
- $0 < \tau_j < 1$  is a good compromise between variance and correlation: the block components are simultaneously stable and as well correlated as possible with their connected block components. This setting can be used when the data block is rank deficient. Ledoit and Wolf [31] consider  $\mathbf{M}_j = \tau_j \mathbf{I} + (1 - \tau_j)(1/n)\mathbf{X}_j^T \mathbf{X}_j$  as a shrinkage estimate of the true covariance matrix  $\Sigma_{jj}$  related to block  $j$ . In case of multicollinearity within blocks or when the number of observations is smaller than the number of variables ( $p_j \gg n$ ), the sample covariance matrix  $(1/n)\mathbf{X}_j^T \mathbf{X}_j$  is a poor estimation of the true covariance matrix. The usual strategy for finding a better estimation is to consider the class of linear combinations of the identity matrix and the sample covariance matrix,  $\{\tau_j \mathbf{I} + (1 - \tau_j)(1/n)\mathbf{X}_j^T \mathbf{X}_j\}$  [32]. Shrinkage parameters between 0 and 1 allow stepping closer to the correlation criterion, even in the case of high multicollinearity or when the number of individuals is smaller than the number of variables. For each block, the determination of the shrinkage parameter is made fully automatic by using one of the various formulas that have been proposed for finding an optimal shrinkage parameter [32]. Depending on the context, the shrinkage parameters should also be determined based on  $V$ -fold cross-validation.

Barker and Rayens [33] PLS for discrimination offer a good opportunity to illustrate the impact of the shrinkage parameters. They consider a block  $\mathbf{X}$  of explanatory variables and a block  $\mathbf{Y}$  of dummy variables describing a categorical variable. They are looking for a block component  $\mathbf{Xa}$  (with a normalized) and a standardized component  $\mathbf{Yb}$  maximizing the following criterion:

$$\max_{\mathbf{a}, \mathbf{b}} \text{cor}^2(\mathbf{Xa}, \mathbf{Yb}) \times \text{var}(\mathbf{Xa}).$$

The rationale of the Barker and Rayens's criterion is based on the following idea: we are not looking for a block component  $\mathbf{Yb}$  that explains its own block well (as  $\mathbf{Y}$  is a group coding matrix) but

one that correlates with  $\mathbf{Xa}$ , hence removing from the covariance criterion ( $\text{cov}^2(\mathbf{Xa}, \mathbf{Yb}) = \text{cor}^2(\mathbf{Xa}, \mathbf{Yb}) \times \text{var}(\mathbf{Xa}) \times \text{var}(\mathbf{Yb})$ ), the  $\text{var}(\mathbf{Yb})$  part. Using the RGCCA formalism, the Barker and Rayens's optimization problem is recovered as follows:

$$\max_{\mathbf{a}, \mathbf{b}} \text{cov}^2(\mathbf{Xa}, \mathbf{Yb}) \quad \text{s.t.} \quad \|\mathbf{a}\|_2 = 1 \text{ and } \text{var}(\mathbf{Yb}) = 1,$$

that is for  $\tau_X = 1$  and  $\tau_Y = 0$ .

The choice to set  $\tau_X = 1$  and more generally to set  $\tau_j$  equals to 1 in the optimization problem in Equation (1) is to some extent surprising. Indeed, it yields a sample covariance matrix equal to the identity for each block. It corresponds to the highest level of regularization that can be applied to RGCCA. The level of regularization can be relaxed by decreasing the value of  $\tau_j$ . However, in high-dimensional settings, the highest level of regularization has proven to be necessary or even insufficient [34, 35]. Additional penalties that promote sparsity are often required. The sparsity parameter  $s_j$ ,  $j=1, \dots, J$  is usually set based on cross-validation procedures (see next section for an illustration). Alternatively, values of  $s_j$ ,  $j=1, \dots, J$  can simply be chosen to result in desired amounts of sparsity.

### Choice of the scheme function $g$

It is possible to choose any continuous convex function. In the literature, classical scheme functions are  $g(x) = x$  (horst scheme),  $g(x) = |x|$  (centroid scheme),  $g(x) = x^2$  (factorial scheme) or, more generally, for any even integer  $m$ ,  $g(x) = x^m$  ( $m$ -scheme). The horst scheme penalizes structural negative correlation between block components, while both the centroid scheme and the  $m$ -scheme enable two components to be negatively correlated. 'How the results of RGCCA/SGCCA depend on the values of  $m$ ?' The answer to this question is related to the notion of fairness. According to [22], a fair model is a model where all blocks contribute equally to the solution in opposition to a model dominated by only a few of the  $J$  sets. If fairness is a major objective, the user must choose  $m=1$ .  $m>1$  is preferable if the user wants to discriminate between blocks [2]. In practice,  $m$  is equal to 1, 2 or 4. The higher the value of  $m$ , the more the method acts as block selector [2].

### Determination of the number of block components

Cross-validation is usually used to determine the number of block components to retain. Depend on the context (supervised or unsupervised), two types of cross-validation can be considered in the framework of RGCCA/SGCCA:

- When the analysis is oriented toward the prediction of a specific phenotype, then the number of components per block can be selected based on the cross-validated prediction accuracy.
- When no external information is available, then the number of components per block can be estimated as follows. For each block  $j$ , some percent of the elements of  $\mathbf{X}_j$  is removed at random from the data matrix. The RGCCA block components are estimated from this partially observed data set. For each block, the missing values are imputed using the reconstruction formula. The number of components that results in the lowest sum of squared errors of the missing values is retained.

Besides, the average variance explained (AVE) by a block component  $\mathbf{y}_j$  can also inform on the number of component to retain. The AVE of  $\mathbf{X}_j$ , denoted by  $\text{AVE}(\mathbf{X}_j)$ , is defined as:

$$\text{AVE}(\mathbf{X}_j) = \frac{1}{p_j} \sum_{h=1}^{p_j} \text{cor}^2(\mathbf{x}_{jh}, \mathbf{y}_j).$$

$\text{AVE}(\mathbf{X}_j)$  varies between 0 and 1 and reflects the proportion of variance captured by  $\mathbf{y}_j$ . The number of block components to retain for  $\mathbf{X}_j$  can be determined using the ‘elbow’ criterion or alternatively, the number of components that explains a predefined percentage of the total variance of  $\mathbf{X}_j$ .

### Visualization of the results

As a component-based method, RGCCA/SGCCA provides the users with graphical representations, including factor plot, correlation circle and biplot. These graphical displays allow visualizing the sources of variability within blocks, the relationships between variables within and between blocks and the amount of correlation between blocks.

### Assessment of the reliability of parameter estimates

It is possible to use a bootstrap resampling method [36, 37] to assess the reliability of parameter estimates obtained using RGCCA/SGCCA.  $B$  bootstrap samples of the same size as the original data are repeatedly sampled with replacement from the original data. RGCCA/SGCCA is then applied to each bootstrap sample to obtain the RGCCA/SGCCA estimates. For RGCCA, we calculate the mean and variance of the estimates across the bootstrap samples, from which we derived  $t$ -ratio and  $P$ -value (under the assumption that the parameter estimates exhibited asymptotic normality) to indicate how reliably parameters were estimated. As several  $P$ -values are constructed simultaneously, Bonferroni or FDR corrections can be applied for controlling the family-wise error rate or the false discovery rate, respectively.

For SGCCA, the percentage of times a specific variable had a non-null weight across bootstrap sample can be derived. In addition, the stability of the selected variables can be measured according to the Fleiss’ $\kappa$  score [38] that estimates the agreement among the  $B$  bootstrap samples. The Fleiss’ $\kappa$  score is always  $\leq 1$ , and the higher the value of  $\kappa$  is, the more stable the methods are with respect to sampling. This resampling procedure, intuitive and pragmatic, is classically used in the PLS community. We may note that alternative resampling-based strategy for variable and stability selection could be considered [39]. This alternative approach has been tested for simultaneous component analysis [40].

## Case study: the SCA data set

### Description of the SCA data set

Neurodegenerative disorders have become the leading cause of disability in Western societies, e.g. SCAs that are autosomal dominant diseases responsible for severe movement disorders. Heterogeneous and high-dimensional sources of information such as omics data (transcriptomics, metabolomics, etc.) and other modalities such as neuroimaging and/or electrophysiological data are routinely acquired to study such complex diseases. Disease mathematical models are thus critically needed to identify biomarkers that are relevant to disease mechanisms and can be used in therapeutic trials. As gene-based therapeutic approaches are being developed in SCA [41], it becomes increasingly important to identify readouts for trials with sufficient effect sizes. Clinical scores are useful, but insufficient, and a single biomarker is likely to fail reflecting the complexity of the neurodegenerative cascades leading to the onset and progression of SCA. An integrated multimodal biomarkers approach is therefore needed to (i) better understand disease pathophysiology and (ii) generate composite scores with greater effect sizes than isolated biomarkers.

SCA belongs to the group of polyglutamine repeat disorders and is characterized by a predominant atrophy of two brain regions: the cerebellum and the pons. More than 40 genetically different SCAs have been defined. The most common—SCA1, SCA2 and SCA3, which together affect about half of the families with a history of SCA—are caused by abnormal CAG repeat expansions, encoding elongated polyglutamine tracts within the proteins associated with each type [42]. Progressive cerebellar ataxia is the prominent symptom of all SCAs. In SCA7, patients present with additional non-neurological signs commonly seen in patients with mitochondrial dysfunction such as pigmentary retinopathy and cardiomyopathy. Depending on the SCA genotype, CAG repeat length explains about 50–70% of the variability in age at onset, i.e. individuals with longer repeats tend to have an earlier onset [43].

The volume of the pons has been shown to be the most sensitive to change in patients with SCA [44], including at the pre-symptomatic phase of the disease in individuals carrying abnormal CAG repeats but who have not yet developed symptoms [45]. Accordingly, the pons volume is likely to closely reflect disease progression and can also be studied longitudinally in controls, unlike motor scales evaluating cerebellar dysfunctions. Therefore, following previous work that we conducted on metabolic dysfunction in polyglutamine repeat disorders [46–48], we chose to perform multiblock analyses to discover relevant associations between the pons volume and various metabolic modalities—calorimetry, metabolomics and lipidomics on plasma, and metabolic imaging by magnetic resonance

**Table 2.** Characteristics of the SCA cohort

	Controls	SCA1	SCA2	SCA3	SCA7	<i>P</i> -value
Number of subjects	35	18	14	22	13	
Sex (M/F)	17/18	9/9	8/6	10/12	7/6	
BMI (kg/m <sup>2</sup> )	25±4	24±6	27±5	24±5	23±3	0.104
Age at examination (years)	48±13	45±15	46±12	50±11	46±14	0.735
Age at disease onset (years)	–	41±12	35±11	42±11	38±13	0.397
SARA score (/40)	0.8±1	10±6	14±7	14±7	10±8	
Disease CAG repeats	–	48±7	40±3	70±6	43±5	

**Table 3.** Description of the SCA multiblock data set

Block $X_j$	Number of variables for $X_j$	Modalities
$X_1$ : Arginine_Proline	$p_1 = 14$	Metabolic pathways including 754 metabolites
$X_2$ : BCAA_Threonine	$p_2 = 9$	
$X_3$ : Carnitine_Lysine	$p_3 = 7$	
$X_4$ : CE_sterols_bile_acids	$p_4 = 47$	
$X_5$ : Essential_fatty_acids	$p_5 = 15$	
$X_6$ : Fatty_acids_Ketone_bodies	$p_6 = 23$	
$X_7$ : GABA_Glutamine_Histidine	$p_7 = 18$	
$X_8$ : Glucose_Alanine_Pyruvate	$p_8 = 4$	
$X_9$ : Glycerides	$p_9 = 177$	
$X_{10}$ : Glycine_Serine	$p_{10} = 16$	
$X_{11}$ : Krebs_cycle	$p_{11} = 5$	
$X_{12}$ : Phenylalanine_Tyrosine	$p_{12} = 12$	
$X_{13}$ : Phospholipids	$p_{13} = 292$	
$X_{14}$ : Purines	$p_{14} = 14$	
$X_{15}$ : Pyrimidines	$p_{15} = 9$	
$X_{16}$ : Sphingolipids	$p_{16} = 56$	
$X_{17}$ : Tryptophan	$p_{17} = 23$	
$X_{18}$ : Urea_cycle	$p_{18} = 5$	
$X_{19}$ : Various	$p_{19} = 8$	
$X_{20}$ : MRS	$p_{20} = 19$	MRS of the cerebellum
$X_{21}$ : CAL	$p_{21} = 3$	
$X_{22}$ : Superblock	$p_{22} = 776$	$X_{22} = [X_1, \dots, X_{21}]$
$X_{23}$ : Pons	$p_{23} = 1$	The volume of the pons

spectroscopy (MRS)—in patients with SCA compared with controls, to gain insight into the pathophysiology of SCA. Our ultimate goal—outside the scope of these analyses—is to study prospectively these biomarkers in longitudinal studies and generate composite scores with greater effect sizes than the pons volume alone.

### Patients and controls

The SCA study (NCT 01470729) was approved by the local ethical committee (AOM10094, CPP Ile de France VI, Ref: 105–10) and performed in a unique cohort of patients with SCA—SCA1 ( $n = 18$ ), SCA2 ( $n = 14$ ), SCA3 ( $n = 22$ ) and SCA7 ( $n = 13$ ). Healthy controls ( $n = 35$ ) with similar sex ratio, age and body mass index (BMI) than patients were also recruited. All participants signed informed consent to be included in the study. Their demographic characteristics are summarized in Table 2. The scale for the assessment and rating of ataxia (SARA, score up to 40) was used to evaluate the severity of the disease [49]. The four SCA subtypes were comparable in terms of duration of disease and SARA scores.

### Application of SGCCA to the SCA data set

We collected standard clinical and brain volumetric metrics in our cohort of SCA patients and healthy controls, and then jointly analyzed modalities (or blocks) reflecting metabolic regulations using calorimetry, metabolomics and lipidomics on plasma, and metabolic imaging by MRS. A full description of the methods used for the acquisition of each modality is available as Supplemental Materials. The main objective of this integrative analysis was to identify variables within each block that (i) well explain their own block and (ii) influence the relationships

between ‘connected’ blocks. The example of the SCA data set was well suited to illustrate the versatility and relevance of SGCCA, as the number of variables within each block made it difficult to identify the most important variables, so that a variable selection procedure was needed. In this section, we intend to instantiate the eight-step guideline described in ‘Practical guidelines for using RGCCA and SGCCA’ section. Moreover, some additional advices to set up the extra parameters according to the nature of the data and the scientific objectives are given. We then illustrate how relationships between the most relevant variables can be displayed and the results interpreted by visualizing the observations and variables in a common space.

### Construction of the multiblock data set

The SCA data set was organized into 23 blocks. A detailed description of each block, including the number of variables per block, is reported in Table 3. Annotated metabolites were classified into metabolite sets mapping various biochemical pathways. Nineteen sets were proposed including 754 metabolites classified by the confidence level of annotation and detected using our metabolomic and lipidomic methods. These blocks  $X_1, \dots, X_{19}$  were defined based on biological knowledge about metabolic pathways from KEGG (Kyoto Encyclopedia of Genes and Genomes), HMDB (Human Metabolome Database) and literature [50–56]. Blocks  $X_{20}$  and  $X_{21}$  contained information on brain MRS, denoted MRS, and calorimetry information, denoted CAL. In the framework of CPCA and HPCA methods, a superblock defined as the concatenation of all the blocks is also used. In the SCA data set, the superblock was defined as  $X_{22} = [X_1, \dots, X_{21}]$ , and the corresponding global components were derived. The space spanned by the global components was viewed as a compromise space that integrated all the modalities. This global space was useful for visualization and eased the interpretation of the results. Finally,  $X_{23}$  contained the volume of the pons.

### Preprocessing

Adjustments for confounding factors (age, gender and BMI) were carried out by residualization (before preprocessing) for each variable of the SCA data set. Residualization consists in regressing each block by age, gender and BMI. To make blocks more comparable, the residual variables were standardized (zero mean and unit variance) and then divided by  $\sqrt{p_j}$  within each block.

### Definition of the design matrix C

In the search of biomarkers associated with the four subtypes of SCA—SCA1, SCA2, SCA3 and SCA7—we applied SGCCA to identify variables from the 21 blocks associated with the pons volume. The between-block connections associated with this objective of analysis are presented in Figure 1. We chose a CPCA structure oriented toward the explanation of the volume of the pons by imposing an additional connection between the superblock and the pons. The ‘divide and conquer’ strategy, by incorporating prior knowledge in the definition of the blocks, yielded valuable improvements and more interpretable results.

### Choice of the scheme function g

In this case, it was not expected that all the blocks, especially the metabolic pathways, contributed equivalently to the process. The block selector behavior of SGCCA was favored by using the scheme function  $g(x) = x^4$ .

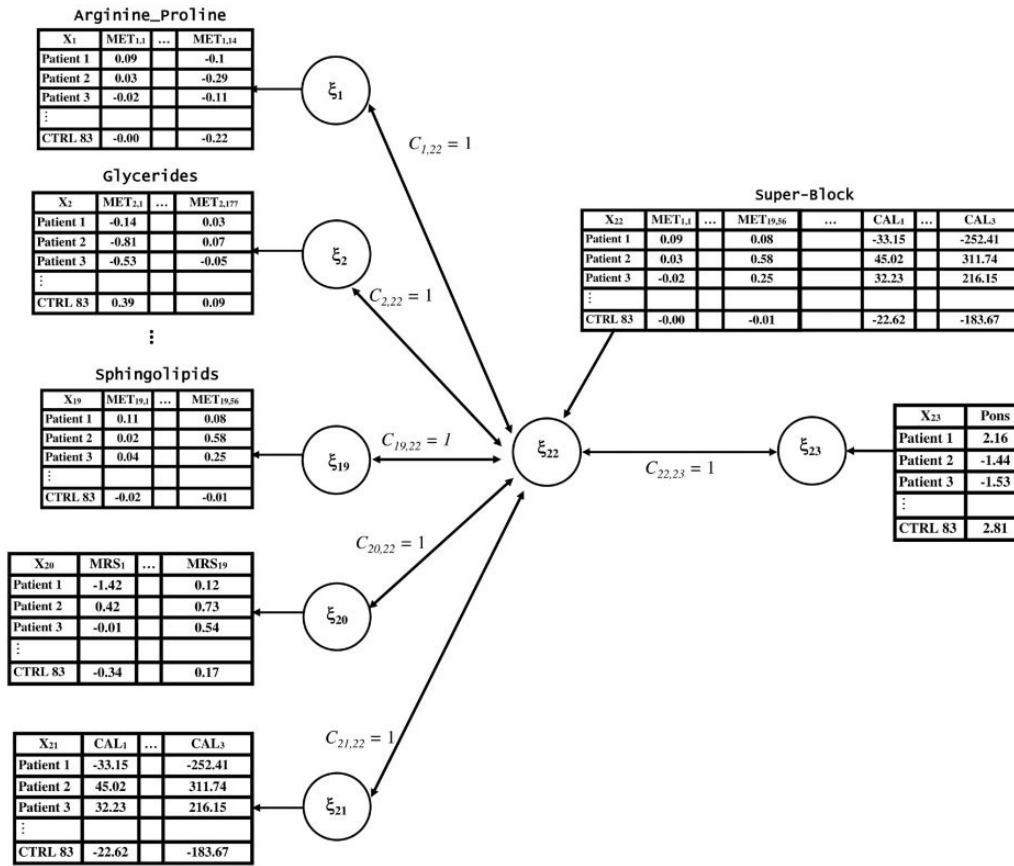


Figure 1. Between-block connections.  $X_1, \dots, X_{21}$  are connected to the superblock  $X_{22}$ , and  $X_{22}$  is connected to the volume of the pons  $X_{23}$ . These between-block connections are encoded through the design matrix  $C$ :  $c_{j,22} = 1, j = 1, \dots, 21, c_{22,23} = 1$  and  $c_{jk} = 0$  otherwise.

#### Determination of the sparsity parameter and the number of block components

SGCCA requires determining the sparsity parameters. For each block  $X_j$ , the sparsity parameter  $s_j, j = 1, \dots, J$  was set using a leave-one-out cross-validation procedure. The value of the parameter  $s_j$  was chosen in a range defined by the following formula  $1 + \{0.05, 0.1, 0.15, 0.2, 0.25, 0.3, 0.35, 0.4\} \times \sqrt{p_j}$ , which allowed us to impose the same degree of sparsity for all the blocks. To select the optimal value, linear models predicting the volume of the pons with respect to the block components were performed, and the optimal parameter was selected with respect to the mean squared error of these models. The optimal values were equal to  $s_j = 1 + 0.2 \times \sqrt{p_j}, j = 1, \dots, J$ .

Moreover, using a deflation strategy, four components per block were built. We denote by  $y_j^{(h)}$  (respectively,  $w_j^{(h)}$ ) the  $h$ th block component (respectively,  $h$ th block weight vector) associated with  $X_j$ .

#### Visualization

As the fourth global component was the most discriminant between patients and controls, the graphical display of the individuals obtained by crossing the global components  $y_{22}^{(1)}$  and  $y_{22}^{(4)}$  and marked with their status (SCA1, SCA2, SCA3, SCA7 and controls) is shown in Figure 2. It is noteworthy that, despite some overlap, the first global component exhibited a separation among some SCA groups, especially patients with SCA7 who were mainly grouped at the bottom. Moreover, the fourth global component captured the discriminative information between

patients and healthy controls as controls concentrated on the right and patients on the left.

Figure 3 shows the variables projected on the compromise space. The sparsity-inducing penalty of SGCCA made the interpretation of the variable space easier. Indeed, only the variables associated with non-null elements in the block weight vector  $w_j^{(1)}$  and  $w_j^{(4)}, j = 1, \dots, J$  (i.e. the ones that contribute to the construction of the first and fourth dimensions) were projected on the compromise space. A variable that is highly expressed for a category of individuals will be projected with a high weight (far from the origin) in the direction of that category. Likewise, the most discriminant variables between patients and controls appeared to be metabolites measured by MRS in the vermis such as total creatine, a marker of energy metabolism and myoinositol (myoIns), a putative glial marker (Figure 3). Interestingly, we previously identified these variables as significantly different between patients and controls [52]. We also showed that these metabolites were associated with SARA scores, which reflect higher disease severity [52]. Moreover, the separation among patients with SCA, and especially patients with SCA7, seemed to be driven by certain lipid species detected in plasma by lipidomic analyses such as sphingolipids and phospholipids (Figure 3).

Figure 3 allows visualizing relationships between variables belonging to the different blocks. This figure suggests relationships between blocks that can be confirmed by a block clustering. As the fourth dimension was the most informative axis for the explanation of the pons, we considered the variables that contribute to the construction of  $y_j^{(4)}, j = 1, \dots, 21$ . Let  $X_j$  be the block that contains the variables associated with non-null elements in the



Figure 2. Sample space associated with the dimensions 1 and 4 of the superblock. Individuals are marked according to the status (CTRL, SCA1, SCA2, SCA3 and SCA7). CTRL: healthy controls.

block weight vector  $w_j^{(4)}$ . This subsection presents the block clustering of  $X_1^*, \dots, X_{21}^*, X_{23}^*$  based on the McKeon's measure [57]. The McKeon's measure quantifies the homogeneity of a set of block components and is defined by the following equation:

$$r_1(X_1 w_1, \dots, X_j w_j) = \frac{\frac{1}{j(j-1)/2} \sum_{j < k} \text{cov}(X_j w_j, X_k w_k)}{\frac{1}{j} \sum_j \text{var}(X_j w_j)} \quad (3)$$

Equation (3) allows evaluating the homogeneity of the solution of any multiblock component methods. The computation of the McKeon's measure was carried out using RGCCA (full between-block connections,  $\tau_j = 1$  for all blocks, and  $g(x) = x$  for a fair analysis). Figure 4 represents the resulting block clustering of  $X_1^*, \dots, X_{21}^*, X_{23}^*$ . Blocks that were the most closely related (e.g. GABA–glutamine–histidine and Krebs cycle) contained variables that were partially redundant, as they belonged to more than one pathway and could thus serve as an internal validation. As previously discussed, the volume of the pons, the most distinctive feature in this model between patients and controls, clustered with the vermis MRS profile. Lipid species, including sphingolipids and phospholipids, also clustered with one another providing further validation to our model.

#### Assessment of the reliability of parameter estimates

To assess the reliability of parameter estimates obtained using SGCCA, 1000 bootstrap samples were derived. SGCCA was then applied to each bootstrap sample (with the sparsity parameters determined at the previous step) to obtain estimates  $w_j^b$ , where  $j$  denotes the block index and  $b$  the bootstrap sample index. The percentage of times a specific variable had a non-null weight was therefore derived. Figure 5 reports those percentages for the blocks that contributed mostly to the construction of the first global component.

Among the lipid species that tended to separate patients with SCA7 from other patients, certain ceramides (Cer) were especially represented in the sphingolipids group, as well as

certain phosphatidylcholines (PCs) in the phospholipids group (Figure 5A and B, respectively). To our knowledge, to date, there has been no metabolomic or lipidomic studies conducted in SCA patients. However, one lipidomic analysis was performed in the cerebellum of a preclinical model of SCA2 and found significant changes in some sphingolipids and cholesterol by-products [58]. Likewise, although conclusions cannot be made without further biological validation, it is noteworthy that both lipid classes, Cer and PC, are highly expressed in the retina [59]. Furthermore, defects in their synthesis are associated with pigmentosa retinopathy [60, 61], which is a distinctive feature of SCA7 compared with SCA1, SCA2 and SCA3.

## Discussion and conclusion

R/SGCCA stands as a unique, general and original way for analyzing high-dimensional multiblock data sets. It allows the selection of a few meaningful variables that underline the between-block connections encoded by the design matrix  $C$ . This design matrix is highly modular to fit any prior knowledge the user has on the links between blocks. The variable selection property results in models more easily interpretable than a model based on all the variables. Being able to select variables means that one can also study the stability of the variable selection process and possibly deduce patterns in the way the variables are selected under sampling. Moreover, the selection of a few meaningful variables from longitudinal studies will enable their combination into a composite score. Such a composite score can be used as a proxy for disease severity and acts as a basis for future therapeutic studies. Indeed, composite scores are likely to provide both a better reflection of the disease process pathology and a larger effect size than any biomarker alone. This is crucial for the assessment of experimental treatments in many neurodegenerative conditions, and especially in rare diseases like SCA where patient's recruitment is challenging. Finally, we showed that having blocks of heterogeneous sizes and nature is taken into account routinely by SGCCA.

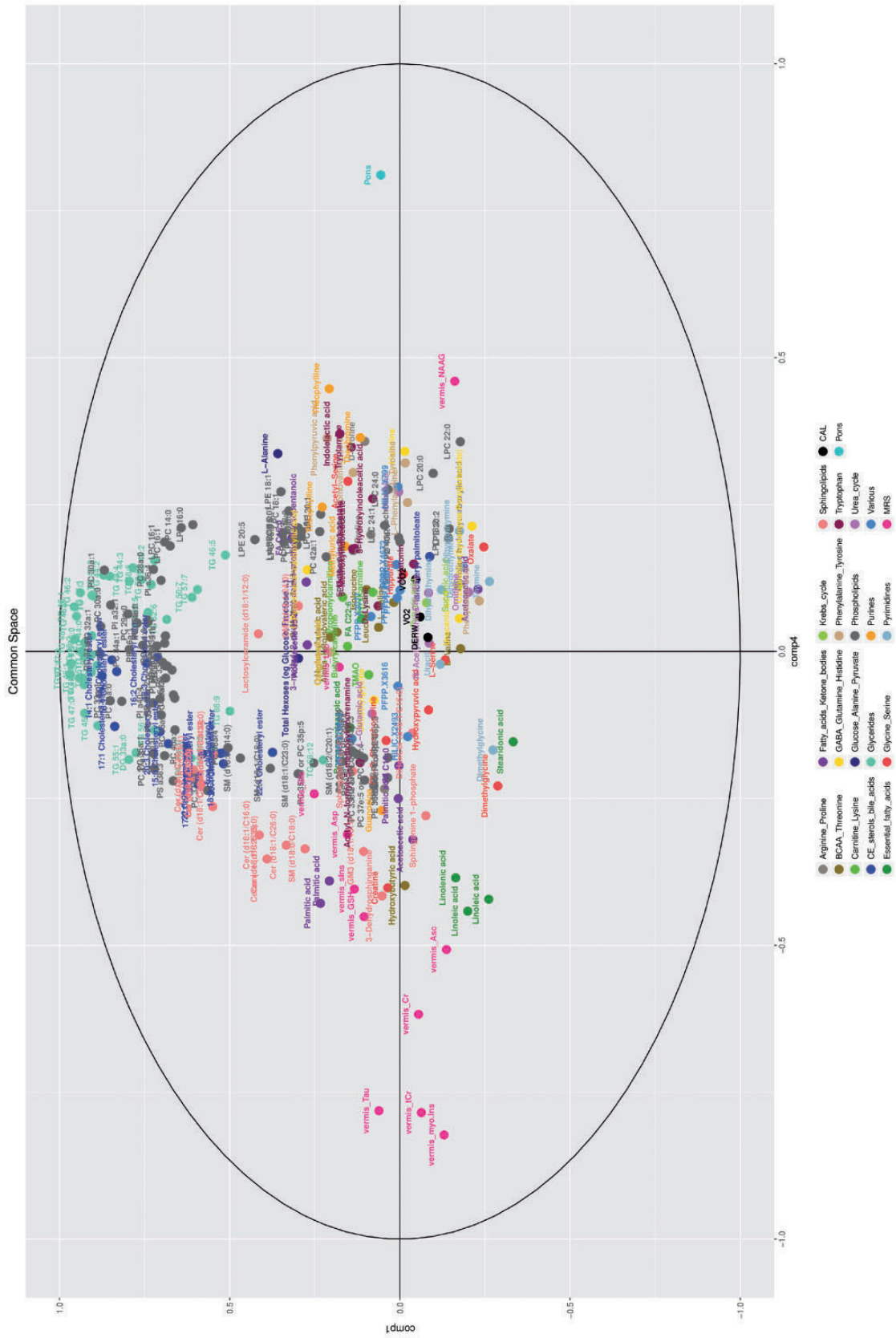


Figure 3. Variables associated with the dimensions 1 and 4 of the superblock. Only the variables that contribute to the construction of components 1 and 4 are visualized in the variables space.

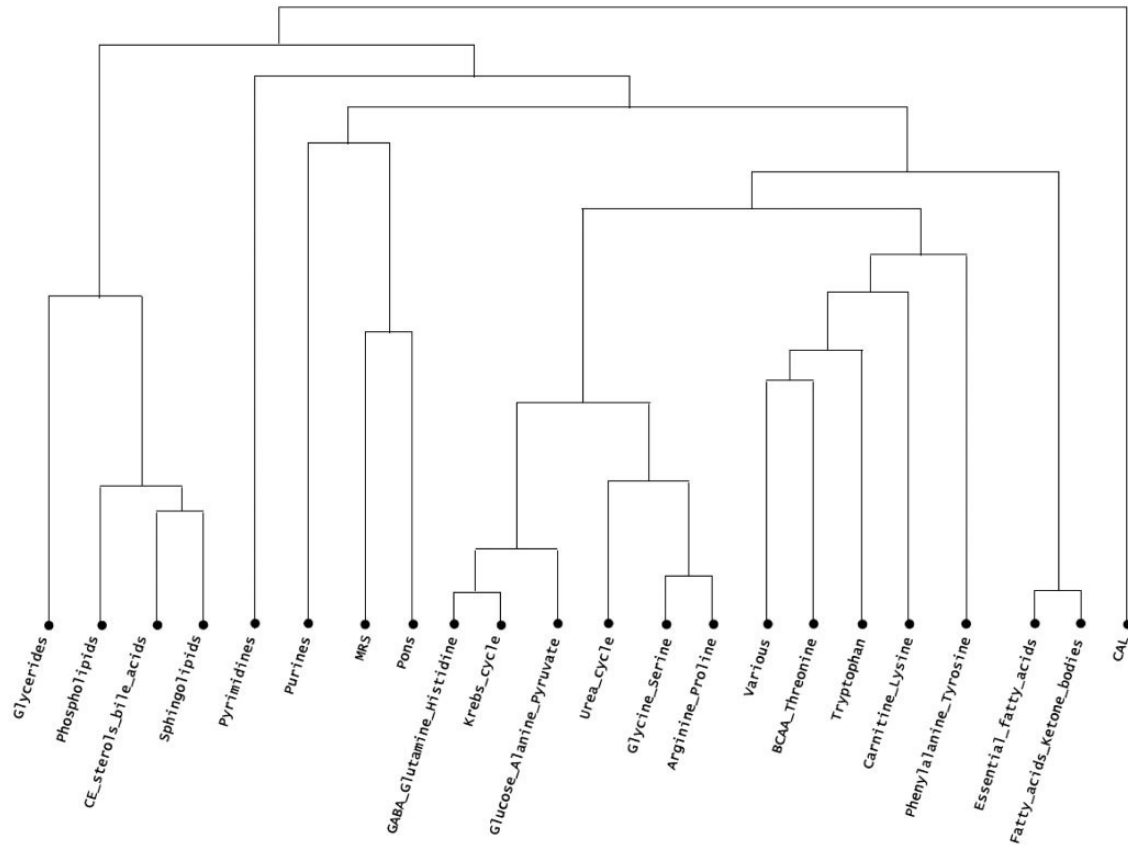


Figure 4. Dendrogram for block clustering based on McKeon measure derived using RGCCA with a full between-block connections,  $\tau_j = 1$  for all blocks, and  $g(x) = x$ .

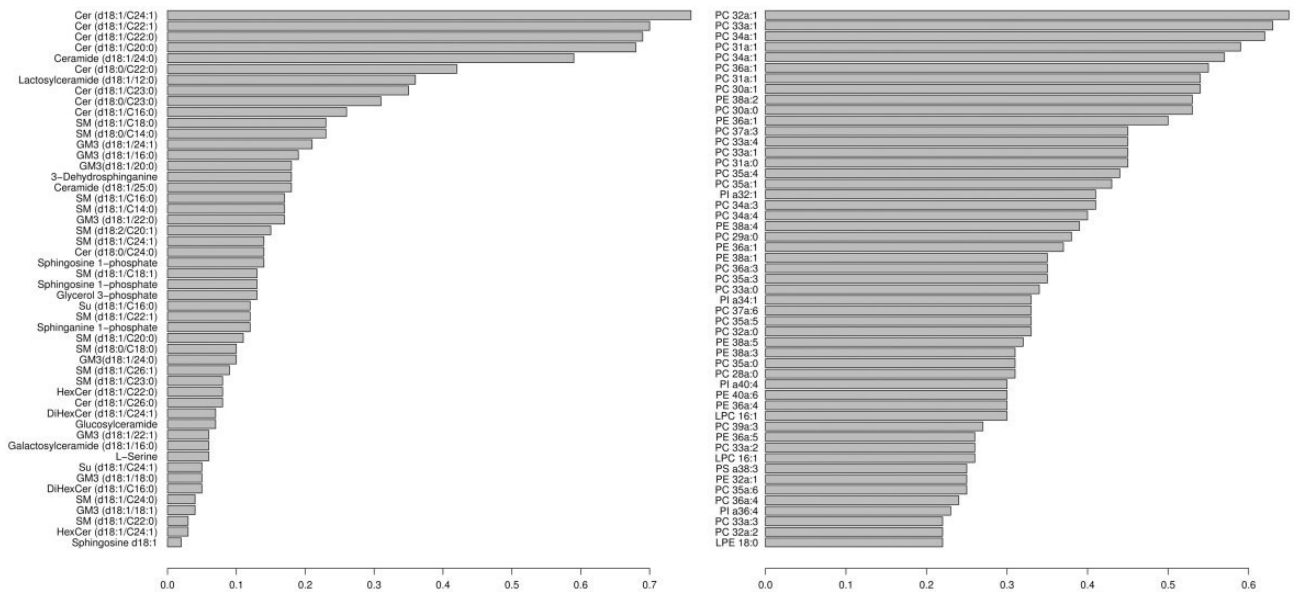


Figure 5. (A) Percentages of times the 'Sphingolipid' variables participate to the construction of the block component. (B) Percentages of times the 'Phospholipids' variables participate to the construction of the block component. We presented the most important variables, as the block contained 292 variables.

Likewise, the application of SGCCA on our SCA data set pinpoints at a possible role of some lipid species in the pathophysiology of SCA7 compared with other SCA, which merits further metabolic explorations.

Of note, RGCCA can also be applied to longitudinal data using the multiway formalism, which accounts for multiple measurements (either in time or in type of acquisition) of a given feature [62]. Multigroup structure (i.e. same sets of

variables observed on different groups of individuals) can also be tackled with RGCCA: the aim is to uncover similar relationships between variables across the various groups [63]. Beyond the example data set used in this study, this framework proves equally efficient to manage and interpret a large variety of biological data types, typically information produced by next-generation sequencing approaches (e.g. DNA-seq, RNA-seq, Methyl-seq, etc.) that are increasingly used to further investigate normal or pathological biological processes.

### Key Points

- The RGCCA-based integrative procedure requires the setting of extra parameters that need to be carefully adjusted. We provide practical guidelines for the use of RGCCA/SGCCA.
- The flexibility and usefulness of RGCCA/SGCCA was illustrated on a unique cohort of patients with four genetic subtypes of SCA, in which we obtained multiple data sets from brain volumetry, MRS and metabolomic and lipidomic data sets.
- We show how to graph RGCCA output.

### Acknowledgements

The authors acknowledge the great contribution of the neurologists who evaluated patients and controls, Dr Maya Tchikviladze, Dr Alina Tataru and Dr Rabab Debs; the study coordinators Céline Jauffret, Daisy Rinaldi and Elodie Petit; and the Centre d'Investigations Cliniques coordinated by Professor Jean-Christophe Corvol and the Unité de Recherche Clinique, especially Karine Martin chief of project.

### Supplementary Data

Supplementary data are available online at <http://bib.oxfordjournals.org/>.

### Funding

This study was sponsored by the Assistance-Publique des Hôpitaux de Paris and supported by grants from the French Ministry of Health (PHRC BIOSCA - ID RCB: 2010-A01324-35), the Cognacq-Jay foundation, the program 'Investissements d'avenir' ANR-10-IAIHU-06 and the patients' association Connaitre les Syndromes Cérébelleux (CSC).

### Availability of data and materials

The data that support the findings are part of a larger ongoing study. They are thus not publicly available yet. However, the data presented in this article are available from the authors on reasonable request.

### Ethics approval

Ethical approval for experiments involving patients was granted by the Comité de Protection des Personnes-Ile de France Paris VI (ID RCB: 2010-A01324-35).

### References

1. Tenenhaus A, Tenenhaus M. Regularized generalized canonical correlation analysis. *Psychometrika* 2011;**76**:257–84.
2. Tenenhaus M, Tenenhaus A, Groenen PJF. Regularized generalized canonical correlation analysis: a framework for sequential multiblock component methods. *Accepted Psychometrika* 2017.
3. Tenenhaus A, Philippe C, Guillemot V, et al. Variable selection for generalized canonical correlation analysis. *Biostatistics* 2014;**15**(3):569–83.
4. Günther OP, Shin H, Nq RT, et al. Novel multivariate methods for integration of genomics and proteomics data: applications in a kidney transplant rejection study. *OMICS* 2014;**18**(11):682–95.
5. Meng C, Zeleznik OA, Thallinger GG, et al. Dimension reduction techniques for the integrative analysis of multi-omics data. *Brief Bioinform* 2016;**17**(4):628–41.
6. Meng C, Kuster B, Culhane AC, et al. A multivariate approach to the integration of multi-omics datasets. *BMC Bioinformatics* 2014;**15**(1):1.
7. Hotelling H. Analysis of a complex of statistical variables into principal components. *J Educ Psychol* 1933;**24**:417–41.
8. Hotelling H. Relation between two sets of variates. *Biometrika* 1936;**28**:321–77.
9. Tucker LR. An inter-battery method of factor analysis. *Psychometrika* 1958;**23**:111–36.
10. Wold S, Martens H, Wold H. The multivariate calibration problem in chemistry solved by the PLS method. *Proc Conf Matrix Pencils* 1983;**973**:286–93.
11. Van den Wollenberg A. Redundancy analysis – an alternative to canonical correlation analysis. *Psychometrika* 1977;**42**:207–19.
12. Carroll J. A generalization of canonical correlation analysis to three or more sets of variables. *Proc 76th Conv Am Psych. Assoc* 1968;**3**:227–8.
13. Carroll J. Equations and tables for a generalization of canonical correlation analysis to three or more sets of variables. 1968, Unpublished Companion paper to Carroll.
14. Wold S, Kettaneh N, Tjessem K. Hierarchical multiblock PLS and PC models for easier model interpretation and as an alternative to variable selection. *J Chemom* 1996;**10**:463–82.
15. Chessel D, Hanafi M. Analyses de la co-inertie de K nuages de points. *Rev Stat Appl* 1996;**44**(2):35–60.
16. Westerhuis JA, Kourti T, MacGregor JF. Analysis of multiblock and hierarchical PCA and PLS models. *J Chemom* 1998;**12**:301–21.
17. Smilde AK, Westerhuis JA, de Jong S. A framework for sequential multiblock component methods. *J Chemom* 2003;**17**(6):323–37.
18. Escofier B, Pagès J. Multiple factor analysis, (AFMULT package). *Comput Stat Data Anal* 1994;**18**:121–40.
19. Horst P. Relations among m sets of variables. *Psychometrika* 1961;**26**:126–49.
20. Kettenring J. Canonical analysis of several sets of variables. *Biometrika* 1971;**58**:433–51.
21. Hanafi M. PLS Path modelling: computation of latent variables with the estimation mode B. *Comput Stat* 2007;**22**:275–92.
22. Van de Geer JP. Linear relations among k sets of variables. *Psychometrika* 1984;**49**:70–94.
23. Hanafi M, Kiers H. Analysis of K sets of data, with differential emphasis on agreement between and within sets. *Comput Stat Data Anal* 2006;**51**:1491–508.
24. Kramer N. Analysis of high dimensional data with partial least squares and boosting. Doctoral dissertation, Technical University of Berlin, 2007.



25. Wold H. Soft modeling: the basic design and some extensions. In *Systems under Indirect Observation: Part 2*. North-Holland, Amsterdam: K.G. Jöreskog and H. Wold, 1982, pp. 1–54.
26. Tenenhaus A and Guillemot, V. RGCCA: Regularized and Sparse Generalized Canonical Correlation Analysis for Multi-Block Data. R package version 2.12. 2017. <https://cran.r-project.org/web/packages/RGCCA/>.
27. Tenenhaus A, Philippe C, Frouin V. Kernel generalized canonical correlation analysis. *Comput Stat Data Anal* 2015;**90**:114–31.
28. Tenenhaus M, Vinzi VE, Chatelin YM, et al. PLS path modeling. *Comput Stat Data Anal* 2005;**48**(1):159–205.
29. Bro S, Smilde AK. Centering and scaling in component analysis. *J Chemom* 2003;**17**(1):16–33.
30. Van Deun K, Smilde AK, van der Werf MJ, et al. A structured overview of simultaneous component based data integration. *BMC Bioinformatics* 2009;**10**:246.
31. Ledoit O, Wolf M. A well conditioned estimator for large-dimensional covariance matrices. *J Multivar Anal* 2004;**88**:365–411.
32. Schäfer J, Strimmer KA. Shrinkage approach to large-scale covariance matrix estimation and implications for functional genomics. *Stat Appl Genet Mol Biol* 2005;**4**(1):32.
33. Barker M, Rayens W. Partial least squares for discrimination. *J Chemom* 2003;**17**:166–73.
34. Bickel PJ, Levina E. Some theory for Fisher's linear discriminant function, 'naive Bayes', and some alternatives when there are many more variables than observations. *Bernoulli* 2004;**10**(6):989–1010.
35. Chun H, Keleş S. Sparse partial least squares regression for simultaneous dimension reduction and variable selection. *J R Stat Soc Ser B Stat Methodol* 2010;**72**(1):3–25.
36. Efron B. Bootstrap methods: another look at the jackknife. *Ann Stat* 1979;**7**:1–26.
37. Efron B. Better bootstrap confidence intervals. *J Am Stat Assoc* 1987;**82**:171–85.
38. Fleiss JL. Measuring nominal scale agreement among many raters. *Psychol Bull* 1971;**76**(5):378.
39. Meinshausen N, Bühlmann P. Stability selection. *J R Stat Soc Ser B Stat Methodol* 2010;**72**(4):417–73.
40. Gu Z, Van Deun K. A variable selection method for simultaneous component based data integration. *Chemom Intell Lab Syst* 2016;**158**:187–99.
41. Keiser MS, Kordower JH, Gonzalez-Alegre P, et al. Broad distribution of ataxin 1 silencing in rhesus cerebella for spinocerebellar ataxia type 1 therapy. *Brain* 2015;**138**(Pt 12):3555–66.
42. Rüb U, Schöls L, Paulson H, et al. Clinical features, neurogenetics and neuropathology of the polyglutamine spinocerebellar ataxias type 1, 2, 3, 6 and 7. *Prog Neurobiol* 2013;**104**:38–66.
43. Durr A. Autosomal dominant cerebellar ataxias: polyglutamine expansions and beyond. *Lancet Neurol* 2010;**9**(9):885–94.
44. Klaes A, Reckziegel E, Franca MC, Jr et al. MR Imaging in Spinocerebellar Ataxias: a systematic review. *AJNR Am J Neuroradiol* 2016;**37**(8):1405–12.
45. Jacobi H, Reetz K, du Montcel ST, et al. Biological and clinical characteristics of individuals at risk for spinocerebellar ataxia types 1, 2, 3, and 6 in the longitudinal RISCA study: analysis of baseline data. *Lancet Neurol* 2013;**12**(7):650–8.
46. Mochel F, Charles P, Seguin F, et al. Early energy deficit in Huntington disease: identification of a plasma biomarker traceable during disease progression. *PLoS One* 2007;**2**(7):e647.
47. Mochel F, Haller RG. Energy deficit in Huntington disease: why it matters. *J Clin Invest* 2011;**121**(2):493–9.
48. Adanyeguh IM, Rinaldi D, Henry PG, et al. Triheptanoin improves brain energy metabolism in patients with Huntington disease. *Neurology* 2015;**84**(5):490–5.
49. Schmitz-Hubsch T, du Montcel ST, Baliko L, et al. Scale for the assessment and rating of ataxia: development of a new clinical scale. *Neurology* 2006;**66**:1717–20.
50. Wishart DS, Tzur D, Knox C. HMDB: the Human Metabolome Database. *Nucleic Acids Res* 2007;**35**:521–6.
51. Wishart DS, Knox C, Guo AC. HMDB: a knowledgebase for the human metabolome. *Nucleic Acids Res* 2009;**37**:603–10.
52. Wishart DS, Knox C, Guo AC. HMDB 3.0 | The Human Metabolome Database in 2013. *Nucleic Acids Res* 2013;**41**:801–7.
53. Kanehisa M, Sato Y, Kawashima M, et al. KEGG: Kyoto Encyclopedia of Genes and Genomes. *Nucleic Acids Res* 2000;**28**:27–30.
54. Kanehisa M, Sato Y, Kawashima M, et al. KEGG as a reference resource for gene and protein annotation. *Nucleic Acids Res* 2016;**44**:457–62.
55. Lamari F, Mochel F, Sedel F, et al. Disorders of phospholipids, sphingolipids and fatty acids biosynthesis: toward a new category of inherited metabolic diseases. *J Inherit Metab Dis* 2013;**36**:411–25.
56. Caspi R, Foerster H, Fulcher CA, et al. The MetaCyc database of metabolic pathways and enzymes and the BioCyc collection of Pathway/Genome Databases. *Nucleic Acids Res* 2008;**36**(Suppl 1):D623–31.
57. McKeon JJ. Canonical analysis: some relation between canonical correlation, factor analysis, discriminant analysis, and scaling theory. *Psychom Monogr* 1966;**13**.
58. Lastres-Becker I, Brodesser S, Lütjohann D, et al. Insulin receptor and lipid metabolism pathology in ataxin-2 knock-out mice. *Hum Mol Genet* 2008;**17**:1465–81.
59. Martin RE, Elliott MH, Brush RS, et al. Detailed characterization of the lipid composition of detergent-resistant membranes from photoreceptor rod outer segment membranes. *Invest Ophthalmol Vis Sci* 2005;**46**(4):1147–54.
60. McMahon A, Butovich IA, Kedziarski W. Epidermal expression of an Elov14 transgene rescues neonatal lethality of homozygous Stargardt disease-3 mice. *J Lipid Res* 2011;**52**(6):1128–38.
61. Lamari F, Mochel F, Saudubray JM. An overview of inborn errors of complex lipid biosynthesis and remodelling. *J Inherit Metab Dis* 2015;**38**(1):3–18.
62. Tenenhaus AL, Brusquet L, Lechuga G. Multiway regularized generalized canonical correlation analysis. In 47èmes Journées de Statistique de la SFDS (JdS 2015), Lille, France, 2015.
63. Tenenhaus A, Tenenhaus M. Regularized generalized canonical correlation analysis for multiblock or multigroup data analysis. *Eur J Oper Res* 2014;**238**:391–403.

# Chapter 8

## Conclusion

We have successfully taken advantage of different MR modalities in the search for biomarkers in view of therapeutic interventions in polyglutamine diseases.

In HD, we validated the use of the Pi/PCr ratio as a biomarker of brain energy metabolism and showed that it was able to capture brain metabolic profiles before and after treatment. We have shown that without therapeutic intervention, abnormal brain metabolism persists over time. We used this biomarker and treatment on another disease characterized by primary brain energy deficiency – GLUT1-DS. In GLUT1-DS, we highlighted the robustness of the Pi/PCr ratio and affirmed the efficacy of triheptanoin on targeting brain energy deficit. These studies have paved the way for two ongoing therapeutic trials in HD to test the anaplerotic properties of triheptanoin (TRIHEP3), as well as a regulator of mitochondrial energy homeostasis, resveratrol (REVHD). Each of these ongoing trials benefits from a large cohort of 100 HD patients and uses MR related measures as primary outcome measures. As previously shown, we expect to confirm abnormal brain energy profiles in HD patients before treatment with an improvement after treatment. We also expect treated patients to have a slower rate of caudate atrophy than the placebo group. Likewise, microstructure alterations as measured with DTI should be less in treated patients than in the placebo group.

In a rate-reaction study using MT we showed that reduced rate of CK might underlie some of the metabolic dysfunction in HD. We are currently using a multimodal approach to try identifying metabolic, functional and structural changes (HDeENERGY) that could further explain the pathogenic mechanism associated with energy deficiency in HD. DWS could complement DTI results in better probing changes in cellular and extracellular compartments in HD. Furthermore, the functional organization of brain networks could give an indication on how different areas of patients' brain consume energy. This study will benefit from a multimodal integration of data to create a link between all MR measures.

A great hindrance to MRS techniques has always been standardization. The use of different MR sequences and analytical techniques have yielded different reports in similar brain regions. Therefore, we have shown in a bi-centric study that MRS studies can be robust and reproducible when improved sequences with shorter  $T_E$ , such as the modified semi-LASER sequence, and the same analytical procedures are used. We have applied this standardized procedure in a unique cohort of patients with SCA and we showed that several

neurochemicals are altered in SCAs. Furthermore, we showed that imaging markers have larger effect sizes than clinical scores. The use of MR markers with high effect sizes would be very helpful for upcoming therapeutic trials in rare diseases such as HD and SCAs.

Integration of different modalities produces composite scores that can better characterize specific diseases than single biomarkers. However, modalities always differ in the type and number of variables they generate. That means using conventional statistical tools to analyze them could fail. We therefore showed how a new multiblock statistical procedure could overcome this challenge and generate multimodal composite scores. Another use of this statistical approach is the extraction of robust biomarkers.

In the upcoming era of gene therapy for polyglutamine diseases, we believe that the MR biomarkers that we have identified can provide important clues in the evaluation of therapeutic benefits in HD and SCA patients. If gene therapies become authorized at the presymptomatic stages of these diseases, MR biomarkers will constitute unavoidable outcome measures. Furthermore, metabolic interventions such as anaplerotic approaches using triheptanoin, which we showed capable of improving brain energy metabolism, may also provide important add-on therapies as energy deficiency occurs very early in the disease process.

## References:

- Achard S, Salvador R, Whitcher B, Suckling J, Bullmore E. A resilient, low-frequency, small-world human brain functional network with highly connected association cortical hubs. *J Neurosci* 2006;26(1):63-72.
- Adanyeguh IM, Henry PG, Nguyen TM, Rinaldi D, Jauffret C, Valabregue R, Emir UE, Deelchand DK, Brice A, Eberly LE, Oz G, Durr A, Mochel F. In Vivo Neurometabolic Profiling in Patients With Spinocerebellar Ataxia Types 1, 2, 3, and 7. *Mov Disord* 2015;30(5):662-670.
- Alcauter S, Barrios FA, Díaz R, Fernández-Ruiz J. Gray and white matter alterations in spinocerebellar ataxia type 7: an in vivo DTI and VBM study. *Neuroimage* 2011;55(1):1-7.
- Alexander AL, Hasan KM, Lazar M, Tsuruda JS, Parker DL. Analysis of partial volume effects in diffusion-tensor MRI. *Magn Reson Med* 2001;45(5):770-780.
- Alexander AL, Lee JE, Lazar M, Field AS. Diffusion tensor imaging of the brain. *Neurotherapeutics* 2007;4(3):316-329.
- Alexander DC, Barker GJ, Arridge SR. Detection and modeling of non-Gaussian apparent diffusion coefficient profiles in human brain data. *Magn Reson Med* 2002;48(2):331-340.
- Almqvist EW, Bloch M, Brinkman R, Craufurd D, Hayden MR. A worldwide assessment of the frequency of suicide, suicide attempts, or psychiatric hospitalization after predictive testing for Huntington disease. *Am J Hum Genet* 1999;64(5):1293-1304.
- Andersson JLR, Skare S, Ashburner J. How to correct susceptibility distortions in spin-echo echo-planar images: application to diffusion tensor imaging. *Neuroimage* 2003;20(2):870-888.
- Andersson JLR, Sotiropoulos SN. An integrated approach to correction for off-resonance effects and subject movement in diffusion MR imaging. *Neuroimage* 2016;125:1063-1078.
- Antonini A, Leenders KL, Spiegel R, Meier D, Vontobel P, Weigell-Weber M, Sanchez-Pernaute R, de Yebenez JG, Boesiger P, Weindl A, Maguire RP. Striatal glucose metabolism

and dopamine D2 receptor binding in asymptomatic gene carriers and patients with Huntington's disease. *Brain* 1996;119 ( Pt 6):2085-2095.

Ashburner J, Friston KJ. Unified segmentation. *Neuroimage* 2005;26(3):839-851.

Basser PJ, Mattiello J, LeBihan D. Estimation of the effective self-diffusion tensor from the NMR spin echo. *J Magn Reson B* 1994a;103(3):247-254.

Basser PJ, Mattiello J, LeBihan D. MR diffusion tensor spectroscopy and imaging. *Biophys J* 1994b;66(1):259-267.

Beckmann CF, DeLuca M, Devlin JT, Smith SM. Investigations into resting-state connectivity using independent component analysis. *Philos Trans R Soc Lond B Biol Sci* 2005;360(1457):1001-1013.

Biswal B, Yetkin FZ, Haughton VM, Hyde JS. Functional connectivity in the motor cortex of resting human brain using echo-planar MRI. *Magn Reson Med* 1995;34(4):537-541.

Branzoli F, Techawiboonwong A, Kan H, Webb A, Ronen I. Functional diffusion-weighted magnetic resonance spectroscopy of the human primary visual cortex at 7 T. *Magn Reson Med* 2013;69(2):303-309.

Cancel G, Duyckaerts C, Holmberg M, Zander C, Yvert G, Lebre AS, Ruberg M, Faucheux B, Agid Y, Hirsch E, Brice A. Distribution of ataxin-7 in normal human brain and retina. *Brain* 2000;123 Pt 12:2519-2530.

Cassidy B, Rae C, Solo V. Brain activity: connectivity, sparsity, and mutual information. *IEEE Trans Med Imaging* 2015;34(4):846-860.

Chaganti SS, McCusker EA, Loy CT. What do we know about Late Onset Huntington's Disease? *J Huntingtons Dis* 2017;6(2):95-103.

Chard DT, Parker GJ, Griffin CM, Thompson AJ, Miller DH. The reproducibility and sensitivity of brain tissue volume measurements derived from an SPM-based segmentation methodology. *J Magn Reson Imaging* 2002;15(3):259-267.

Chen W, Zhu XH, Adriany G, Ugurbil K. Increase of creatine kinase activity in the visual cortex of human brain during visual stimulation: a <sup>31</sup>P magnetization transfer study. *Magn Reson Med* 1997;38(4):551-557.

Chen X, Tang TS, Tu H, Nelson O, Pook M, Hammer R, Nukina N, Bezprozvanny I. Deranged calcium signaling and neurodegeneration in spinocerebellar ataxia type 3. *J Neurosci* 2008;28(48):12713-12724.

Choe AS, Jones CK, Joel SE, Muschelli J, Belegu V, Caffo BS, Lindquist MA, van Zijl PC, Pekar JJ. Reproducibility and Temporal Structure in Weekly Resting-State fMRI over a Period of 3.5 Years. *PLoS One* 2015;10(10):e0140134.

Clarke CE, Lowry M, Quarrell OW. No change in striatal glutamate in Huntington's disease measured by proton magnetic resonance spectroscopy. *Parkinsonism Relat Disord* 1998;4(3):123-127.

Cohen J. (1988). *Statistical power analysis for the behavioral sciences* (2nd ed.). USA: Lawrence Erlbaum Associates.

Cole DM, Smith SM, Beckmann CF. Advances and pitfalls in the analysis and interpretation of resting-state FMRI data. *Front Syst Neurosci* 2010;4:8.

Concha L, Livy DJ, Beaulieu C, Wheatley BM, Gross DW. In vivo diffusion tensor imaging and histopathology of the fimbria-fornix in temporal lobe epilepsy. *J Neurosci* 2010;30(3):996-1002.

Costa Mdo C, Paulson HL. Toward understanding Machado-Joseph disease. *Prog Neurobiol* 2012;97(2):239-257.

Courchesne E, Yeung-Courchesne R, Press GA, Hesselink JR, Jernigan TL. Hypoplasia of cerebellar vermal lobules VI and VII in autism. *N Engl J Med* 1988;318(21):1349-1354.

Cui L, Jeong H, Borovecki F, Parkhurst CN, Tanese N, Kraine D. Transcriptional repression of PGC-1 $\alpha$  by mutant huntingtin leads to mitochondrial dysfunction and neurodegeneration. *Cell* 2006;127(1):59-69.

Daianu M, Jahanshad N, Villalon-Reina JE, Prasad G, Jacobs RE, Barnes S, Zlokovic BV, Montagne A, Thompson PM. 7T Multi-shell Hybrid Diffusion Imaging (HYDI) for Mapping Brain Connectivity in Mice. *Proc SPIE Int Soc Opt Eng* 2015;9413.

Damiano M, Diguët E, Malgorn C, D'Aurelio M, Galvan L, Petit F, Benhaim L, Guillermier M, Houitte D, Dufour N, Hantraye P, Canals JM, Alberch J, Delzescaux T, Deglon N, Beal MF, Brouillet E. A role of mitochondrial complex II defects in genetic models of Huntington's disease expressing N-terminal fragments of mutant huntingtin. *Hum Mol Genet* 2013;22(19):3869-3882.

David G, Abbas N, Stevanin G, Durr A, Yvert G, Cancel G, Weber C, Imbert G, Saudou F, Antoniou E, Drabkin H, Gemmill R, Giunti P, Benomar A, Wood N, Ruberg M, Agid Y, Mandel JL, Brice A. Cloning of the SCA7 gene reveals a highly unstable CAG repeat expansion. *Nat Genet* 1997;17(1):65-70.

de Graaf RA. (2007). *In vivo NMR spectroscopy: Principles and techniques* (2nd ed.). Chichester, UK: John Wiley & Sons Ltd.

De Vivo DC, Trifiletti RR, Jacobson RI, Ronen GM, Behmand RA, Harik SI. Defective glucose transport across the blood-brain barrier as a cause of persistent hypoglycorrhachia, seizures, and developmental delay. *N Engl J Med* 1991;325(10):703-709.

Della Nave R, Foresti S, Tessa C, Moretti M, Ginestroni A, Gavazzi C, Guerrini L, Salvi F, Piacentini S, Mascalchi M. ADC mapping of neurodegeneration in the brainstem and cerebellum of patients with progressive ataxias. *Neuroimage* 2004;22(2):698-705.

Dhollander T, Raffelt D, Connelly A. Unsupervised 3-tissue response function estimation from single-shell or multi-shell diffusion MR data without a co-registered T1 image. *ISMRM Workshop on Breaking the Barriers of Diffusion MRI* 2016:5.

Djousse L, Knowlton B, Cupples LA, Marder K, Shoulson I, Myers RH. Weight loss in early stage of Huntington's disease. *Neurology* 2002;59(9):1325-1330.

Du F, Cooper AJ, Thida T, Sehovic S, Lukas SE, Cohen BM, Zhang X, Ongur D. In vivo evidence for cerebral bioenergetic abnormalities in schizophrenia measured using <sup>31</sup>P magnetization transfer spectroscopy. *JAMA Psychiatry* 2014;71(1):19-27.



du Montcel ST, Charles P, Ribai P, Goizet C, Le Bayon A, Labauge P, Guyant-Marechal L, Forlani S, Jauffret C, Vandenberghe N, N'Guyen K, Le Ber I, Devos D, Vincitorio CM, Manto MU, Tison F, Hannequin D, Ruberg M, Brice A, Durr A. Composite cerebellar functional severity score: validation of a quantitative score of cerebellar impairment. *Brain* 2008;131(Pt 5):1352-1361.

Durr A. Autosomal dominant cerebellar ataxias: polyglutamine expansions and beyond. *Lancet neurology* 2010;9(9):885-894.

Edelman RR. The history of MR imaging as seen through the pages of radiology. *Radiology* 2014;273(2 Suppl):S181-200.

Edelman RR, Warach S. Magnetic resonance imaging (1). *N Engl J Med* 1993;328(10):708-716.

Elias S, Thion MS, Yu H, Sousa CM, Lasgi C, Morin X, Humbert S. Huntingtin regulates mammary stem cell division and differentiation. *Stem Cell Reports* 2014;2(4):491-506.

Ercan E, Magro-Checa C, Valabregue R, Branzoli F, Wood ET, Steup-Beekman GM, Webb AG, Huizinga TW, van Buchem MA, Ronen I. Glial and axonal changes in systemic lupus erythematosus measured with diffusion of intracellular metabolites. *Brain* 2016;139(Pt 5):1447-1457.

Fan HC, Ho LI, Chi CS, Chen SJ, Peng GS, Chan TM, Lin SZ, Harn HJ. Polyglutamine (PolyQ) diseases: genetics to treatments. *Cell Transplant* 2014;23(4-5):441-458.

Finkbeiner S. Huntington's Disease. *Cold Spring Harb Perspect Biol* 2011;3(6).

Fischl B, Salat DH, Busa E, Albert M, Dieterich M, Haselgrove C, van der Kouwe A, Killiany R, Kennedy D, Klaveness S, Montillo A, Makris N, Rosen B, Dale AM. Whole brain segmentation: automated labeling of neuroanatomical structures in the human brain. *Neuron* 2002;33(3):341-355.

Freeborough PA, Fox NC. The boundary shift integral: an accurate and robust measure of cerebral volume changes from registered repeat MRI. *IEEE Trans Med Imaging* 1997;16(5):623-629.

Friedman JE. Anticipation in hereditary disease: the history of a biomedical concept. *Hum Genet* 2011;130(6):705-714.

Furrer SA, Mohanachandran MS, Waldherr SM, Chang C, Damian VA, Sopher BL, Garden GA, La Spada AR. Spinocerebellar ataxia type 7 cerebellar disease requires the coordinated action of mutant ataxin-7 in neurons and glia, and displays non-cell-autonomous bergmann glia degeneration. *J Neurosci* 2011;31(45):16269-16278.

Garali I, Adanyeguh IM, Ichou F, Perlberg V, Seyer A, Colsch B, Mozer I, Guillemot V, Durr A, Mochel F, Tenenhaus A. A strategy for multimodal data integration: application to biomarkers identification in spinocerebellar ataxia. *Brief Bioinform* 2017.

Gennarino VA, Singh RK, White JJ, De Maio A, Han K, Kim JY, Jafar-Nejad P, di Ronza A, Kang H, Sayegh LS, Cooper TA, Orr HT, Sillitoe RV, Zoghbi HY. Pumilio1 haploinsufficiency leads to SCA1-like neurodegeneration by increasing wild-type Ataxin1 levels. *Cell* 2015;160(6):1087-1098.

Grafton ST, Mazziotta JC, Pahl JJ, St George-Hyslop P, Haines JL, Gusella J, Hoffman JM, Baxter LR, Phelps ME. Serial changes of cerebral glucose metabolism and caudate size in persons at risk for Huntington's disease. *Arch Neurol* 1992;49(11):1161-1167.

Gras D, Roze E, Caillet S, Meneret A, Doummar D, Billette de Villemeur T, Vidailhet M, Mochel F. GLUT1 deficiency syndrome: an update. *Rev Neurol (Paris)* 2014;170(2):91-99.

Gruetter R, Tkac I. Field mapping without reference scan using asymmetric echo-planar techniques. *Magn Reson Med* 2000;43(2):319-323.

Guerrini L, Lolli F, Ginestroni A, Belli G, Della Nave R, Tessa C, Foresti S, Cosottini M, Piacentini S, Salvi F, Plasmati R, De Grandis D, Siciliano G, Filla A, Mascalchi M. Brainstem neurodegeneration correlates with clinical dysfunction in SCA1 but not in SCA2. A quantitative volumetric, diffusion and proton spectroscopy MR study. *Brain* 2004;127(Pt 8):1785-1795.

Guimarães RP, D'Abreu A, Yasuda CL, França MCJ, Silva BH, Cappabianco FA, Bergo FP, Lopes-Cendes IT, Cendes F. A multimodal evaluation of microstructural white matter damage in spinocerebellar ataxia type 3. *Mov Disord* 2013;28(8):1125-1132.

Gusella JF, MacDonald ME. Huntington's disease: seeing the pathogenic process through a genetic lens. *Trends Biochem Sci* 2006;31(9):533-540.

Gusella JF, Wexler NS, Conneally PM, Naylor SL, Anderson MA, Tanzi RE, Watkins PC, Ottina K, Wallace MR, Sakaguchi AY, Young AB, Shoulson I, Bonilla E, Martin JB. A polymorphic DNA marker genetically linked to Huntington's disease. *Nature* 1983;306(5940):234-238.

Guyenet SJ, Mookerjee SS, Lin A, Custer SK, Chen SF, Sopher BL, La Spada AR, Ellerby LM. Proteolytic cleavage of ataxin-7 promotes SCA7 retinal degeneration and neurological dysfunction. *Hum Mol Genet* 2015;24(14):3908-3917.

Hedreen JC, Peyser CE, Folstein SE, Ross CA. Neuronal loss in layers V and VI of cerebral cortex in Huntington's disease. *Neurosci Lett* 1991;133(2):257-261.

Heinen R, Bouvy WH, Mendrik AM, Viergever MA, Biessels GJ, de Bresser J. Robustness of Automated Methods for Brain Volume Measurements across Different MRI Field Strengths. *PLoS One* 2016;11(10):e0165719.

Hernandez-Castillo CR, Galvez V, Mercadillo R, Diaz R, Campos-Romo A, Fernandez-Ruiz J. Extensive white matter alterations and its correlations with ataxia severity in SCA 2 patients. *PLoS One* 2015;10(8):e0135449.

Hernandez-Castillo CR, Vaca-Palomares I, Galvez V, Campos-Romo A, Diaz R, Fernandez-Ruiz J. Cognitive deficits correlate with white matter deterioration in spinocerebellar ataxia type 2. *J Int Neuropsychol Soc* 2016;22(4):486-491.

Hobbs NZ, Henley SM, Wild EJ, Leung KK, Frost C, Barker RA, Scahill RI, Barnes J, Tabrizi SJ, Fox NC. Automated quantification of caudate atrophy by local registration of serial MRI: evaluation and application in Huntington's disease. *Neuroimage* 2009;47(4):1659-1665.

Holm S. A simple sequentially rejective multiple test procedure. *Scand J Statist* 1979;6:65-70.

Hunt RH, Thomas KM. Magnetic resonance imaging methods in developmental science: a primer. *Dev Psychopathol* 2008;20(4):1029-1051.

Iglesias JE, Van Leemput K, Bhatt P, C. C, Dutt S, Schuff N, Truran-Sacrey D, Boxer A, Fischl B, Alzheimer's Disease Neuroimaging Initiative. Bayesian segmentation of brainstem structures in MRI. *Neuroimage* 2015;113:184-195.

Ilg W, Bastian AJ, Boesch S, Burciu RG, Celnik P, Claassen J, Feil K, Kalla R, Miyai I, Nachbauer W, Schols L, Strupp M, Synofzik M, Teufel J, Timmann D. Consensus paper: management of degenerative cerebellar disorders. *Cerebellum* 2014;13(2):248-268.

Ingram M, Wozniak EAL, Duvick L, Yang R, Bergmann P, Carson R, O'Callaghan B, Zoghbi HY, Henzler C, Orr HT. Cerebellar Transcriptome Profiles of ATXN1 Transgenic Mice Reveal SCA1 Disease Progression and Protection Pathways. *Neuron* 2016;89(6):1194-1207.

Irwin S, Vandelft M, Pinchev D, Howell JL, Graczyk J, Orr HT, Truant R. RNA association and nucleocytoplasmic shuttling by ataxin-1. *J Cell Sci* 2005;118(Pt 1):233-242.

Jenkinson M, Bannister P, Brady JM, Smith SM. Improved optimisation for the robust and accurate linear registration and motion correction of brain images. *Neuroimage* 2002;17(2):825-841.

Jessen F, Gur O, Block W, Ende G, Frolich L, Hammen T, Wiltfang J, Kucinski T, Jahn H, Heun R, Maier W, Kolsch H, Kornhuber J, Traber F. A multicenter (1)H-MRS study of the medial temporal lobe in AD and MCI. *Neurology* 2009;72(20):1735-1740.

Jeurissen B, Tournier JD, Dhollander T, Connelly A, Sijbers J. Multi-tissue constrained spherical deconvolution for improved analysis of multi-shell diffusion MRI data. *Neuroimage* 2014;103:411-426.

Jiang H, Poirier MA, Liang Y, Pei Z, Weiskittel CE, Smith WW, DeFranco DB, Ross CA. Depletion of CBP is directly linked with cellular toxicity caused by mutant huntingtin. *Neurobiol Dis* 2006;23(3):543-551.

Jiru F. Introduction to post-processing techniques. *Eur J Radiol* 2008;67(2):202-217.

Jissendi Tchofo P, Baleriaux D. Brain (1)H-MR spectroscopy in clinical neuroimaging at 3T. *J Neuroradiol* 2009;36(1):24-40.

Kang JS, Klein JC, Baudrexel S, Deichmann R, Nolte D, Hilker R. White matter damage is related to ataxia severity in SCA3. *J Neuro* 2014;261(2):291-299.

Kawaguchi Y, Okamoto T, Taniwaki M, Aizawa M, Inoue M, Katayama S, Kawakami H, Nakamura S, Nishimura M, Akiguchi I, et al. CAG expansions in a novel gene for Machado-Joseph disease at chromosome 14q32.1. *Nat Genet* 1994;8(3):221-228.

Kremer B, Goldberg P, Andrew SE, Theilmann J, Telenius H, Zeisler J, Squitieri F, Lin B, Bassett A, Almqvist E, et al. A worldwide study of the Huntington's disease mutation. The sensitivity and specificity of measuring CAG repeats. *N Engl J Med* 1994;330(20):1401-1406.

La Spada AR, Fu YH, Sopher BL, Libby RT, Wang X, Li LY, Einum DD, Huang J, Possin DE, Smith AC, Martinez RA, Koszdin KL, Treuting PM, Ware CB, Hurley JB, Ptacek LJ, Chen S. Polyglutamine-expanded ataxin-7 antagonizes CRX function and induces cone-rod dystrophy in a mouse model of SCA7. *Neuron* 2001;31(6):913-927.

Labbadia J, Novoselov SS, Bett JS, Weiss A, Paganetti P, Bates GP, Cheetham ME. Suppression of protein aggregation by chaperone modification of high molecular weight complexes. *Brain* 2012;135(Pt 4):1180-1196.

Lagouge M, Argmann C, Gerhart-Hines Z, Meziane H, Lerin C, Daussin F, Messadeq N, Milne J, Lambert P, Elliott P, Geny B, Laakso M, Puigserver P, Auwerx J. Resveratrol improves mitochondrial function and protects against metabolic disease by activating SIRT1 and PGC-1alpha. *Cell* 2006;127(6):1109-1122.

Lam YC, Bowman AB, Jafar-Nejad P, Lim J, Richman R, Fryer JD, Hyun ED, Duvick LA, Orr HT, Botas J, Zoghbi HY. ATAXIN-1 interacts with the repressor Capicua in its native complex to cause SCA1 neuropathology. *Cell* 2006;127(7):1335-1347.

Lanska DJ. George Huntington (1850-1916) and hereditary chorea. *J Hist Neurosci* 2000;9(1):76-89.

Lauterbach EC, Cummings JL, Duffy J, Coffey CE, Kaufer D, Lovell M, Malloy P, Reeve A, Royall DR, Rummans TA, Salloway SP. Neuropsychiatric correlates and treatment of lenticulostriatal diseases: a review of the literature and overview of research opportunities in Huntington's, Wilson's, and Fahr's diseases. A report of the ANPA Committee on Research. American Neuropsychiatric Association. *J Neuropsychiatry Clin Neurosci* 1998;10(3):249-266.

Lee HC, Wei YH. Mitochondrial role in life and death of the cell. *J Biomed Sci* 2000;7(1):2-15.

Leonardi N, Richiardi J, Gschwind M, Simioni S, Annoni JM, Schluep M, Vuilleumier P, Van De Ville D. Principal components of functional connectivity: a new approach to study dynamic brain connectivity during rest. *Neuroimage* 2013;83:937-950.

Liu J, Tang TS, Tu H, Nelson O, Herndon E, Huynh DP, Pulst SM, Bezprozvanny I. Deranged calcium signaling and neurodegeneration in spinocerebellar ataxia type 2. *J Neurosci* 2009;29(29):9148-9162.

Lo EH. Degeneration and repair in central nervous system disease. *Nat Med* 2010;16(11):1205-1209.

Luo Y, de Graaf RA, DelaBarre L, Tannus A, Garwood M. BISTRO: an outer-volume suppression method that tolerates RF field inhomogeneity. *Magn Reson Med* 2001;45(6):1095-1102.

Mandelli ML, De Simone T, Minati L, Bruzzone MG, Mariotti C, Fancellu R, Savoiaro M, Grisoli M. Diffusion tensor imaging of spinocerebellar ataxias types 1 and 2. *AJNR Am J Neuroradiol* 2007;28(10):1996-2000.

Manto MU. The wide spectrum of spinocerebellar ataxias (SCAs). *Cerebellum* 2005;4(1):2-6.

Marrelec G, Krainik A, Duffau H, Pelegrini-Issac M, Lehericy S, Doyon J, Benali H. Partial correlation for functional brain interactivity investigation in functional MRI. *Neuroimage* 2006;32(1):228-237.

Mascalchi M, Toschi N, Giannelli M, Ginestroni A, Della Nave R, Nicolai E, Bianchi A, Tessa C, Salvatore E, Aiello M, Soricelli A, Diciotti S. Progression of microstructural damage in spinocerebellar ataxia type 2: a longitudinal DTI study. *AJNR Am J Neuroradiol* 2015;36(6):1096-10101.

Mitchell IJ, Cooper AJ, Griffiths MR. The selective vulnerability of striatopallidal neurons. *Prog Neurobiol* 1999;59(6):691-719.

Mochel F. Triheptanoin for the treatment of brain energy deficit: A 14-year experience. *J Neurosci Res* 2017.

Mochel F, Charles P, Seguin F, Barritault J, Coussieu C, Perin L, Le Bouc Y, Gervais C, Carcelain G, Vassault A, Feingold J, Rabier D, Durr A. Early energy deficit in Huntington disease: identification of a plasma biomarker traceable during disease progression. *PLoS One* 2007;2(7):e647.

Mochel F, Duteil S, Marelli C, Jauffret C, Barles A, Holm J, Sweetman L, Benoist JF, Rabier D, Carlier PG, Durr A. Dietary anaplerotic therapy improves peripheral tissue energy metabolism in patients with Huntington's disease. *Eur J Hum Genet* 2010;18(9):1057-1060.

Mochel F, Hainque E, Gras D, Adanyeguh IM, Caillet S, Heron B, Roubertie A, Kaphan E, Valabregue R, Rinaldi D, Vuillaumier S, Schiffmann R, Ottolenghi C, Hogrel JY, Servais L, Roze E. Triheptanoin dramatically reduces paroxysmal motor disorder in patients with GLUT1 deficiency. *J Neurol Neurosurg Psychiatry* 2016;87(5):550-553.

Mochel F, Haller RG. Energy deficit in Huntington disease: why it matters. *J Clin Invest* 2011;121(2):493-499.

Mochel F, N'Guyen TM, Deelchand D, Rinaldi D, Valabregue R, Wary C, Carlier PG, Durr A, Henry PG. Abnormal response to cortical activation in early stages of Huntington disease. *Mov Disord* 2012;27(7):907-910.

Mori S, Zhang J. Principles of diffusion tensor imaging and its applications to basic neuroscience research. *Neuron* 2006;51(5):527-539.

Myers RH. Huntington's disease genetics. *NeuroRx* 2004;1(2):255-262.

Nicholls DG. Mitochondrial calcium function and dysfunction in the central nervous system. *Biochim Biophys Acta* 2009;1787(11):1416-1424.

O'Donnell LJ, Westin CF. An introduction to diffusion tensor image analysis. *Neurosurg Clin N Am* 2011;22(2):185-196, viii.

Okazawa H, Rich T, Chang A, Lin X, Waragai M, Kajikawa M, Enokido Y, Komuro A, Kato S, Shibata M, Hatanaka H, Mouradian MM, Sudol M, Kanazawa I. Interaction between mutant ataxin-1 and PQBP-1 affects transcription and cell death. *Neuron* 2002;34(5):701-713.

Olson AL, Pessin JE. Structure, function, and regulation of the mammalian facilitative glucose transporter gene family. *Annu Rev Nutr* 1996;16:235-256.

Olson SD, Kambal A, Pollock K, Mitchell GM, Stewart H, Kalomoiris S, Cary W, Nacey C, Pepper K, Nolte JA. Examination of mesenchymal stem cell-mediated RNAi transfer to Huntington's disease affected neuronal cells for reduction of huntingtin. *Mol Cell Neurosci* 2012;49(3):271-281.

Orr HT, Chung MY, Banfi S, Kwiatkowski TJ, Jr., Servadio A, Beaudet AL, McCall AE, Duvick LA, Ranum LP, Zoghbi HY. Expansion of an unstable trinucleotide CAG repeat in spinocerebellar ataxia type 1. *Nat Genet* 1993;4(3):221-226.

Orr HT, Zoghbi HY. Trinucleotide repeat disorders. *Annu Rev Neurosci* 2007;30:575-621.

Oz G, Hutter D, Tkac I, Clark HB, Gross MD, Jiang H, Eberly LE, Bushara KO, Gomez CM. Neurochemical alterations in spinocerebellar ataxia type 1 and their correlations with clinical status. *Mov Disord* 2010;25(9):1253-1261.

Palhan VB, Chen S, Peng GH, Tjernberg A, Gamper AM, Fan Y, Chait BT, La Spada AR, Roeder RG. Polyglutamine-expanded ataxin-7 inhibits STAGA histone acetyltransferase activity to produce retinal degeneration. *Proc Natl Acad Sci U S A* 2005;102(24):8472-8477.

Pauling L, Coryell CD. The Magnetic Properties and Structure of Hemoglobin, Oxyhemoglobin and Carbonmonoxyhemoglobin. *Proc Natl Acad Sci U S A* 1936;22(4):210-216.

Paulson HL. Dominantly inherited ataxias: lessons learned from Machado-Joseph disease/spinocerebellar ataxia type 3. *Semin Neurol* 2007;27(2):133-142.

Paulson HL. The spinocerebellar ataxias. *J Neuroophthalmol* 2009;29(3):227-237.

Paulson HL, Bonini NM, Roth KA. Polyglutamine disease and neuronal cell death. *Proc Natl Acad Sci U S A* 2000;97(24):12957-12958.

Petersen MV, Lund TE, Sunde N, Frandsen J, Rosendal F, Juul N, Østergaard K. Probabilistic versus deterministic tractography for delineation of the cortico-subthalamic hyperdirect pathway in patients with Parkinson disease selected for deep brain stimulation. *J Neurosurg* 2016;126(5):1657-1668.

Pierpaoli C, Basser PJ. Toward a quantitative assessment of diffusion anisotropy. *Magn Reson Med* 1996;36(893-906).



Plewes DB, Kucharczyk W. Physics of MRI: a primer. *J Magn Reson Imaging* 2012;35(5):1038-1054.

Prakash N, Hageman N, Hua X, Toga AW, Perlman SL, Salamon N. Patterns of fractional anisotropy changes in white matter of cerebellar peduncles distinguish spinocerebellar ataxia-1 from multiple system atrophy and other ataxia syndromes. *Neuroimage* 2009;47(Suppl 2):T72-81.

Pulst SM, Nechiporuk A, Nechiporuk T, Gispert S, Chen XN, Lopes-Cendes I, Pearlman S, Starkman S, Orozco-Diaz G, Lunke A, DeJong P, Rouleau GA, Auburger G, Korenberg JR, Figueroa C, Sahba S. Moderate expansion of a normally biallelic trinucleotide repeat in spinocerebellar ataxia type 2. *Nat Genet* 1996;14(3):269-276.

Quincozes-Santos A, Gottfried C. Resveratrol modulates astroglial functions: neuroprotective hypothesis. *Ann N Y Acad Sci* 2011;1215:72-78.

Raffelt D, Tournier JD, Crozier S, Connelly A, Salvado O. Reorientation of fiber orientation distributions using apodized point spread functions. *Magn Reson Med* 2012a;67:844-855.

Raffelt D, Tournier JD, Fripp J, Crozier S, Connelly A, Salvado O. Symmetric diffeomorphic registration of fibre orientation distributions. *Neuroimage* 2011;56(3):1171-1180.

Raffelt D, Tournier JD, Rose S, Ridgway GR, Henderson R, Crozier S, Salvado O, Connelly A. Apparent Fibre Density: a novel measure for the analysis of diffusion-weighted magnetic resonance images. *Neuroimage* 2012b;59(4):3976-3994.

Raffelt DA, Smith RE, Ridgway GR, Tournier JD, Vaughan DN, Rose S, Henderson R, Connelly A. Connectivity-based fixel enhancement: Whole-brain statistical analysis of diffusion MRI measures in the presence of crossing fibres. *Neuroimage* 2015;117:40-55.

Raffelt DA, Tournier JD, Smith RE, Vaughan DN, Jackson G, Ridgway GR, Connelly A. Investigating white matter fibre density and morphology using fixel-based analysis. *Neuroimage* 2017;144(Pt A):58-73.

Rawlins MD, Wexler NS, Wexler AR, Tabrizi SJ, Douglas I, Evans SJ, Smeeth L. The Prevalence of Huntington's Disease. *Neuroepidemiology* 2016;46(2):144-153.

Reetz K, Costa AS, Mirzazade S, Lehmann A, Juzek A, Rakowicz M, Boguslawska R, Schöls L, Linnemann C, Mariotti C, Grisoli M, Dürr A, van d, Warrenburg, B. P., Timmann D, Pandolfo M, Bauer P, Jacobi H, Hauser TK, Klockgether T, Schulz JB, Ataxia Study Group Investigators. Genotype-specific patterns of atrophy progression are more sensitive than clinical decline in SCA1, SCA3 and SCA6. *Brain* 2013;136(Pt 3):905-917.

Roe CR, Sweetman L, Roe DS, David F, Brunengraber H. Treatment of cardiomyopathy and rhabdomyolysis in long-chain fat oxidation disorders using an anaplerotic odd-chain triglyceride. *J Clin Invest* 2002;110(2):259-269.

Ronen I, Valette J. Diffusion-weighted magnetic resonance spectroscopy. *eMagRes* 2015;4:733-750.

Rozenfeld MN, Nemeth AJ, Walker MT, Mohan P, Wang X, Parrish TB, Opal P. An investigation of diffusion imaging techniques in the evaluation of spinocerebellar ataxia and multisystem atrophy. *J Clin Neurosci* 2015;22(1):166-172.

Rüb U, Schöls L, Paulson H, Auburger G, Kermer P, Jen JC, Seidel K, Korf HW, Deller T. Clinical features, neurogenetics and neuropathology of the polyglutamine spinocerebellar ataxias type 1, 2, 3, 6 and 7. *Prog Neurobiol* 2013;104:38-66.

Ruocco HH, Lopes-Cendes I, Li LM, Cendes F. Evidence of thalamic dysfunction in Huntington disease by proton magnetic resonance spectroscopy. *Mov Disord* 2007;22(14):2052-2056.

Salvador R, Suckling J, Schwarzbauer C, Bullmore E. Undirected graphs of frequency-dependent functional connectivity in whole brain networks. *Philos Trans R Soc Lond B Biol Sci* 2005;360(1457):937-946.

Samartzis L, Dima D, Fusar-Poli P, Kyriakopoulos M. White matter alterations in early stages of schizophrenia: a systematic review of diffusion tensor imaging studies. *J Neuroimaging* 2014;24(2):101-110.

Saudou F, Humbert S. The Biology of Huntingtin. *Neuron* 2016;89(5):910-926.

Sawilowsky S. New effect size rules of thumb. *J Mod Appl Stat Methods* 2009;8(2):467-474.

Schlaier JR, Beer AL, Faltermeier R, Fellner C, Steib K, Lange M, Greenlee MW, Brawanski AT, Anthofer JM. Probabilistic vs. deterministic fiber tracking and the influence of different seed regions to delineate cerebellar-thalamic fibers in deep brain stimulation. *Eur J Neurosci* 2017.

Schmitz-Hübsch T, du Montcel ST, Baliko L, Berciano J, Boesch S, Depondt C, Giunti P, Globas C, Infante J, Kang JS, Kremer B, Mariotti C, Melegh B, Pandolfo M, Rakowicz M, Ribai P, Rola R, Schöls L, Szymanski S, van de Warrenburg BP, Dürr A, Klockgether T, Fancellu R. Scale for the assessment and rating of ataxia: development of a new clinical scale. *Neurology* 2006;66(11):1717-1720.

Schulte J, Littleton JT. The biological function of the Huntingtin protein and its relevance to Huntington's Disease pathology. *Curr Trends Neurol* 2011;5:65-78.

Schulz JB, Borkert J, Wolf S, Schmitz-Hübsch T, Rakowicz M, Mariotti C, Schöls L, Timmann D, van de Warrenburg B, Dürr A, Pandolfo M, Kang JS, Mandly AG, Nagele T, Grisoli M, Boguslawska R, Bauer P, Klockgether T, Hauser TK. Visualization, quantification and correlation of brain atrophy with clinical symptoms in spinocerebellar ataxia types 1, 3 and 6. *Neuroimage* 2010;49(1):158-168.

Serra HG, Duvick L, Zu T, Carlson K, Stevens S, Jorgensen N, Lysholm A, Burrig E, Zoghbi HY, Clark HB, Andresen JM, Orr HT. ROR $\alpha$ -mediated Purkinje cell development determines disease severity in adult SCA1 mice. *Cell* 2006;127(4):697-708.

Shao J, Diamond MI. Polyglutamine diseases: emerging concepts in pathogenesis and therapy. *Hum Mol Genet* 2007;16 Spec No. 2:R115-123.

Smith RE, Tournier JD, Calamante F, Connelly A. SIFT: Spherical-deconvolution informed filtering of tractograms. *Neuroimage* 2013;67:298-312.

Smith SM. Fast robust automated brain extraction. *Hum Brain Mapp* 2002;17(3):143-155.

Smith SM. The future of fMRI connectivity. *Neuroimage* 2012;62(2):1257-1266.

Smith SM, Jenkinson M, Johansen-Berg H, Rueckert D, Nichols TE, Mackay CE, Watkins KE, Ciccarelli O, Cader MZ, Matthews PM, Behrens TE. Tract-based spatial statistics: voxelwise analysis of multi-subject diffusion data. *Neuroimage* 2006;31(4):1487-1505.

Smith SM, Jenkinson M, Woolrich MW, Beckmann CF, Behrens TE, Johansen-Berg H, Bannister PR, De Luca M, Drobnjak I, Flitney DE, Niazy RK, Saunders J, Vickers J, Zhang Y, De Stefano N, Brady JM, Matthews PM. Advances in functional and structural MR image analysis and implementation as FSL. *Neuroimage* 2004;23(S1):208-219.

Smith SM, Zhang Y, Jenkinson M, Chen J, Matthews PM, Federico A, De Stefano N. Accurate, robust, and automated longitudinal and cross-sectional brain change analysis. *Neuroimage* 2002;17(1):479-489.

Soong BW, Liu RS. Positron emission tomography in asymptomatic gene carriers of Machado-Joseph disease. *J Neurol Neurosurg Psychiatry* 1998;64(4):499-504.

Sosnovik DE, Weissleder R. Emerging concepts in molecular MRI. *Curr Opin Biotechnol* 2007;18(1):4-10.

Stevanin G, Durr A, Brice A. Clinical and molecular advances in autosomal dominant cerebellar ataxias: from genotype to phenotype and physiopathology. *Eur J Hum Genet* 2000;8(1):4-18.

Strom AL, Forsgren L, Holmberg M. A role for both wild-type and expanded ataxin-7 in transcriptional regulation. *Neurobiol Dis* 2005;20(3):646-655.

Synofzik M, Ilg W. Motor training in degenerative spinocerebellar disease: ataxia-specific improvements by intensive physiotherapy and exergames. *Biomed Res Int* 2014;2014:583507.

Tabrizi SJ, Reilmann R, Roos RA, Durr A, Leavitt B, Owen G, Jones R, Johnson H, Craufurd D, Hicks SL, Kennard C, Landwehrmeyer B, Stout JC, Borowsky B, Scahill RI, Frost C, Langbehn DR. Potential endpoints for clinical trials in premanifest and early Huntington's disease in the TRACK-HD study: analysis of 24 month observational data. *Lancet neurology* 2012;11(1):42-53.

Tabrizi SJ, Scahill RI, Durr A, Roos RA, Leavitt BR, Jones R, Landwehrmeyer GB, Fox NC, Johnson H, Hicks SL, Kennard C, Craufurd D, Frost C, Langbehn DR, Reilmann R, Stout JC. Biological and clinical changes in premanifest and early stage Huntington's disease in the TRACK-HD study: the 12-month longitudinal analysis. *Lancet neurology* 2011;10(1):31-42.

Tabrizi SJ, Scahill RI, Owen G, Durr A, Leavitt BR, Roos RA, Borowsky B, Landwehrmeyer B, Frost C, Johnson H, Craufurd D, Reilmann R, Stout JC, Langbehn DR. Predictors of phenotypic progression and disease onset in premanifest and early-stage Huntington's disease in the TRACK-HD study: analysis of 36-month observational data. *Lancet neurology* 2013;12(7):637-649.

The Huntington's Disease Collaborative Research Group. A novel gene containing a trinucleotide repeat that is expanded and unstable on Huntington's disease chromosomes. *Cell* 1993;72(6):971-983.

Tournier JD, Calamante F, Connelly A. Robust determination of the fibre orientation distribution in diffusion MRI: non-negativity constrained super-resolved spherical deconvolution. *Neuroimage* 2007;35(4):1459-1472.

Tournier JD, Calamante F, Connelly A. Improved probabilistic streamlines tractography by 2nd order integration over fibre orientation distributions. *Proc Intl Soc Mag Reson Med* 2010:1670.

Trushina E, Dyer RB, Badger JD, 2nd, Ure D, Eide L, Tran DD, Vrieze BT, Legendre-Guillemain V, McPherson PS, Mandavilli BS, Van Houten B, Zeitlin S, McNiven M, Aebersold R, Hayden M, Parisi JE, Seeberg E, Dragatsis I, Doyle K, Bender A, Chacko C, McMurray CT. Mutant huntingtin impairs axonal trafficking in mammalian neurons in vivo and in vitro. *Mol Cell Biol* 2004;24(18):8195-8209.

Tsai CC, Kao HY, Mizutani A, Banayo E, Rajan H, McKeown M, Evans RM. Ataxin 1, a SCA1 neurodegenerative disorder protein, is functionally linked to the silencing mediator of retinoid and thyroid hormone receptors. *Proc Natl Acad Sci U S A* 2004;101(12):4047-4052.

Tuch DS, Reese TG, Wiegell MR, Makris N, Belliveau JW, Wedeen VJ. High angular resolution diffusion imaging reveals intravoxel white matter fiber heterogeneity. *Magn Reson Med* 2002;48(4):577-582.

Tustison N, Avants B, Cook P, Zheng Y, Egan A, Yushkevich P, Gee JC. N4ITK: Improved N3 Bias Correction. *IEEE Trans Med Imaging* 2010;29(6):1310-1320.

van den Bogaard SJ, Dumas EM, Teeuwisse WM, Kan HE, Webb A, Roos RA, van der Grond J. Exploratory 7-Tesla magnetic resonance spectroscopy in Huntington's disease

provides in vivo evidence for impaired energy metabolism. *J Neurol* 2011;258(12):2230-2239.

Veraart J, Fieremans E, Novikov DS. Diffusion MRI noise mapping using random matrix theory. *Magn Reson Med* 2016a;76(5):1582-1593.

Veraart J, Novikov DS, Christiaens D, Ades-Aron B, Sijbers J, Fieremans E. Denoising of diffusion MRI using random matrix theory. *Neuroimage* 2016b;142:394-406.

Videnovic A. Treatment of huntington disease. *Curr Treat Options Neurol* 2013;15(4):424-438.

Vijayalaxmi, Fatahi M, Speck O. Magnetic resonance imaging (MRI): A review of genetic damage investigations. *Mutat Res Rev Mutat Res* 2015;764:51-63.

Vonsattel JP, DiFiglia M. Huntington disease. *J Neuropathol Exp Neurol* 1998;57(5):369-384.

Vonsattel JP, Myers RH, Stevens TJ, Ferrante RJ, Bird ED, Richardson EP, Jr. Neuropathological classification of Huntington's disease. *J Neuropathol Exp Neurol* 1985;44(6):559-577.

Walker FO. Huntington's disease. *Lancet* 2007;369(9557):218-228.

Weber JJ, Sowa AS, Binder T, Hubener J. From pathways to targets: understanding the mechanisms behind polyglutamine disease. *Biomed Res Int* 2014;2014:701758.

Wiegell MR, Larsson HB, Wedeen VJ. Fiber crossing in human brain depicted with diffusion tensor MR imaging. *Radiology* 2000;217(3):897-903.

Wilkins B, Lee N, Gajawelli N, Law M, Leporé N. Fiber estimation and tractography in diffusion MRI: development of simulated brain images and comparison of multi-fiber analysis methods at clinical b-values. *Neuroimage* 2015;109:341-356.

Winkler AM, Ridgway GR, Webster MA, Smith SM, Nichols TE. Permutation inference for the general linear model. *Neuroimage* 2014;92:381-397.

Wright DK, Johnston LA, Kershaw J, Ordidge R, O'Brien TJ, Shultz SR. Changes in apparent fiber density and track-weighted imaging metrics in white matter following experimental traumatic brain injury. *J Neurotrauma* 2017.

Yamada M, Sato T, Tsuji S, Takahashi H. CAG repeat disorder models and human neuropathology: similarities and differences. *Acta Neuropathol* 2008;115(1):71-86.

Yoo YJ, Oh J. Identification of early neurodegenerative change in presymptomatic spinocerebellar ataxia type 1: A diffusion tensor imaging study. *Parkinsonism Relat Disord* 2017;36:109-110.

Yushkevich PA, Piven J, Hazlett HC, Smith RG, Ho S, Gee JC, Gerig G. User-guided 3D active contour segmentation of anatomical structures: significantly improved efficiency and reliability. *Neuroimage* 2006;31(3):1116-1128.

## **Annex**

### **Triheptanoïn dramatically reduces paroxysmal motor disorder in patients with GLUT1 deficiency.**

Mochel F, Hainque E, Gras D, Adanyeguh IM, Caillet S, Heron B, Roubertie A, Kaphan E, Valabregue R, Rinaldi D, Vuillaumier S, Schiffmann R, Ottolenghi C, Hogrel JY, Servais L, Roze E. J Neurol Neurosurg Psychiatry (2016)





OPEN ACCESS

## SHORT REPORT

## Triheptanoin dramatically reduces paroxysmal motor disorder in patients with GLUT1 deficiency

Fanny Mochel,<sup>1,2</sup> Elodie Hainque,<sup>1,3</sup> Domitille Gras,<sup>1,4</sup> Isaac M Adanyeguh,<sup>1</sup> Samantha Caillet,<sup>5</sup> Bénédicte Héron,<sup>6</sup> Agathe Roubertie,<sup>7,8</sup> Elsa Kaphan,<sup>9</sup> Romain Valabregue,<sup>1,10</sup> Daisy Rinaldi,<sup>1</sup> Sandrine Vuillaumier,<sup>11</sup> Raphael Schiffmann,<sup>12</sup> Chris Ottolenghi,<sup>13,14</sup> Jean-Yves Hogrel,<sup>15</sup> Laurent Servais,<sup>16</sup> Emmanuel Roze<sup>1,3</sup>

► Additional material is published online only. To view please visit the journal online (<http://dx.doi.org/10.1136/jnnp-2015-311475>).

For numbered affiliations see end of article.

**Correspondence to**

Dr Fanny Mochel, Institut du Cerveau et de la Moelle épinière, Aile 4A, Groupe Hospitalier Pitié-Salpêtrière, Paris 75013, France; [fanny.mochel@upmc.fr](mailto:fanny.mochel@upmc.fr)

Received 2 July 2015

Revised 29 September 2015

Accepted 14 October 2015

**ABSTRACT**

**Objective** On the basis of our previous work with triheptanoin, which provides key substrates to the Krebs cycle in the brain, we wished to assess its therapeutic effect in patients with glucose transporter type 1 deficiency syndrome (GLUT1-DS) who objected to or did not tolerate ketogenic diets.

**Methods** We performed an open-label pilot study with three phases of 2 months each (baseline, treatment and withdrawal) in eight patients with GLUT1-DS (7–47 years old) with non-epileptic paroxysmal manifestations. We used a comprehensive patient diary to record motor and non-motor paroxysmal events. Functional <sup>31</sup>P-NMR spectroscopy was performed to quantify phosphocreatine (PCr) and inorganic phosphate (Pi) within the occipital cortex during (activation) and after (recovery) a visual stimulus.

**Results** Patients with GLUT1-DS experienced a mean of 30.8 (±27.7) paroxysmal manifestations (52% motor events) at baseline that dropped to 2.8 (±2.9, 76% motor events) during the treatment phase (p=0.028). After withdrawal, paroxysmal manifestations recurred with a mean of 24.2 (±21.9, 52% motor events; p=0.043). Furthermore, brain energy metabolism normalised with triheptanoin, that is, increased Pi/PCr ratio during brain activation compared to the recovery phase (p=0.021), and deteriorated when triheptanoin was withdrawn.

**Conclusions** Treatment with triheptanoin resulted in a 90% clinical improvement in non-epileptic paroxysmal manifestations and a normalised brain bioenergetics profile in patients with GLUT1-DS.

**Trial registration number** NCT02014883.

**INTRODUCTION**

Glucose transporter type 1 deficiency syndrome (GLUT1-DS) is caused by impaired glucose transport across the blood–brain barrier and into astrocytes, leading to cerebral energy deficiency.<sup>1</sup> GLUT1-DS is caused by mutation in the *SLC2A1* gene encoding the glucose transporter GLUT1. The phenotype typically comprises psychomotor retardation and permanent motor disorders, associated with paroxysmal manifestations including seizures and non-epileptic paroxysmal episodes.<sup>1,2</sup> With age, seizures tend to become less prominent, whereas the frequency of non-epileptic paroxysmal episodes increases.<sup>3</sup> In patients with milder forms of the disease, paroxysmal movement disorders,

especially dyskinesia, may be the main or the sole manifestations of the disease and can occur at any age.<sup>3,4</sup> Ketogenic diets, which provide ketone bodies to the brain and compensate for the lack of glucose, represent the standard of care in GLUT1-DS<sup>1,5</sup> and are efficient on seizures control but less on movement disorders.<sup>2</sup> Moreover, many patients, especially adolescents and adults, have difficulties in complying with the difficult constraints of these long-term diets and their side effects.

Triheptanoin is an odd-chain triglyceride with anaplerotic properties—that is, replenishing the pool of metabolic intermediates in the Krebs cycle. Unlike even-chain fatty acids metabolised to acetyl-CoA only, triheptanoin can indeed provide both acetyl-CoA and propionyl-CoA, two key carbon sources for the Krebs cycle. We showed that triheptanoin was able to produce C5-ketone bodies and restore energy metabolism and neurotransmission in pyruvate carboxylase (PC) deficiency, a severe metabolic disease that affects anaplerosis in the brain.<sup>6</sup> Recently, we demonstrated that triheptanoin is able to correct bioenergetics in the brain of patients with Huntington's disease (HD), a neurodegenerative disease associated with brain energy deficit.<sup>7</sup> Here, we wished to obtain a proof-of-concept of the therapeutic effect of triheptanoin in patients with GLUT1-DS with non-epileptic paroxysmal manifestations for whom a ketogenic diet was not a therapeutic option.

**SUBJECTS AND METHODS**

Participants were enrolled in an interventional clinical protocol (NCT02014883) at the Pitié-Salpêtrière Hospital promoted by INSERM and approved by the local ethical committee. All participants and/or their legal guardians signed a written informed consent before participating in the study. Four children and four adults were enrolled with GLUT1-DS as defined by low cerebrospinal fluid to blood glucose ratio and a *SLC2A1* missense mutation predicted to be pathogenic by prediction software programs. Patients had a chronic history of non-epileptic paroxysmal motor disorders, especially paroxysmal exercise-induced dyskinesia, non-kinesigenic dyskinesia, limb weakness, headache, drowsiness and dysphoria. Three patients also presented a mild cognitive deficit. All patients were on a normal diet prior to their enrolment as either they objected to or did not tolerate ketogenic diets. The

**To cite:** Mochel F, Hainque E, Gras D, et al. *J Neurol Neurosurg Psychiatry* Published Online First: [please include Day Month Year] doi:10.1136/jnnp-2015-311475

## Movement disorders

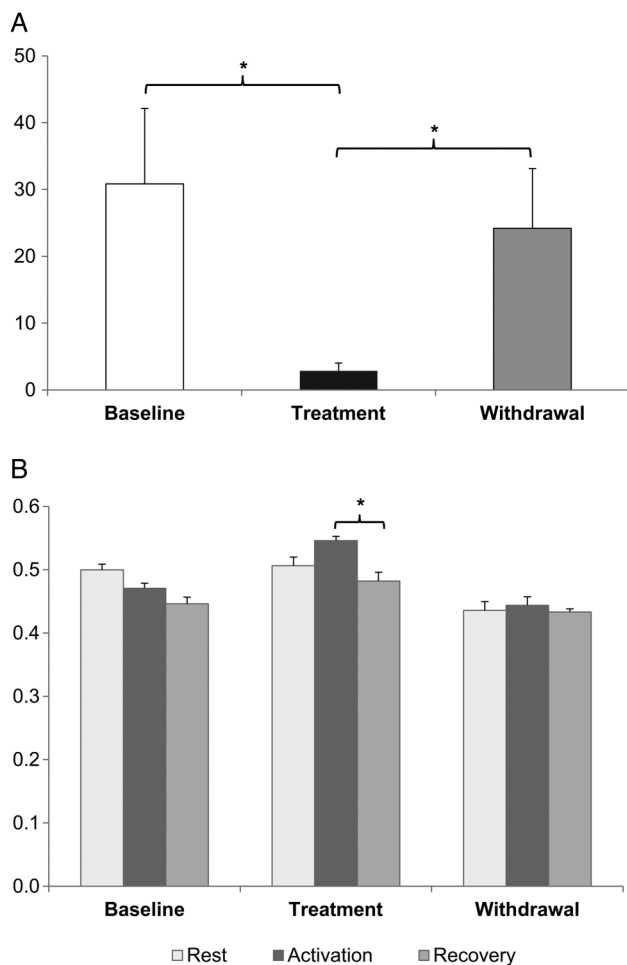
study was divided into three phases of 2 months each (baseline, treatment and withdrawal). A trained dietician determined the patient's caloric intake and adjusted their daily menus so that their diet remained isocaloric when triheptanoin was introduced. During the treatment phase, each patient was required to ingest 1 g/kg body-weight of triheptanoin per day, divided into 3–4 intakes during meals.

During each study phase, the patients and/or their legal guardians had to fill a comprehensive patient diary to record all motor (seizure, abnormal movement, body stiffness, body weakness, abnormal speech) and non-motor (headache, lethargy, mood swing) paroxysmal events (see online supplementary table e1). The approximate duration of each episode was recorded

(minutes). At each visit, recordings of all paroxysmal events were reviewed with the evaluating physician and items were grouped into motor and non-motor episodes. At each visit, patients were also evaluated with a 6 min walk test (6MWT), a nine-hole peg-board test (9HPT) and the clinical global impression-improvement scale (CGI-I). The 6MWT was performed in a corridor, between two cones separated by a distance of 25 m, in order to get the maximal distance covered during 6 min by walking. Both the dominant and non-dominant hands were tested twice during the 9HPT and the best score for each hand was recorded. Blood samples were collected after an overnight fast for standard analyses, plasma C3-carnitine and C5-ketone bodies.<sup>6</sup>

To assess the effect of triheptanoin on brain energy metabolism, functional <sup>31</sup>P-NMR spectroscopy (f-MRS) was performed at 3 T at the end of each study phase in patients >15 years old (n=5). We targeted the visual cortex using a surface coil as it is easily stimulated and is close to the scalp, allowing an increased sensitivity to the surface coil. Furthermore, visual stimulation results in a large increase in glucose uptake and cerebral blood flow.<sup>8</sup> Data were collected for 4 min at rest, 8 min during visual activation, 8 min after stimulation and analysed as described.<sup>7,9</sup> The ratio of inorganic phosphate over phosphocreatine (Pi/PCr) was calculated to determine the brain response to cortical activation as it is directly related to the ADP levels which regulate mitochondrial oxidative metabolism.<sup>10</sup>

Paired t tests were used for plasma analyses before and after treatment. For clinical parameters, Friedman tests were used to test the global hypothesis that all study phases were equal. If significant, Wilcoxon signed-rank tests were applied for pairwise phase comparisons with an  $\alpha$  of 0.05. For the Pi/PCr ratio, repeated measures analysis of variance (ANOVA) were used to test the global hypothesis that all time points (rest, activation and recovery) were equal. If significant, paired t tests were applied for pairwise time comparisons with an  $\alpha$  of 0.05.



**Figure 1** (A) Number of total paroxysmal manifestations in patients with glucose transporter type 1 deficiency syndrome (GLUT1-DS) during the three phases of the study (baseline, treatment and withdrawal) of 2 months each. A significant reduction of non-epileptic paroxysmal manifestations was observed when patients were treated with triheptanoin for 2 months (\* $p < 0.05$ ). Of note, the total number of events was comparable between the baseline and withdrawal phases. Error bars represent SEM. (B) Changes in the inorganic phosphate and phosphocreatine (Pi/PCr) ratio from <sup>31</sup>P-NMR spectroscopy (f-MRS) studies during the three phases of the study (baseline, treatment and withdrawal). During baseline, f-MRS showed an abnormal brain energy profile in patients with GLUT1-DS with no change in the Pi/PCr ratio during visual stimulation. After 2 months of treatment with triheptanoin, the profile was corrected and we observed an increase in the Pi/PCr ratio during visual stimulation followed by a decrease during recovery (\* $p = 0.021$ ). Error bars represent SEM of within-subject differences using the method of Morey.

**Table 1** Main characteristics of patients with GLUT1-DS during the baseline, treatment and withdrawal phases

	Patients						Mean
	P1	P2	P3	P4	P5	P6	
Sex	F	F	M	M	M	M	
Age	23	20	7	14	16	47	21.2
<b>Baseline</b>							
Total events	10	20	13	26	31	85	30.8
Motor events	6	16	10	1	12	54	16.5
6MWT (m)	502	558	458	514	471	504	501
9HPT(D/ND) (s)	17/18	18/23	19/21	15/17	18/22	14/16	17/19
<b>Treatment</b>							
Total events	4	7	5	0	1	0	2.8
Motor events	2	7	3	0	1	0	2.2
6MWT (m)	453	580	425	484	496	500	490
9HPT(D/ND) (s)	17/19	17/20	19/19	17/21	17/18	15/18	17/19
<b>Withdrawal</b>							
Total events	10	11	5	20	36	63	24.2
Motor events	9	9	1	1	15	40	12.5
6MWT (m)	532	528	461	496	475	510	500
9HPT(D/ND) (s)	15/22	14/20	17/17	17/19	18/20	15/15	16/19

Total events: all motor and non-motor paroxysmal manifestations during each 2-month-phase. Motor events: all motor paroxysmal episodes during each 2-month-phase. 6MWT: Total distance walked (metres). 9HPT-D: the best score (seconds) obtained with the dominant hand. 9HPT-ND: best score (seconds) with the non-dominant hand. GLUT1-DS, glucose transporter type 1 deficiency syndrome; 6MWT, 6 min walk test; 9HPT, nine-hole pegboard test



## Movement disorders

Shire-HGT. RS has a patent application regarding the use of triheptanoin in GLUT1-DS (WO2014093901). RS received research support and honoraria from Genzyme Corporation, Shire and Amicus Therapeutics. JY-H received research funding from Roche and Valerion therapeutics. LS received research funding from Roche and Valerion therapeutics. ER received research funding from Merz-Pharma, Orkyn, IP santé and Ultragenyx; served on scientific advisory boards for Orkyn and Merz-pharma; received speech honorarium from Merz-pharma, Novartis, Ipsen-Pharma and Orkyn, received travel funding from Ipsen-Pharma, Teva, Abbvie and Merz-Pharma.

**Patient consent** Obtained.

**Ethics approval** Comité de Protection des Personnes, Ile-de-France VI (Paris 6).

**Provenance and peer review** Not commissioned; externally peer reviewed.

**Open Access** This is an Open Access article distributed in accordance with the Creative Commons Attribution Non Commercial (CC BY-NC 4.0) license, which permits others to distribute, remix, adapt, build upon this work non-commercially, and license their derivative works on different terms, provided the original work is properly cited and the use is non-commercial. See: <http://creativecommons.org/licenses/by-nc/4.0/>

## REFERENCES

- De Vivo DC, Trifiletti RR, Jacobson RI, *et al*. Defective glucose transport across the blood-brain barrier as a cause of persistent hypoglycorrhachia, seizures, and developmental delay. *N Engl J Med* 1991;325:703–9.
- Leen WG, Klepper J, Verbeek MM, *et al*. Glucose transporter-1 deficiency syndrome: the expanding clinical and genetic spectrum of a treatable disorder. *Brain* 2010;133:655–70.
- Gras D, Roze E, Caillet S, *et al*. GLUT1 deficiency syndrome: an update. *Rev Neurol (Paris)* 2014;170:91–9.
- Pons R, Collins A, Rotstein M, *et al*. The spectrum of movement disorders in Glut-1 deficiency. *Mov Disord* 2010;25:275–81.
- Klepper J, Leiendecker B. Glut1 deficiency syndrome and novel ketogenic diets. *J Child Neurol* 2013;28:1045–8.
- Mochel F, DeLonlay P, Touati G, *et al*. Pyruvate carboxylase deficiency: clinical and biochemical response to anaplerotic diet therapy. *Mol Genet Metab* 2005;84:305–12.
- Adanyeguh IM, Rinaldi D, Henry PG, *et al*. Triheptanoin improves brain energy metabolism in patients with Huntington disease. *Neurology* 2015;84:490–5.
- Sappey-Marinié D, Calabrese G, Fein G, *et al*. Effect of photic stimulation on human visual cortex lactate and phosphates using <sup>1</sup>H and <sup>31</sup>P magnetic resonance spectroscopy. *J Cereb Blood Flow Metab* 1992;12:584–92.
- Mochel F, N'Guyen TM, Deelchand D, *et al*. Abnormal response to cortical activation in early stages of Huntington disease. *Mov Disord* 2012;27:907–10.
- Chance B, Eleff S, Leigh JS, *et al*. Mitochondrial regulation of phosphocreatine/inorganic phosphate ratios in exercising human muscle: a gated <sup>31</sup>P NMR study. *Proc Natl Acad Sci USA* 1981;78:6714–18.
- Kim TH, Borges K, Petrou S, *et al*. Triheptanoin reduces seizure susceptibility in a syndrome-specific mouse model of generalized epilepsy. *Epilepsy Res* 2013;103:101–5.
- Marin-Valencia I, Good LB, Ma Q, *et al*. Heptanoate as a neural fuel: energetic and neurotransmitter precursors in normal and glucose transporter I-deficient (G1D) brain. *J Cereb Blood Flow Metab* 2013;33:175–82.
- Hadera MG, Smeland OB, McDonald TS, *et al*. Triheptanoin partially restores levels of tricarboxylic acid cycle intermediates in the mouse pilocarpine model of epilepsy. *J Neurochem* 2014;129:107–19.
- Francis JS, Markov V, Leone P. Dietary triheptanoin rescues oligodendrocyte loss, dysmyelination and motor function in the nur7 mouse model of Canavan disease. *J Inher Metab Dis* 2014;37:369–81.
- Pascual JM, Liu P, Mao D, *et al*. Triheptanoin for glucose transporter type I deficiency (G1D): modulation of human ictogenesis, cerebral metabolic rate, and cognitive indices by a food supplement. *JAMA Neurol* 2014;71:1255–65.



## Triheptanoin dramatically reduces paroxysmal motor disorder in patients with GLUT1 deficiency

Fanny Mochel, Elodie Hainque, Domitille Gras, Isaac M Adanyeguh, Samantha Caillet, Bénédicte Héron, Agathe Roubertie, Elsa Kaphan, Romain Valabregue, Daisy Rinaldi, Sandrine Vuillaumier, Raphael Schiffmann, Chris Ottolenghi, Jean-Yves Hogrel, Laurent Servais and Emmanuel Roze

*J Neurol Neurosurg Psychiatry* published online November 3, 2015

---

Updated information and services can be found at:

<http://jnnp.bmj.com/content/early/2015/11/03/jnnp-2015-311475>

---

*These include:*

### Supplementary Material

Supplementary material can be found at:

<http://jnnp.bmj.com/content/suppl/2015/11/02/jnnp-2015-311475.DC1.html>

### References

This article cites 15 articles, 4 of which you can access for free at:

<http://jnnp.bmj.com/content/early/2015/11/03/jnnp-2015-311475#BIBL>

### Open Access

This is an Open Access article distributed in accordance with the Creative Commons Attribution Non Commercial (CC BY-NC 4.0) license, which permits others to distribute, remix, adapt, build upon this work non-commercially, and license their derivative works on different terms, provided the original work is properly cited and the use is non-commercial. See: <http://creativecommons.org/licenses/by-nc/4.0/>

### Email alerting service

Receive free email alerts when new articles cite this article. Sign up in the box at the top right corner of the online article.

---

### Topic Collections

Articles on similar topics can be found in the following collections

[Open access](#) (187)

---

### Notes

---

To request permissions go to:

<http://group.bmj.com/group/rights-licensing/permissions>

To order reprints go to:

<http://journals.bmj.com/cgi/reprintform>

To subscribe to BMJ go to:

<http://group.bmj.com/subscribe/>